Development and Application of Finite-Temperature Green's Function Methods in Quantum Chemistry

by

Alexei A. Kananenka

A dissertation submitted in partial fulfillment
of the requirements for the degree of
Doctor of Philosophy
(Chemistry)
in the University of Michigan
2017

Doctoral Committee:

Assistant Professor Dominika K. Zgid, Chair
Professor Eitan Geva
Assistant Professor Emanuel Gull
Professor Adam J. Matzger

Alexei A. Kananenka

akanane@umich.edu

ORCID iD: 0000-0001-9422-7203

Посвящается моим дорогим родителям,
Анатолию Петровичу и Ольге Владимировне Кононенко
(To my dear parents, Anatolii and Olga Kananenka)

Acknowledgments

I wish to express my gratitude and admiration for my advisor, Professor Dominika Zgid. I am indebted to Dominika for believing in me and for letting me join her group. Her encouragement, enthusiasm, and guidance was invaluable during my Ph.D. Dominika helped me to learn how to plan and prioritize research projects, how to give a very professional and easy to follow presentations, how to be critical and open-minded researcher. Under Dominika's supervision I became a better scientist and a better person. Her dedication to research and teaching will remain the model and the reference to me for a long time. Her door was always open for research and career-related questions. She always maintained a very friendly and supportive atmosphere in the group. Finally, I am thankful for Dominika's support in my fellowship and postdoc applications throughout all these years. It has been a privilege and pleasure to work with Dominika.

I am thankful to Professor Emanuel Gull for his help with several projects. He taught me how to approach and understand a new concept with confidence. Our discussions about many-body theory, dynamical mean field theory and numerical algorithms were extremely valuable. Last, but not least, I would like to thank Emanuel for supporting my fellowship and postdoc applications.

I would like to thank Professor Eitan Geva for supervising my rotation project and introducing me to the field of quantum dynamics. Multiple discussions with Eitan have changed my perspective on the field. I will always remember Eitan's detail oriented approach to research and teaching. I am thankful to Eitan for helping me with my fellowship and postdoc applications and with my career choices.

I thank Professor Adam Matzger for tracking my progress as my thesis committee member and his guidance in my future career.

I want to thank Dr. Alexander Rusakov for being my colleague and a friend. A great deal of my theoretical and practical knowledge of quantum chemistry, condensed matter physics and mathematical analysis stemmed from our multiple discussions. I am thankful to Alexander for critical reading of my manuscripts and extremely valuable suggestions how to improve my writing skills.

I want to thank Dr. Jordan Phillips for many hours we spent discussing research and American popular culture. Several interesting ideas for research projects emerged during our lengthy conversations at ACS conference in Boston, MA. I am especially thankful to Jordan for our very smooth and productive work on several projects.

I am thankful to the current and former members of the Zgid group—Alicia Welden, Blair Winograd, Dr. Avijit Shee, Dr. Tran Lan, Yao Li, Yike Liu and Ryan Whitcomb for the science we did together and for the friendly and enjoyable atmosphere they all maintained.

I want to acknowledge Dr. Alexander Schubert, Dr. Xiang Sun, Dr. Chang-Yu Hsieh for the opportunity to do research together. I learned a lot from working with you.

Last but certainly not least, I want to thank my family for their love and support throughout all these years. I am sure they are very happy to see me finishing my Ph.D. I could not be where I am without you.

This thesis summarizes results of scientific research conducted by the author, Alexei Kananenka under the supervision of Prof. Dominika Zgid and in a collaboration with members of Prof. Zgid's group: Dr. Tran Nguyen Lan, Dr. Jordan Phillips, Alicia Welden, and Prof. Emanuel Gull (University of Michigan).

Chapter 2 is based on the article "Systematically improvable multiscale solver for correlated electron systems" [Physical Review B **91 (12)**, 121111(R) (2015)] by A.

A. Kananenka, E. Gull and D. Zgid. The project was proposed by Dr. Zgid. Alexei Kananenka adopted existing GF2 computer code to Hubbard model and wrote the DCA computer code.

Chapter 3 is based on the article "Fractional charge and spin errors in self-consistent Green's function theory" [The Journal of Chemical Physics **142 (19)**, 194108 (2015)] by J. J. Phillips, A. A. Kananenka and D. Zgid. Alexei Kananenka adjusted existing computer code for fractional charge HF and DFT methods and performed corresponding calculations. Alexei Kananenka and Prof. Zgid participated in revising of the manuscript.

Chapter 4 is based on the article "Towards ab initio self-energy embedding theory in quantum chemistry" [The Journal of Chemical Physics **143 (24)**, 241102 (2015)] by T. N. Lan, A. A. Kananenka and D. Zgid. The project was proposed by Dr. Zgid. Alexei Kananenka participated in writing a computer code and obtaining the results.

Chapter 5 is based on the article "Efficient Temperature-Dependent Green's Functions Methods for Realistic Systems: Compact Grids for Orthogonal Polynomial Transforms" [Journal of Chemical Theory and Computation **12 (2)**, 564571 (2016)] by A. A. Kananenka, J. J. Phillips and D. Zgid. Alexei Kananenka adopted existing computer code, performed all the calcualtions and drafted the manuscript.

Chapter 6 is based on the article "Efficient Temperature-Dependent Green's Function Methods for Realistic Systems: Using Cubic Spline Interpolation to Approximate Matsubara Green's Functions" [Journal of Chemical Theory and Computation **12 (5)**, 22502259 (2016)] by A. A. Kananenka, A. R. Welden, T. N. Lan, E. Gull and D. Zgid. Alexei Kananenka adopted existing computer code, performed all the calculations except for LW functional. A. Welden wrote a computer code for LW functional and performed corresponding calculations. Alexei Kananenka drafted the manuscript, which was finalized by Prof. Gull and Prof. Zgid.

Chapter 7 is based on the article "Rigorous Ab Initio Quantum Embedding for

Quantum Chemistry Using Green's Function Theory: Screened Interaction, Nonlocal Self-Energy Relaxation, Orbital Basis, and Chemical Accuracy" [Journal of Chemical Theory and Computation **12 (10)**, 48564870 (2016)] by T. N. Lan, A. A. Kananenka and D. Zgid. Alexei Kananenka attached TRIQS code to SEET computer code and performed all corresponding calculations. Also Alexei Kananenka wrote a computer code based on existing GAUSSIAN code for orbital localization and performed corresponding calculations.

Chapter 8 is based on the article "Combining Density Functional Theory and Green's Function Theory: Range-Separated, Non-local, Dynamic, and Orbital-Dependent Hybrid Functional" [arXiv:1707.00595] by A. A. Kananenka and D. Zgid. Alexei Kananenka proposed the details of the project, wrote a computer code, performed all the calcualtions and drafted the manuscript, which was finalized Prof. Zgid.

Contents

List of Figures

List of Tables

List of Abbreviations

B3LYP	—	Becke, three-parameter, Lee–Yang–Parr hybrid
C	—	correlation
CASPT2	—	complete active space second-order perturbation theory
CASSCF	—	complete active space self-consistent field
CT-HYB	—	continuous-time quantum Monte Carlo hybridization expansion
CT-QMC	—	continuous-time quantum Monte Carlo
DFT	—	density functional theory
DMFT	—	dynamical mean-field theory
DMRG	—	density matrix renormalization group
ED	—	exact diagonalization
FCI	—	full configuration interaction
FFT	—	fast Fourier transform
FLEX	—	fluctuation-exchange approximation
GF2	—	second-order Green's function theory
HF	—	Hartree–Fock
IP	—	ionization potential
LDA	—	local density approximation
MP2	—	Second-order Møller–Plesset perturbation theory

NEVPT2 — n-electron valence state second-order perturbation theory

NO — natural orbitals

PBEh — Perdew–Burke–Ernzerhof hybrid

RASCI — restricted active space configuration interaction

RNO — regionalized natural orbitals

RPA — random phase approximation

S — Slater

SEET — self-energy embedding theory

SIE — self-interaction error

VWN — Vosko–Wilk–Nusair

X — exchange

XC — exchange-correlation

List of Symbols

E_h	—	atomic unit of energy (1 hartree = 2625.50 kJ·mol^{-1}= 27.2114 eV)
a_0	—	Bohr radius (1 $a_0 = 5.29177211\times10^{-11}$ m)
k_B	—	Boltzmann constant ($k_B = 1.38064852\times10^{-23}$ m^2·kg·s^{-2}·K^{-1})
e	—	elementary charge ($e = 1.60217657\times10^{-19}$ C
$\hbar$	—	reduced Planck constant ($\hbar = 1.05457180\times10^{-34}$ J·s·rad^{-1})
Ω	—	grand potential
$G(\tau)$	—	imaginary time Green's function
$\Sigma(\tau)$	—	imaginary time self-energy
$G(i\omega_n)$	—	imaginary frequency Green's function
$\Sigma(i\omega_n)$	—	imaginary frequency self-energy
Φ	—	Luttinger–Ward functional
$i\omega_n$	—	Matsubara frequency
$\mathbf{r}$	—	position vector

Abstract

Recent progress in materials synthesis combined with advances in computational science have opened up an opportunity to design new materials with specific properties. Semiconductors, heterostructures, and thin layered films are used for energy harvesting and solar cells. Transition metal oxides and metallic surfaces with deposited magnetic molecules are used for signal conversion, nonvolatile memory modules and spintronics. Due to growing complexity of the new materials the most efficient approach to their design requires combined experimental and theoretical effort. In order to advance our understanding of the complicated physics of the modern materials new theoretical methods based on controlled, reliable, computationally efficient and systematically improvable approximations describing correlation and finite-temperature effects are needed.

Density functional theory (DFT) remains a method of choice for materials science calculations due to its low computational cost. However, despite all recent efforts, the majority DFT applications are limited to weakly correlated systems and zero temperature. The lack of systematic improvability, inaccurate treatment of strongly correlated systems will continue to restrict the domain of DFT applications.

The multi-reference wave-function methods can provide an accurate description of the strongly correlated systems. Unfortunately, these methods are computationally expensive. In spite of recent improvement the computational complexity will likely to hinder the applications of wave-function based methods to materials science in foreseeable future.

Finite-temperature Green's function methods offer several advantages such as systematic improvability, access to the excitation spectrum, thermodynamic properties and straightforward implementation of embedding frameworks. It has been realized

long time ago and has been successfully used in condensed matter physics to study model systems. The applications of such methods to realistic systems are impeded due to lack of theoretical approaches providing chemical accuracy and efficient computational algorithms.

In this dissertation, these shortcomings are addressed by developing self-energy embedding theory and its extensive comparison to established quantum chemistry methods. New numerical algorithms for efficient application of the finite-temperature Green's function methods to molecular and extended systems were developed. Properties of the second-order Green's function theory (GF2) in the context of quantum chemistry were investigated. Additionally, a new range-separated hybrid functional combining GF2 and DFT was developed and benchmarked.

Chapter 1

Introduction

Dem Anwenden muss das Erkennen vorausgehen.

Insight must precede application.

Max Planck

1.1 From wave functions to Green's functions

1.1.1 Wave functions

It was a long time ago when computational quantum chemistry was considered a subject of purely academic interest. Since the 1960s, the discipline has grown dramatically to become an equal partner in all areas of chemical research ranging from organic synthesis to solid state chemistry, from biology to material sciences, from astrophysics to chemical engineering. Recent advances of computational methods together with the increasing computational power have made possible routine applications of quantum chemistry methods to solve problems that only few years ago seemed to be beyond the reach of rigorous quantum-mechanical treatment. Developments in quantum chemistry have also created a productive overlap with mathematics, theoretical physics and statistical mechanics.

One of the central challenges of quantum chemistry is the solution of the time-

independent, non-relativistic Born–Oppenheimer electronic Schrödinger equation

$$\hat{H}\Psi = E\Psi, \tag{1.1}$$

where E is the electronic energy, $\Psi = \Psi(\mathbf{x}_1, \mathbf{x}_2, \ldots, \mathbf{x}_n)$ is the wave function, and $\mathbf{x} = (\mathbf{r}, \sigma)$ represents the spatial $\mathbf{r}$ and spin σ coordinates collectively. The Hamiltonian $\hat{H}$ is given by (atomic units $\hbar = e^2 = m_e = 1$ are assumed throughout)

$$\hat{H} = \hat{T} + \hat{V}_{ne} + \hat{V}_{ee}, \tag{1.2}$$

where

$$\hat{T} = -\sum_{i=1}^{n} \frac{1}{2}\nabla_i^2 \tag{1.3}$$

is the kinetic energy operator,

$$\hat{V}_{ne} = -\sum_{i=1}^{n}\sum_{I=1}^{N} \frac{Z_I}{|\mathbf{r}_i - \mathbf{r}_I|} \tag{1.4}$$

is the electron-nucleus interaction energy operator, and

$$\hat{V}_{ee} = \sum_{i>j=1}^{n} \frac{1}{|\mathbf{r}_i - \mathbf{r}_j|} \tag{1.5}$$

is the electron-electron interaction energy operator. The Schrödinger equation describes a system of n electrons moving in the field of N nuclei with atomic numbers Z_I, $\mathbf{r}_i$ and $\mathbf{r}_I$ are the coordinate vectors of electron i and nuclei I, respectively. Equation 1.1 must be solved subject to appropriate boundary conditions.

The square of the wave function

$$|\Psi(\mathbf{x}^n)|^2 = \Psi(\mathbf{x}_1, \mathbf{x}_2, \ldots, \mathbf{x}_n)\Psi^*(\mathbf{x}_1, \mathbf{x}_2, \ldots, \mathbf{x}_n), \tag{1.6}$$

is the probability density and $|\Psi(\mathbf{x}^n)|d\mathbf{r}^n$ is a probability of finding the system with position coordinates between $\mathbf{r}^n$ and $\mathbf{r}^n + d\mathbf{r}^n$ and spin coordinates equal to σ^n. Where $d\mathbf{r}^n = d\mathbf{r}_1 d\mathbf{r}_2 \dots d\mathbf{r}_n$, $\mathbf{x}^n$ stands for the set $\mathbf{x}_1, \mathbf{x}_2, \dots, \mathbf{x}_n$, and σ^n stands for the set $\sigma_1, \sigma_2, \dots, \sigma_n$. The exact wave function Ψ satisfies the following properties:

1. The wave function is antisymmetric with respect to the permutation of any pair of electrons

$$P_{ij}\Psi = -\Psi, \tag{1.7}$$

   where P_{ij} is the permutation operator.

2. It is a square-integrable and, therefore, normalizable function

$$\langle\Psi|\Psi\rangle = 1. \tag{1.8}$$

3. The wave function is an eigenstate of a particle number operator

$$\hat{n}|\Psi\rangle = n|\Psi\rangle. \tag{1.9}$$

4. The energy obtained by solving Schrödinger equation is stable with respect to all possible variations $\delta\Psi$ which are orthogonal to the exact wave function

$$\langle\delta\Psi|\Psi\rangle = 0, \quad \langle\delta\Psi|\hat{H}\Psi\rangle = 0. \tag{1.10}$$

5. The exact wave function is size-extensive. This means that for a system composed of noninteracting subsystems, the total energy is the sum of the energies of the individual subsystems.

6. The exact stationary states are eigenfunctions of the total and projected spin

operators[1]

$$S^2\Psi = S(S+1) \quad \text{and} \quad S_z\Psi = M\Psi. \tag{1.11}$$

7. The exact stationary states under Born–Oppenheimer approximation serve as a basis for an irreducible representation of the molecular point group. This also means that the wave function is an eigenfunction of the orbital angular momentum operators

$$L^2\Psi = L(L+1)\Psi \quad \text{and} \quad L_z\Psi = M_L\Psi. \tag{1.12}$$

8. At the electron coalescence the molecular Hamiltonian becomes singular. This is reflected in the exact wave function as a characteristic Coulomb cusp condition

$$\lim_{r_{ij}\to 0} \left\langle \frac{\partial\Psi}{\partial r_{ij}} \right\rangle_{sph} = \frac{1}{2}\Psi(r_{ij}=0), \tag{1.13}$$

   where $r_{ij} = |\mathbf{r}_i - \mathbf{r}_j|$ and $\langle \ldots \rangle_{sph}$ denotes the spherical average.

9. All molecular properties calculated from the exact wave function are invariant under gauge transformation of the potentials of electromagnetic fields.

Using wave function formalism the expectation value of a general n-electron operator $\hat{O}_n$ can is obtained from

$$\langle \hat{O}_n \rangle = \int d\mathbf{x}_1 \int d\mathbf{x}_2 \ldots \int d\mathbf{x}_n \Psi^*(\mathbf{x}_1, \mathbf{x}_2, \ldots, \mathbf{x}_n)\hat{O}_n\Psi(\mathbf{x}_1, \mathbf{x}_2, \ldots, \mathbf{x}_n). \tag{1.14}$$

The ground state wave function Ψ_0 and ground state energy E_0 can be found using the variational principle for the ground state. The expectation value of the energy is

[1] In the exact nonrelativistic theory.

given by the following expression

$$E[\Psi] = \frac{\langle \Psi | \hat{H} | \Psi \rangle}{\langle \Psi | \Psi \rangle}, \tag{1.15}$$

where

$$\langle \Psi | \hat{H} | \Psi \rangle = \int d\mathbf{x}_1 \int d\mathbf{x}_2 \ldots \int d\mathbf{x}_n \Psi^*(\mathbf{x}_1, \mathbf{x}_2, \ldots, \mathbf{x}_n) \hat{H} \Psi(\mathbf{x}_1, \mathbf{x}_2, \ldots, \mathbf{x}_n). \tag{1.16}$$

The minimization of a functional $E[\Psi]$ with respect to all allowed n-electron wave functions will give the ground state wave function Ψ_0 and ground state energy E_0

$$E_0 = \min_{\Psi} E[\Psi] \quad \text{and} \quad E[\Psi_0] = E_0. \tag{1.17}$$

If instead of the exact wave function an approximate one $\overline{\Psi}$ is used then the energy will correspond to the upper bound of the true ground state energy: $E[\overline{\Psi}] > E[\Psi], \forall \overline{\Psi} \neq \Psi$.

1.1.2 The Hartree–Fock approximation

Solving Eq. 1.1 for realistic many-electron systems is an inconceivably difficult task since the wave function Ψ describes the correlated motion of n interacting electrons. One approximate wave function that satisfies the constraints explained above can be constructed as an antisymmetrized product of n orthonormal spin orbitals $\phi_p(\mathbf{x})$, as a product of spatial $\phi_p(\mathbf{r})$ and spin $\alpha(\sigma)$ or $\beta(\sigma)$ functions, and represented by the *Slater*

determinant

$$\Phi(\mathbf{x}_1, \mathbf{x}_2, \ldots, \mathbf{x}_n) = \frac{1}{\sqrt{n!}} \begin{vmatrix} \phi_1(\mathbf{x}_1) & \phi_2(\mathbf{x}_1) & \ldots & \phi_n(\mathbf{x}_1) \\ \phi_1(\mathbf{x}_2) & \phi_2(\mathbf{x}_2) & \ldots & \phi_n(\mathbf{x}_2) \\ \vdots & \vdots & \ddots & \vdots \\ \phi_1(\mathbf{x}_n) & \phi_2(\mathbf{x}_n) & \ldots & \phi_n(\mathbf{x}_n) \end{vmatrix}. \tag{1.18}$$

The Hartree–Fock approximation [1] amounts to finding orthonormal orbitals $\phi_p(\mathbf{x})$ that minimize Eq. 1.15 for the expectation value of the energy

$$E_{HF}[\Phi] = \frac{\langle \Phi | \hat{H} | \Phi \rangle}{\langle \Phi | \Phi \rangle}. \tag{1.19}$$

The exact wave function Ψ of an interacting many-body system is never a single Slater determinant. Since the minimization is restricted to the wave function of the form of Eq. 1.18 the Hartree–Fock energy E_{HF} is always higher than the exact ground state energy of a system. The difference between exact energy of an n-electron system and the Hartree–Fock energy of the same system is called *correlation energy*

$$E_c = E - E_{HF}. \tag{1.20}$$

It is always negative for the reasons explained above. Nowadays extensive research is being carried out in the field of explicitly correlated quantum chemistry methods. Most of these methods use the Slater determinant as the reference wave function and build the correlated wave function on top of it. One drawback that nearly every wave-function method faces is the excruciatingly complicated structure of the wave function. For n electron system the wave function is the function of $3n$ spatial and n spin degrees of freedom. Moreover the total number of n-electron Slater determinants required to describe the exact wave function grows as $\binom{n}{K}$, where K is the number of spin orbitals

$\phi_p(\mathbf{x})$. Thus for even small molecules this number of truly huge. For example, for benzene molecule (C_6H_6) in a moderate basis set the number of Slater determinants in the expansion is approximately 10^{28}. This leads us to a very important question: Can the wave function formalism be avoided and its role be passed over to simpler physical quantities? The next section introduces several such quantities: electron density, reduced density matrices and Green's functions. For a long time the two-electron reduced density matrix was deemed to be the simplest mathematical object necessary to describe a real many-electron system. However in 1964 Walter Kohn and Pierre Hohenberg showed that a very simple one-electron quantity—electron density can be used as a basic variable in the electronic structure calculations to predict exact ground state energy of an interacting many-body system [2]. They reduced the problem of solving a many-body Schrödinger equation 1.1 to a problem of minimization of a density functional. This idea was later became a workhorse of a modern Kohn–Sham density functional theory [3]. Within this framework the intractable many-body problem of interacting electrons in a static external potential is reduced to a tractable problem of non-interacting electrons moving in some effective potential. This potential includes the external potential, as well as electronic exchange and correlation effects. Apparent simplicity of this approach is, however, deceptive. While the existence and uniqueness of exchange-correlation functional are guaranteed, its form is not known, and sufficiently accurate explicit approximations have not yet emerged. The problem is worsened by the absence of systematic ways of improving density functionals. Therefore, the search for a simple quantity, yet allowing for a systematic improvement towards the exact description of a realistic many-body systems is still open.

1.1.3 Reduced density matrices

In this section we consider a more general description of quantum states that cannot be described by a wave function. The first step is to generalize Eq. 1.6 to include two

sets of variables and introduce a new symbol γ

$$\gamma(\mathbf{x}_1, \mathbf{x}_2, \ldots, \mathbf{x}_n; \mathbf{x}'_1, \mathbf{x}'_2, \ldots, \mathbf{x}'_n) = \Psi(\mathbf{x}_1, \mathbf{x}_2, \ldots, \mathbf{x}_n)\Psi^*(\mathbf{x}'_1, \mathbf{x}'_2, \ldots, \mathbf{x}'_n) \tag{1.21}$$

The two sets of independent variables in Eq. 1.21 can be thought of as two sets of indices denoting an element of a matrix

$$\langle \mathbf{x}_1, \mathbf{x}_2, \ldots, \mathbf{x}_n | \hat{\gamma} | \mathbf{x}'_1, \mathbf{x}'_2, \ldots, \mathbf{x}'_n \rangle = \gamma(\mathbf{x}_1, \mathbf{x}_2, \ldots, \mathbf{x}_n; \mathbf{x}'_1, \mathbf{x}'_2, \ldots, \mathbf{x}'_n). \tag{1.22}$$

Equivalently Eq. 1.22 can be understood as a coordinate representation of the Hermitian operator called *density operator* $\hat{\gamma}$.

At zero temperature $\hat{\gamma}$ is represented by a pure state $\hat{\gamma} = |\Psi\rangle\langle\Psi|$, where a ket vector $|\Psi\rangle$ denotes the state in the Hilbert space. The expectation value of an operator $\hat{O}_n$ is given by

$$\langle \hat{O}_n \rangle = \mathrm{Tr}\left[\hat{\gamma}\hat{O}_n\right], \tag{1.23}$$

where Tr[$\cdot$] denotes a trace. The density matrix formalism becomes necessary when the state of the system cannot be described by a wave function. This happens when the system of interest is part of a larger closed system or when the system is in thermal equilibrium with other macroscopic systems. In such case it is impossible to write a system's Hamiltonian in terms of only systems degrees of freedom. Thereby the wave function formalism cannot be applied. Pure states can be described by the wave function, while mixed states cannot. In latter case the density operator is generalized to the *ensemble density operator*

$$\hat{\Gamma} = \sum_p p_i |\Psi_i\rangle\langle\Psi_i|, \tag{1.24}$$

where p_i is the probability of the system being in state $|\Psi_i\rangle$

$$p_i = \frac{e^{-\beta E_i}}{\sum_k e^{-\beta E_k}}, \tag{1.25}$$

where $\beta = 1/(k_B T)$ is the inverse temperature, k_B is the Boltzmann constant and the sum is over complete set of all pure states.

The Hamiltonian operator shown in Eqs. 1.2–1.5 contains only one- and two-electron operators and is spin free. Operators corresponding to other observables are similarly represented by one- or two-electron operators. Therefore, it should be possible to simplify the expression for the expectation value Eq. 1.14 by integrating out degrees of freedom of $n-2$ electrons. This leads us to the so-called reduced density matrices. For example, two-electron reduced density matrix is defined as[2]

$$\gamma_2(\mathbf{x}_1, \mathbf{x}_2; \mathbf{x}_1', \mathbf{x}_2') = n(n-1) \int d\mathbf{x}_3 \int d\mathbf{x}_4 \ldots \int d\mathbf{x}_n \gamma(\mathbf{x}_1, \mathbf{x}_2, \ldots, \mathbf{x}_n; \mathbf{x}_1', \mathbf{x}_2', \cdots, \mathbf{x}_n). \tag{1.26}$$

The two-electron reduced density matrix being integrated over $\mathbf{x}_1$ and $\mathbf{x}_2$ degrees of freedom produces the total number of electron pairs

$$\int d\mathbf{x}_1 d\mathbf{x}_2 \gamma_2(\mathbf{x}_1, \mathbf{x}_2; \mathbf{x}_1, \mathbf{x}_2) = \frac{n(n-1)}{2}, \tag{1.27}$$

and its eigenvalues are called *natural geminals* or two-electron functions and are proportional to the populations of two-electron states. The two-electron reduced density matrix determines the expectation value of the two-electron operators $\hat{O}_2 = \sum_{i<j}^{n} O_2(\mathbf{x}_i, \mathbf{x}_j)$ (e.g. interaction operator $\hat{V}_{ee}$) as follows

$$\langle \hat{O}_2 \rangle = \int d\mathbf{x}_1 \int d\mathbf{x}_2 \left[O_2(\mathbf{x}_1, \mathbf{x}_2) \gamma_2(\mathbf{x}_1, \mathbf{x}_2; \mathbf{x}_1', \mathbf{x}_2') \right]_{\mathbf{x}_1' = \mathbf{x}_1, \mathbf{x}_2' = \mathbf{x}_2}. \tag{1.28}$$

[2]The prefactor $n(n-1)$ in Eq. 1.26 is a convenient normalization factor. The number of unique pairs is $n(n-1)/2$.

This suggests that it should be possible to obtain the expectation value of the Hamiltonian, thus overcoming necessity to deal with complicated wave functions. However it turns out difficult to find necessary and sufficient conditions for a γ_2 to be a legitimate function in the sense that it must coming from an antisymmetric wave function and, therefore, represent a realistic n-electron system. This is the n-representability problem for the two-electron reduced density matrix [4–6].

If all but one electron coordinates (and spins) are integrated out we obtain the one-electron reduced density matrix

$$\gamma_1(\mathbf{x}_1, \mathbf{x}_1') = n \int d\mathbf{x}_2 \int d\mathbf{x}_3 \ldots \int d\mathbf{x}_n \gamma_1(\mathbf{x}_1, \mathbf{x}_2, \ldots, \mathbf{x}_n; \mathbf{x}_1', \mathbf{x}_2, \cdots, \mathbf{x}_n). \tag{1.29}$$

It normalizes to the total number of electrons n

$$\mathrm{Tr}\gamma_1(\mathbf{x}_1, \mathbf{x}_1') = \int d\mathbf{x}_1 \gamma_1(\mathbf{x}_1, \mathbf{x}_1) = n. \tag{1.30}$$

The eigenvectors of one-electron reduced density matrix are named *natural orbitals* and the eigenvalues correspond to natural orbital occupations. The one-electron reduced density matrix can provide the expectation values of only one-electron operators $\hat{O}_1 = \sum_i^n O_1(\mathbf{x}_i)$ as follows

$$\langle \hat{O}_1 \rangle = \int d\mathbf{x}_1 \left[O_1(\mathbf{x}_1) \gamma_1(\mathbf{x}_1, \mathbf{x}_1') \right]_{\mathbf{x}_1' = \mathbf{x}_1}. \tag{1.31}$$

This equation tells us that in order to calculate the expectation value of one-electron operators only knowledge of γ_1 is required. This is a serious simplification since γ_1 is much less complicated than the wave function or even γ_2. This is the chief reason of why one-electron reduced density matrices are so popular in computational quantum chemistry. The one-electron reduced density matrix, however does not allow one to obtain the expectation values of two-electron operators, such as $\hat{V}_{ee}$ or the Hamiltonian

$\hat{H}$, and therefore it is not possible to obtain the total energy of the system. The time-dependent extension of the one-electron reduced density matrix is called a one-electron Green's function $G(\mathbf{x}, \mathbf{x}'; t - t')$

$$\gamma(\mathbf{x}, \mathbf{x}') = -i \lim_{t' \to t} G(\mathbf{x}, \mathbf{x}'; t - t'). \tag{1.32}$$

and as will be shown later allows one to obtain the expectation value of electron-electron operator. This means that the one-electron Green's function can be a convenient quantity in computational quantum chemistry since it combines the computational tractability similar to other one-electron quantities with the ability to provide the total energy of the system in a rigorous way.

The simplest quantity in the hierarchy of density matrices can be obtained by summing the diagonal elements of $\gamma(\mathbf{x}, \mathbf{x}')$ over the spin variable

$$\rho(\mathbf{r}) = \sum_{\sigma} \gamma(\mathbf{r}, \sigma; \mathbf{r}, \sigma) \tag{1.33}$$

or, equivalently, in terms of the wave function

$$\rho(\mathbf{r}) = n \sum_{\sigma_1, \ldots, \sigma_n} \int d\mathbf{x}_2 \ldots \int d\mathbf{x}_n \Psi^*(\mathbf{x}, \mathbf{x}_2, \ldots, \mathbf{x}_n) \Psi(\mathbf{x}, \mathbf{x}_2, \ldots, \mathbf{x}_n). \tag{1.34}$$

This quantity is called the electron density and it only depends on one set of coordinates x, y, z. The electron density is directly accessible in experiments. Owing to its simplicity the electron density can only provide the expectation values of multiplicative one-electron operators.

In general the reduced density matrix of order k is given by the following formula

$$\gamma_k(\mathbf{x}_1, \mathbf{x}_2, \ldots, \mathbf{x}_n; \mathbf{x}'_1, \mathbf{x}'_2, \ldots, \mathbf{x}'_n) =$$

$$\binom{n}{p} \int d\mathbf{x}_{p+1}, \ldots, \int d\mathbf{x}_n \gamma(\mathbf{x}_1, \mathbf{x}_2, \ldots, \mathbf{x}_p, \mathbf{x}_{p+1}, \ldots, \mathbf{x}_n; \mathbf{x}'_1, \mathbf{x}'_2, \ldots, \mathbf{x}'_p, \mathbf{x}'_{p+1}, \ldots, \mathbf{x}'_n).$$

Similar expressions exists and same properties hold for the ensemble density matrices describing mixed states. Conditions of n-representability of Γ_1 are known. Γ_1, given by Eq. 1.24 is said to be n representable if $0 \leq n_i \leq 1 \ \forall i$ where n_i are the eigenvalues of Γ_1.

1.1.4 One-electron Green's function

As mentioned earlier the one-electron Green's function is the dynamic generalization of the one-electron reduced density matrix. Similarly to the hierarchy of n-electron reduced density matrices introduced in the previous section there exist a hierarchy of n-electron Green's functions. The discussion here, however, will be limited to the one-electron Green's functions only. More detailed discussion can be found in excellent introductory books: "Feynman Diagram Techniques in Condensed Matter Physics" by R. A. Jishi [7], "Many-Body Quantum Theory in Condensed Matter Physics: An Introduction" by H. Bruus and K. Flensberg [8]. More involved discussions of various topics related to this dissertation can be found in the following books: "Nonequilibrium Many-Body Theory of Quantum Systems: A Modern Introduction" by G. Stefanucci and R. van Leeuwen [9] as well as "Quantum Theory of Many-Particle Systems" by A. L. Fetter and J. D. Walecka [10].

Time-dependent dynamic correlation function for any two one-electron operators $\hat{A}(t)$ and $\hat{B}(t')$ is defined as

$$C_{AB}(t,t') = -i\langle \mathcal{T}\hat{A}(t)\hat{B}(t')\rangle, \tag{1.35}$$

where $\langle \ldots \rangle$ stands for grand canonical ensemble average,

$$\langle \ldots \rangle = \frac{\mathrm{Tr}\left[e^{-\beta\bar{H}} \ldots\right]}{\mathrm{Tr}\left[e^{-\beta\bar{H}}\right]}, \tag{1.36}$$

where $\bar{H} = \hat{H} - \mu\hat{n}$ and μ is the chemical potential. Positive time-ordering operator $\mathcal{T}$,

acting on a product of operators rearranges them in order of increasing time from right to left, introducing a minus sign every time two fermionic operators are interchanged:

$$\mathcal{T}\hat{A}(t)\hat{B}(t') = \begin{cases} \hat{A}(t)\hat{B}(t') & t > t' \\ -\hat{B}(t')\hat{A}(t) & t < t', \end{cases} \tag{1.37}$$

Next, we introduce the retarded correlation function $C^R_{AB}(t,t')$

$$C^R_{AB}(t,t') = -i\theta(t-t')\langle\{\hat{A}(t),\hat{B}(t')\}\rangle, \tag{1.38}$$

where $\{\hat{A},\hat{B}\} = \hat{A}\hat{B} + \hat{B}\hat{A}$ is the anticommutator, and $\theta(t-t')$ is the step function equals to 1 if $t > t'$, and 0 otherwise. $C^R_{AB}(t,t')$ is non-zero only if $t > t'$ explaining its name "retarded". The retarded correlation functions are the most useful correlation functions in chemical physics since they determine the response of a system to external probes and, therefore, directly related to experimentally measured quantities. There exists a plethora of correlation functions besides the retarded ones. For example, the advanced correlation functions are defined as follows

$$C^A_{AB}(t,t') = i\theta(t'-t)\langle\{\hat{A}(t),\hat{B}(t')\}\rangle \tag{1.39}$$

A thorough discussion of various types of correlation and Green's function is given in many excellent books, see e.g. Refs. [7, 8, 10]. Discussion in this section will be limited to retarded correlation and Green's functions.

An important special case of the correlation function corresponds to the following choice of one-electron operators $\hat{A} = \hat{c}$ and $\hat{B} = \hat{c}^\dagger$ where $\hat{c}^\dagger$ and $\hat{c}$ are electron creation operator and electron annihilation operators respectively. The retarded Green's

function in this representation is defined by

$$G^R_{i\sigma,j\sigma'}(t,t') = -i\theta(t-t')\langle\{\hat{c}_{i\sigma}(t), \hat{c}^\dagger_{j\sigma'}(t')\}\rangle. \tag{1.40}$$

The physical meaning of this Green's function becomes transparent after performing following manipulations. Assuming that $t > t'$ we can rewrite the retarded Green's function as follows

$$\begin{aligned} iG^R_{i\sigma,j\sigma'}(t,t') &= \frac{\mathrm{Tr}\left[e^{-\beta\bar{H}}\hat{c}_{i\sigma}\hat{c}^\dagger_{j\sigma'}\right]}{\mathrm{Tr}\left[e^{-\beta\bar{H}}\right]} \\ &= \frac{\sum_n e^{-\beta\bar{E}_n}\langle n|e^{i\bar{H}t/\hbar}\hat{c}_{i\sigma}e^{-i\bar{H}(t-t')/\hbar}\hat{c}^\dagger_{j\sigma'}e^{-i\bar{H}t'/\hbar}|n\rangle}{\mathrm{Tr}\left[e^{-\beta\bar{H}}\right]}, \end{aligned} \tag{1.41}$$

where a complete set of eigenstates of the Hamiltonian $\bar{H}$ was used, and $\mathrm{Tr}\,[\ldots] = \sum_n\langle n|\ldots|n\rangle$. Next we define two states:

$$\begin{aligned} |\alpha\rangle &= e^{-i\bar{H}(t-t')/\hbar}\hat{c}^\dagger_{j\sigma'}e^{-i\bar{H}t'/\hbar}|n\rangle, \\ |\beta\rangle &= c^\dagger_{i\sigma}e^{-i\bar{H}t/\hbar}|n\rangle \end{aligned} \tag{1.42}$$

and each matrix element in Eq. 1.41 can be written as $\langle n|\ldots|n\rangle = \langle\beta|\alpha\rangle$. It represents the probability amplitude for a system in state $|\alpha\rangle$ to be found in state $|\beta\rangle$. Therefore the physical meaning of the retarded Green's function can be summarized as follows. At t=0 the system begins at state $|n\rangle$, then operator $e^{-i\bar{H}t'/\hbar}$ takes it to state $e^{-i\bar{H}t'/\hbar}|n\rangle$. At this time, operator $\hat{c}^\dagger_{j\sigma'}$ inserts a particle with the spin projection σ' onto orbital j. During the next step the operator $e^{-i\bar{H}(t-t')/\hbar}$ takes the system to time t. The state $|\alpha\rangle$ is the state of the system at time t if a particle with spin coordinate σ' was placed onto the orbital j at earlier time t'. It is easy to see that state $|\beta\rangle$ is the state of the system when an extra particle with spin projection σ was added onto the orbital i it at time t. This means that the matrix element $\langle n|\ldots|n\rangle$ is the probability amplitude

of finding the system with an extra particle with spin σ occupying orbital i at time t if a particle (not necessarily the same since electrons are indistinguishable) with spin σ' was added onto orbital j earlier at time t'. Probability of different states is built in Eq. 1.41 via $\frac{\mathrm{Tr}\left[e^{-\beta\bar{H}}...\right]}{\mathrm{Tr}\left[e^{-\beta\bar{H}}\right]}$. Therefore $iG^R_{i\sigma,j\sigma'}(t,t')$ represents an ensemble average of the propagation described above.

It is also possible to write expression for the one-electron retarded Green's function in terms of eigenstates and eigenvalues of the underlying Hamiltonian. To this end we first note that for time-independent Hamiltonians $G^R_{i\sigma,j\sigma'}(t,t')$ given by Eq. 1.40 depends only on time difference $t-t'$ and not on individual time variables t and t'. Taking this into account and since the Hamiltonian does not depend on spin we can rewrite Eq. 1.40 as

$$G^R_{ij,\sigma}(t) = -i\theta(t)\langle\hat{c}_{i\sigma}(t)\hat{c}^\dagger_{j\sigma}(0)\rangle - i\theta(t)\langle\hat{c}^\dagger_{j\sigma}(0)\hat{c}_{i\sigma}(t)\rangle. \tag{1.43}$$

and focus on the first term

$$\begin{aligned}
\langle\hat{c}_{i\sigma}(t)\hat{c}^\dagger_{j\sigma}(0)\rangle &= Z^{-1}\sum_n \langle n|e^{-\beta\bar{H}}e^{i\bar{H}t/\hbar}\hat{c}_{i\sigma}(t)e^{-i\bar{H}t/\hbar}\hat{c}^\dagger_{j\sigma}(0)|n\rangle \\
&= Z^{-1}\sum_{nm} \langle n|e^{-\beta\bar{H}}e^{i\bar{H}/\hbar}\hat{c}_{i\sigma}(t)|m\rangle\langle m|e^{-i\bar{H}t/\hbar}\hat{c}^\dagger_{j\sigma}(0)|n\rangle \\
&= Z^{-1}\sum_{nm} e^{-\beta\bar{E}_n}e^{-i(\bar{E}_m-\bar{E}_n)t/\hbar}\langle n|\hat{c}_{i\sigma}(t)|m\rangle\langle m|\hat{c}^\dagger_{j\sigma}(0)|n\rangle
\end{aligned} \tag{1.44}$$

where $Z^{-1} = \mathrm{Tr}\left[e^{-\beta\bar{H}}\right]$ and $\bar{E}_k = E_k - \mu n_k$ where n_k is the number of particles in state $|k\rangle$. Further simplification is available for orthogonal one-electron bases, for which Eq. 1.44 becomes

$$\begin{aligned}
\langle\hat{c}_{i\sigma}(t)\hat{c}^\dagger_{j\sigma}(0)\rangle &= Z^{-1}\sum_{nm} e^{-\beta\bar{E}_n}e^{-i(\bar{E}_m-\bar{E}_n)t/\hbar}\left|\langle m|\hat{c}^\dagger_{j\sigma}|n\rangle\right|^2 \\
&= -\int_{-\infty}^{\infty}\frac{d\epsilon}{2\pi}P_{jj,\sigma}e^{-i\epsilon t},
\end{aligned} \tag{1.45}$$

A spectral function $P_{jj,\sigma}$ is given by

$$P_{jj,\sigma} = -2\pi Z^{-1} \sum_{nm} e^{-\beta \bar{E}_n} \left| \langle m|\hat{c}^{\dagger}_{j\sigma}(\mathbf{r})|n\rangle \right|^2 \delta\left(\epsilon - \left(\bar{E}_m - \bar{E}_n\right)/\hbar\right). \tag{1.46}$$

Similar derivation should be performed for the second term in Eq. 1.40 and leads to the expression similar to Eq. 1.46. Adding two terms together and performing the Fourier transform

$$G^R_{jj,\sigma}(\omega) = \int_{-\infty}^{\infty} dt e^{i\omega t} G^R_{jj,\sigma}(t) \tag{1.47}$$

we obtain

$$G^R_{jj,\sigma}(t) = i \int_{-\infty}^{\infty} \frac{d\epsilon}{2\pi} P_{jj,\sigma}(\epsilon)(1 + e^{-\beta\epsilon}) \int_0^{\infty} e^{i(\omega-\epsilon)t} dt. \tag{1.48}$$

The second integral oscillatory but can be evaluated as follows

$$\int_0^{\infty} dt e^{i(\omega-\epsilon)t} = \lim_{\zeta\to 0^+} \int_0^{\infty} e^{i(\omega-\epsilon+i\zeta)t} dt = \lim_{\zeta\to 0^+} \frac{-1}{i(\omega-\epsilon+i\zeta)}. \tag{1.49}$$

Spectral density $A_{jj,\sigma}(\epsilon)$ is related to the spectral function through

$$\begin{aligned} A_{jj,\sigma}(\epsilon) &= -P_{jj,\sigma}(\epsilon)(1 + e^{-\beta\hbar\epsilon}) \\ &= 2\pi Z^{-1} \sum_{nm} e^{-\beta \bar{E}_n} \left| \langle m|\hat{c}^{\dagger}_{j\sigma}|n\rangle \right|^2 (1 + e^{-\beta\hbar\epsilon}) \delta\left(\epsilon - \left(\bar{E}_m - \bar{E}_n\right)/\hbar\right) \end{aligned} \tag{1.50}$$

Finally we obtain the spectral representation of real frequency one-electron retarded Green's function $G^R_{jj,\sigma}(\omega)$ by combining Eqs. 1.49 and 1.50

$$G^R_{jj,\sigma}(\omega) = \lim_{\zeta\to 0} \int_{-\infty}^{\infty} \frac{d\epsilon}{2\pi} \frac{A_{jj,\sigma}(\epsilon)}{\omega - \epsilon + i\zeta}. \tag{1.51}$$

It is straightforward to derive a similar spectral representation of real frequency advanced one-electron Green's function.

The spectral function for a noninteracting system consists of a series of δ peaks

corresponding to the eigenvalues of one-electron effective Hamiltonian. When the electron-electron interaction is turned on the structure of spectral function becomes more elaborate. The spectral function in the momentum space[3] $A(\vec{k}, \epsilon)$ can be directly obtained from photoemission experiments. During such experiments the system absorbs a photon, leading to ejecting an electron with the momentum $\vec{k}$ whose kinetic energy is then measured at some distance. One such technique is called angle-resolved photoemission spectroscopy (ARPES) which uses soft X-rays to measure the distribution of the density of single-particle electronic excitations (or, simply the distribution of electrons). It is one of the most direct methods of studying the electronic structure of the solids.

In almost all scenarios the exact eigenstates of the system are not available preventing practical use of the approach described above. Systematic pathway to the exact one-electron Green's function is provided by the perturbation theory. The zero-temperature perturbation expansion is possible to derive using the real time one-electron Green's function. On the other hand, the finite-temperature perturbation theory is extremely difficult to derive based on real time one-electron Green's function due to the presence of $e^{-\beta \bar{H}}$ factor. This factor is real while $e^{\pm i \bar{H} t/\hbar}$ is imaginary. The mismatch in the exponents causes difficulties in formal treatment of perturbation expansion. Significant simplifications arise when imaginary time one-electron Green's functions are used instead of real time ones. The next section provides a brief summary of imaginary time one-electron Green's function formalism.

1.1.5 Matsubara Green's functions

It turns out that a more convenient formalism can be obtained if time and frequency arguments are changed to the corresponding imaginary quantities: $t \to it = \tau$ and $\omega \to i\omega$. This is not merely a mathematical trick simplifying finite-temperature per-

[3]Momentum space is the set of all momentum vectors $\vec{k}$ a physical system can have.

turbative treatment of interacting systems, the imaginary time Green's function has its own significance: it yields the equilibrium thermodynamic properties of the system. The one-electron imaginary time and imaginary frequency Green's functions commonly referred to as Matsubara Green's function due to their inventor Japanese physicist Takeo Matsubara [11].

Imaginary time Green's function is defined as

$$G_{i\sigma,j\sigma'}(\tau,\tau') = -\langle \mathcal{T}\hat{c}_{i\sigma}(\tau)\hat{c}^{\dagger}_{j\sigma'}(\tau')\rangle, \tag{1.52}$$

where i and j denote the indices of one-electron orbitals and Heisenberg picture imaginary-time dependent electron creation and annihilation operators are given by

$$\begin{aligned} \hat{c}_{i\sigma}(\tau) &= e^{\bar{H}\tau/\hbar}\hat{c}_{i\sigma}e^{-\bar{H}\tau/\hbar}, \\ \hat{c}^{\dagger}_{i\sigma}(\tau) &= e^{\bar{H}\tau/\hbar}\hat{c}^{\dagger}_{i\sigma}e^{-\bar{H}\tau/\hbar}. \end{aligned} \tag{1.53}$$

As in the case of real time Green's functions the imaginary time Green's functions are the important examples of the imaginary time correlation functions $C_{AB}(\tau,\tau') = -\langle \mathcal{T}\hat{A}(\tau)\hat{B}(\tau')\rangle$. The imaginary time Green's function for $\tau > \tau'$ gives the probability amplitude of finding the system with an extra particle occupying the one-electron orbital i with spin projection σ at time τ if at an earlier time τ' a particle with spin projection of σ' was introduced into the one-electron orbital j. If $\tau < \tau'$ the $G_{i\sigma,j\sigma'}(\tau,'\tau')$ describes the probability amplitude of finding the system with one particle less with spin projection σ' at time τ' occupying orbital j if one particle with spin projection σ was removed at time τ from the orbital i.

Below we briefly describe the most important properties of Matsubara Green's functions.

1. For time-independent Hamiltonians $G_{i\sigma,j\sigma'}(\tau,\tau')$ depends only on time difference $\tau - \tau'$ and not on τ and τ' independently. In such case we will simply write

$G_{ij,\sigma}(\tau)$, since the Hamiltonian does not depend on spin.

2. For $\tau > 0$ function $G_{ij,\sigma}(\tau)$ is antiperiodic in the following sense

$$G_{ij,\sigma}(\tau) = -G_{ij,\sigma}(\tau - \beta). \tag{1.54}$$

3. The Fourier series for $G_{ij,\sigma}(\tau)$ is given by

$$G_{ij,\sigma}(\tau) = \frac{1}{\beta} \sum_{n}^{\infty} G_{ij,\sigma}(i\omega_n) e^{-i\omega_n \tau}. \tag{1.55}$$

Using the periodicity property illustrated above we find that only specific values of imaginary frequencies $i\omega_n$ are allowed:

$$\omega_n = (2n+1)\pi/\beta \quad n = 0, 1, 2, \ldots. \tag{1.56}$$

Imaginary frequency $i\omega_n$ for each ω_n satisfying Eq. 1.56 is denoted as Matsubara frequency and the set of all such points forms the so-called Matsubara frequency (or imaginary frequency) grid. It is important to note that the finite-temperature information is encoded into Matsubara frequencies through the inverse temperature $\beta = k_B/T$ i.e. the location of and spacing between the grid points.

Matsubara Green's functions are related to the retarded real time and real frequency one-electron Green's function introduced above by analytical continuation. There exist analytic function $G_{ij,\sigma}(z)$, where z is a complex frequency argument in the upper half place such that it equals to $G_{ij,\sigma}(i\omega_n)$ on the imaginary axis and $G_{ij,\sigma}(\omega)$ on the real axis. Matsubara Green's functions are easier to compute and therefore an analytical continuation can be, at least in principle, used to obtain real frequency Green's functions. The spectral representation of imaginary time Green's function can be found similarly to that of real time one-electron Green's function. The Fourier

transform of the imaginary time Green's function is given by (for simplicity we consider time invariant systems, and orthogonal one-electron basis)

$$G_{jj,\sigma}(i\omega_n) = \int_0^\beta G_{jj,\sigma}(\tau) e^{i\omega_n \tau} d\tau. \tag{1.57}$$

For the $\tau > 0$ case we can expand the definition of the imaginary-time Green's function as follows

$$\begin{aligned} G_{jj,\sigma}(\tau > 0) &= -Z^{-1} \mathrm{Tr}\left[e^{-\beta \bar{H}} e^{\bar{H}\tau/\hbar} \hat{c}_{j\sigma} e^{-\bar{H}\tau/\hbar} \hat{c}^\dagger_{j\sigma} \right] \\ &= -Z^{-1} \sum_{nm} \langle n | e^{-\beta \bar{H}} e^{\bar{H}\tau/\hbar} \hat{c}_{j\sigma} | m \rangle \langle n | e^{-\bar{H}\tau/\hbar} \hat{c}^\dagger_{j\sigma} | n \rangle \\ &= -Z^{-1} \sum_{nm} e^{-\beta \bar{E}_n} e^{-(\bar{E}_m - \bar{E}_n)\tau/\hbar} \left| \langle m | \hat{c}^\dagger_{j\sigma} | n \rangle \right|^2 \\ &= \int_{-\infty}^{\infty} \frac{d\epsilon}{2\pi} P_{jj,\sigma}(\epsilon) e^{-\epsilon\tau}, \end{aligned} \tag{1.58}$$

where

$$P_{jj,\sigma}(\epsilon) = -2\pi Z^{-1} \sum_{nm} e^{-\beta \bar{E}_n} \left| \langle m | \hat{c}^\dagger_{j\sigma} | n \rangle \right|^2 \delta\left(\epsilon - (\bar{E}_m - \bar{E}_n) \right). \tag{1.59}$$

After integration over imaginary time domain given by a finite interval $[0, \beta]$ Eq. 1.57 becomes

$$G_{jj,\sigma}(i\omega_n) = \int_{-\infty}^{\infty} \frac{d\epsilon}{2\pi} \frac{A_{jj,\sigma}(\epsilon)}{i\omega_n - \epsilon}, \tag{1.60}$$

where $A_{jj,\sigma}(\epsilon) = -P_{jj,\sigma}(\epsilon)(1 + e^{-\beta\epsilon})$. The one-electron retarded Green's function Eq. 1.51 looks fairly similar to Eq. 1.60. To establish connection between these two Green's functions we assume that $G_{jj,\sigma}(i\omega_n)$ is known for the upper half of the imaginary axis i.e. for all positive Matsubara frequencies $i\omega_n$ and consider the following function

$$\mathcal{G}_{jj,\sigma}(z) = \int_{-\infty}^{\infty} \frac{d\epsilon}{2\pi} \frac{A_{jj,\sigma}(\epsilon)}{z - \epsilon} \tag{1.61}$$

which is analytic everywhere except for $z = \epsilon$ i.e. real axis. From Eqs. 1.51, 1.60

and 1.61 it follows that

$$G^R_{jj,\sigma}(\omega) = \mathcal{G}_{jj,\sigma}(z = \omega + i0^+) \quad \text{and} \quad G_{jj,\sigma}(i\omega_n) = \mathcal{G}_{jj,\sigma}(z = i\omega_n) \tag{1.62}$$

where we explicitly state that $\lim_{\zeta\to 0}$ is approached from the 0^+ side. Equation 1.62 suggests that provided $\mathcal{G}_{jj,\sigma}(z)$ is known both $G^R_{jj,\sigma}(\omega)$ and $G_{jj,\sigma}(i\omega_n)$ can be found, at least formally. Since $\mathcal{G}_{jj,\sigma}(z)$ is known on the set of point in the complex plane and in order to obtain $\mathcal{G}_{jj,\sigma}(z)$ everywhere else in the complex plane analytical continuation is needed. In short, the one-electron retarded Green's function can be obtained by $G^R_{jj,\sigma}(\omega) = G_{jj,\sigma}(i\omega_n)|_{i\omega_n\to\omega+i0^+}$. Although there is no robust algorithm for doing so the idea comes down to replacing $i\omega_n$ with z. If the resulting function is analytic in the upper-half plane then it is $\mathcal{G}_{jj,\sigma}(z)$ and $G^R_{jj,\sigma}(\omega)$ can be obtained by replacing z with $\omega + i0^+$.

Matsubara Green's function can be used to calculate the thermodynamic equilibrium properties of the system. For example, the ensemble average of a general one-electron operator $\hat{O}_1$ is given by

$$\begin{aligned}
\langle \hat{O}_1 \rangle &= \sum_{ij}\sum_{\sigma\sigma'} \int d\mathbf{r}\phi^*_i(\mathbf{r})O(\mathbf{r})\phi_j(\mathbf{x})\langle \hat{c}^\dagger_{i\sigma}\hat{c}_{j\sigma}\rangle = \sum_{ij}\sum_{\sigma\sigma'} O_{ij}\langle \hat{c}^\dagger_{i\sigma}\hat{c}_{j\sigma'}\rangle \\
&= \lim_{\tau\to\tau^+}\sum_{ij}\sum_{\sigma\sigma'} O_{ij}\langle \hat{c}^\dagger_{i\sigma}(\tau)\hat{c}_{j\sigma'}(\tau^+)\rangle \\
&= -\lim_{\tau\to\tau^+}\sum_{ij}\sum_{\sigma\sigma'} O_{ij}G_{j\sigma',i\sigma}(\tau^+,\tau),
\end{aligned} \tag{1.63}$$

where $\tau^+ = \tau + 0^+$ denotes the time infinitesimally later than τ. For instance, the ensemble average of the kinetic energy is given by

$$\langle T\rangle = -\lim_{\tau\to\tau^+}\sum_{ij}\sum_{\sigma} t_{ij}G_{j\sigma,i\sigma}(\tau^+,\tau), \tag{1.64}$$

where

$$t_{ij} = \int d\mathbf{r}\phi_i^*(\mathbf{r}) \left(-\frac{1}{2}\nabla_{\mathbf{r}}^2\right) \phi_j(\mathbf{r}). \tag{1.65}$$

Similarly we can obtain the ensemble average of electron-electron interaction energy [7, 10].

We have shown that at finite temperature the grand canonical ensemble averages of one-electron operators and electron-electron interaction operator can be conveniently calculated using Matsubara Green's function. The usefulness of Matsubara formalism goes beyond that and provides a way to calculating system's static thermodynamic properties such as Gibbs and Helmholtz free energies, electronic entropy, internal energy and forces. In order to understand how these properties can be calculated we need to introduce a very important quantity—the self-energy, which contains all the information about static and dynamical electronic correlation in the system, and will be discussed in more detail in the next section.

1.2 Electronic correlation

1.2.1 Electronic correlation in wave-function methods

In order to successfully develop methods capable of treating electron-electron correlation it is very important to have a clear understanding of the nature of this phenomenon. In this section we briefly discuss electronic correlation from a general point of view and in the next section we will explain how it can be accounted for in the Green's function methods. The term "electronic correlation" appeared first in the work of Eugene Wigner and Frederick Seitz [12, 13]. They studied the electronic structure and cohesive energy of metals and discussed what nowadays is known as the "correlation energy" and the "Fermi correlation". Former, as was mentioned earlier (Eq. 1.20) [14] is the difference between exact nonrelativistic energy and Hartree–Fock energy while latter

comes about from the antisymmetry property of the wave function and is built into the Slater determinant. The correlation energy of an atom or molecule is usually approximately only 1% of the total energy. This seemingly small fraction of the total energy becomes however important when energy differences instead of total energies are of interest, for instance in the studies of binding process.

We begin our discussion by considering electron-electron correlation in statistical sense. The motion of two particles is said to be statistically uncorrelated if the pair probability distribution function $P_{12}(\mathbf{x}_1, \mathbf{x}_2)$ can be written as a product of two independent distribution functions for individual particles [15]

$$P_{12}(\mathbf{x}_1, \mathbf{x}_2) = P_1(\mathbf{x}_1) P_2(\mathbf{x}_2). \tag{1.66}$$

The conditional electron density $P_{12}(\mathbf{x}_1|\mathbf{x}_2) = P_{12}(\mathbf{x}_1, \mathbf{x}_2)/P_2(\mathbf{x}_2)$, which is the probability distribution function for particle 1 when particle 2 is at $\mathbf{x}_2$, in the case of two uncorrelated particles becomes simply

$$P_{12}(\mathbf{x}_1|\mathbf{x}_2) = P_1(\mathbf{x}_1), \tag{1.67}$$

emphasizing the uncorrelated nature of the two particles. Whenever Eqs. 1.66 and 1.67 do not hold the particles are said to be statistically *correlated*. For indistinguishable particles such as electrons $P_1(\mathbf{x}_1)$ and $P_{12}(\mathbf{x}_1|\mathbf{x}_2)$ are connected to the electron density $\rho(\mathbf{x})$ and the diagonal part of the two-electron reduced density matrix called two-electron density $\gamma(\mathbf{x}_1, \mathbf{x}_2) = \gamma(\mathbf{x}_1, \mathbf{x}_2; \mathbf{x}_1', \mathbf{x}_2')$ as follows

$$\begin{aligned} P_1(\mathbf{x}) = P_2(\mathbf{x}) &= \frac{\rho(\mathbf{x})}{n}, \\ P_{12}(\mathbf{x}_1, \mathbf{x}_2) &= \frac{1}{n(n-1)} \gamma(\mathbf{x}_1, \mathbf{x}_2). \end{aligned} \tag{1.68}$$

The two-electron density can be partitioned into an uncorrelated density-dependent

part and a part that describes all the correlation effects

$$\gamma(\mathbf{x}_1, \mathbf{x}_2) = \rho(\mathbf{x}_1)\rho(\mathbf{x}_2) + \gamma^{corr}(\mathbf{x}_1, \mathbf{x}_2). \tag{1.69}$$

Therefore, if two electrons are independent we obtain [16]

$$\gamma(\mathbf{x}_1, \mathbf{x}_2) = \frac{n-1}{n}\rho(\mathbf{x}_1)\rho(\mathbf{x}_2). \tag{1.70}$$

In practice $\gamma(\mathbf{x}_1, \mathbf{x}_2)$ is always smaller than given by Eq. 1.70 when two electrons are close and larger when they are far apart. This illustrates the tendency of electrons to avoid each other. There are several reasons for such behavior. In what follows we consider two most important of them: Pauli principle and Coulomb repulsion. The Pauli principle i.e. the antisymmetry of the wave function, with respect to interchange of any pair of electrons comes from indistinguishable nature of electrons obeying the Fermi statistics. This the origin of so-called Fermi correlation also known as exchange. It reduces the probability of like-spin electrons to be close in space. In fact $\gamma_2(\mathbf{x}_1, \mathbf{x}_1) = 0$ manifesting that the probability of finding two electrons with the same spin at the same point in space is zero. This is known as *exchange hole* [17, 18]. It surrounds every electron and no other electron with the same spin can penetrate it. This hole is a direct consequence of the antisymmetry of the wave function and has nothing to do with the electron-electron repulsion which is due to electrostatics. The latter is the origin of a so-called *Coulomb* correlation. It reduces the probability of two electrons being found in the same region of space due to their mutual repulsion. Since the Hartree–Fock wave function accounts for the Fermi correlation, the Coulomb hole [18, 19] can be defined as the difference between exact hole $\rho^{XC}_{hole}(\mathbf{x}_1|\mathbf{x}_2)$ and Hartree–Fock hole $\rho^{HF}_{hole}(\mathbf{x}_1|\mathbf{x}_2)$

$$\rho^{C}_{hole}(\mathbf{x}_1|\mathbf{x}_2) = \rho^{XC}_{hole}(\mathbf{x}_1|\mathbf{x}_2) - \rho^{HF}_{hole}(\mathbf{x}_1|\mathbf{x}_2), \tag{1.71}$$

where the exact hole includes effects of exchange and correlation and defined as

$$\rho_{hole}^{XC}(\mathbf{x}_1|\mathbf{x}_2) = \frac{\gamma_2^{corr}(\mathbf{x}_1, \mathbf{x}_2)}{\rho(\mathbf{x}_2)} \tag{1.72}$$

and the Hartree–Fock hole is calculated from the Hartree–Fock two-electron density

$$\rho_{hole}^{HF}(\mathbf{x}_1|\mathbf{x}_2) = \frac{\gamma_2^{HF}(\mathbf{x}_1, \mathbf{x}_2)}{\rho(\mathbf{x}_2)}. \tag{1.73}$$

Coulomb hole describes the correlation between electrons of unlike spin. It is not as deep as Fermi hole and has a cusp [20, 21] i.e. the discontinuity in its first derivative. In the Hartree–Fock theory the molecular orbitals are optimized by minimization of the total energy with the Slater determinant which corresponds to a particular distribution of electrons. It is a mean-field theory in the sense that the Coulomb repulsion between electrons is taken care of via an effective one-particle potential. One systematic way of improving the description of Coulomb correlation over the single-determinant picture is to expand the wave function as a linear combinations of Slater determinants. Such expansion determines the so-called *configuration interaction* (CI) wave function

$$\Psi^{CI} = \sum_j c_j |\Phi_j\rangle, \tag{1.74}$$

where each determinant corresponds to a particular distribution of electrons. This is the wave function perspective on *dynamical* correlation. Another type of correlation is called *static*. It arises from the degeneracies of several Slater determinants i. e. when more than one Slater determinant contributes significantly to the ground state and, therefore, all such configurations must to be included in order to obtain a correct description of the system. Most prominent example is the bond breaking process, accurate description of which requires at least two configurations to be included.

There exist a plethora of the wave-function methods capable of addressing either

static or dynamic correlation or both. Here, we focus on the Green's function methods and, therefore, in what follows we discuss how Matsubara Green's functions can be used to construct a theory amenable of, at least in principle, describing electron-electron correlation exactly.

1.2.2 Electronic correlation in Green's function methods

In the presence of electron-electron interactions the solution of Schrödinger equation becomes extremely complicated problem. Since the calculation of one-electron Green's function requires the full solution of Schrödinger equation there is no apparent advantage of employing one-electron Green's function formalism. However as we will show in this section it is possible to obtain a fully interacting one-electron Green's function without explicit knowledge of all eigenstates of the Hamiltonian.

A general time-independent Hamiltonian can be written in the following form

$$\bar{H} = \hat{H}_0 - \mu\hat{n} + \hat{V}, \tag{1.75}$$

where $\bar{H}_0$ is the zero-order or noninteracting Hamiltonian and $\hat{V}$ is the electron-electron interaction term. Let's now define an imaginary time interaction picture operator $A(\tau)$ as

$$A(\tau) = e^{\bar{H}_0\tau/\hbar}\hat{A}e^{-\bar{H}_0\tau/\hbar}, \tag{1.76}$$

where in order to distinguish interaction picture operators from Heisenberg picture operators the former will not be capped. The imaginary time Green's function defined in terms of Heisenberg picture electron creation and annihilation operators was given by Eq. 1.52. Let's now consider the following product of two Heisenberg picture operators

$$\begin{aligned}\hat{c}(\tau)\hat{c}^\dagger(\tau) &= e^{\bar{H}\tau/\hbar}e^{-\bar{H}_0\tau/\hbar}c(\tau)e^{\bar{H}_0\tau/\hbar}e^{-\bar{H}(\tau-\tau')/\hbar}e^{-\bar{H}_0\tau'/\hbar}c^\dagger(\tau')e^{\bar{H}_0\tau'}e^{-\bar{H}\tau'/\hbar} \\ &= \hat{U}(0,\tau)c(\tau)\hat{U}(\tau,\tau')c^\dagger(\tau')\hat{U}(\tau',0),\end{aligned} \tag{1.77}$$

where the imaginary time interaction picture U operator is defined as

$$U(\tau,\tau') = e^{\bar{H}_0\tau/\hbar}e^{-\bar{H}(\tau-\tau')/\hbar}e^{-\bar{H}_0\tau'/\hbar}. \tag{1.78}$$

The equation of motion of $U(\tau,\tau')$ is given by

$$\frac{\partial}{\partial\tau}U(\tau,\tau') = -V(\tau)U(\tau,\tau'). \tag{1.79}$$

where V is the interaction operator in the imaginary time interaction picture representation $V(\tau) = e^{\bar{H}_0\tau/\hbar}\hat{V}e^{-\bar{H}_0\tau/\hbar}$. Equation 1.79 can be solved by integrating both sides iteratively. The final expression for $U(\tau,\tau')$ can be written in terms of infinite expansion [7–9]

$$U(\tau,\tau') = \sum_{m=0}^{\infty}\frac{1}{m!}\left(-\frac{1}{\hbar}\right)^m\int_{\tau'}^{\tau}d\tau_1\ldots\int_{\tau'}^{\tau}d\tau_m\mathcal{T}\left[V(\tau_1)\ldots V(\tau_m)\right], \tag{1.80}$$

where the time-ordering operator $\mathcal{T}$ rearranges $V(\tau_1),\ldots,V(\tau_m)$ in order of increasing time from right to left.

In order to obtain expression for Matsubara Green's function in terms of operator $U(\tau,\tau')$ we first insert $\tau=\beta$ and $\tau'=0$ into Eq. 1.78

$$U(\beta,0) = e^{\beta\bar{H}_0}e^{-\beta\bar{H}} \tag{1.81}$$

from which we obtain $e^{-\beta\bar{H}} = e^{-\beta\bar{H}_0}U(\beta,0)$ and use this exponential factor in the definition of the Matsubara Green's function

$$\begin{aligned}
G_{ij,\sigma}(\tau) &= -\langle c_{i\sigma}(\tau)c^{\dagger}_{j\sigma}(0)\rangle = -Z^{-1}\mathrm{Tr}\left[e^{-\beta\bar{H}}\mathcal{T}c_{i\sigma}(\tau)c^{\dagger}_{j\sigma}(0)\right] \\
&= -Z^{-1}\mathrm{Tr}\left[e^{-\beta\bar{H}_0}U(\beta,0)\mathcal{T}c_{i\sigma}(\tau)c^{\dagger}_{j\sigma}(0)\right] \\
&= -Z^{-1}\mathrm{Tr}\left[e^{-\beta\bar{H}_0}\hat{U}(\beta,0)\mathcal{T}U(0,\tau)c_{i\sigma}(\tau)U(\tau,0)\hat{c}^{\dagger}_{j\sigma'}(0)\right].
\end{aligned} \tag{1.82}$$

for $\tau > 0$ action of $\mathcal{T}$ on the string of operators in Eq. 1.82 results in the following

$$\hat{U}(\beta,0)\mathcal{T}U(0,\tau)c_{i\sigma}(\tau)U(\tau,0)c^{\dagger}_{j\sigma}(0) = U(\beta,\tau)c_{i\sigma}(\tau)U(\tau,0)c^{\dagger}_{j\sigma}(0), \tag{1.83}$$

where $U(\beta,\tau) = U(\beta,0)U(0,\tau)$, which is easy to proof following the definition of U. Thus $G_{ij,\sigma}(\tau > 0)$ may be written as

$$G_{ij,\sigma}(\tau > 0) = -Z^{-1}\mathrm{Tr}\left[e^{-\beta\bar{H}_0}\mathcal{T}U(\beta,0)c_{i\sigma}(\tau)c^{\dagger}_{j\sigma}(0)\right]. \tag{1.84}$$

Similar consideration of $\tau < 0$ case gives the following expression for the Green's function

$$G_{ij,\sigma}(\tau < 0) = -Z^{-1}\mathrm{Tr}\left[e^{-\beta\bar{H}_0}\mathcal{T}U(\beta,0)c_{i\sigma}(\tau)c^{\dagger}_{j\sigma}(0)\right]. \tag{1.85}$$

which is identical to Eq. 1.84. Therefore, the imaginary time Green's function written in terms of interaction picture operators becomes

$$G_{ij,\sigma}(\tau) = -Z^{-1}\mathrm{Tr}\left[e^{-\beta\bar{H}_0}\mathcal{T}U(\beta,0)c_{i\sigma}(\tau)c^{\dagger}_{j\sigma}(0)\right]. \tag{1.86}$$

It remains to write the grand partition function Z in terms of the operator U

$$Z = \mathrm{Tr}\left[e^{-\beta\bar{H}}\right] = \mathrm{Tr}\left[e^{-\beta\bar{H}_0}e^{\beta\bar{H}_0}e^{-\beta\bar{H}}\right] = \mathrm{Tr}\left[e^{-\beta\bar{H}_0}U(\beta,0)\right]. \tag{1.87}$$

Finally we can write the following expression for the Green's function

$$G_{ij,\sigma}(\tau) = -\frac{\mathrm{Tr}\left[e^{-\beta\bar{H}_0}\mathcal{T}U(\beta,0)c_{i\sigma}(\tau)c^{\dagger}_{j\sigma}(0)\right]}{\mathrm{Tr}\left[e^{-\beta\bar{H}_0}U(\beta,0)\right]}, \tag{1.88}$$

and dividing the numerator and denominator by $Z_0 = \mathrm{Tr}\left[e^{-\beta\bar{H}_0}\right]$ we obtain the following result

$$G_{ij,\sigma}(\tau) = -\frac{\langle\mathcal{T}U(\beta,0)c_{i\sigma}(\tau)c^{\dagger}_{j\sigma}(0)\rangle_0}{\langle U(\beta,0)\rangle_0}, \tag{1.89}$$

where $\langle \ldots \rangle_0 = \mathrm{Tr}\left[e^{-\beta \bar{H}_0} \ldots\right] / \mathrm{Tr}\left[e^{-\beta \bar{H}_0}\right]$ denotes the ensemble average over the non-interacting system. The product of two fermionic operators $c_{i\sigma}(\tau) c^{\dagger}_{j\sigma'}(0)$ can be interchanged with $U(\beta, 0)$ without changing the overall sign because operators in $U(\beta, 0)$ are bosonic. Using Eq. 1.80 we finally obtain a very important result

$$G_{ij,\sigma}(\tau) = -\frac{\sum_{m=0}^{\infty} \frac{1}{m!} \left(-\frac{1}{\hbar}\right)^m \langle \int_0^\beta d\tau_1 \ldots \int_0^\beta d\tau_n \mathcal{T} c_{i\sigma}(\tau) c^{\dagger}_{j\sigma}(0) V(\tau_1) \ldots V(\tau_m) \rangle_0}{\sum_{m=0}^{\infty} \frac{1}{m!} \left(-\frac{1}{\hbar}\right)^m \langle \int_0^\beta d\tau_1 \ldots \int_0^\beta d\tau_n \mathcal{T} V(\tau_1) \ldots V(\tau_2) \ldots \rangle_0}. \quad (1.90)$$

This expression is remarkable in the sense that it gives the prescription to calculate exact imaginary time Green's function $G_{ij,\sigma}(\tau)$ in terms of ensemble average over non-interacting system, which can be obtained using Wick's theorem. It states that the ensemble average over a noninteracting system of the time-ordered product of interaction picture operators is equal to the sum over all possible contracted pairs of operators [7, 22]

$$\langle \mathcal{T}\left[ABCD\ldots\right] \rangle_0 = \overbrace{A B}\overbrace{C D}\ldots + \overbrace{A\,\overbrace{B C}\,D}\ldots + \overbrace{\overbrace{A B}\overbrace{C D}}\ldots + \ldots, \quad (1.91)$$

where the contraction of two interaction picture operators A and B is defined as

$$\overbrace{A B} = \langle \mathcal{T} A B \rangle_0 = \frac{\mathrm{Tr}\left[e^{-\beta \bar{H}_0} A B\right]}{\mathrm{Tr}\left[e^{-\beta \bar{H}_0}\right]}. \quad (1.92)$$

Expansion of Eq. 1.90 to order m leads to complicated algebraic expression. This expression contains integrals over all intermediate imaginary time variables and the sum over all intermediate orbital and spin indices. For example, let us obtain all expressions resulting from expanding the denominator of Eq. 1.90 to the first order in the electron-electron interaction

$$\mathcal{N} = \int_0^\beta d\tau_1 \langle \mathcal{T} c_{i\sigma}(\tau) c^{\dagger}_{j\sigma}(0) V(\tau_1) \rangle_0 \quad (1.93)$$

where the electron-electron interaction operator in imaginary-time interaction picture

$$V(\tau_1) = \frac{1}{2} \sum_{klmn} \sum_{\mu\mu'} v_{klmn,\mu\mu'} c^\dagger_{k\mu}(\tau_1) c^\dagger_{l\mu'}(\tau_1) c_{n\mu'}(\tau_1) c_{m\mu}(\tau_1). \tag{1.94}$$

Now consider the following ensemble average over noninteracting system

$$\begin{aligned}
\langle \mathcal{T} c_{i\sigma}(\tau) c^\dagger_{j\sigma}(0) c^\dagger_{k\mu}(\tau_1) c^\dagger_{l\mu'}(\tau_1) c_{n\mu'}(\tau_1) c_{m\mu}(\tau_1) \rangle_0 = \\
+G^0_{ij,\sigma}(\tau) G^0_{nk,\mu}(0) G^0_{ml,\mu'}(0) \delta_{\mu\mu'} \\
-G^0_{ij,\sigma}(\tau) G^0_{mk,\mu}(0) G^0_{nl,\mu'}(0) \\
-G^0_{ik,\sigma}(\tau - \tau_1) G^0_{nj,\mu'}(\tau_1) G^0_{ml,\mu} \delta_{\sigma\mu} \delta_{\sigma\mu'} \delta_{\mu\mu'} \\
+G^0_{ik,\sigma}(\tau - \tau_1) G^0_{mj,\mu}(\tau_1) G^0_{nl,\mu'} \delta_{\sigma\mu} \\
+G^0_{il,\sigma}(\tau - \tau_1) G^0_{nj,\mu'}(\tau_1) G^0_{mk,\mu}(0) \delta_{\sigma\mu'} \\
-G^0_{il,\sigma}(\tau - \tau_1) G^0_{mj,\mu}(\tau_1) G^0_{nk,\mu'}(0) \delta_{\sigma\mu'} \delta_{\sigma\mu} \delta_{\mu\mu'}.
\end{aligned} \tag{1.95}$$

where Wick's theorem Eq. 1.91 as well as the definition of the noninteracting Green's function $G^0_{ij,\sigma}(\tau) = -\langle \mathcal{T} c_{i\sigma}(\tau) c^\dagger_{j\sigma}(0) \rangle_0$ was used. There are six expressions at the first order and the number of terms grows very fast with the perturbation order. In order to simplify the treatment of finite-order perturbation theory Richard Feynman introduced a graphical representation of the Green's function as a sum of diagrams [7–10, 23–27]. Each diagram contains series of noninteracting Green's function lines and electron-electron interaction terms and can be connected or disconnected. A connected diagram is the one in which every internal point is connected via a series of connected lines to the external points. For instance, first term in Eq. 1.95 corresponds to the diagram "c" shown in Fig. 1.1 and is an example of a disconnected diagram. Third and fourth terms in Eq. 1.95 are identical to fifth and sixth terms and are illustrated by diagrams "b" and "a", respectively. Equation 1.95 was obtained by expanding the numerator of Eq. 1.90 to the first order. The purpose of the denominator in Eq. 1.90

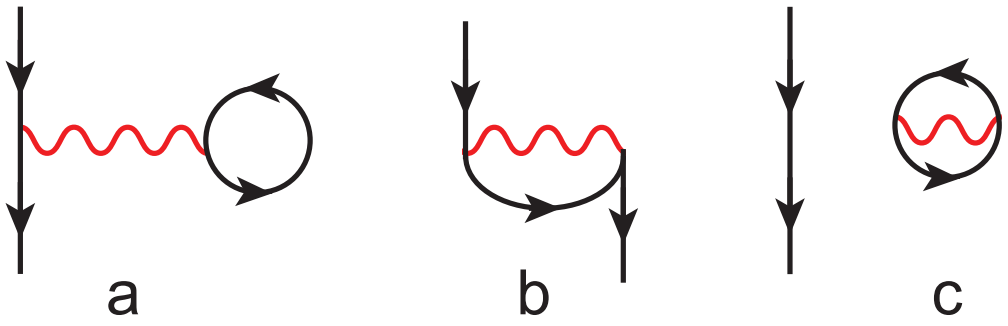

Figure 1.1: Two connected first-order Green's function Feynman diagrams: Hartree (a) and exchange (b) and one disconnected first-order diagram that does not contribute to the perturbative expansion. $G^0_{ij,\sigma}(\tau)$ is shown by black solid lines. Electron-electron interaction v_{klmn} is shown by a red wavy line.

is to cancel all disconnected diagrams [7, 9, 10]. Therefore, not all diagrams eventually contribute to the expression for the Green's function. Only connected and topologically nonequivalent diagrams have to be considered. There are only two such diagrams at the first order perturbation. The diagram "a" in Fig. 1.1 is called direct or Hartree and the diagram "b" is called exchange diagram. Diagrams can be drawn in terms of both imaginary time and imaginary frequency Green's function and constitute a powerful tool of the many-body theory. The detailed description of diagrammatic techniques can be found in several books (e.g. Ref. [7, 9, 27]).

Every connected diagram in the perturbation expansion for the Green's function contains two external Green's function lines at its ends (see e.g. Fig. 1.1). Therefore, every diagram translated into algebraic form is given by the following expression in the frequency domain

$$\begin{aligned}
\mathbf{G}_\sigma(i\omega_n) &= \mathbf{G}^0_\sigma(i\omega_n) + \mathbf{G}^0_\sigma(i\omega_n)\mathbf{\Sigma}_\sigma(i\omega_n)\mathbf{G}^0_\sigma(i\omega_n) \\
&+ \mathbf{G}^0_\sigma(i\omega_n)\mathbf{\Sigma}_\sigma(i\omega_n)\mathbf{G}^0_\sigma(i\omega_n)\mathbf{\Sigma}_\sigma(i\omega_n)\mathbf{G}^0_\sigma(i\omega_n) + \dots \\
&= \mathbf{G}^0_\sigma(i\omega_n) + \mathbf{G}^0_\sigma(i\omega_n)\mathbf{\Sigma}_\sigma(i\omega_n)\mathbf{G}_\sigma(i\omega_n), \qquad (1.96)
\end{aligned}$$

where $\mathbf{\Sigma}_\sigma(\omega_n)$ is called the one-electron self-energy. Some of the self-energy diagrams can be separated into two pieces by cutting a single Green's function lines. These diagrams are called reducible, as opposed to the self-energy diagrams that cannot be separated into two parts by cutting a single Green's function line. Latter are called proper or irreducible self-energy. Equation 1.96 is called Dyson equation, named after Freeman Dyson [28, 29]. It connects a noninteracting Green's function with the interacting one through the self-energy. The exact representation of interacting Green's function can be obtained by solving Dyson equation for it

$$\mathbf{G}_\sigma(i\omega_n) = \left[\left[\mathbf{G}^0_\sigma(i\omega_n)\right]^{-1} - \mathbf{\Sigma}_\sigma(i\omega_n)\right]^{-1}. \tag{1.97}$$

The self-energy can be understood as effective potential which incorporates all the electron-electron correlation effects in the system at single-particle level. It is connected to the concept of quasi-particle as follows. When a real particle propagates through the system it interacts with the environment and thus becomes surrounded by a "cloud". The real particle together with its cloud forms a quasi-particle. Quasi-particles are also called elementary excitations of the system [30–32]. This cloud serves as a screen weakening the interaction between real particles. The quasi-particles have finite life-time and effective mass. These properties are observed experimentally. The self-energy represents the difference between energy of a free particle and energy of a quasi-particle created from the same particle. The exact self-energy is as difficult to obtain as the exact Green's function. However, similarly to the perturbation series for the Green's function, there exist perturbation series for the self-energy. A variety of different approaches are based on either truncation of the series at a finite order or summation of a specific types of the self-energy Feynman diagrams to infinity.

1.3 Hubbard model

The Hubbard model is the most famous model used in condensed matter physics calculations to describe the metal to insulator phase transition caused by electronic degrees of freedom. It was proposed in 1963 by British physicist John Hubbard [33, 34]. The model describes interacting particles in a lattice. The Hubbard Hamiltonian consists of two terms

$$\hat{H} = -t \sum_{\langle i,j \rangle \sigma} \left(\hat{c}^{\dagger}_{i\sigma} \hat{c}_{j\sigma} + \hat{c}^{\dagger}_{j\sigma} \hat{c}_{i\sigma} \right) + U \sum_{i=1} \hat{n}_{i\uparrow} \hat{n}_{i\downarrow}, \tag{1.98}$$

where $\langle i, j \rangle$ means that the summation is performed over nearest-neighboring lattice sites only and $\hat{n}_{i\sigma} = \hat{c}^{\dagger}_{i\sigma} \hat{c}_{i\sigma}$ is the spin-density operator. The first term is the kinetic energy. It describes the "hopping" of a particle between lattice sites. It is restricted to nearest-neighbour lattice sites and a positive real number t gives the amplitude of the hopping process. The second term is the on-site electron-electron repulsion described by interaction strength U. It represents the potential energy of electron-electron interaction and is limited to on-site interactions only. The interplay between t and U is responsible for emergence of a Mott insulator phase when U dominates over "hopping" amplitude t either because electron-electron interaction is strong, corresponding to large U or in the limit of infinite spacing between lattice sites corresponding to small hopping amplitude t. Consequently, the Hubbard model predicted the transition from metal to insulator in certain metal oxides. The one-dimensional Hubbard model was solved analytically by Elliot Lieb [35] in 1968 but the exact solution in arbitrary dimensions has not been obtained yet and currently is an active area of research.

1.4 Anderson impurity model

In 1961 Philip Anderson, based on earlier work of Jacques Friedel (e.g. Ref. [36, 37]), proposed the single-impurity model Hamiltonian [38] describing the interplay

of charge and spin fluctuations of an impurity immersed into an environment. For example, it is used to describe d and f electrons of a transition metal embedded into the environment created by other (conduction) electrons. The interaction of impurity electrons with conduction electrons causes an interesting physics. Anderson impurity model was successfully used to explain a variety of experimental observations including famous Kondo-type problems [39, 40], for instance heavy fermion systems and Kondo insulators. The Anderson impurity Hamiltonian consists of several terms: a single-site impurity part described by the operators $\hat{c}_\sigma$ and $\hat{c}^\dagger_\sigma$ and an environment or "bath", described by operators $\hat{a}_{i\sigma}$ and $\hat{a}^\dagger_{i\sigma}$:

$$\hat{H}_{AIM} = \hat{H}_{imp} + \hat{H}_{bath} + \hat{H}_{coupling}, \tag{1.99}$$

$$\hat{H}_{imp} = \sum_\sigma \epsilon \hat{c}^\dagger_\sigma \hat{c}_\sigma + U \hat{n}_\uparrow \hat{n}_\downarrow, \tag{1.100}$$

$$\hat{H}_{bath} = \sum_{\langle ij \rangle \sigma} t_{ij} \hat{a}^\dagger_{i\sigma} \hat{a}_{j\sigma}, \tag{1.101}$$

$$\hat{H}_{coupling} = \sum_{i\sigma} \left(V_i \hat{c}^\dagger_\sigma \hat{a}_{i\sigma} + V_i^* \hat{c}_\sigma \hat{a}^\dagger_{i\sigma} \right), \tag{1.102}$$

where $\hat{H}_{imp}$ is the pure impurity Hamiltonian, $\hat{H}_{bath}$ is the pure bath Hamiltonian and $\hat{H}_{coupling}$ is the coupling between impurity and bath with V_i being the hybridization term between impurity and bath orbital i. It allows the electrons to hop between impurity site and bath orbitals. The solution of the Anderson impurity model i.e. the correlated Matsubara Green's function or the self-energy can be obtained with the help of so-called quantum impurity solvers [41–46]. In 1989 Walter Metzner and Dieter Vollhardt [47] showed that in the limit of infinite dimensions the generally intractable lattice problem described, for instance, by the Hubbard model can be mapped into a single-site (local) problem described by the Anderson impurity Hamiltonian. This significant milestone of the history of condensed matter physics has opened up a way to practical studies of strongly correlated systems with the dynamical mean-field the-

ory [43, 48, 49] (DMFT)—a non-perturbative and thermodynamically consistent approximation scheme for finite-dimensional systems. It was quickly realized that DMFT is a powerful tool for investigations of electronic structure of realistic materials [50–54]. DMFT continues to attract attention as its cluster extensions become available [49, 55–57].

1.5 Luttinger–Ward functional and thermodynamics

In this section we explore connections between static properties which describe the thermodynamics of the system and dynamical quantities which describe one-electron properties of the system. The thermodynamics of an open system is described by a thermodynamical grand potential

$$\Omega = E - TS - \mu n, \tag{1.103}$$

where S is the entropy, E is the internal energy, μ is the chemical potential, and n is the total number of particles in the system. In 1960 Joaquin Luttinger and John Ward found a connection between the grand potential Ω and exact Matsubara Green's function $G = G(i\omega_n)$, the self-energy $\Sigma = \Sigma(i\omega_n)$ [9, 10, 26, 58]

$$\Omega = \frac{1}{\beta}\left[\Phi_{LW} - \mathrm{Tr}\left(\Sigma G + \ln\left(\Sigma - G_0^{-1}\right)\right)\right], \tag{1.104}$$

where G_0 is the reference Green's function typically corresponding to the noninteracting Green's function and Φ_{LW} is the Luttinger–Ward functional [58]. It is a scalar functional of a Green's function. The Luttinger–Ward functional is defined diagrammatically as the sum of all closed, irreducible diagrams of one-electron Green's functions

Figure 1.2: Φ_{LW} diagrams for up to the second order in electron-electron interactions (red line). One-electron Green's functions are shown by black solid lines.

and electron-electron interaction or, algebraically, by the following expression

$$\Phi_{LW} = \sum_{m=1}^{\infty} \frac{1}{2m} \left(\sum_{n} \Sigma^{(m)}(i\omega_n) G(i\omega_n) \right). \tag{1.105}$$

where $\Sigma^{(m)}(i\omega_n)$ is a self-energy containing all irreducible and topologically inequivalent diagrams of order m. For example, Feynman diagrams for the Φ_{LW} up to the second order are shown in Fig. 1.2. The Luttinger–Ward functional does not have a direct physical meaning but nonetheless is quite useful. It is symmetric under infinitesimal variation of the Green's function. These properties ensure the conservation of momentum, energy and total number of particles in the system. The functional derivative of the Luttinger–Ward functional with respect to the Matsubara Green's function is the (Φ-derivable) self-energy

$$\Sigma_{ji}[G] = \beta \frac{\delta \Phi_{LW}[G]}{\delta G_{ij}}. \tag{1.106}$$

It defines the functional $\Sigma_{ij}[G]$ which gives the exact self-energy of the system if the exact Green's function is used. Correspondingly a self-energy which is not a functional derivative of Luttinger–Ward functional with respect to the one-electron Green's function is called non-Φ-derivable. Diagrammatically taking functional derivatives corresponds to "opening" any of the Green's function lines of a Φ_{LW} diagram. For example, the first and second-order self-energy diagrams obtained by functional differentiation the $\Phi_{LW}[G]$ diagrammatically shown in Fig. 1.2 are illustrated in Fig. 1.3. Φ-derivability is a key property of the self-energy. For instance, Φ-derivable self-energies satisfy some important relations e.g. $\Sigma_{ij}(\tau) = -\Sigma_{ij}(\tau - \beta)$. Secondly, approximations

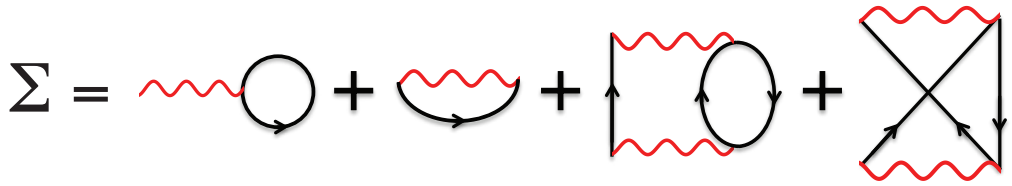

Figure 1.3: Σ diagrams for up to the second order in electron-electron interaction (red line). One-electron Green's functions are shown by black solid lines.

based on such self-energies satisfy the conservation laws. In 1961 Gordon Baym and Leo Kadanoff [59] showed a very important result that any diagrammatic truncation of the Luttinger–Ward functional obeys the conservation laws. Not only the finite-order perturbation theory, based on such truncation, but also other approximations such as fully self-consistent GW [60] approach or DMFT are also Φ-derivable.

The functional $\Phi[G]$ is universal since it is completely determined by the interaction part of the Hamiltonian. This means that for two systems with the same electron-electron interaction $\hat{V}_{ee}$ but different one-electron properties (e.g. kinetic energy, and electron-nuclei interaction energy) the functional $\Phi[G]$ is identically the same. Consequently for a noninteracting system $\Phi[G_0] = 0$.

The grand potential is a functional of a Green's function $\Omega[G]$ (or, equivalently a functional of a self-energy). If one-electron Green's function is a self-consistent solution of the Dyson equation then Ω is the total energy of a system and its functional derivative with respect to the one-electron Green's function vanishes

$$\frac{\delta\Omega[G]}{\delta G} = 0, \tag{1.107}$$

which means that it is stationary with respect to variations in the one-electron Green's function G. This also guarantees the conservation e.g. of a total number of particles given by a negative derivative of the grand potential Ω with respect to the chemical potential μ. However if the Dyson equation for G is solved with the non-Φ-derivable self-energy, then the total number of particles is not necessarily conserved.

The grand potential is related to the partition function Z as follows

$$\Omega = -\frac{1}{\beta} \ln Z \tag{1.108}$$

which allows to calculate all macroscopic equilibrium thermodynamic properties from the grand potential:

- Helmholtz free energy

$$F = E - TS = \Omega + \mu N. \tag{1.109}$$

- Gibbs free energy

$$G = E - TS + PV = \Omega + \mu N + PV. \tag{1.110}$$

- Electronic entropy

$$S = \frac{E - \Omega - \mu N}{T}. \tag{1.111}$$

- The internal energy E is given by the Galitskii–Migdal [61] formula

$$E = \frac{1}{2}\mathrm{Tr}\left[(h + F)\gamma_1\right] + \frac{2}{\beta}\sum_{n}^{\infty} \mathrm{Re}\left[G(i\omega_n)\Sigma(i\omega_n)\right], \tag{1.112}$$

  where γ_1 is the one-electron reduced density matrix, h is the one-electron Hamiltonian matrix and F is the Fock matrix.

In summary, the Luttinger–Ward functional provides a basis for a variational principle connecting static thermodynamic properties of the system with the dynamic physical quantities.

1.6 Description and outline of the present work

Green's function methods have a long history in condensed matter physics [9, 10, 26, 27]. The diagrammatic expansion for the self-energy or Green's function have been explored in nearly every possible way with many successful methods ranging from approximate and computationally inexpensive to exact but almost impractical due to their prohibitive computational cost: GF2, GW, DMFT, FLEX and quantum Monte Carlo methods. Only very recently Green's function methods begun to enter the field of computational quantum chemistry with the application of zero-temperature GW and random phase approximations to the calculation of total energies, properties of a weakly bound molecules, surface adsorption [62, 63], photoemission spectra [64], and optical spectra [65], to name just a few.

In the contrast to remarkable progress achieved in the development and application of zero-temperature Green's function methods, the application of finite-temperature Green's function methods are very rare in computational quantum chemistry. The complication arises from a broad energy scale of realistic systems and intricate interplay between kinetic and potential energy leading to strong correlation responsible for many interesting phenomena such as a huge change in the resistivity or unusually dramatic volume changes upon metal-insulator transition, unprecedentedly high transition temperatures, d-wave superconductivity, spin and charge ordered phases, rotational symmetry breaking states, and many more. Successful studies of these phenomena require new, robust, computationally efficient methods.

Chapter 2 presents a new Green's function based embedding framework called the self-energy embedding theory (SEET). Its main idea is to embed a high-level description of a chemically active degrees of freedom into the secondary, inactive degrees of freedom, treated at a low-level method. We illustrate the application of this method to the Hubbard model.

Chapter 3 presents a theory and implementation of the open-shell second-order Green's function method (GF2). We analyze the fractional charge and spin errors in GF2 and compare it to established quantum chemistry methods such as second-order Møller–Plesset theory (MP2), density functional theory and random phase approximation. We report an important benefit of iterative GF2 calculations in comparison to its non iterative wave function counterpart MP2.

In Chapter 4 we extend the SEET to the *ab initio* Hamiltonians. We present several proof-of-principle applications of SEET to small molecules, discuss different partitioning schemes as well as provide comparison to other quantum chemistry methods. We illustrate that SEET yields results of comparable quality to most accurate quantum chemistry methods with the same active space. Additionally, we discuss the most important characteristics of SEET and show that it avoids many complications pertinent to many established quantum chemistry methods.

Chapters 5 and 6 present algorithmic developments paving the way for the applications of GF2 and SEET to large realistic systems. Chapter 5 illustrates an adaptation of the orthogonal polynomial representation of imaginary time Green's function and self-energy to realistic systems. In Chapter 6 we employed a popular cubic spline interpolation technique to develop an efficient algorithm allowing to reduce the computational cost and storage associated with imaginary frequency quantities. We illustrate that using methods presented in Chapters 5 and 6 GF2 and SEET can be applied to systems considerably larger than Hubbard model or simple molecules.

Chapter 7 present a thorough discussion of SEET in the context of quantum chemistry. We focus our discussion on many practical aspects such as the choice of best orbital basis, impurity solver, and many steps necessary to reach chemical accuracy. Different approaches to selecting strongly correlated orbitals based on spatial or energy domain are compared. Finally, on a set of carefully chosen molecular examples, we demonstrate that SEET can be as accurate as established wave function quantum

chemistry methods.

In Chapter 8 a rigorous framework combining one-electron Green's function theory and density functional theory based on a separation of electron-electron interaction into short-range and long-range components is presented. The local density approximation is applied to short-range interactions while the long-range contribution to the electron-electron interaction is treated by GF2. This results in a new, non-local, dynamic and orbital-dependent exchange-correlation functional of a one-electron Green's function. We illustrate that this functional produces molecular properties similar to GF2. But, unlike standard GF2 calculations, the calculations employing the new functional benefit from faster basis set convergence. We also show that such range-separated hybrids can be used to scale down the self-energy, thereby providing an additional sparsity to the self-energy matrix.

Bibliography

[1] C. C. J. Roothaan, "New developments in molecular orbital theory", *Rev. Mod. Phys.* **23**, 69 (1951).

[2] P. Hohenberg and W. Kohn, "Inhomogeneous electron gas", *Phys. Rev.* **136**, B864 (1964).

[3] W. Kohn and L. J. Sham, "Self-consistent equations including exchange and correlation effects", *Phys. Rev.* **140**, A1133 (1965).

[4] A. J. Coleman, "Structure of fermion density matrices", *Rev. Mod. Phys.* **35**, 668 (1963).

[5] D. A. Mazziotti, "Significant conditions for the two-electron reduced density matrix from the constructive solution of n representability", *Phys. Rev. A* **85**, 062507 (2012).

[6] "Reduced-density-matrix mechanics: With application to many-electron atoms and molecules", in *Adv. Chem. Phys.*, Vol. 134, edited by D. A. Mazziotti, Wiley (2007).

[7] A. R. Jishi, *Feynman Diagram Techniques in Condensed Matter Physics*, Cambridge University Press: Cambridge, UK (2014).

[8] H. Bruus and K. Flensberg, *Many-Body Quantum Theory in Condensed Matter Physics: An Introduction*, Oxford University Press: Oxford, UK (2004).

[9] G. Stefanucci and R. van Leeuwen, *Nonequilibrium Many-Body Theory of Quantum Systems: A Modern Introduction*, Cambridge University Press: Cambridge, UK (2013).

[10] A. L. Fetter and J. D. Walecka, *Quantum Theory of Many-Particle Systems*, Dover Publications: Mineola, NY, USA (2003).

[11] T. Matsubara, "A new approach to quantum-statistical mechanics", *Prog. Theor. Phys.* **14**, 351 (1955).

[12] E. Wigner and F. Seitz, "On the constitution of metallic sodium", *Phys. Rev.* **43**, 804 (1933).

[13] E. Wigner and F. Seitz, "On the constitution of metallic sodium. II", *Phys. Rev.* **46**, 509 (1934).

[14] P.-O. Löwdin, "Correlation problem in many-electron quantum mechanics I. Review of different approaches and discussion of some current ideas", *Adv. Chem. Phys.* pp. 207–322 (1959).

[15] C. Hättig, W. Klopper, A. Khn, and D. P. Tew, "Explicitly correlated electrons in molecules", *Chem. Rev.* **112**, 4 (2012).

[16] W. Kutzelnigg, G. Del Re, and G. Berthier, "Correlation coefficients for electronic wave functions", *Phys. Rev.* **172**, 49 (1968).

[17] W. L. Luken, "Properties of the Fermi hole in molecules", *Croat. Chem. Acta* **57**, 1283 (1984).

[18] M. Buijse and E. J. Baerends, "Density functional theory of molecules, clusters, and solids", Kluwer: Dordrecht, Netherlands (1995).

[19] P. Ros, "Exact and simulated coulomb holes and coulomb correlations potentials for the ground state of the He isoelectronic systems", *Chem. Phys.* **42**, 9 (1979).

[20] T. Kato, "On the eigenfunctions of many-particle systems in quantum mechanics", *Commun. Pure App. Math.* **10**, 151 (1957).

[21] W. A. Bingel, "The behaviour of the second-order density matrix at the coulomb singularities of the Schrödinger equation", *Theor. Chim. Acta* **5**, 341 (1966).

[22] G. C. Wick, "The evaluation of the collision matrix", *Phys. Rev.* **80**, 268 (1950).

[23] R. P. Feynman, "Space-time approach to quantum electrodynamics", *Phys. Rev.* **76**, 769 (1949).

[24] R. P. Feynman, "The theory of positrons", *Phys. Rev.* **76**, 749 (1949).

[25] G. D. Mahan, *Many-Particle Physics*, Springer Science: New York, NY, USA (2000).

[26] A. A. Abrikosov, L. P. Gorkov, and I. E. Dzyaloshinski, *Methods of Quantum Field Theory in Statistical Physics*, Dover Publications: NY, USA (1963).

[27] R. D. Mattuck, *A guide to Feynman Diagrams in the Many-Body Problem*, Dover Publications: NY, USA (1992).

[28] F. J. Dyson, "The radiation theories of Tomonaga, Schwinger, and Feynman", *Phys. Rev.* **75**, 486 (1949).

[29] F. J. Dyson, "The s matrix in quantum electrodynamics", *Phys. Rev.* **75**, 1736 (1949).

[30] D. Bohm and D. Pines, "A collective description of electron interactions. I. Magnetic interactions", *Phys. Rev.* **82**, 625 (1951).

[31] D. Pines and D. Bohm, "A collective description of electron interactions: II. collective vs individual particle aspects of the interactions", *Phys. Rev.* **85**, 338 (1952).

[32] D. Bohm and D. Pines, "A collective description of electron interactions: III. coulomb interactions in a degenerate electron gas", *Phys. Rev.* **92**, 609 (1953).

[33] J. Hubbard, "Electron correlations in narrow energy bands", *Proc. R. Soc. London A.* **276**, 238 (1963).

[34] "The Hubbard model at half a century", *Nat. Phys.* **9**, 523 (2013).

[35] E. H. Lieb and F. Y. Wu, "Absence of Mott transition in an exact solution of the short-range, one-band model in one dimension", *Phys. Rev. Lett.* **20**, 1445 (1968).

[36] J. Friedel, "On some electrical and magnetic properties of metallic solid solutions", *Can. J. Phys.* **34**, 1190 (1956).

[37] de Faget de Casteljau, P. and Friedel, J., "Étude de la résistivité et du pouvoir thermoélectrique des impuretés dissoutes dans les métaux nobles", *J. Phys. Radium* **17**, 27 (1956).

[38] P. W. Anderson, "Localized magnetic states in metals", *Phys. Rev.* **124**, 41 (1961).

[39] J. Kondo, "Resistance minimum in dilute magnetic alloys", *Prog. Theor. Phys.* **32**, 37 (1964).

[40] A. Hewson, *The Kondo Problem to Heavy Fermions*, Cambridge Studies in Magnetism, Cambridge University Press: Cambridge, UK (1997).

[41] K. G. Wilson, "The renormalization group: Critical phenomena and the Kondo problem", *Rev. Mod. Phys.* **47**, 773 (1975).

[42] E. Gull, A. J. Millis, A. I. Lichtenstein, A. N. Rubtsov, M. Troyer, and P. Werner, "Continuous-time Monte Carlo methods for quantum impurity models", *Rev. Mod. Phys.* **83**, 349 (2011).

[43] A. Georges and G. Kotliar, "Hubbard model in infinite dimensions", *Phys. Rev. B* **45**, 6479 (1992).

[44] M. Caffarel and W. Krauth, "Exact diagonalization approach to correlated fermions in infinite dimensions: Mott transition and superconductivity", *Phys. Rev. Lett.* **72**, 1545 (1994).

[45] N. Bickers and D. Scalapino, "Conserving approximations for strongly fluctuating electron systems. I. Formalism and calculational approach", *Ann. Phys.* **193**, 206 (1989).

[46] R. Bulla, T. A. Costi, and T. Pruschke, "Numerical renormalization group method for quantum impurity systems", *Rev. Mod. Phys.* **80**, 395 (2008).

[47] W. Metzner and D. Vollhardt, "Correlated lattice fermions in $d = \infty$ dimensions", *Phys. Rev. Lett.* **62**, 324 (1989).

[48] A. Georges, G. Kotliar, W. Krauth, and M. J. Rozenberg, "Dynamical mean-field theory of strongly correlated fermion systems and the limit of infinite dimensions", *Rev. Mod. Phys.* **68**, 13 (1996).

[49] T. Maier, M. Jarrell, T. Pruschke, and M. H. Hettler, "Quantum cluster theories", *Rev. Mod. Phys.* **77**, 1027 (2005).

[50] G. Kotliar, S. Y. Savrasov, K. Haule, V. S. Oudovenko, O. Parcollet, and C. A. Marianetti, "Electronic structure calculations with dynamical mean-field theory", *Rev. Mod. Phys.* **78**, 865 (2006).

[51] K. Held, "Electronic structure calculations using dynamical mean field theory", *Adv. Phys.* **56**, 829 (2007).

[52] D. Vollhardt, "Dynamical meanfield theory of electronic correlations in models and materials", *AIP Conference Proceedings* **1297**, 339 (2010).

[53] G. Kotliar and D. Vollhardt, "Strongly correlated materials: Insights from dynamical mean-field theory", *Physics Today* **57**, 53 (2004).

[54] S. V. Savrasov, G. Kotliar, and E. Abrahams, "Correlated electrons in *delta*-plutonium within a dynamical mean-field picture", *Nature* **410**, 793 (2001).

[55] M. H. Hettler, A. N. Tahvildar-Zadeh, M. Jarrell, T. Pruschke, and H. R. Krishnamurthy, "Nonlocal dynamical correlations of strongly interacting electron systems", *Phys. Rev. B* **58**, R7475 (1998).

[56] A. I. Lichtenstein and M. I. Katsnelson, "Antiferromagnetism and d-wave superconductivity in cuprates: A cluster dynamical mean-field theory", *Phys. Rev. B* **62**, R9283 (2000).

[57] G. Kotliar, S. Y. Savrasov, G. Pálsson, and G. Biroli, "Cellular dynamical mean field approach to strongly correlated systems", *Phys. Rev. Lett.* **87**, 186401 (2001).

[58] J. M. Luttinger and J. C. Ward, "Ground-state energy of a many-fermion system. II", *Phys. Rev.* **118**, 1417 (1960).

[59] G. Baym and L. P. Kadanoff, "Conservation laws and correlation functions", *Phys. Rev.* **124**, 287 (1961).

[60] L. Hedin, "New method for calculating the one-particle Green's function with application to the electron-gas problem", *Phys. Rev.* **139**, A796 (1965).

[61] V. M. Galitskii and A. B. Migdal, "Application of quantum field theory methods to the many body problem", *J. Exptl. Theoret. Phys.* **34**, 139 (1958).

[62] G. P. Chen, V. K. Voora, M. M. Agee, S. G. Balasubramani, and F. Furche, "Random-phase approximation methods", *Annu. Rev. Phys. Chem.* **68**, 421 (2017).

[63] X. Ren, P. Rinke, C. Joas, and M. Scheffler, "Random-phase approximation and its applications in computational chemistry and materials science", *J. Mat. Sc.* **47**, 7447 (2012).

[64] F. Bruneval and M. Gatti, "First principles approaches to spectroscopic properties of complex materials", Springer Berlin Heidelberg: Germany.

[65] M. Rohlfing and S. G. Louie, "Electron-hole excitations and optical spectra from first principles", *Phys. Rev. B* **62**, 4927 (2000).

Chapter 2

Systematically improvable multiscale solver for correlated electron systems

A. A. Kananenka, E. Gull and D. Zgid,

Physical Review B, **91 (12)** 121111(R) (2015)

2.1 Introduction and general framework

The theoretical description of strongly correlated materials has proven to be challenging, mainly because many of their interesting properties are caused by the interplay of subtle electronic correlation effects on low energy scales. Since simultaneous treatment of both strong and weak correlations is of major importance for the quantitative description of these systems, two main conceptual approaches are used: the reduction to a few "relevant" degrees of freedom or essential orbitals around the Fermi level and the subsequent construction of a model system or, alternatively, the treatment of the entire system using methods which significantly approximate correlation effects.

The first approach, with methods including exact diagonalization (ED) [1–4] and its variants, [5, 6] density matrix renormalization group (DMRG), [7] dynamical mean field theory (DMFT) [8, 9] and lattice quantum Monte Carlo (QMC) [10] applied to model Hamiltonians, can yield very precise results for model systems. When applied to realistic systems, its main uncertainties and possible sources of errors lie in the

construction of the parameters of the effective model.

The second approach, which includes implementations of the density functional theory (DFT), [11, 12] Hartree–Fock (HF), Hedin's GW, [13] the random phase approximation (RPA), [14] Møller–Plesset second order perturbation theory (MP2), [15] second-order Green's function theory (GF2) [16, 17] or QMC, [18] avoids constructing an effective model by treating the full Hamiltonian with all orbitals and interactions, but relies on potentially severe approximations to the electronic correlations.

Multiscale methods for extended systems combining the best aspects of both approaches, e.g. by solving the system using DFT or GW and using the result to construct a model system, have been implemented as the GW+DMFT [19–32] and DFT+DMFT [22, 23] method.

Constructing a robust multiscale method is a formidable problem and an active field of research. First, different energy scales have to be defined and a set of strongly correlated orbitals requiring a higher level treatment has to be chosen. Second, the non-local Coulomb interactions present in realistic materials have to be included by a suitable choice of "screened" interactions. Third, correlations in the weakly correlated orbitals should not be completely neglected but rather be treated perturbatively, if a quantitative material-dependent description is desired.

In this Chapter, we present a general framework for a multiscale algorithm in which a self-energy describing strongly correlated orbitals is self-consistently embedded into the self-energy obtained from a method able to treat long-range interaction and correlation effects. We call this general framework "self-energy embedding theory" (SEET). A mathematically rigorous procedure for identifying the strongly correlated orbitals and systematically increasing the accuracy of the treatment of the weakly correlated orbitals is an integral part of our procedure. The strongly and the weakly correlated subspaces are treated using different methods. As an example, we will choose exact diagonalization (ED) to yield the self-energy for the strongly correlated orbitals and

the self-consistent second-order Green's function method (GF2) [16] for the weakly correlated part, and call the resulting algorithm SEET(ED-in-GF2). However,we note that our scheme is general and independent of the algorithms used to treat the weakly and strongly treated subspaces: ED could be replaced by, e.g., (CT)-QMC, while GF2 could be replaced with fluctuation exchange approximation (FLEX), GW, or the Parquet method.

Here we illustrate SEET(ED-in-GF2) and calibrate it using impurity problems, since a method capable of treating multiscale problems such as realistic materials should also yield accurate results for model systems. Impurity problems have a continuous dispersion but only a finite number of interaction terms. Nevertheless, they exhibit strongly and weakly correlated regimes and a number of phases and phase transitions that are very well understood and for which numerically exact comparison algorithms exist. [33] The restriction to these models allows us to provide the stringent tests on the accuracy of SEET in a well-controlled test environment. In the future, we aim to apply SEET to realistic materials, where it has the potential to become a method complementary to GW+DMFT or DFT+DMFT.

In order to generate a wide range of correlated phases, we generate our impurity parameters from a four-site dynamical cluster approximation (DCA) [9, 34] to the two-dimensional (2D) Hubbard model, i.e. test our method as a "DCA impurity solver", so that our results can be compared against numerically exact CT-QMC data. [35, 36] We emphasize that while we have developed a numerically efficient impurity solver, we do not envisage this as the main use of SEET, and we mainly resort to impurity models for the sake of generating comparisons to reliable known results.

SEET in the ED-in-GF2 variant is computationally affordable, as GF2 scales as $\mathcal{O}(N^5)$, where N is the number of orbitals in a unit cell. Additionally, SEET is amenable to parallelization on large machines. The scaling of GF2 can be further reduced to $\mathcal{O}(N^4)$ by employing density fitted integrals, [16] and the strongly cor-

related orbitals can be treated by ED as pairs, further reducing the numerical cost. Consequently, large systems containing many unit cells or k points containing multiple orbitals can be treated simultaneously, providing non-local effects and momentum dependence.

In Section 2.2, we introduce SEET(ED-in-GF2). Section 2.3 shows results for our test model, and Section 2.4 contains conclusions of our work.

2.2 The SEET(ED-in-GF2) method applied to an impurity model

We consider an impurity problem with N impurity orbitals a_i coupled to an infinitely many bath orbitals c_λ described by a general Hamiltonian

$$\hat{H} = \sum_{ij} t_{ij} a_i^\dagger a_j + \sum_{ijkl} U_{ijkl} a_i^\dagger a_j^\dagger a_l a_k + \sum_{i\lambda} V_{i\lambda} a_i^\dagger c_\lambda + \sum_{\lambda} \epsilon_\lambda c_\lambda^\dagger c_\lambda + H.c., \tag{2.1}$$

where t and U are material-specific one- and two-body operators, V is the hybridization strength, and ϵ_λ is the c-electron dispersion. The single-particle properties of this Hamiltonian are described by a noninteracting Matsubara Green's function for a electrons

$$G_0(i\omega) = [i\omega + \mu - t - \Delta(i\omega)]^{-1}, \tag{2.2}$$

with $\Delta(i\omega)$ encapsulating the properties of the c electrons and μ being the chemical potential. In SEET(ED-in-GF2), we obtain the interacting Green's function G^{GF2} of this N-orbital impurity problem iteratively, starting from $G^{GF2} = G_0$, by self-consistent second-order perturbation theory (GF2),[16, 17]

$$[\Sigma^{GF2}(\tau)]_{ij} = -\sum_{klmnpq} [G^{GF2}(\tau)]_{kl} [G^{GF2}(\tau)]_{mn} [G^{GF2}(-\tau)]_{pq} U_{iqmk} \big(2U_{lnpj} - U_{nlpj}\big) \tag{2.3}$$

and the corresponding GF2 Green's function

$$G^{GF2}(i\omega) = \left[[G_0^{GF2}(i\omega)]^{-1} - \Sigma^{GF2}(i\omega)\right]^{-1}. \tag{2.4}$$

Note that GF2 can be solved self-consistently and includes an exchange diagram important for describing systems with a localized electronic density, but does not include higher order RPA-like diagrams that are present, e.g., in GW. We then evaluate the one-body density matrix using the converged GF2 Green's function and choose a set of $n < N$ orbitals corresponding to eigenvalues of the one-body density matrix which are significantly different from 0 or 2. These n orbitals, which we will call "strongly correlated", are used to build an n-orbital impurity problem which is then solved with a method more accurate than GF2 to compute a self-energy. Here, we use ED [37] to solve this impurity problem. The resulting ED self-energy is used to modify the GF2 self-energy and to obtain the total self-energy in the natural orbital basis as

$$[\Sigma]_{ij} = [\Sigma^{ED}_{strong}]_{\mu\nu} + [\Sigma^{GF2}]_{ij} - [\Sigma^{GF2}_{strong}]_{\mu\nu}. \tag{2.5}$$

The indices i and j run over all N orbitals, while μ and ν run only over the n strongly correlated orbitals. The total self-energy is schematically illustrated in Fig. 2.1.

As the n correlated orbitals are chosen in the eigenbasis of the one-body density matrix, a transformation of the one-body and two-body integrals in this n-orbital subspace to the eigenbasis is necessary. Note, that even for cases where model Hamiltonians with simplified (e.g. local or density-density) interaction structures are studied, this transformation generates general interactions U_{ijkl}. This n-orbital impurity problem with non-local interaction U_{ijkl} is then treated by the ED solver requiring an additional bath discretization step which may introduce fitting errors. We emphasize that these are small for the cases studied here and that, in principle, any solver suitable to describe strong correlations and able to treat general multiorbital interactions can be employed,

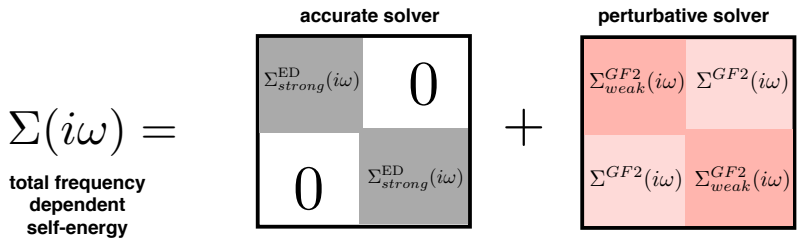

Figure 2.1: The total self-energy in natural orbital basis produced in the SEET with ED-in-GF2 scheme.

including QMC solvers based on the hybridization expansion [38] which do not require a bath discretization step.

The ED-in-GF2 procedure is iterated, and the GF2 calculation updates $[\Sigma^{GF2}]_{ij}$ for the N orbitals since $i, j = 1, \ldots, N$ where

$$[\Sigma^{GF2}_{weak}]_{\mu\nu} = [\Sigma^{GF2}]_{\mu\nu} - [\Sigma^{GF2}_{strong}]_{\mu\nu} \tag{2.6}$$

is responsible for removal of diagrams later included at the ED level. Subsequent ED calculation updates the strongly part of self-energy $[\Sigma^{ED}_{strong}]_{\mu\nu}$. The iterative updates stop when the total self-energy in Eq. 2.5 is converged to a predefined accuracy. We present a detailed algorithmic description of this framework in the Appendix.

The algorithm, both in its general form and in the ED-in-GF2 variant, is based on a diagrammatic formulation in which a "double counting" [39] problem does not appear. The single-particle formulation avoids vertex functions, which are often difficult to handle, and is based on static (or frequency-independent) interactions. [40–42]

2.3 Results

We calibrate SEET(ED-in-GF2) for the 2×2 dynamical cluster approximation (DCA) to the 2D Hubbard model,[9, 34] and consequently the Hamiltonian from Eq. 2.1 is defined for t describing nearest neighbor hopping only and U exclusively on-site inter-

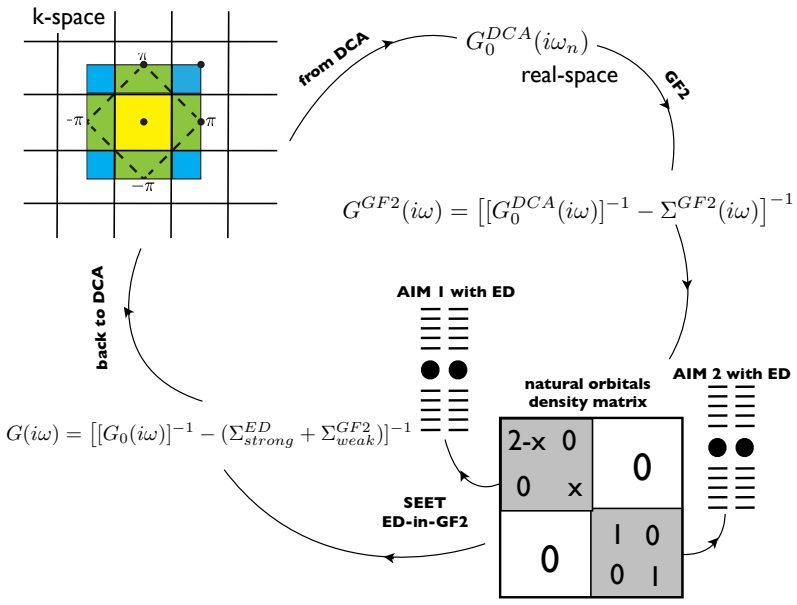

Figure 2.2: Schematic view of the DCA+ED-in-GF2 procedure used for treating the four-site cluster DCA approximation to the 2D Hubbard model. Note that "strong" denotes quantities in the correlated subspace, and "weak" quantities defined on the entire system.

actions. DCA provides the noninteracting Green's function [in Eq. 2.2] which is then employed to obtain the GF2 self-energy from Eq. 2.3. Subsequently, we construct the one-body density matrix and choose a pair of two-site impurities to be treated by ED. The occupations of the four site cluster in natural orbitals are $2-x$, 1, 1, x, where for most regimes x is not a small number, thus the orbitals with occupations $2-x$, and x are no longer weakly correlated. This motivates us to choose two separate impurity problems with orbitals occupied as (1,1) and ($2-x$,x) and treat them as a pair of two-site impurities embedded into the GF2 description. This means that only the interactions between these two-site impurities are treated at the GF2 level. A schematic description of the DCA+ED-in-GF2 iterative scheme is shown in Fig. 2.2. SEET allows us to treat multiple embedded impurities which is computationally advantageous since in realistic cases the number of strongly correlated orbitals may be too large for current solvers such as ED or the hybridization expansion QMC.

Testing ED-in-GF2 using SEET on the DCA approximation to the 2D Hubbard

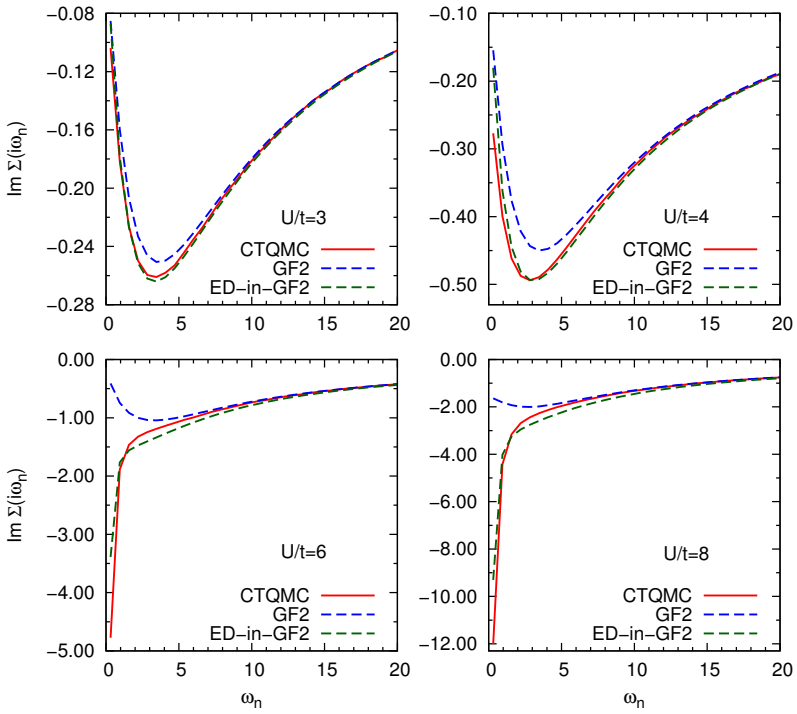

Figure 2.3: The imaginary part of the on-site CT-QMC, GF2 and ED-in-GF2 self-energy obtained for a four-site cluster of the half-filled 2D Hubbard model for various interaction strength with $\beta = 10t$.

model provides a worst case scenario for a multiscale embedding scheme, since in multiple regimes the four-site cluster does not display a separation of energy scales or any "weakly" and "strongly" correlated orbitals as typically found in realistic materials. Rather, in the Mott regime of the 2D Hubbard model, all orbitals are strongly correlated, providing a stringent test of the SEET with ED-in-GF2 method.

In Fig. 2.3, the imaginary part of the self-energy is plotted for the half-filled case. For weak coupling, i.e. $U/t < 4$, GF2 recovers the QMC results well. While for $U/t = 3$ ED-in-GF2 corrects the GF2 result only slightly, for $U/t = 4$, the improvement is more substantial. In this case, the ED-in-GF2 recovers QMC results and is a quantitative correction to the qualitatively correct GF2 curve.

As expected, in the Mott regime, $U/t = 6$ and 8, GF2 fails to recover the self-energy even qualitatively. Note that an iterated perturbation theory (IPT)-like fitting of the large-U limit to the atomic limit would be possible for this particular example but not

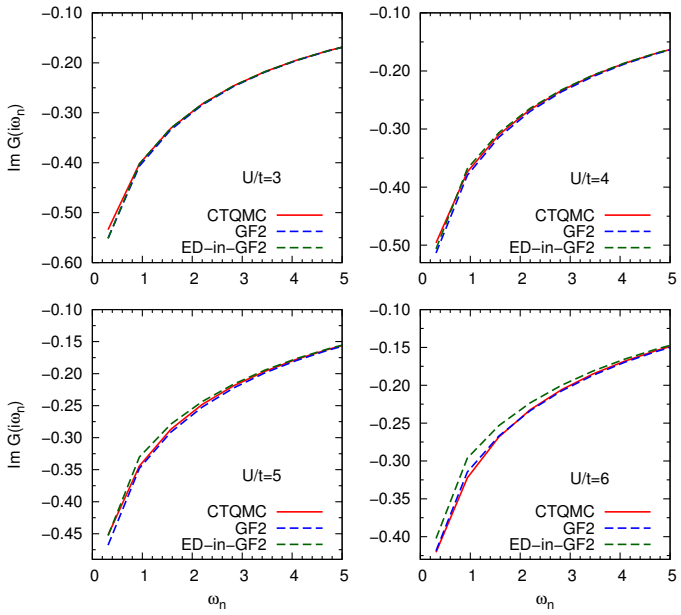

Figure 2.4: The imaginary part of the on-site CT-QMC, GF2 and ED-in-GF2 Matsubara Green's function obtained for a four-site cluster of the 2D Hubbard model at 10% doping, for $U/t = 3, 4, 5$, and 6 with $\beta = 10t$.

in general, as it requires the determination of the local physics at exponential (in n) cost. In the Mott regime, ED-in-GF2 recovers to a decent quantitative accuracy the QMC self-energy for both $U/t = 6$ and 8.

In Figs. 2.4 and 2.5, we examine several interesting regimes at 10% doping, where the system exhibits the behavior of a strongly correlated Fermi liquid. In these cases, we report real and imaginary parts of the Green's functions rather than self-energies, since a slight difference in chemical potentials between different methods results in a shift of the Hartree term in the large-ω limit.

The imaginary part of Green's function shows a good quantitative agreement between CT-QMC and ED-in-GF2 for multiple U/t regimes. The real part of the Green's function shows more differences than the imaginary part. In the weak coupling regime illustrated in Fig. 2.5, for $U/t = 3$ and $U/t = 4$, all the QMC, GF2 and ED-in-GF2 real parts of Green's functions are close. The $U/t = 5$ and $U/t = 6$ regimes are more correlated and GF2 yields a qualitatively incorrect result. ED-in-GF2 corrects this

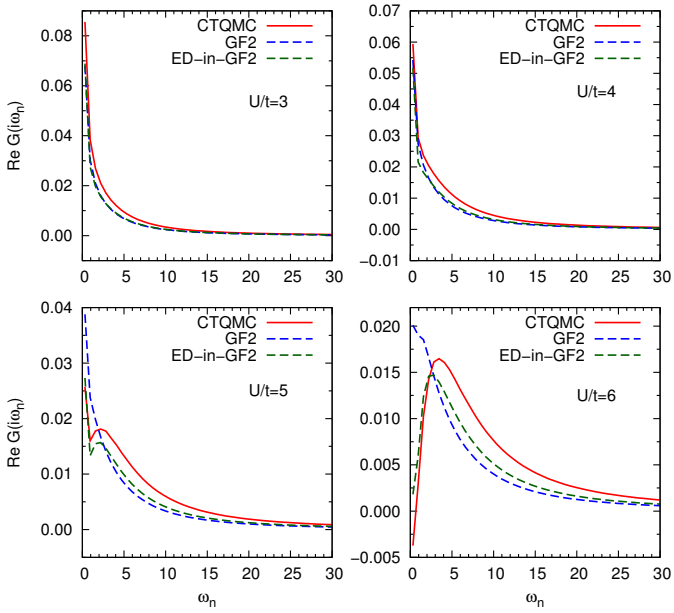

Figure 2.5: The real part of the on-site CT-QMC, GF2 and ED-in-GF2 Matsubara Green's function obtained for a four-site cluster of the 2D Hubbard model at 10% doping, for $U/t = 3, 4, 5$, and 6 with $\beta = 10t$.

result and provides a quantitative agreement with CT-QMC.

2.4 Conclusions

We introduced a general self-energy embedding theory (SEET) for correlated systems and performed a comparison of SEET(ED-in-GF2) on a strongly correlated system for which the exact solution is known, the four-site cluster DCA approximation to the 2D Hubbard model. This model has a continuous dispersion and shows a range of correlated phases, thus providing us with a detailed assessment of strengths and weaknesses of our method. However, it does not illustrate the effect of non-local interactions. Since in multiple regimes a clear separation of energy scales is not present, this model provides a rigorous test for a multiscale method. We were able to show that ED-in-GF2 provides accurate results for the four-site Hubbard model in the weakly correlated, intermediately correlated, and strongly correlated regimes, at and away from half filling. While the solution in the strongly correlated embedded subset of orbitals has exponen-

tial scaling in our case, the total self-energy for the strongly correlated orbitals can be assembled using solutions of multiple small impurity problems. The calculation of the properties of the weakly coupled orbitals with GF2 scales as $\mathcal{O}(N^5)$, making SEET(ED-in-GF2) an ideal tool for the simulation of realistic materials. Extensions using other diagrammatic or correlated methods, such as SEET(QMC-in-GF2) or methods based on GW, are straightforward.

In real materials, the number of weakly correlated orbitals in the unit cell is significantly larger than the number of strongly correlated orbitals, thus providing an ideal situation where many orbitals can be treated cheaply by GF2 while the number of orbitals treated by ED remains small. Moreover, the SEET(ED-in-GF2) hybrid is easy to implement and, since it does not use frequency-dependent effective interactions, can be trivially extended to employ different solvers for the strongly correlated part, such as truncated CI variants with a suitably chosen active space or QMC hybridization expansions. Similarly, the weakly correlated part can be treated by different levels of perturbation theory or cheap truncated CI methods, instead of GF2. Our ED-in-GF2 method can be adjusted to yield more accurate results, either by increasing the order of the perturbative treatment (e.g., by employing FLEX or GW), or by increasing the number of orbitals treated by ED. These limits therefore provide a rigorous assessment of the convergence of the self-energies. Since a set of strongly correlated orbitals in SEET is chosen based on a unique mathematical criterion, the method has the potential for becoming a black box method for realistic correlated material calculations.

Bibliography

[1] E. R. Davidson, "The iterative calculation of a few of the lowest eigenvalues and corresponding eigenvectors of large real-symmetric matrices", *J. Comput. Phys.* **17**, 87 (1975).

[2] H. Lin, J. Gubernatis, H. Gould, and J. Tobochnik, "Exact diagonalization methods for quantum systems", *Comput. Phys.* **7**, 400 (1993).

[3] A. Liebsch and H. Ishida, "Temperature and bath size in exact diagonalization dynamical mean field theory", *J. Phys.: Condensed Matter* **24**, 053201 (2012).

[4] M. Capone, L. de' Medici, and A. Georges, "Solving the dynamical mean-field theory at very low temperatures using the Lanczos exact diagonalization", *Phys. Rev. B* **76**, 245116 (2007).

[5] D. Zgid and G. K.-L. Chan, "Dynamical mean-field theory from a quantum chemical perspective", *J. Chem. Phys.* **134**, 094115 (2011).

[6] D. Zgid, E. Gull, and G. K.-L. Chan, "Truncated configuration interaction expansions as solvers for correlated quantum impurity models and dynamical mean-field theory", *Phys. Rev. B* **86**, 165128 (2012).

[7] S. R. White, "Density matrix formulation for quantum renormalization groups", *Phys. Rev. Lett.* **69**, 2863 (1992).

[8] A. Georges, G. Kotliar, W. Krauth, and M. J. Rozenberg, "Dynamical mean-field theory of strongly correlated fermion systems and the limit of infinite dimensions", *Rev. Mod. Phys.* **68**, 13 (1996).

[9] T. Maier, M. Jarrell, T. Pruschke, and M. H. Hettler, "Quantum cluster theories", *Rev. Mod. Phys.* **77**, 1027 (2005).

[10] R. Blankenbecler, D. J. Scalapino, and R. L. Sugar, "Monte carlo calculations of coupled boson-fermion systems. I", *Phys. Rev. D* **24**, 2278 (1981).

[11] P. Hohenberg and W. Kohn, "Inhomogeneous electron gas", *Phys. Rev.* **136**, B864 (1964).

[12] R. Parr and W. Yang, *Density-Functional Theory of Atoms and Molecules*, Oxford University Press: Oxford, UK (1994).

[13] L. Hedin, "New method for calculating the one-particle Green's function with application to the electron-gas problem", *Phys. Rev.* **139**, A796 (1965).

[14] D. Bohm and D. Pines, "A collective description of electron interactions. I. Magnetic interactions", *Phys. Rev.* **82**, 625 (1951).

[15] C. Møller and M. S. Plesset, "Note on an approximation treatment for many-electron systems", *Phys. Rev.* **46**, 618 (1934).

[16] J. J. Phillips and D. Zgid, "Communication: The description of strong correlation within self-consistent Green's function second-order perturbation theory", *J. Chem. Phys.* **140**, 241101 (2014).

[17] N. E. Dahlen and R. van Leeuwen, "Self-consistent solution of the Dyson equation for atoms and molecules within a conserving approximation", *J. Chem. Phys.* **122**, 164102 (2005).

[18] W. M. C. Foulkes, L. Mitas, R. J. Needs, and G. Rajagopal, "Quantum Monte Carlo simulations of solids", *Rev. Mod. Phys.* **73**, 33 (2001).

[19] S. Biermann, F. Aryasetiawan, and A. Georges, "First-principles approach to the electronic structure of strongly correlated systems: Combining the GW approximation and dynamical mean-field theory", *Phys. Rev. Lett.* **90**, 086402 (2003).

[20] S. Biermann, F. Aryasetiawan, and A. Georges, in *Physics of Spin in Solids: Materials, Methods and Applications*, edited by S. Halilov (2005), NATO Science Series II: Mathematics, Physics and Chemistry, Vol. 156, Springer, Berlin.

[21] K. Karlsson, "Self-consistent GW combined with single-site dynamical mean field theory for a Hubbard model", *J. Phys.: Condensed Matter* **17**, 7573 (2005).

[22] G. Kotliar, S. Y. Savrasov, K. Haule, V. S. Oudovenko, O. Parcollet, and C. A. Marianetti, "Electronic structure calculations with dynamical mean-field theory", *Rev. Mod. Phys.* **78**, 865 (2006).

[23] K. Held, "Electronic structure calculations using dynamical mean field theory", *Adv. Phys.* **56**, 829 (2007).

[24] J. M. Tomczak, M. Casula, T. Miyake, F. Aryasetiawan, and S. Biermann, "Combined GW and dynamical mean-field theory: Dynamical screening effects in transition metal oxides", *EPL (Europhys. Lett.)* **100**, 67001 (2012).

[25] M. Casula, P. Werner, L. Vaugier, F. Aryasetiawan, T. Miyake, A. J. Millis, and S. Biermann, "Low-energy models for correlated materials: Bandwidth renormalization from Coulombic screening", *Phys. Rev. Lett.* **109**, 126408 (2012).

[26] M. Casula, A. Rubtsov, and S. Biermann, "Dynamical screening effects in correlated materials: Plasmon satellites and spectral weight transfers from a Green's function ansatz to extended dynamical mean field theory", *Phys. Rev. B* **85**, 035115 (2012).

[27] T. Ayral, P. Werner, and S. Biermann, "Spectral properties of correlated materials: Local vertex and nonlocal two-particle correlations from combined GW and dynamical mean field theory", *Phys. Rev. Lett.* **109**, 226401 (2012).

[28] C. Taranto, M. Kaltak, N. Parragh, G. Sangiovanni, G. Kresse, A. Toschi, and K. Held, "Comparing quasiparticle GW+DMFT and LDA+DMFT for the test bed material $SrVO_3$", *Phys. Rev. B* **88**, 165119 (2013).

[29] R. Sakuma, P. Werner, and F. Aryasetiawan, "Electronic structure of $SrVO_3$ within GW+DMFT", *Phys. Rev. B* **88**, 235110 (2013).

[30] P. Hansmann, T. Ayral, L. Vaugier, P. Werner, and S. Biermann, "Long-range coulomb interactions in surface systems: A first-principles description within self-consistently combined GW and dynamical mean-field theory", *Phys. Rev. Lett.* **110**, 166401 (2013).

[31] T. Ayral, S. Biermann, and P. Werner, "Screening and nonlocal correlations in the extended Hubbard model from self-consistent combined GW and dynamical mean field theory", *Phys. Rev. B* **87**, 125149 (2013).

[32] S. Biermann, "Dynamical screening effects in correlated electron materials-a progress report on combined many-body perturbation and dynamical mean field theory: "GW + DMFT"", *J. Phys.: Condensed Matter* **26**, 173202 (2014).

[33] E. Gull, A. J. Millis, A. I. Lichtenstein, A. N. Rubtsov, M. Troyer, and P. Werner, "Continuous-time Monte Carlo methods for quantum impurity models", *Rev. Mod. Phys.* **83**, 349 (2011).

[34] M. H. Hettler, M. Mukherjee, M. Jarrell, and H. R. Krishnamurthy, "Dynamical cluster approximation: Nonlocal dynamics of correlated electron systems", *Phys. Rev. B* **61**, 12739 (2000).

[35] E. Gull, P. Werner, O. Parcollet, and M. Troyer, "Continuous-time auxiliary-field Monte Carlo for quantum impurity models", *EPL (Europhys. Lett.)* **82**, 57003 (2008).

[36] E. Gull, P. Staar, S. Fuchs, P. Nukala, M. S. Summers, T. Pruschke, T. C. Schulthess, and T. Maier, "Submatrix updates for the continuous-time auxiliary-field algorithm", *Phys. Rev. B* **83**, 075122 (2011).

[37] M. Caffarel and W. Krauth, "Exact diagonalization approach to correlated fermions in infinite dimensions: Mott transition and superconductivity", *Phys. Rev. Lett.* **72**, 1545 (1994).

[38] P. Werner and A. J. Millis, "Hybridization expansion impurity solver: General formulation and application to Kondo lattice and two-orbital models", *Phys. Rev. B* **74**, 155107 (2006).

[39] M. Karolak, G. Ulm, T. Wehling, V. Mazurenko, A. Poteryaev, and A. Lichtenstein, "Double counting in LDA+DMFT-the example of NiO", *J. Electron Spectrosc. Relat. Phenom.* **181**, 11 (2010), proceedings of International Workshop on Strong Correlations and Angle-Resolved Photoemission Spectroscopy 2009.

[40] F. Aryasetiawan, M. Imada, A. Georges, G. Kotliar, S. Biermann, and A. I. Lichtenstein, "Frequency-dependent local interactions and low-energy effective models from electronic structure calculations", *Phys. Rev. B* **70**, 195104 (2004).

[41] L. Vaugier, H. Jiang, and S. Biermann, "Hubbard U and Hund exchange J in transition metal oxides: Screening versus localization trends from constrained random phase approximation", *Phys. Rev. B* **86**, 165105 (2012).

[42] R. Sakuma and F. Aryasetiawan, "First-principles calculations of dynamical screened interactions for the transition metal oxides MO (M=Mn, Fe, Co, Ni)", *Phys. Rev. B* **87**, 165118 (2013).

Chapter 3

Fractional charge and spin errors in self-consistent Green's function theory

J. J. Phillips, A. A. Kananenka and D. Zgid,

The Journal of Chemical Physics, **142 (19)** 194108 (2015)

3.1 Introduction

Self-consistent single-particle electronic structure methods are of great interest because they combine conceptual and computational simplicity while being free of a starting reference bias. Probably the most well known example of this is density functional theory (DFT) [1, 2]. Often these methods are designed to satisfy known constraints that an exact electronic structure theory should obey. For example, the total electronic energy should vary linearly in the fractional electron occupancy between integer electron numbers [3–6], while for a simple one-electron system like the hydrogen atom the energy should be degenerate with respect to variations in the fractional spin [7]. To the extent that a method disobeys these two exact constraints such a method will display many electron self-interaction and static correlation errors, respectively. To understand how these errors are connected to fractional electron behavior, let us consider the H_2 molecule in the infinite dissociation limit in two different scenarios:

First let us focus on a *fractional charge error*. If an extra electron were placed on

this system with fractional occupancies on each H atom given by n_a, n_b, $n_a + n_b = 1$, then the net energy change of the system would be $E_\Delta = -(n_a A + n_b A) = -A$, where A is the electron affinity of the hydrogen atom. The energy of each subsystem would vary linearly in the occupation, and the total energy of the entire $[H_2]^-$ system would be the same regardless if the extra electron were delocalized across both atoms, or localized only on one. If the energy of the subsystem varied nonlinearly, then either the delocalized or localized solution would become unphysically lower in energy depending on whether the curve was convex or concave. This unphysical behavior would be a simple manifestation of many electron self-interaction error.

Let us examine now a *fractional spin error*. For neutral singlet H_2 in the infinite dissociation limit each H atom should have half a spin up and down electron, and the energy of the singlet should be identical to that of broken-symmetry solutions where spin up and spin down electrons have localized on different atoms. Therefore a method's failure to yield equivalent energies for one-electron H with fractional or integer spin is equivalent to the failure to describe multireference static correlation energy.

From this simple example it is clear that fractional charge and fractional spin errors are deeply connected to many electron self-interaction and static correlation errors. For this reason these errors have been studied extensively, and are known to have severe negative consequences for a given method's description of properties that depend on electron delocalization and static correlation effects [7–12]. This language of fractional charge and spin has traditionally been used exclusively within the DFT community to analyze approximate density functionals. However these concepts have begun to make inroads into other areas such as wave-function [13] and many-body theory [14–18], and density-matrix theory as well [19]. For example it has been shown that MP2 (second-order Møller–Plesset [20]) possesses relatively little fractional charge error, but displays a massive diverging fractional spin error (which is an alternative way of stating that MP2 diverges for strong correlations) [14]. Double-hybrid density functionals

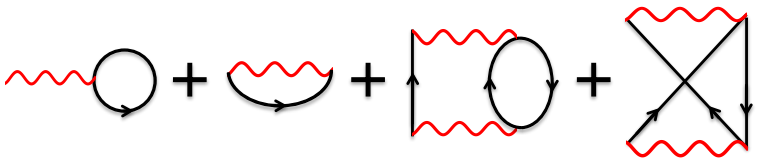

Figure 3.1: Feynman diagrams for the second-order self-energy in GF2. Here a red wavy line represents a two-electron integral, while a black arrow line represents a Green's function. From left to right the diagrams shown are the first-order Hartree and exchange diagrams, and the second-order pair bubble and second-order exchange.

that include some MP2 correlation are expected to have a similar fractional electron behavior [21, 22]. The random phase approximation (RPA) [23–26] on the other hand has minimal fractional spin error, but a severe fractional charge error [15]. The closely related GW approximation [27] displays a fractional charge error similar to RPA, but a larger fractional spin error[18].

Motivated by these works, we find it interesting to extend this analysis to self-consistent Green's function theory in a second-order approximation (GF2) [28, 29]. Similar to MP2, GF2 includes all diagrams to second order in the bare electron-electron interaction, as shown in Fig. 3.1, and is therefore exact for one-electron systems. However in contrast to MP2 these diagrams are evaluated with self-consistent Green's functions, obtained by iterative solution of the Dyson equation

$$\begin{aligned} G(\omega) &= G_0(\omega) + G_0(\omega)\Sigma(\omega)G_0(\omega) + G_0(\omega)\Sigma(\omega)G_0(\omega)\Sigma(\omega)G_0(\omega) + \cdots \\ &= G_0(\omega)\left(\sum_n \big(\Sigma(\omega)G_0(\omega)\big)^n\right) \\ &= \big[G_0(\omega)^{-1} - \Sigma(\omega)\big]^{-1}. \end{aligned} \tag{3.1}$$

Here $G_0(\omega)$ is the Green's function of a noninteracting system, while $\Sigma(\omega)$ is the proper self-energy, which in GF2 is truncated at second order and written as an approximate functional of the Green's function, $\Sigma[G(\omega)]$. Because of the structure of the Dyson equation, the self-consistent $G(\omega)$ will contain an infinite order summation of the second order proper self-energy parts, $\Sigma(\omega)$. As we recently showed, this sum-

mation of diagrams allows GF2 to give reasonably fine results for strongly correlated systems such as stretched hydrogen lattices [28] when MP2 would diverge. In the language of fractional electron errors, this suggests that GF2 improves tremendously over MP2 for fractional spins as a result of the self-consistent infinite order summation. An interesting question that arises then is what effect does this Dyson summation have on the more general fractional electron behavior? Relative to other methods such as RPA, GW, approximate DFT, and Hartree–Fock (HF), MP2 has only a very small fractional charge error [14], and consequently little many electron self-interaction error (SIE). Ideally one would hope that GF2 improves on the disastrous fractional spin error of MP2 without deteriorating MP2's impressively small fractional charge error. To investigate this question, here we will generalize our previous GF2 implementation [28] to open-shell systems and then investigate its fractional charge and spin behavior.

Before closing this section it should be emphasized that what is challenging about the fractional charge and fractional spin errors is that any attempt to reduce one error tends to exacerbate the other [15, 30, 31]. For example, a semilocal DFT functional (such as BLYP [32, 33], or PBE [34]) will tend to have a large fractional charge error but a relatively smaller fractional spin error. On the other end of the extreme Hartree–Fock will have significantly less fractional charge error but a much greater fractional spin error. Any hybrid of these two (B3LYP [33, 35] or PBEh [34, 36], for example) will essentially trade one error for the other to the extent that the HF-type exchange is admixed in place of DFT exchange. What is worth noting is that, in the language of hybrid DFT, the Fock matrix in GF2 contains full HF-type exchange (which in Green's function theory is usually referred to as first order exchange) yet we will show GF2 yields *both* less fractional charge and fractional spin error than HF, B3LYP, and PBEh. This unique result comes about from a combination of the Dyson summation with including all diagrams to second order.

3.2 Spin-unrestricted GF2 theory

To study open-shell systems we generalize $\mathbf{G}(\omega)$ to have two spin blocks

$$\mathbf{G} = \begin{bmatrix} \mathbf{G}_\alpha & \mathbf{0} \\ \mathbf{0} & \mathbf{G}_\beta \end{bmatrix}, \tag{3.2}$$

where the spin-up and spin-down blocks are given by

$$\mathbf{G}_\sigma(\omega) = \big[(\mu_\sigma + \omega)\mathbf{S} - \mathbf{F}_\sigma - \mathbf{\Sigma}_\sigma(\omega)\big]^{-1}, \quad \sigma = \alpha, \beta \tag{3.3}$$

The off-diagonal spin-blocks of $\mathbf{G}(\omega)$ here are identically $\mathbf{0}$, meaning we do not allow for the possibility of spin-flips, and our solutions are constrained to be eigenstates of $\hat{S}_z$. In Eq. 3.3 $\mathbf{S}$ and $\mathbf{F}_\sigma$ are the overlap and Fock matrices, $\mathbf{\Sigma}_\sigma(\omega)$ is the self-energy, μ_σ is the chemical potential, and ω is an imaginary frequency. By introducing μ_α, μ_β as separate chemical potentials we can allow for different numbers of electrons in the respective correlated density matrices, $\mathbf{P}_\alpha$, $\mathbf{P}_\beta$, which are given by $\mathbf{P}_\sigma = -\mathbf{G}_\sigma(\tau = 1/k_B T)$, $\sigma = \alpha, \beta$, where $\mathbf{G}_\sigma(\tau)$ is the Green's function fast Fourier transformed (FFT) to the imaginary time domain, and $1/k_B T$ is the inverse temperature. The expression for $\mathbf{F}_\sigma$ is the standard result from spin-unrestricted HF theory,

$$\begin{aligned} F_{ij}^\alpha &= h_{ij} + \sum_{kl} (P_{kl}^\alpha + P_{kl}^\beta) \mathrm{v}_{ijkl} - P_{kl}^\alpha \mathrm{v}_{iklj}, \\ F_{ij}^\beta &= h_{ij} + \sum_{kl} (P_{kl}^\alpha + P_{kl}^\beta) \mathrm{v}_{ijkl} - P_{kl}^\beta \mathrm{v}_{iklj}. \end{aligned} \tag{3.4}$$

However, unlike HF theory the density matrices that enter this expression are those obtained from the Green's function and thus include electron correlation effects from solving the Dyson equation. This covers the electron-electron interaction from zeroth through first order (the first order diagrams in Fig. 3.1 are described by the HF mean-

field). At second order in GF2 the electron-electron interaction is described by the frequency-dependent self-energy, which is given in the imaginary time domain as

$$\begin{aligned}
\Sigma^{\alpha}_{ij}(\tau) = \sum_{klmnpq} &- G^{\alpha}_{mn}(\tau)G^{\alpha}_{kl}(\tau)G^{\alpha}_{pq}(-\tau)\mathrm{v}_{imqk}\big(\mathrm{v}_{lpnj} - \mathrm{v}_{nplj}\big) \\
&- G^{\alpha}_{mn}(\tau)G^{\beta}_{kl}(\tau)G^{\beta}_{pq}(-\tau)\mathrm{v}_{imqk}\mathrm{v}_{lpnj}, \\
\Sigma^{\beta}_{ij}(\tau) = \sum_{klmnpq} &- G^{\beta}_{mn}(\tau)G^{\beta}_{kl}(\tau)G^{\beta}_{pq}(-\tau)\mathrm{v}_{imqk}\big(\mathrm{v}_{lpnj} - \mathrm{v}_{nplj}\big) \\
&- G^{\beta}_{mn}(\tau)G^{\alpha}_{kl}(\tau)G^{\alpha}_{pq}(-\tau)\mathrm{v}_{imqk}\mathrm{v}_{lpnj}. \qquad (3.5)
\end{aligned}$$

The reasoning for this expression is that at second order a spin-up (down) electron can have a pair-bubble interaction with both spin-up and down electrons, yet the second-order exchange can only proceed between like-spin electrons because we do not allow for the possibility of spin-flips. Once $\mathbf{\Sigma}_{\sigma}(\tau)$ has been built it can be FFT to the frequency domain, and then we can rebuild $\mathbf{G}_{\sigma}(\omega)$ with Eq. 3.3. Looking at Eqs. 3.3, 3.4, and 3.5, the spin-up and spin-down Green's functions are coupled by the fact that $\mathbf{G}_{\beta}$ appears in the expression for $\mathbf{\Sigma}_{\alpha}$ (likewise with $\mathbf{G}_{\alpha}$ for $\mathbf{\Sigma}_{\beta}$), and that $\mathbf{G}_{\beta}$ contributes to $\mathbf{F}_{\alpha}$ through $\mathbf{P}_{\beta} = -\mathbf{G}_{\beta}(\tau = 1/k_BT)$ (likewise with $\mathbf{G}_{\alpha}$, $\mathbf{P}_{\alpha}$ and $\mathbf{F}_{\beta}$). Therefore Eqs. 3.3, 3.4 and 3.5 will need to be solved self-consistently, and at every iteration μ_{α} and μ_{β} will need to be adjusted to give the desired number of α and β electrons. To start this self-consistent procedure we use a HF Green's function generated by output from the DALTON program [37]. Note when $\mathbf{G}_{\alpha} = \mathbf{G}_{\beta}$, then $\mathbf{\Sigma}_{\alpha} = \mathbf{\Sigma}_{\beta}$ and Eq. 3.5 reduces to the familiar expression for spin-restricted GF2 [28, 29].

The energy is evaluated as

$$E = \frac{1}{2}\mathrm{Tr}\big[(\mathbf{h}+\mathbf{F}_{\alpha})\mathbf{P}_{\alpha}+(\mathbf{h}+\mathbf{F}_{\beta})\mathbf{P}_{\beta}\big]+k_BT\sum_{n}\mathrm{Re}\Big[\mathrm{Tr}\big[\mathbf{G}_{\alpha}(\omega_n)\mathbf{\Sigma}_{\alpha}(\omega_n)+\mathbf{G}_{\beta}(\omega_n)\mathbf{\Sigma}_{\beta}(\omega_n)\big]\Big], \qquad (3.6)$$

where ω_n is a Matsubara frequency, $\omega_n = (2n+1)\pi k_BT$. This can be understood as essentially a spin-unrestricted HF-like energy expression supplemented with a frequency-

dependent correlation contribution from GF2. However it should be understood that all quantities are evaluated using the correlated $\mathbf{P}_\sigma$ as obtained from $\mathbf{G}_\sigma$.

Because the GF2 approximation includes in the proper self-energy all exchange and Coulomb type diagrams to second order, it is by construction exact for one-electron systems, i.e. it is one-electron self-interaction and self-correlation free. Less clear however is its many electron self-interaction error (SIE) for general systems. To this end in the following we investigate the fractional electron behavior of GF2 for several archetypical cases, and compare to standard density functional theory calculations ran with GAUSSIAN 09 [38].

3.3 Results

First we consider a single hydrogen atom with fractional spin up and down electron occupations, n_α, n_β, that are varied in the interval $0 \leq n_\alpha \leq 1.0$ and $0 \leq n_\beta \leq 1.0$. For this case with an exact method the energy should change linearly in the fractional electron number $n = n_\alpha + n_\beta$, while for constant n it should be invariant with respect to changes in the fractional spin $m = n_\alpha - n_\beta$. Furthermore, there should be a discontinuity in the slope $dE(n)/dn$ across the line $n_\alpha + n_\beta = 1.0$. Hence the resulting energy surface should be two flat planes that intersect along a seam. In Fig. 3.2 we show the exact result, compared against that obtained with spin-unrestricted GF2. If first we focus only on the edge of the plane where one occupation is held fixed at integer values of 0 or 1.0, this corresponds to the fractional charge behavior of a method and thus SIE. It is clear that GF2 reproduces the exact linear behavior almost perfectly, similar to the result for MP2 in Ref. [14]. Now if we focus on the more interesting region towards the interior, discrepancies between GF2 and the exact flat-plane behavior become apparent. To see this more clearly, in Fig. 3.3 we plot the difference between GF2 and its interpolated flat-plane surface. Looking at the diagonal

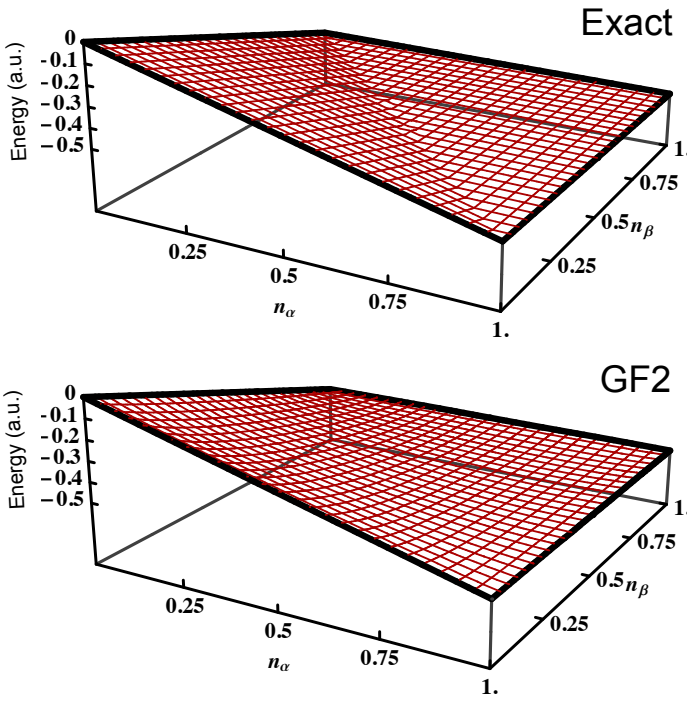

Figure 3.2: The total energy for hydrogen with fractional spin up and down occupations n_α, n_β evaluated with aug-cc-pVDZ. Top: the exact result. Bottom: GF2.

region connecting the coordinates $\{n_\alpha = 1.0,\ n_\beta = 0.0\}$ and $\{n_\alpha = 0.0,\ n_\beta = 1.0\}$ we find a hill of fractional spin error, where GF2 is not able to fully recover the static correlation energy. On either side of the hill ($n_\alpha + n_\beta < 1.0$ and $n_\alpha + n_\beta > 1.0$) we find shallow valleys where GF2 moderately overestimates the correlation energy. The GF2 results here for fractional spin are in severe contrast to the MP2 result from Fig. 4 of Ref. [14], which rapidly diverges to $-\infty$ correlation energy as one moves towards the center at $\{n_\alpha = 0.5,\ n_\beta = 0.5\}$.

For purpose of comparison, we also show in Fig. 3.3 the surface obtained with PBEh, as well as the GF2 result obtained when the second-order exchange (SOX) diagram is neglected in the self-energy (we call this GF2-NoSOX for short). Neglect of the SOX diagram introduces an unphysical one-electron self-correlation error at second order. Because many electron SIE and static correlation are known to be connected [15, 31, 39–41], GF2-NoSOX should provide an interesting contrast to standard GF2. First let us compare the energy landscapes for GF2 and PBEh. Despite being a hybrid

functional, PBEh still yields a significant fractional charge error along the outer rim of the surface, along with a pronounced hill of fractional spin error running through the center. The GF2 energy landscape in contrast is appreciably flatter, with less fractional spin and fractional charge error. This is notable, because it has been stressed that simultaneously reducing the fractional charge and spin errors in a single-particle method is very difficult [15]. For example, RPA+X (RPA with HF-type exchange) greatly improves over the fractional charge error of RPA, but at the price of gaining a considerably larger fractional spin error that is comparable to Hartree–Fock [15]. Now let us examine the GF2-NoSOX result. As mentioned, neglect of the SOX diagram introduces a self-correlation error at second order, and as a result GF2-NoSOX gives significant fractional charge errors comparable to PBEh. At the same time, the hill of fractional spin error is appreciably reduced relative to both PBEh and GF2.

To see the static correlation error more clearly, in Fig. 3.4 we plot the energy with respect to fractional spin $m = n_\alpha - n_\beta$ for hydrogen with GF2, GF2-NoSOX, PBEh, B3LYP, and HF. This corresponds to the line running along the energy surface from the coordinates $\{n_\alpha = 1.0,\ n_\beta = 0.0\}$ to $\{n_\alpha = 0.0,\ n_\beta = 1.0\}$. As stated previously an exact method should give a flat energy curve from $m = -1$ to $m = 1$. For example, HF has a massive hill at $m = 0$, which reflects the complete absence of static correlation energy in this method. Hybrid DFT yields much smaller fractional spin errors, with B3LYP being slightly lower than PBEh, likely because it includes less HF-type exchange than PBEh. In comparison the fractional spin error is relatively lower for GF2, as a result of the infinite order summation from the Dyson equation recovering some static correlation. GF2-NoSOX has a much reduced fractional spin error relative to all four methods, with its energy at $m = 0$ being not much different from that at $m = \pm 1$. It has been understood for some time that SIE can mimic static correlation [15, 31, 39–41]. Usually this is considered in the context of SIE resulting from incomplete cancellation of Coulomb and exchange terms at first order. GF2-NoSOX's

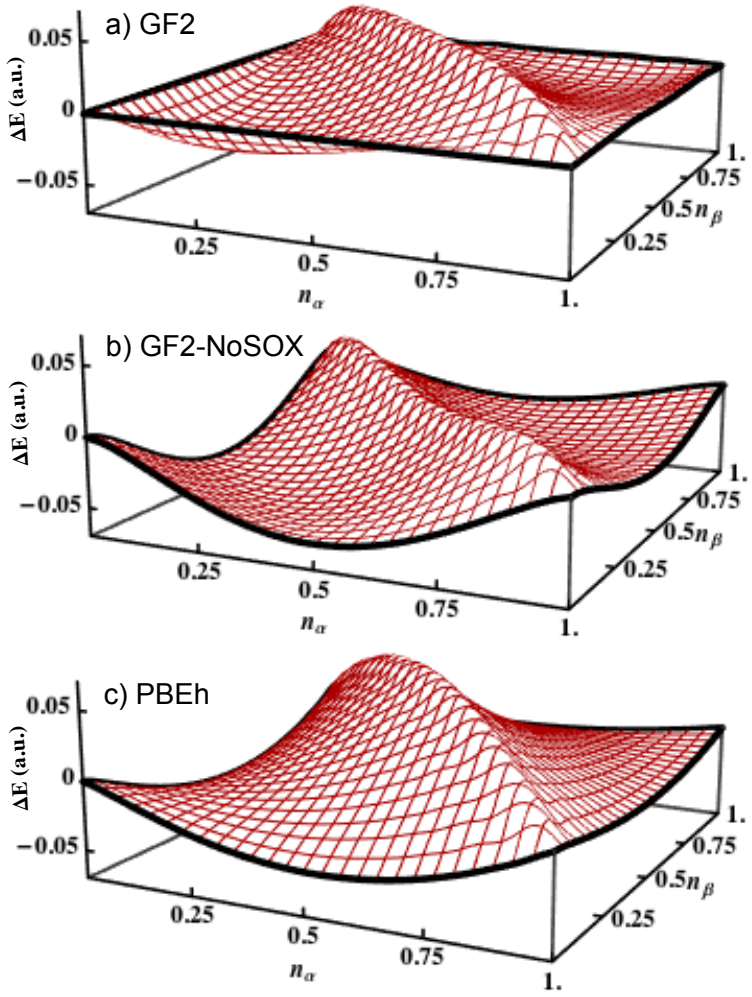

Figure 3.3: The energy difference $\Delta E = E - E_{\text{lin}}$ for the hydrogen atom with fractional spin up and down occupations n_α, n_β, where E is the energy evaluated with fractional electron number, and E_{lin} is the flat-plane linear interpolation for a) GF2, b) GF2-NoSOX, and c) hybrid PBEh. All calculations are with aug-cc-pVDZ.

small fractional spin error in contrast is purely arising from incomplete cancellation of Coulomb and exchange terms at second order, resulting in an unphysical one-electron self-correlation that mimics static correlation energy, analogous to the situation that occurs with RPA+SOSEX [31] (second-order screened exchange). We think this is an example of getting the right result for the wrong reason. Furthermore, GF2-NoSOX must obtain this slightly reduced fractional spin error at the price of gaining a tremendous fractional charge error, which is not a desirable trade. In contrast, from comparing Figs. 3.4 and 3.3 it is clear that GF2 has less static-correlation error than typical hybrid density functionals, and importantly achieves this while being essentially one and two electron self-interaction free. This means GF2 genuinely recovers some static correlation energy, rather than fortuitously exploiting spurious self-interaction or self-correlation. It is worth mentioning that a similar analysis has been performed for RPA and RPA+X [15]. Comparing our GF2 result in Fig. 3.4 to Fig. 1 in Ref.[15], GF2 yields an appreciably smaller fractional spin error than RPA+X, but is still larger than RPA.

Finally, to analyze the fractional charge error in closer detail we consider the energy of helium with respect to fractional electron number. In Fig. 3.5 we plot $E^X(n) - E^X_{\text{lin}}$, where $E^X(n)$ is the energy from method X for electron number $1.0 \leq n \leq 2.0$, while E^X_{lin} is the linear-interpolation between integer points with the same method. A method is said to be M-electron SIE free if $E^X(n) - E^X_{\text{lin}} = 0$ for $M - 1 \leq n \leq M$ [5]. We find that GF2 has a very small concave curvature. In contrast HF is moderately concave, while PBEh, B3LYP, and GF2-NoSOX are significantly convex. This clearly establishes that GF2 is one and almost perfectly two electron SIE free. Interestingly, comparing Fig. 3.5 to Fig. 4 in Ref. [15], it is reasonable to conclude that GF2 should have less SIE than both RPA and RPA+X.

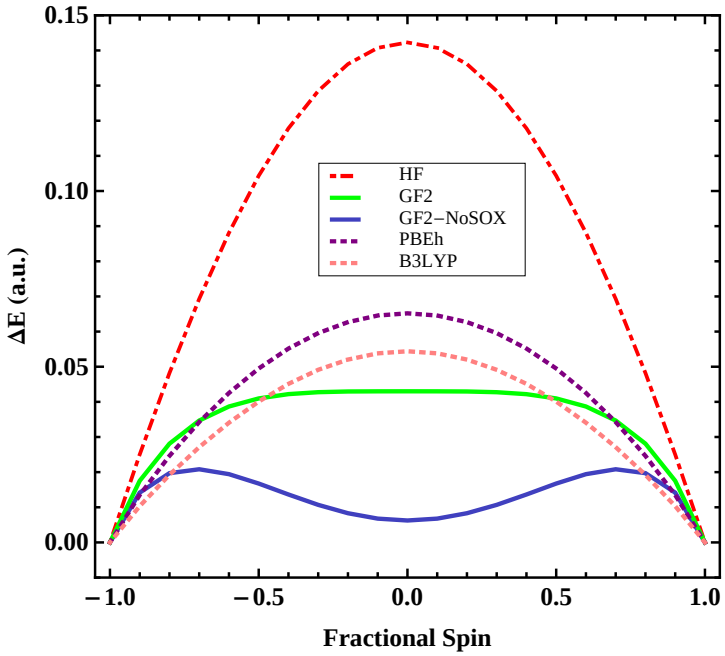

Figure 3.4: The energy difference $\Delta E = E^X - E^X_{\text{int}}$ for the fractional spin hydrogen atom, where E^X is the energy from method X evaluated with the fractional spin population $m = n_\alpha - n_\beta$, $n_\alpha + n_\beta = 1$, and E^X_{int} is the energy from X with integer $m = \pm 1$. All calculations are with aug-cc-pVDZ.

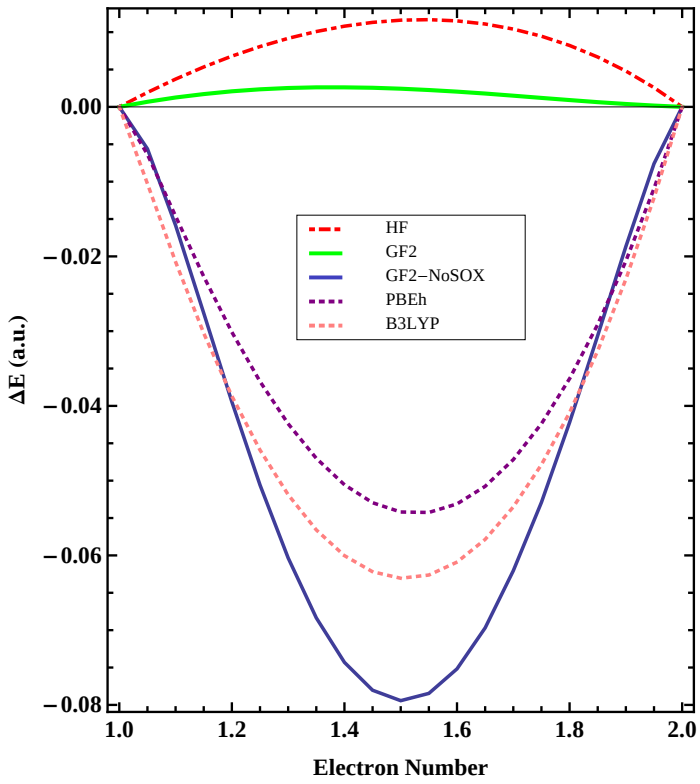

Figure 3.5: The energy difference $\Delta E = E^X - E^X_{\text{lin}}$ for the helium atom, where E^X is the energy from method X evaluated with fractional electron number, and E^X_{lin} is the linear interpolation from method X. All calculations are with cc-pVTZ.

3.4 Conclusions

We have analyzed fractional electron errors in self-consistent Green's function theory by generalizing our previous GF2 implementation [28] to open-shell systems. Overall we find that GF2 has a very small fractional charge error, and a moderate fractional spin error. In comparison to other well known methods, we find that GF2 has both less static correlation and self-interaction error than hybrid density functionals such as B3LYP and PBEh, as well as RPA+X and HF. Because the GW approximation is diagrammatically identical to RPA, GF2 will very likely have significantly less self-interaction error than GW as well. Furthermore, it has been shown that CCSD has a roughly similar fractional charge error to MP2 [13]. From this it stands to reason that GF2 and CCSD will have comparable fractional charge errors.

Essentially, by virtue of the Dyson summation GF2 greatly improves on the tremendous fractional spin error of MP2, but without deteriorating MP2's relatively excellent fractional charge behavior. These results could suggest a way towards removing the fractional spin error from double hybrid density functionals [21, 22]. As a further salient point, GF2 is fully self-consistent and thus the converged density should reflect the relative lack of many-electron self-interaction error in a second-order approximation. MP2 in contrast is by definition a perturbative scheme that does not revise the underlying mean-field reference, and thus inherits the Hartree–Fock density with its bias towards localization. This suggests that GF2 could find good application for properties that sensitively depend on electron delocalization. For example, much of the interesting physics in transition metal complexes depends on the slight delocalization of unpaired d electrons onto ligands, which is determined by the interplay of dynamic correlation and self-interaction error effects [42].

Conceptually, GF2 is essentially a self-consistent single-particle theory where the energy is expressed as a functional of the single-particle Green's function $E[G]$, in

obvious analogy to DFT with density functionals $E[\rho]$. In terms of the energy, it is fair to say GF2 is a "Green's function functional" with desirable fundamental properties compared to standard hybrid density functionals.

Bibliography

[1] P. Hohenberg and W. Kohn, "Inhomogeneous electron gas", *Phys. Rev.* **136**, B864 (1964).

[2] W. Kohn and L. J. Sham, "Self-consistent equations including exchange and correlation effects", *Phys. Rev.* **140**, A1133 (1965).

[3] J. P. Perdew, R. G. Parr, M. Levy, and J. L. Balduz, "Density-functional theory for fractional particle number: Derivative discontinuities of the energy", *Phys. Rev. Lett.* **49**, 1691 (1982).

[4] P. Mori-Sánchez, A. J. Cohen, and W. Yang, "Many-electron self-interaction error in approximate density functionals", *J. Chem. Phys.* **125**, 201102 (2006).

[5] A. Ruzsinszky, J. P. Perdew, G. I. Csonka, O. A. Vydrov, and G. E. Scuseria, "Density functionals that are one- and two- are not always many-electron self-interaction-free, as shown for H_2^+, He_2^+, LiH^+, and Ne_2^+", *J. Chem. Phys.* **126**, 104102 (2007).

[6] J. P. Perdew, A. Ruzsinszky, G. I. Csonka, O. A. Vydrov, G. E. Scuseria, V. N. Staroverov, and J. Tao, "Exchange and correlation in open systems of fluctuating electron number", *Phys. Rev. A* **76**, 040501 (2007).

[7] A. J. Cohen, P. Mori-Sánchez, and W. Yang, "Fractional spins and static correlation error in density functional theory", *J. Chem. Phys.* **129**, 121104 (2008).

[8] O. A. Vydrov, G. E. Scuseria, and J. P. Perdew, "Tests of functionals for systems with fractional electron number", *J. Chem. Phys.* **126**, 154109 (2007).

[9] A. J. Cohen, P. Mori-Sánchez, and W. Yang, "Fractional charge perspective on the band gap in density-functional theory", *Phys. Rev. B* **77**, 115123 (2008).

[10] P. Mori-Sánchez, A. J. Cohen, and W. Yang, "Localization and delocalization errors in density functional theory and implications for band-gap prediction", *Phys. Rev. Lett.* **100**, 146401 (2008).

[11] E. R. Johnson, P. M. Sánchez, A. J. Cohen, and W. Yang, "Delocalization errors in density functionals and implications for main-group thermochemistry", *J. Chem. Phys.* **129**, 204112 (2008).

[12] E. R. Johnson and J. Contreras-García, "Communication: A density functional with accurate fractional-charge and fractional-spin behaviour for s-electrons", *J. Chem. Phys.* **135**, 081103 (2011).

[13] S. N. Steinmann and W. Yang, "Wave function methods for fractional electrons", *J. Chem. Phys.* **139**, 074107 (2013).

[14] A. J. Cohen, P. Mori-Sánchez, and W. Yang, "Second-order perturbation theory with fractional charges and fractional spins", *J. Chem. Theory Comput.* **5**, 786 (2009).

[15] P. Mori-Sánchez, A. J. Cohen, and W. Yang, "Failure of the random-phase-approximation correlation energy", *Phys. Rev. A* **85**, 042507 (2012).

[16] H. van Aggelen, Y. Yang, and W. Yang, "Exchange-correlation energy from pairing matrix fluctuation and the particle-particle random-phase approximation", *Phys. Rev. A* **88**, 030501 (2013).

[17] W. Yang, P. Mori-Sánchez, and A. J. Cohen, "Extension of many-body theory and approximate density functionals to fractional charges and fractional spins", *J. Chem. Phys.* **139**, 104114 (2013).

[18] M. Hellgren, F. Caruso, D. R. Rohr, X. Ren, A. Rubio, M. Scheffler, and P. Rinke, "Static correlation and electron localization in molecular dimers from the self-consistent RPA and GW approximation", *Phys. Rev. B* **91**, 165110 (2015).

[19] H. Van Aggelen, P. Bultinck, B. Verstichel, D. Van Neck, and P. W. Ayers, "Incorrect diatomic dissociation in variational reduced density matrix theory arises from the flawed description of fractionally charged atoms", *Phys. Chem. Chem. Phys.* **11**, 5558 (2009).

[20] C. Møller and M. S. Plesset, "Note on an approximation treatment for many-electron systems", *Phys. Rev.* **46**, 618 (1934).

[21] N. Q. Su and X. Xu, "Toward the construction of parameter-free doubly hybrid density functionals", *Int. J. Quantum Chem.* **115**, 589 (2014).

[22] N. Q. Su, W. Yang, P. Mori-Sánchez, and X. Xu, "Fractional charge behavior and band gap predictions with the XYG3 type of doubly hybrid density functionals", *J. Phys. Chem. A* **118**, 9201 (2014).

[23] D. Bohm and D. Pines, "A collective description of electron interactions. I. Magnetic interactions", *Phys. Rev.* **82**, 625 (1951).

[24] D. Pines and D. Bohm, "A collective description of electron interactions: II. collective vs individual particle aspects of the interactions", *Phys. Rev.* **85**, 338 (1952).

[25] D. Bohm and D. Pines, "A collective description of electron interactions: III. coulomb interactions in a degenerate electron gas", *Phys. Rev.* **92**, 609 (1953).

[26] M. Gell-Mann and K. A. Brueckner, "Correlation energy of an electron gas at high density", *Phys. Rev.* **106**, 364 (1957).

[27] L. Hedin, "New method for calculating the one-particle Green's function with application to the electron-gas problem", *Phys. Rev.* **139**, A796 (1965).

[28] J. J. Phillips and D. Zgid, "Communication: The description of strong correlation within self-consistent Green's function second-order perturbation theory", *J. Chem. Phys.* **140**, 241101 (2014).

[29] N. E. Dahlen and R. van Leeuwen, "Self-consistent solution of the Dyson equation for atoms and molecules within a conserving approximation", *J. Chem. Phys.* **122**, 164102 (2005).

[30] R. Haunschild, T. M. Henderson, C. A. Jiménez-Hoyos, and G. E. Scuseria, "Many-electron self-interaction and spin polarization errors in local hybrid density functionals", *J. Chem. Phys.* **133**, 134116 (2010).

[31] T. M. Henderson and G. E. Scuseria, "The connection between self-interaction and static correlation: a random phase approximation perspective", *Mol. Phys.* **108**, 2511 (2010).

[32] A. D. Becke, "Density-functional exchange-energy approximation with correct asymptotic behavior", *Phys. Rev. A* **38**, 3098 (1988).

[33] C. Lee, W. Yang, and R. G. Parr, "Development of the Colle-Salvetti correlation-energy formula into a functional of the electron density", *Phys. Rev. B* **37**, 785 (1988).

[34] J. P. Perdew, K. Burke, and M. Ernzerhof, "Generalized gradient approximation made simple", *Phys. Rev. Lett.* **77**, 3865 (1996).

[35] A. D. Becke, "Density-functional thermochemistry. III. The role of exact exchange", *J. Chem. Phys.* **98**, 5648 (1993).

[36] C. Adamo and V. Barone, "Toward reliable density functional methods without adjustable parameters: The PBE0 model", *J. Chem. Phys.* **110**, 6158 (1999).

[37] K. Aidas, C. Angeli, K. L. Bak, V. Bakken, R. Bast, L. Boman, O. Christiansen, R. Cimiraglia, S. Coriani, P. Dahle, E. K. Dalskov, U. Ekström, T. Enevoldsen, J. J. Eriksen, P. Ettenhuber, B. Fernández, L. Ferrighi, H. Fliegl, L. Frediani, K. Hald, A. Halkier, C. Hättig, H. Heiberg, T. Helgaker, A. C. Hennum, H. Hettema, E. Hjertenæs, S. Høst, I.-M. Høyvik, M. F. Iozzi, B. Jansík, H. J. Aa. Jensen, D. Jonsson, P. Jørgensen, J. Kauczor, S. Kirpekar, T. Kjærgaard, W. Klopper, S. Knecht, R. Kobayashi, H. Koch, J. Kongsted, A. Krapp, K. Kristensen, A. Ligabue, O. B. Lutnæs, J. I. Melo, K. V. Mikkelsen, R. H. Myhre, C. Neiss, C. B. Nielsen, P. Norman, J. Olsen, J. M. H. Olsen, A. Osted, M. J. Packer, F. Pawlowski, T. B. Pedersen, P. F. Provasi, S. Reine, Z. Rinkevicius, T. A.

Ruden, K. Ruud, V. V. Rybkin, P. Sałek, C. C. M. Samson, A. S. de Merás, T. Saue, S. P. A. Sauer, B. Schimmelpfennig, K. Sneskov, A. H. Steindal, K. O. Sylvester-Hvid, P. R. Taylor, A. M. Teale, E. I. Tellgren, D. P. Tew, A. J. Thorvaldsen, L. Thøgersen, O. Vahtras, M. A. Watson, D. J. D. Wilson, M. Ziolkowski, and H. Ågren, "The Dalton quantum chemistry program system", *Wiley Interdiscip. Rev. Comput. Mol. Sci.* **4**, 269 (2014).

[38] M. J. Frisch, G. W. Trucks, H. B. Schlegel, G. E. Scuseria, M. A. Robb, J. R. Cheeseman, G. Scalmani, V. Barone, B. Mennucci, G. A. Petersson, H. Nakatsuji, M. Caricato, X. Li, H. P. Hratchian, A. F. Izmaylov, J. Bloino, G. Zheng, J. L. Sonnenberg, M. Hada, M. Ehara, K. Toyota, R. Fukuda, J. Hasegawa, M. Ishida, T. Nakajima, Y. Honda, O. Kitao, H. Nakai, T. Vreven, J. A. Montgomery, Jr., J. E. Peralta, F. Ogliaro, M. Bearpark, J. J. Heyd, E. Brothers, K. N. Kudin, V. N. Staroverov, R. Kobayashi, J. Normand, K. Raghavachari, A. Rendell, J. C. Burant, S. S. Iyengar, J. Tomasi, M. Cossi, N. Rega, J. M. Millam, M. Klene, J. E. Knox, J. B. Cross, V. Bakken, C. Adamo, J. Jaramillo, R. Gomperts, R. E. Stratmann, O. Yazyev, A. J. Austin, R. Cammi, C. Pomelli, J. W. Ochterski, R. L. Martin, K. Morokuma, V. G. Zakrzewski, G. A. Voth, P. Salvador, J. J. Dannenberg, S. Dapprich, A. D. Daniels, Ö. Farkas, J. B. Foresman, J. V. Ortiz, J. Cioslowski, and D. J. Fox, "Gaussian 09 Revision A.01", Gaussian, Inc., Wallingford, CT, 2009.

[39] V. Polo, E. Kraka, and D. Cremer, "Electron correlation and the self-interaction error of density functional theory", *Mol. Phys.* **100**, 1771 (2002).

[40] J. E. Bates and F. Furche, "Communication: Random phase approximation renormalized many-body perturbation theory", *J. Chem. Phys.* **139**, 171103 (2013).

[41] F. Caruso, D. R. Rohr, M. Hellgren, X. Ren, P. Rinke, A. Rubio, and M. Scheffler, "Bond breaking and bond formation: How electron correlation is captured in many-body perturbation theory and density-functional theory", *Phys. Rev. Lett.* **110**, 146403 (2013).

[42] J. Cabrero, C. J. Calzado, D. Maynau, R. Caballol, and J. P. Malrieu, "Metalligand delocalization in magnetic orbitals of binuclear complexes", *J. Phys. Chem. A* **106**, 8146 (2002).

Chapter 4

Towards *ab initio* self-energy embedding theory in quantum chemistry

T. N. Lan, A. A. Kananenka and D. Zgid,

The Journal of Chemical Physics, **143 (24)** 241102 (2016)

4.1 Introduction

Strongly correlated systems such as materials and molecules containing transition metal atoms present a significant challenge for both quantum chemistry and condensed matter physics. The quantitative description of these systems is difficult since both the strong (static) and weak (dynamical) correlations present between electrons have to be included.

In quantum chemistry, multi-reference perturbation theories, namely complete active space second-order perturbation theory [1, 2] (CASPT2) and n-electron valence state second-order perturbation theory [3, 4] (NEVPT2), are commonly employed to simultaneously handle both types of correlations yielding quantitative accuracy without any adjustable parameters. Nevertheless, these methods are prohibitively expensive for extended systems since the largest computationally accessible active space has up to 16 electrons in 16 orbitals, thus treating only very few strongly correlated orbitals in the whole system. Recently, significant efforts have been devoted to enlarge the

active space using DMRG [5–9], RAS [10, 11], SplitCAS [12, 13], and GAS [14, 15] techniques. In these methods evaluating and storing intermediates involving 3- and 4-body reduced density matrices (RDMs) is extremely demanding as the number of active orbitals increases. A different class of approaches simultaneously treating static and dynamical correlations combines multi-configurational methods and density functional theory (MC-DFT) [16–20]. However, some of these methods suffer from the double counting [16] of correlation and lack of systematic approaches to improve the DFT part.

In condensed matter, the dynamical mean-field theory (DMFT), formulated in many-body Green's function language, has been extensively used to deal with the strongly correlated systems [21–24]. In DMFT, only local correlations are treated, whereas non-local correlations are neglected. The combination of DFT and DMFT methods called LDA+DMFT was developed to include non-local correlation between unit cells [22, 25], and it has been widely used to describe the strongly correlated materials, for instance, see Refs. 25–27. LDA+DMFT has been also applied to molecular systems, such as H_2 molecule [28] and transition metal complexes [29–33]. Similar to MC-DFT methods, LDA+DMFT suffers from the double counting problem and the DFT part cannot be systematically improved. Moreover, in LDA+DMFT the impurity Hamiltonian is frequently parameterized using empirical on-site Coulomb interactions that are adjusted to fit experiments [34]. Other diagrammatic methods, such as GW+DMFT [35, 36] and FLEX+DMFT (here, FLEX stands for fluctuation exchange) [37], were developed but their application to molecular systems has not yet been established. Moreover, some of these methods rely on mapping of the system of interest to an effective low energy Hamiltonian that is subsequently solved by DMFT. If high quantitative accuracy is desired such procedures may become problematic since the mapping onto an effective model can introduce uncontrolled errors.

Recently, we have developed a general multiscale framework, called the self-energy

embedding theory (SEET), in which the self-energy describing strongly correlated orbitals (active orbitals) is self-consistently embedded into the self-energy obtained from a method that treats non-local correlation effects [38]. SEET employing the full configuration interaction (FCI) method to describe few strongly correlated orbitals embedded in the self-energy obtained from the self-consistent second-order Green's function method (GF2) was first calibrated for the 2D Hubbard lattice showing promising results.

In this paper, we generalize SEET to molecular quantum chemical *ab initio* Hamiltonians. The GF2 method is used to describe the non-local correlations, while strong correlations within the active space are captured by the FCI method. To maintain consistency with our previous work, we denote the method as SEET(FCI/GF2), where FCI/GF2 stands for the methods used to describe the strongly/weakly correlated orbitals. In this paper, we demonstrate that the main advantages of SEET are **(i)** Green's function language giving access to the energy as well as spectroscopic quantities such as photoelectron spectrum, **(ii)** diagrammatic formulation allowing for the exact double counting removal, **(iii)** systematic improvability, **(iv)** simultaneous treatment of multiple active spaces, **(v)** no need for any high-order density matrix in the active space.

4.2 Theory

In this section, we will present SEET generalization to molecular *ab initio* Hamiltonians. In the first step of SEET, starting either from the HF or DFT Green's function, we perform self-consistent GF2 calculation [39, 40] in the AO basis for the whole molecule.

At convergence, the second-order self-energy in the time domain reads,

$$\left[\Sigma^{GF2}_{mol}(i\tau)\right]_{ij} = -\sum_{klmnpq}\left[G^{GF2}_{mol}(i\tau)\right]_{kl}\left[G^{GF2}_{mol}(i\tau)\right]_{mn}\left[G^{GF2}_{mol}(-i\tau)\right]_{pq} v_{ikmq}\left(2v_{ljpn} - v_{pjln}\right), \tag{4.1}$$

where $\mathbf{G}^{GF2}_{mol}(i\tau)$ is the Green's function in the time domain and $v_{ijkl} = \int d\mathbf{r}_1 d\mathbf{r}_2 \phi^*_i(\mathbf{r}_1)\phi_j(\mathbf{r}_1)v(\mathbf{r}_1 - \mathbf{r}_2)\phi^*_k(\mathbf{r}_2)\phi_l(\mathbf{r}_2)$ are 2-electron integrals in an AO basis. $\mathbf{\Sigma}^{GF2}_{mol}(i\tau)$ is then transformed to the $i\omega$ imaginary frequency domain using the Fourier transformation. The 1-body density matrix $\mathbf{P}$ is directly evaluated using the converged GF2 Green's function, $\mathbf{P} = -2\mathbf{G}^{GF2}_{mol}(i\tau = \beta)$ with $\beta = 1/(k_B T)$ as inverse temperature. This density matrix is then diagonalized to obtain natural orbitals (NOs) and occupation numbers. Active orbitals are then chosen from this set of NOs, as is done in traditional CAS type methods. Thus, at the GF2 convergence, we obtain a set of active orbitals and $\mathbf{\Sigma}^{GF2}_{mol}(i\omega)$ with a corresponding Green's function $\mathbf{G}^{GF2}_{mol}(i\omega)$ both transformed to the NO basis.

After choosing active orbitals, we set up an impurity problem for these orbitals as

$$[G_{mol}(i\omega)]_{act} = \left[(i\omega + \mu)\,\mathbf{1} - \mathbf{f}^{nodc}_{act} - \mathbf{\Delta}(i\omega) - \mathbf{\Sigma}_{mol}(i\omega)\right]^{-1}, \tag{4.2}$$

where all the matrices are in the NO basis and subscript *act* stands for a subset of active orbitals. In the first iteration of SEET, $[\mathbf{G}_{mol}(i\omega)]_{act} = [\mathbf{G}^{GF2}_{mol}(i\omega)]_{act}$. The chemical potential is denoted as μ. The hybridization $\mathbf{\Delta}(i\omega)$ describes coupling of the active orbitals to the remaining weakly correlated ones and the impurity Hamiltonian can be written as

$$H_{act+bath} = H_{act} + \sum_{ub} V_{ub}\left(a^\dagger_u a_b + a^\dagger_b a_u\right) + \sum_b \epsilon_b a^\dagger_b a_b, \tag{4.3}$$

where H_{act} is the full Hamiltonian within the active space,

$$H_{act} = \sum_{uv} f_{uv}^{nodc} a_u^\dagger a_v + \frac{1}{2} \sum_{uvtw} v_{uvtw} a_u^\dagger a_t^\dagger a_v a_w, \tag{4.4}$$
$$f_{uv}^{nodc} = h_{uv} + \sum_{\mu\lambda} P_{\mu\lambda} \left(v_{uv\mu\lambda} - \frac{1}{2} v_{u\lambda\mu v} \right) - \sum_{tw} P_{tw} \left(v_{uvtw} - \frac{1}{2} v_{tvuw} \right),$$

where $u, v, t, w, ...$ indices describe active orbitals, μ, λ are general orbital indeces, and b index is used for bath orbitals. The 1-body density matrix evaluated in GF2 is denoted as $\mathbf{P}$. The couplings V and the orbital energies ϵ are fitted to the hybridization $\mathbf{\Delta}(i\omega)$ between active space and non-interacting bath. For a given hybridization $\mathbf{\Delta}(i\omega)$, the active space Green's function and self-energy, $\mathbf{G}_{act}^{FCI}(i\omega)$ and $\mathbf{\Sigma}_{act}^{FCI}(i\omega)$, are evaluated using the FCI solver. Subsequently, the hybridization is updated and SEET iterations which are DMFT-like are performed until convergence, for details see Refs. 38, 41.

Let us focus now on the molecular self-energy from Eq. 4.2 that is constructed as

$$\mathbf{\Sigma}_{mol}(i\omega) = \mathbf{\Sigma}_{non-local}^{GF2}(i\omega) + \mathbf{\Sigma}_{act}^{FCI}(i\omega), \tag{4.5}$$

where the non-local weakly correlated part of the GF2 self-energy $\mathbf{\Sigma}_{non-local}^{GF2}(i\omega)$ is a difference between the GF2 self-energy of the whole molecule and that of the active, strongly correlated (local part), $\mathbf{\Sigma}_{non-local}^{GF2}(i\omega) = \mathbf{\Sigma}_{mol}^{GF2}(i\omega) - \mathbf{\Sigma}_{act}^{GF2}(i\omega)$. The $\mathbf{\Sigma}_{non-local}^{GF2}(i\omega)$ term stands for an effective many-body field experienced by strongly correlated electrons in the active space. The presence of this term eliminates the need for effective U integrals in the active space since all non-local interactions between the active and remaining orbitals are described by the non-local self-energy term. In general, the embedding self-energy $\mathbf{\Sigma}_{non-local}^{GF2}(i\omega)$ that comes from GF2 should be updated after all the DMFT-like iterations involving FCI Green's function solver are finished. In this paper, however, we performed a self-consistent GF2 procedure only once followed by the iterations updating FCI Green's function.

Generally, SEET(FCI/GF2) consists of two levels of theory: perturbation and diagonalization. This is, from the theoretical point of view, similar to multi-reference second-order perturbation theories. It is therefore worth doing the comparison in Tab. 4.1 between SEET(FCI/GF2) and multi-reference second-order perturbation theories, namely CASPT2/NEVPT2.

Table 4.1: Comparison between NEVPT2/CASPT2 and SEET(FCI/GF2) methods.

NEVPT2/CASPT2	SEET(FCI/GF2)
Perturbation on top of diagonalization	Diagonalization (impurity solver) on top of perturbation
Depends on the 0th-order $\hat{H}$ and the 1st-order CI space	Independent of the 0th-order $\hat{H}$,1st-order CI space not required
Perturbation depends on the diagonalization step	Perturbation and diagonalization are implemented separately
Single active space	Multiple active spaces
Requires 1-, 2-, 3-, 4-RDMs for perturbation	Requires only 1-body Green's function for perturbation
Intruder states in CASPT2	No intruder states
PT2 only describes dynamical correlation	GF2 partially captures strong correlation
Frequency independent	Frequency dependence (spectroscopic quantities)
No convergence in frequency grid is required	Requires convergence in frequency grid
No bath fitting procedure	Requires bath fitting procedure in impurity solver

4.3 Results

We report few proof-of-concept examples to show that our SEET(FCI/GF2) theory is applicable to quantum chemistry. Unless otherwise noted, the ORCA program [42] was used for all calculations using standard methods (e.g., MP2, CASSCF, NEVPT2, and FCI). The local modified DALTON code [43] was used to generate RHF input necessary for GF2 and to evaluate FCI active space Green's functions [44]. We use different β and number of frequencies for different geometries to converge (in frequency grid) the electronic energy to 10^{-4} a.u.

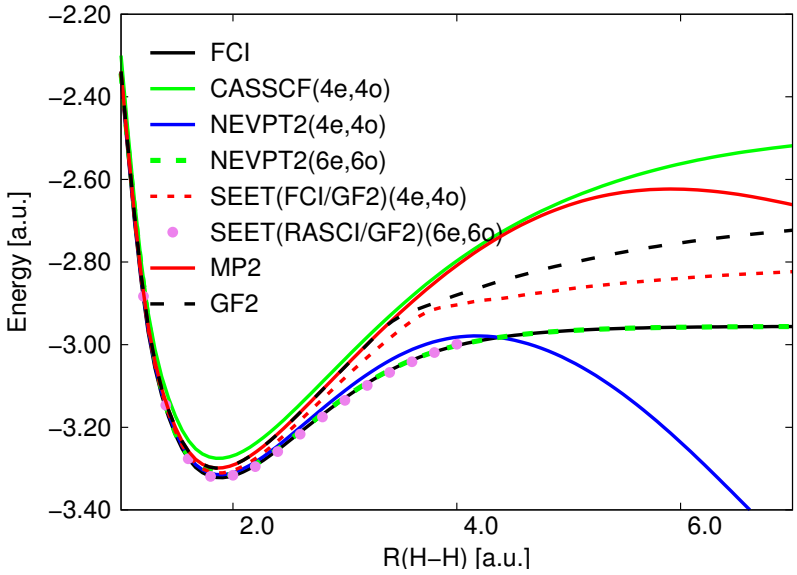

Figure 4.1: Potential energy curve of H_6 ring with TZ basis.

In Fig. 4.1, we present results for the H_6 ring dissociation in a TZ basis [45]. MP2 and GF2 appear identical around the equilibrium in the single-reference regime. Upon bond stretching, the multi-reference character leads to a separation of GF2 away from MP2. In the stretched regime, the full active space requires 6 electrons in 6 σ-type orbitals, consequently, NEVPT2(6e,6o) agrees very well with FCI. In SEET, the impurity system consists of 6 active and 12 bath orbitals with possibly 18 electrons. This impurity is intractable with FCI, and we employed RASCI as an impurity solver. Evidently,

SEET(RASCI/GF2)(6e,6o) provides the dissociation curve that agrees well with the FCI reference. To extend the SEET(RASCI/GF2)(6e,6o) curve beyond $R = 4.0$ a.u. we would require thousands of frequency grid points. This is not an inherent problem and can be avoided by employing a compact spline interpolation of Green's functions. The description of such a method will be published and calibrated elsewhere. When smaller active space is used, CASSCF(4e,4o) incorrectly describes the dissociation and NEVPT2(4e,4o) diverges beyond the equilibrium due to missing static correlation. Interestingly, although SEET(FCI/GF2)(4e,4o) is very close to NEVPT2(4e,4o) at the equilibrium, it does not diverge and remains nearly parallel to FCI at long distances. This is because GF2 itself partially recovers the static correlation [39] missed in NEVPT2 when the small active space is used.

In Fig. 4.2, we consider the potential energy curve of Li_2 molecule in a TZ basis. Both CASSCF(2e,2o) and NEVPT2(2e,2o) yield curves parallel to FCI. Although GF2 yields lower energies than CASSCF(2e,2o) around the minimum, for stretched geometries GF2 is not parallel to the FCI curve. When static correlation is properly treated by using active space on top of GF2, i.e. SEET(FCI/GF2)(2e,2o), the dissociation is correctly described and the curve falls between NEVPT2(2e,2o) and FCI curves.

Let us show now that SEET allows us to split the full active space into smaller active spaces composed of molecular orbitals (MOs) belonging to particular fragments. We show here only small molecules with small active spaces; however, in systems with large active space that are currently too large for CAS type methods, the active space splitting in SEET can be used to qualitatively describe the dissociation (strong correlation) regime. We consider the Li_4 cluster made from two parallel Li dimers as shown in the inset of Fig. 4.3. The distance between these two dimers is fixed and kept long enough to avoid any coupling between them. The cluster is stretched following the parallel direction as shown in the inset of Fig. 4.3. GF2 and MP2 yield too deep dissociation curves and as expected both curves separate for distances larger than 9.0 a.u. In this

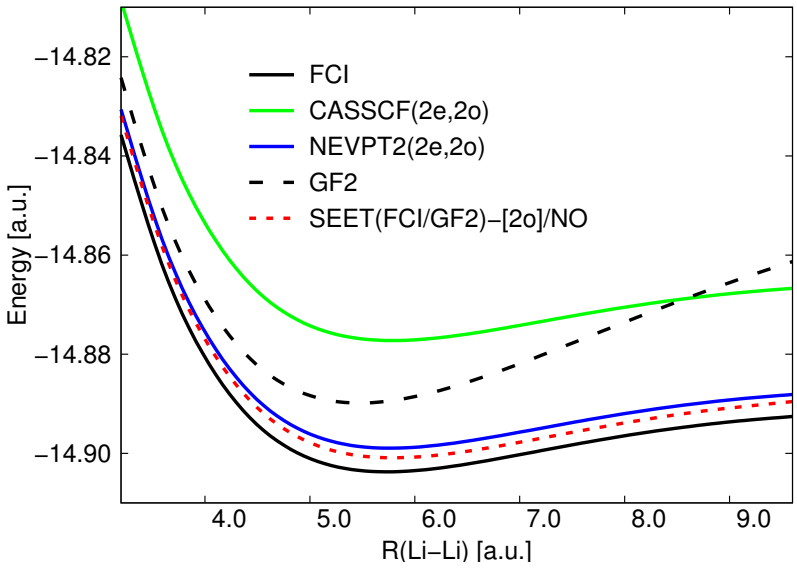

Figure 4.2: Potential energy curve of Li_2 with TZ basis.

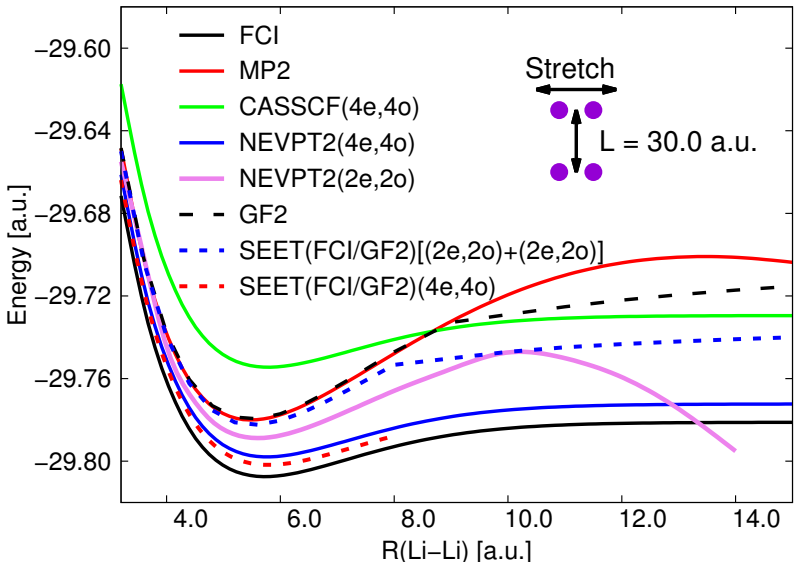

Figure 4.3: Potential energy curve of Li_4 with TZ basis. The inset shows the geometry of Li_4 cluster that includes two Li dimers separated by a fixed distance $L = 30.0$ a.u.

system, the full active space comprises two pairs of σ-type MOs. Consequently, both CASSCF(4e,4o) and NEVPT2(4e,4o) methods yield correct dissociation curves within a given basis set, whereas NEVPT2(2e,2o) with only one pair of MOs in active space diverges to $-\infty$ at $R > 10.0$ a.u. The SEET(FCI/GF2)(4e,4o) curve remains between

NEVPT2(4e,4o) and FCI curves. For Li_4, similarly to SEET(RASCI/GF2)(6e,6o) for the H_6 ring, to calculate SEET energies beyond $R = 8.0$ a.u. with 10^{-4} a.u. accuracy requires thousands of frequency points. We will present solutions to this issue elsewhere.

In SEET, the full active space of two pairs of MOs can be split into two smaller equivalent active spaces, where each active space includes one pair of MOs. As shown in Fig. 4.3, SEET(FCI/GF2)[(2e,2o)+(2e,2o)] dissociation curve does not diverge and remains nearly parallel to the FCI one at long distances. While for the example of two parallel Li dimers, it is possible to localize orbitals on each fragment before splitting the full active space (similarly to the active space decomposition (ASD) developed by Parker and coworkers [46]), we avoid doing so since we aim to demonstrate that despite missing many CI configurations when the active space consisting of MOs of the same symmetry (i.e. $\sigma-$type MO) is split, SEET can avoid divergences and recover a dissociation limit parallel to the FCI curve. Moreover, it is evident that SEET results can be systematically improved by enlarging the active space.

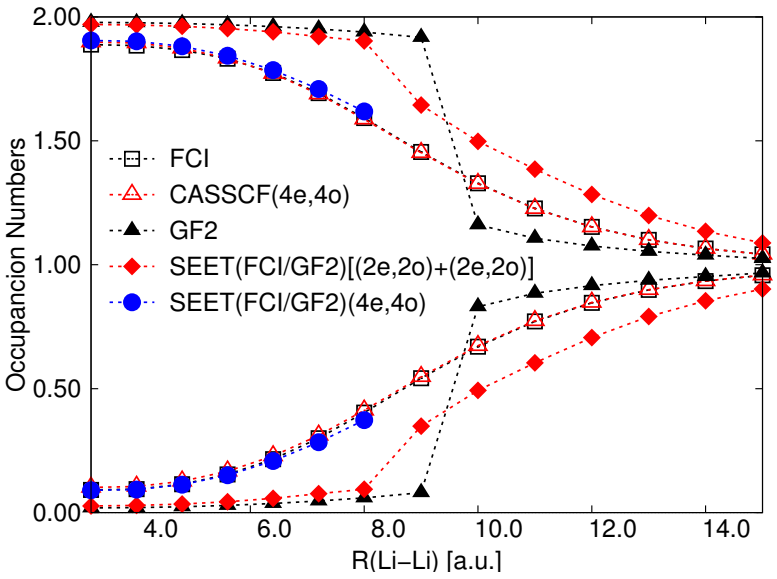

Figure 4.4: Occupation numbers of Li_4.

To further explore active space splitting, in Fig. 4.4, as a function of bond stretch-

ing in Li_4 cluster, we plot orbital occupations of valence MOs obtained by FCI, CASSCF, GF2, and SEET(FCI/GF2) methods. FCI occupations smoothly shift from single-reference to multi-reference as the bond length increases. CASSCF(4e,4o) and SEET(FCI/GF2)(4e,4o) occupations are in a very good agreement with FCI reference. In GF2, occupations suddenly jump from single-reference to multi-reference regime at $R = 9.0$ a.u. This is reflected by a kink in the GF2 dissociation curve, see Fig. 4.3. Furthermore, beyond this point, GF2 occupation numbers are even closer to 1.0 than those of FCI, indicating that GF2 overestimates static correlation in the Li_4 cluster. On the other hand, when performing FCI in two active spaces on top of GF2, namely SEET(FCI/GF2)[(2e,2o)+(2e,2o)], the single- to multi-reference transition becomes much smoother indicating that SEET(FCI/GF2)[(2e,2o)+(2e,2o)] describes the correlations in a more balanced way than GF2 by itself.

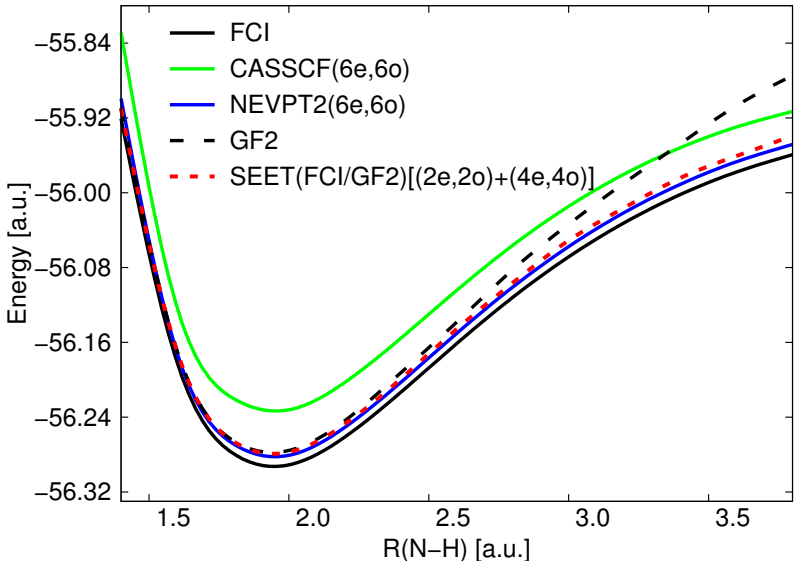

Figure 4.5: Potential energy curve of NH_3 with 6-31G basis.

Finally, we show that the full active space in SEET(FCI/GF2) can be split into smaller groups, where each group consists of different symmetry MOs. To this end, we consider NH_3 molecule in the 6-31G basis [47]. Fig. 4.5 displays the dissociation curves from FCI, CASSCF, NEVPT2, GF2, and SEET(FCI/GF2) calculations. For

NH_3 molecule, the full active space is composed of 4 $\pi-$type and 2 $\sigma-$type orbitals. Both CASSCF(6e,6o) and NEVPT2(6e,6o) correctly reproduce the FCI dissociation behavior. Although GF2 yields the energy that is comparable to NEVPT2(6e,6o) energy at the equilibrium, it significantly differs from NEVPT2(6e,6o) at longer distances. In the SEET(FCI/GF2) method, the full active space is split into two smaller active spaces with different orbital symmetries. One group consists of 2 $\sigma-$type orbitals and 4 $\pi-$type orbitals are included in the other one. It is evident that the SEET(FCI/GF2)[(2e,2o)+(4e,4o)] curve is close to that of NEVPT2(6e,6o) within the range of distances considered. This stands in contrast to the GF2 behavior which has large error for stretched geometries. Let us point out that in conventional CAS methods, it is also possible to split the full active space into smaller active spaces with the different orbital symmetries [12, 13]; however, such a procedure requires a complicated implementation. In SEET, the active space splitting does not require any additional implementation.

In conclusion, we have presented a generalization of the SEET method to *ab initio* Hamiltonians for molecular systems. GF2 and FCI were used to treat correlations in non-local (weakly correlated) and local (strongly correlated) subspaces, respectively, in a perturb and diagonalize type of scheme. The performance of SEET(FCI/GF2) was illustrated using small molecules in small basis sets. We demonstrated that SEET(FCI/GF2) provides results of comparable quality to NEVPT2 with the same active space. Additionally, unlike conventional multi-reference perturbation theories, SEET avoids intruder states and does not require high-order RDMs, and furthermore, the full active space can be split into smaller active spaces without any additional implementation. In contrast to LDA+DMFT, the double counting problem does not appear in SEET and the accuracy can be improved either by increasing the perturbation order or by enlarging the active space. Since the non-local interactions are described by the non-local self-energy, we do not require effective interactions U in the

strongly correlated orbitals. These advantages show that SEET is a promising method to describe challenging strongly correlated, large molecules.

Bibliography

[1] K. Andersson, P. Å. Malmqvist, B. O. Roos, A. J. Sadlej, and K. Wolinski, "Second-order perturbation theory with a CASSCF reference function", *J. Phys. Chem.* **94**, 5483 (1990).

[2] G. Ghigo, B. O. Roos, and P. Å. Malmqvist, "A modified definition of the zeroth-order Hamiltonian in multiconfigurational perturbation theory (CASPT2)", *Chem. Phys. Lett.* **396**, 142 (2004).

[3] C. Angeli, R. Cimiraglia, S. Evangelisti, T. Leininger, and J.-P. Malrieu, "Introduction of n-electron valence states for multireference perturbation theory", *J. Chem. Phys.* **114**, 10252 (2001).

[4] C. Angeli, R. Cimiraglia, and J.-P. Malrieu, "n-electron valence state perturbation theory: A spinless formulation and an efficient implementation of the strongly contracted and of the partially contracted variants", *J. Chem. Phys.* **117**, 9138 (2002).

[5] S. R. White and R. L. Martin, "Ab initio quantum chemistry using the density matrix renormalization group", *J. Chem. Phys.* **110**, 4127 (1999).

[6] G. K.-L. Chan and D. Zgid, "The density matrix renormalization group in quantum chemistry", in *Annu. Rep. Comput. Chem.*, Vol. 5, edited by R. A. Wheeler, Elsevier (2009).

[7] D. Zgid and M. Nooijen, "The density matrix renormalization group self-consistent field method: Orbital optimization with the density matrix renormalization group method in the active space", *J. Chem. Phys.* **128**, 144116 (2008).

[8] Y. Kurashige and T. Yanai, "High-performance ab initio density matrix renormalization group method: Applicability to large-scale multireference problems for metal compounds", *J. Chem. Phys.* **130**, 234114 (2009).

[9] K. H. Marti and M. Reiher, "New electron correlation theories for transition metal chemistry", *Phys. Chem. Chem. Phys.* **13**, 6750 (2011).

[10] P. Å. Malmqvist, A. Rendell, and B. O. Roos, "The restricted active space self-consistent-field method, implemented with a split graph unitary group approach", *J. Phys. Chem.* **94**, 5477 (1990).

[11] P. Å. Malmqvist, K. Pierloot, A. R. M. Shahi, C. J. Cramer, and L. Gagliardi, "The restricted active space followed by second-order perturbation theory method: Theory and application to the study of CuO_2 and Cu_2O_2 systems", *J. Chem. Phys.* **128**, 204109 (2008).

[12] G. L. Manni, F. Aquilante, and L. Gagliardi, "Strong correlation treated via effective hamiltonians and perturbation theory", *J. Chem. Phys.* **134**, 034114 (2011).

[13] G. Li Manni, D. Ma, F. Aquilante, J. Olsen, and L. Gagliardi, "SplitGAS method for strong correlation and the challenging case of Cr_2", *J. Chem. Theory Comput.* **9**, 3375 (2013).

[14] D. Ma, G. L. Manni, and L. Gagliardi, "The generalized active space concept in multiconfigurational self-consistent field methods", *J. Chem. Phys.* **135**, 044128 (2011).

[15] K. D. Vogiatzis, G. Li Manni, S. J. Stoneburner, D. Ma, and L. Gagliardi, "Systematic expansion of active spaces beyond the CASSCF limit: A GASSCF/SplitGAS benchmark study", *J. Chem. Theory Comput.* **11**, 3010 (2015).

[16] J. Gräfenstein and D. Cremer, "The combination of density functional theory with multi-configuration methods–CAS-DFT", *Chem. Phys. Lett.* **316**, 569 (2000).

[17] J. Gräfenstein and D. Cremer, "Development of a CAS-DFT method covering non-dynamical and dynamical electron correlation in a balanced way", *Mol. Phys.* **103**, 279 (2005).

[18] R. Pollet, A. Savin, T. Leininger, and H. Stoll, "Combining multideterminantal wave functions with density functionals to handle near-degeneracy in atoms and molecules", *J. Chem. Phys.* **116**, 1250 (2002).

[19] G. Li Manni, R. K. Carlson, S. Luo, D. Ma, J. Olsen, D. G. Truhlar, and L. Gagliardi, "Multiconfiguration pair-density functional theory", *J. Chem. Theory Comput.* **10**, 3669 (2014).

[20] R. K. Carlson, D. G. Truhlar, and L. Gagliardi, "Multiconfiguration pair-density functional theory: A fully translated gradient approximation and its performance for transition metal dimers and the spectroscopy of $Re_2Cl_8^{2-}$", *J. Chem. Theory Comput.* **11**, 4077 (2015).

[21] A. Georges, G. Kotliar, W. Krauth, and M. J. Rozenberg, "Dynamical mean-field theory of strongly correlated fermion systems and the limit of infinite dimensions", *Rev. Mod. Phys.* **68**, 13 (1996).

[22] G. Kotliar, S. Y. Savrasov, K. Haule, V. S. Oudovenko, O. Parcollet, and C. A. Marianetti, "Electronic structure calculations with dynamical mean-field theory", *Rev. Mod. Phys.* **78**, 865 (2006).

[23] G. Kotliar and D. Vollhardt, "Strongly correlated materials: Insights from dynamical mean-field theory", *Physics Today* **57**, 53 (2004).

[24] K. Held, "Electronic structure calculations using dynamical mean field theory", *Adv. Phys.* **56**, 829 (2007).

[25] F. Lechermann, A. Georges, A. Poteryaev, S. Biermann, M. Posternak, A. Yamasaki, and O. Andersen, "Dynamical mean-field theory using wannier functions: A flexible route to electronic structure calculations of strongly correlated materials", *Phys. Rev. B* **74**, 125120 (2006).

[26] A. I. Lichtenstein, M. I. Katsnelson, and G. Kotliar, "Finite-temperature magnetism of transition metals: An *ab initio* dynamical mean-field theory", *Phys. Rev. B* **87**, 067205 (2001).

[27] X. Ren, I. Leonov, G. Keller, M. Kollar, I. Nekrasov, and D. Vollhardt, "LDA+DMFT computation of the electronic spectrum of NiO", *Phys. Rev. B* **74**, 195114 (2006).

[28] J. Lee and K. Haule, "Dynamical mean field theory for diatomic molecules and the exact double counting", *Phys. Rev. B* **91**, 155144 (2015).

[29] D. Boukhvalov, L. Vergara, V. Dobrovitski, M. Katsnelson, A. Lichtenstein, P. Kögerler, J. Musfeldt, and B. Harmon, "Correlation effects in the electronic structure of the Mn_4 molecular magnet", *Phys. Rev. B* **77**, 180402 (2008).

[30] C. Weber, D. J. Cole, D. D. O'Regan, and M. C. Payne, "Renormalization of myoglobin–ligand binding energetics by quantum many-body effects", *Proc. Natl. Acad. Sci. USA* **111**, 5790 (2014).

[31] C. Weber, D. D. O'Regan, N. D. Hine, P. B. Littlewood, G. Kotliar, and M. C. Payne, "Importance of many-body effects in the kernel of hemoglobin for ligand binding", *Phys. Rev. Lett.* **110**, 106402 (2013).

[32] J. Chen, A. J. Millis, and C. A. Marianetti, "Density functional plus dynamical mean-field theory of the spin-crossover molecule $Fe(phen)_2(NCS)_2$", *Phys. Rev. B* **91**, 241111 (2015).

[33] H. Park, A. J. Millis, and C. A. Marianetti, "Density functional versus spin-density functional and the choice of correlated subspace in multivariable effective action theories of electronic structure", *Phys. Rev. B* **92**, 035146 (2015).

[34] L. Vaugier, H. Jiang, and S. Biermann, "Hubbard U and Hund exchange J in transition metal oxides: Screening versus localization trends from constrained random phase approximation", *Phys. Rev. B* **86**, 165105 (2012).

[35] S. Biermann, F. Aryasetiawan, and A. Georges, "First-principles approach to the electronic structure of strongly correlated systems: Combining the GW approximation and dynamical mean-field theory", *Phys. Rev. Lett.* **90**, 086402 (2003).

[36] J. M. Tomczak, M. Casula, T. Miyake, F. Aryasetiawan, and S. Biermann, "Combined GW and dynamical mean-field theory: Dynamical screening effects in transition metal oxides", *EPL (Europhys. Lett.)* **100**, 67001 (2012).

[37] M. Kitatani, N. Tsuji, and H. Aoki, "FLEX+DMFT approach to the d-wave superconducting phase diagram of the two-dimensional hubbard model", *Phys. Rev. B* **92**, 085104 (2015).

[38] A. A. Kananenka, E. Gull, and D. Zgid, "Systematically improvable multiscale solver for correlated electron systems", *Phys. Rev. B* **91**, 121111 (2015).

[39] J. J. Phillips and D. Zgid, "Communication: The description of strong correlation within self-consistent Green's function second-order perturbation theory", *J. Chem. Phys.* **140**, 241101 (2014).

[40] J. J. Phillips, A. A. Kananenka, and D. Zgid, "Fractional charge and spin errors in self-consistent Green's function theory", *J. Chem. Phys.* **142**, 194108 (2015).

[41] D. Zgid and G. K.-L. Chan, "Dynamical mean-field theory from a quantum chemical perspective", *J. Chem. Phys.* **134**, 094115 (2011).

[42] F. Neese, "The ORCA program system", *Wiley Interdiscip. Rev. Comput. Mol. Sci.* **2**, 73 (2012).

[43] K. Aidas, C. Angeli, K. L. Bak, V. Bakken, R. Bast, L. Boman, O. Christiansen, R. Cimiraglia, S. Coriani, P. Dahle, E. K. Dalskov, U. Ekström, T. Enevoldsen, J. J. Eriksen, P. Ettenhuber, B. Fernández, L. Ferrighi, H. Fliegl, L. Frediani, K. Hald, A. Halkier, C. Hättig, H. Heiberg, T. Helgaker, A. C. Hennum, H. Hettema, E. Hjertenæs, S. Høst, I.-M. Høyvik, M. F. Iozzi, B. Jansík, H. J. Aa. Jensen, D. Jonsson, P. Jørgensen, J. Kauczor, S. Kirpekar, T. Kjærgaard, W. Klopper, S. Knecht, R. Kobayashi, H. Koch, J. Kongsted, A. Krapp, K. Kristensen, A. Ligabue, O. B. Lutnæs, J. I. Melo, K. V. Mikkelsen, R. H. Myhre, C. Neiss, C. B. Nielsen, P. Norman, J. Olsen, J. M. H. Olsen, A. Osted, M. J. Packer, F. Pawlowski, T. B. Pedersen, P. F. Provasi, S. Reine, Z. Rinkevicius, T. A. Ruden, K. Ruud, V. V. Rybkin, P. Sałek, C. C. M. Samson, A. S. de Merás, T. Saue, S. P. A. Sauer, B. Schimmelpfennig, K. Sneskov, A. H. Steindal, K. O. Sylvester-Hvid, P. R. Taylor, A. M. Teale, E. I. Tellgren, D. P. Tew, A. J. Thorvaldsen, L. Thøgersen, O. Vahtras, M. A. Watson, D. J. D. Wilson, M. Ziolkowski, and H. Ågren, "The Dalton quantum chemistry program system", *Wiley Interdiscip. Rev. Comput. Mol. Sci.* **4**, 269 (2014).

[44] D. Zgid, E. Gull, and G. K.-L. Chan, "Truncated configuration interaction expansions as solvers for correlated quantum impurity models and dynamical mean-field theory", *Phys. Rev. B* **86**, 165128 (2012).

[45] T. H. Dunning, "Gaussian basis functions for use in molecular calculations. III. Contraction of (10s6p) atomic basis sets for the first-row atoms", *J. Chem. Phys.* **55**, 716 (1971).

[46] S. M. Parker, T. Seideman, M. A. Ratner, and T. Shiozaki, "Communication: Active-space decomposition for molecular dimers", *J. Chem. Phys.* **139**, 021108 (2013).

[47] W. J. Hehre, R. Ditchfield, and J. A. Pople, "Self-consistent molecular orbital methods. XII. Further extensions of gaussian-type basis sets for use in molecular orbital studies of organic molecules", *J. Chem. Phys.* **56**, 2257 (1972).

Chapter 5

Efficient temperature-dependent Green's functions methods for realistic systems: compact grids for orthogonal polynomial transforms

A. A. Kananenka, J. J. Phillips and D. Zgid

Journal of Chemical Theory and Computation, **12 (2)** 564–571 (2016)

5.1 Introduction

The use of numerical grids in calculations for realistic systems has a long history in quantum chemistry simulations. For example, in density functional theory (DFT) a numerical integration is necessary for the evaluation of the exchange-correlation contribution to the density functional [1–5]. Similarly, in Laplace transformed MP2 (LT-MP2) a quadrature is used to represent an integral that leads to the removal of the energy denominators [6–11]. Recently, an implementation of the random phase approximation (RPA) [12] appeared that uses an efficient imaginary time grid to yield a temperature-independent RPA energy. The above mentioned methods are just a few examples of using efficient quadrature, a more extensive literature on the subject can be found in Refs. [13–32]. Thus, it is fair to say that extensive knowledge ex-

ist on representing temperature-independent quantities on a grid when ground state methods are used. However, very little is known about how to efficiently represent temperature-dependent data on finite-temperature imaginary axis Matsubara grids.

Several factors distinguish the finite-temperature Green's function from the zero-temperature Green's function formalism. Firstly, let us note that the temperature-dependent Green's function is a discrete object for which the grid points $i\omega_n$ are spaced according to the Matsubara grid $w_n = (2n+1)\pi/\beta$, where $n \in \mathbb{Z}$, $\beta = 1/(k_{\mathrm{B}}T)$ is the inverse temperature and k_{B} is the Boltzmann constant. In comparison, the zero-temperature Green's function represented on the imaginary axis is a continuous function. Similarly, the temperature-dependent imaginary time Green's function is an antiperiodic function between 0 and β, while the zero-temperature Green's function of imaginary time is a non-periodic function decaying rapidly and smoothly to zero. Consequently, traditional quadratures developed for zero-temperature RPA Green's functions used in Ref. [12] or LT-MP2 to represent denominators [6] are not suitable for temperature-dependent Green's function calculations.

Currently, temperature-dependent Green's function calculations are mostly done for low-energy model systems. An excellent compact representation of Green's functions in terms of Legendre polynomials was proposed by Boehnke *et al.* in Ref. [33] and used for single-site dynamical mean-field theory calculations for the Hubbard model. While temperature-dependent Green's function calculations for large realistic systems are still in their infancy, one can easily imagine that they could be very important in materials science for materials with small band gaps where the change of properties with temperature is significant and multiple states can be easily populated, or for a system which exhibits a temperature-dependent phase transition caused by the electronic degrees of freedom.

Unlike the low-energy models, the orbital energies in realistic systems span a huge energy window frequently varying even between -3000 eV to 300 eV, as shown in

Fig. 5.1. Thus, when quantitative accuracy in the calculations of realistic systems is desired, new challenges arise that are not present in model system calculations.

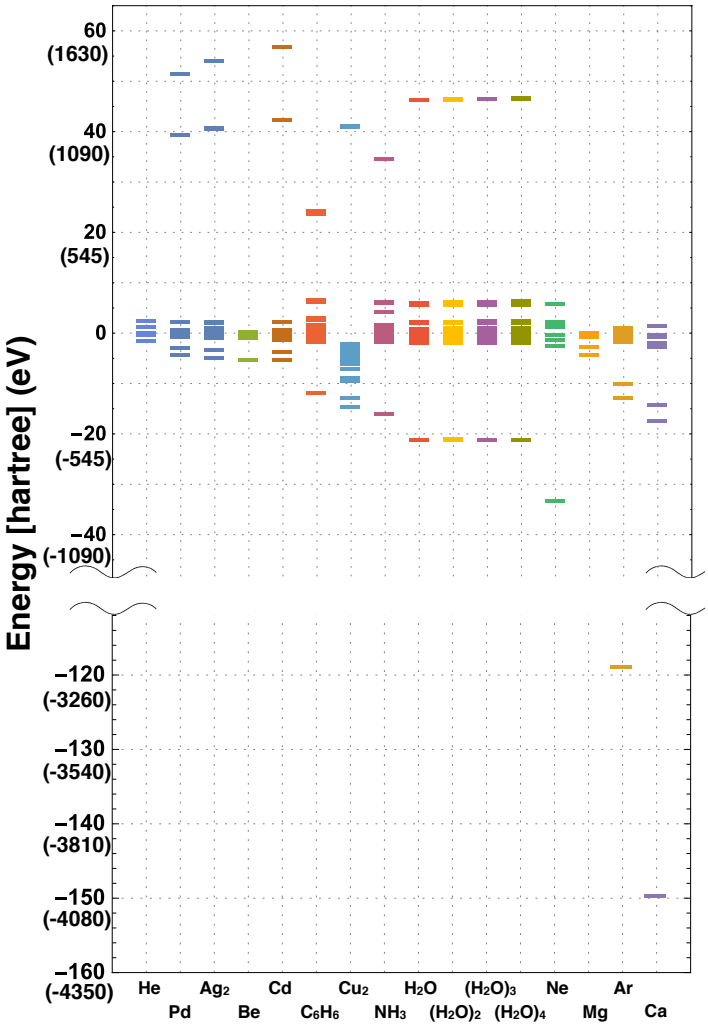

Figure 5.1: Orbital energies for atoms and molecules in large basis sets containing diffuse orbitals.

The temperature-dependent Green's functions have to be represented on a numerical grid with a spacing defined by the temperature but covering the energy window spanned by the realistic system. This usually results in a grid containing thousands of frequencies. Consequently, the Fourier transform from the imaginary time to the imaginary frequency axis, according to Nyquist theorem, requires twice as many imaginary time points as frequency points to yield accurate results. Having several thousand data

points makes the calculations for realistic systems extremely challenging even if each grid point can be calculated in parallel.

Motivated by the aforementioned challenges, we first determine how the imaginary time grid can be truncated to a reasonable size and how the resulting errors can be controlled. To achieve this, we replace the numerical Fourier transform ($i\tau \rightarrow i\omega$) with an orthogonal polynomial transform ($i\tau \rightarrow L$) and ($L \rightarrow i\omega$), where L denotes expansion coefficients of a Green's function or self-energy in an orthogonal polynomial basis. Subsequently, we examine if **(i)** the expansion coefficients L can be produced using a smaller number of grid points than currently employed in the numerical Fourier transform, and if **(ii)** the number of expansion coefficients L is small enough that they can be easily stored in realistic calculations.

This Chapter is organized as follows. In Section 5.2, we review the necessary theoretical background leading to compact imaginary time grids and orthogonal polynomial transforms ($i\tau \rightarrow L \rightarrow i\omega$) using Legendre expansion coefficients. In Section 5.3, we discuss how an orthogonal polynomial transform can be used in the second-order iterative Green's function method (GF2) to reduce the size of the imaginary time grid. In Section 5.4, we present numerical results showing that the required number of imaginary time points is much smaller than in the original uniform and power-law grid, and that the number of required expansion coefficients can be kept small even if micro-Hartree ($\mu \mathrm{E}_h$) accuracy is desired. Finally, we present conclusions in Section 5.5.

5.2 Theory

In many Green's function methods two Green's function ($\mathbf{G}$) or self-energy ($\mathbf{\Sigma}$) representations are used: an imaginary time representation $\mathbf{G}(i\tau)$ or $\mathbf{\Sigma}(i\tau)$ and imaginary frequency representation $\mathbf{G}(i\omega)$ or $\mathbf{\Sigma}(i\omega)$. In an efficient implementation, one frequently changes from $i\tau$ to $i\omega$ and back, depending on which representation is

more computationally advantageous for a particular step in the calculation. Note that while the above statement is general and the $i\tau$ to $i\omega$ transform may be present in temperature-independent calculations such as RPA or GW [12, 34, 35], in this Chapter we focus exclusively on the imaginary time and frequency used for temperature-dependent Green's functions [36–39].

Thus, often a Green's function method proceeds according to the scheme illustrated in Fig. 5.2, where the computational bottleneck lies in the evaluation of $\mathbf{\Sigma}(i\tau)$.

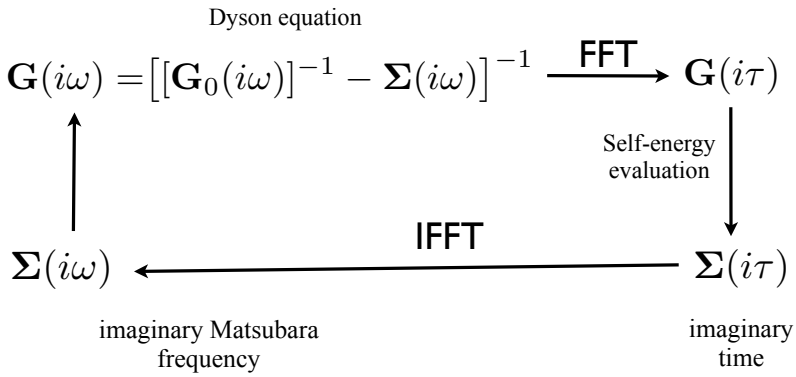

Figure 5.2: An example of the representation change between imaginary time and frequency in Green's function methods. We denote the noninteracting and interacting/correlated Green's function as $\mathbf{G}_0(i\omega)$ and $\mathbf{G}(i\omega)$, respectively.

In numerical methods imaginary time quantities are discretized on a grid. The number of imaginary time points used to represent $\mathbf{\Sigma}(i\tau)$ enters as a prefactor in the computational scaling of the $\mathbf{G}(i\tau) \rightarrow \mathbf{\Sigma}(i\tau)$ step. A sizable prefactor makes such calculations for large system impossible.

There are two reasons for the large size of imaginary time grids for temperature-dependent Green's functions. Firstly enough points are required to preserve the temperature dependence, and secondly a significant number of points is required to make a numerical Fourier transform accurate.

5.2.1 Orthogonal polynomial representation of the self-energy

Because Legendre polynomials form a complete orthogonal basis on the interval $[-1, 1]$ any function, including the Green's function and self-energy, can be expanded in terms of Legendre polynomials. A detailed description of Legendre polynomials and their use as an expansion basis can be found in Ref. [40]. We consider a single-particle temperature-dependent imaginary time self-energy $\mathbf{\Sigma}(i\tau)$ on the interval $[0, \beta]$. The Legendre polynomial expansion of the self-energy on this interval is given by

$$\Sigma_{ij}(i\tau) = \sum_{l \geq 0}^{\infty} \frac{\sqrt{2l+1}}{\beta} P_l(x(i\tau)) \Sigma_{ij}^l, \tag{5.1}$$

where $P_l(x(i\tau))$ is a Legendre polynomial of rank l and Σ_{ij}^l is the corresponding expansion coefficient,

$$\Sigma_{ij}^l = \sqrt{2l+1} \int_0^\beta d(i\tau) P_l(x(i\tau)) \Sigma_{ij}(i\tau), \tag{5.2}$$

and $x(i\tau) = 2(i\tau)/\beta - 1$ maps the interval $[0, \beta]$ onto $[-1, 1]$. Note that different orthogonal polynomials, e.g. Chebyshev or Legendre, can be used as a basis. However, all results presented here should be valid regardless of the representation [33, 41].

In the past, several advantages of using an orthogonal polynomial representation of the Green's function (and self-energy) were explored. Boehnke *et al.* [33] used the Legendre polynomial representation of Green's functions as a noise filter in continuous-time hybridization expansion quantum Monte Carlo (CT-HYB) [42, 43] calculations and to construct a more compact representation of Green's functions than the Matsubara axis representation. The compactness of the Legendre representation of Green's functions was subsequently explored in Refs. [44, 45].

In this Chapter, we focus on another advantage of using the Legendre representation

that is relevant to computational time savings when Fourier transforming quantities from imaginary time to imaginary frequency. The Fourier transform in the Legendre basis can be done as a two step transform [33] ($\mathbf{\Sigma}(i\tau) \rightarrow L$) and ($L \rightarrow \mathbf{\Sigma}(i\omega)$). We note that using the Legendre basis in the first step ($\mathbf{\Sigma}(i\tau) \rightarrow L$) leads to a dramatic reduction of the number of imaginary time points in comparison to performing a regular Fast Fourier transform ($\mathbf{\Sigma}(i\tau) \rightarrow \mathbf{\Sigma}(i\omega)$). This reduction is especially important for methods where the evaluation of the self-energy or Green's function on the imaginary time axis is a computational bottleneck. The second step ($L \rightarrow \mathbf{\Sigma}(i\omega)$) is unitary and can be written as matrix multiplication

$$\Sigma_{ij}(i\omega_n) = \sum_{l\geq 0}^{\infty} \Sigma_{ij}^{l} \frac{\sqrt{2l+1}}{\beta} \int_0^\beta d(i\tau) e^{i\omega_n \tau} P_l(x(i\tau)) = \sum_{l\geq 0}^{\infty} T_{nl} \Sigma_{ij}^{l},$$

where T_{nl} is the unitary matrix with elements defined as

$$T_{nl} = (-1)^n i^{l+1} \sqrt{2l+1} j_l \left(\frac{(2n+1)\,\pi}{2} \right), \tag{5.3}$$

where $j_l(z)$ are the spherical Bessel functions of the second kind.

Even though the Legendre series is infinite in principle, in all practical calculations only a finite number of expansion coefficients is used, and for all atomic and molecular systems studied here the expansion coefficients decay very fast. In the worst case, only a few hundreds of them are necessary (see Section 5.4), therefore only $\mathcal{O}(N_l n^2)$ double precision numbers have to be stored, where n is the number of orbitals and N_l is the number of terms in the Legendre expansion. In contrast to calculations employing the orthogonal polynomial transform, a typical numerical Fourier transform may require tens to hundreds of thousands of imaginary time grid points N_τ, making the cost of evaluation of the self-energy very significant.

5.2.2 Sparse imaginary time grid

In this section, we examine the number of imaginary time grid points necessary to perform the Legendre transform ($\mathbf{\Sigma}(i\tau) \rightarrow L$) accurately. This assessment is absolutely vital to the success of many approaches where evaluation of the self-energy on the time grid is the computational bottleneck.

To estimate the number of grid points necessary we performed calculations for atoms and molecules using different numbers of imaginary time points. While both atoms and molecules that we use here as test examples do not display different physics for a large range of temperatures due to the size of the gap present in these systems, they are very challenging examples since we strive to calculate the electronic energy for very low temperatures (large value of inverse temperature $\beta = 100$ [1/a.u.]). Consequently, our grid spacing has to be very small and the grid has to span the significant energy window shown in Fig. 5.1, thus requiring very many points if the uniform or power-law grids are used. For numerical Fourier transforms we used two different grids, a uniform grid and power-law grid as described below. For the ($\mathbf{\Sigma}(i\tau) \rightarrow L$) transform, we used a modification of the power-law grid to compute a fixed number of Legendre coefficients. We have chosen 200 expansion coefficients since such a number of coefficients allows us to calculate the energy to $\mu \mathrm{E}_h$ accuracy.

5.2.3 Uniform imaginary time grid

The grid points are uniformly spaced within the interval $[0, \beta]$ where the antiperiodic $\mathbf{G}(i\tau)$ or $\mathbf{\Sigma}(i\tau)$ is represented.

5.2.4 Power-law time grid

Because the imaginary time self-energy is sharply peaked around endpoints (0 and $\pm\beta$) it is convenient to use non-uniformly spaced grids to represent it. A power-law

grid [46] is constructed to be dense around endpoints and sparse between them where the imaginary time self-energy is close to zero. The power-law grid is defined by two parameters: the power coefficient p and the uniform coefficient u. The first step in creating such a grid is placing points with the coordinates $\tau_j = \beta/2^j, j \in \{0, ..., p-1\}$ starting from each endpoint and also placing a midpoint at $\beta/2$. Consequently, such a grid has $2p+1$ power points. Then, each interval between power points is divided into $2u$ uniformly spaced subintervals. Thus the total number of grid points is $N_\tau = 2u(p+1)+1$.

5.2.5 $(\mathbf{\Sigma}(i\tau) \to L)$ transform with a power-law grid

We evaluated Legendre expansion coefficients employing only a fraction of the original power-law grid. We kept the number of power points fixed at $p = 12$ and chose the number of uniform points as $u = 2^n$ where $n \in \{1, ..., 5\}$. The resulting grid has $2u(p+1)+1$ imaginary time points that correspond to 53, 105, 209, 417 and 833 points for $n \in \{1, ..., 5\}$ respectively. In comparison, calculations with the standard power-law grid required at least $n = 8$ to be converged.

Using the uniform, power-law grid and orthogonal polynomial transform, we evaluated the Matsubara self-energy $\mathbf{\Sigma}(i\omega)$. In Fig. 5.3, we show the convergence of the self-energy for different grids. We set as our reference the self-energy obtained with 200 Legendre polynomials and plot the norm of the matrix $\left(||\mathbf{A}|| = \left[\sum_{ij} (A_{ij})^2\right]^{1/2}\right)$ defined as the difference between the reference self-energy and the self-energy calculated with different numbers of points and different grids for the Ne atom using aug-cc-pVDZ basis set [47–49].

As seen in Fig. 5.3, the $(\mathbf{\Sigma}(i\tau) \to L)$ and $(L \to \mathbf{\Sigma}(i\omega))$ transforms converge much faster than the regular $(\mathbf{\Sigma}(i\tau) \to \mathbf{\Sigma}(i\omega))$ Fourier transform performed using a uniform or power-law grid.

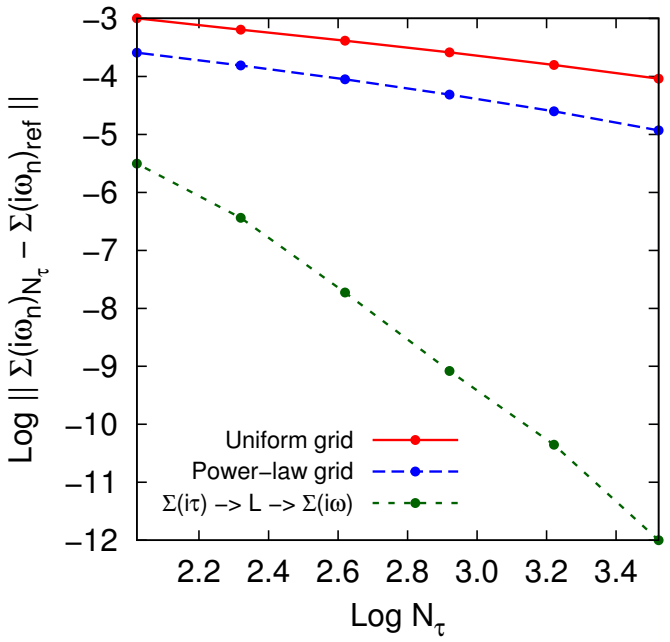

Figure 5.3: Convergence of the self-energy $\mathbf{\Sigma}(i\omega_n)$ as a function of number of imaginary time points, for the Ne atom with aug-cc-pVDZ basis set, and $\beta = 100$ [1/a.u.].

5.3 Self-consistent second-order Green's function theory using orthogonal polynomial transform

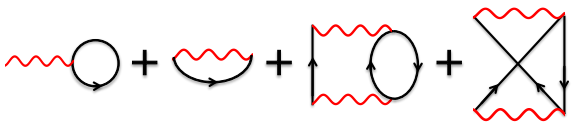

Figure 5.4: GF2 is the second-order approximation to the self-energy. It includes two first order self-energy diagrams (from left to right): Hartree (direct), Fock (exchange) and two second-order self-energy diagrams: direct and exchange.

In this section, as an application to realistic calculations, we briefly describe the framework of the self-consistent second-order Green's function theory (GF2) using an orthogonal polynomial transform.

GF2 employs the second-order approximation to the self-energy resulting in inclusion of all Feynman self-energy diagrams up to the second order, as shown in Fig. 5.4.

The first two diagrams are already included at mean-field level. Within spin-restricted GF2, the last two diagrams are translated into the following expression for the imaginary time self-energy

$$\Sigma_{ij}(i\tau_n) = -\sum_{klmnpq} G_{kl}(i\tau_n)G_{mn}(i\tau_n)G_{pq}(-i\tau_n)v_{ikmq}\left(2v_{ljpn} - v_{pjln}\right), \tag{5.4}$$

where $\mathbf{G}(i\tau_n)$ is an imaginary time Green's function and v_{ijkl} are two-electron integrals defined as

$$v_{ijkl} = \int\int d\mathbf{r}_1 d\mathbf{r}_2 \phi_i^*(\mathbf{r}_1)\phi_j(\mathbf{r}_1)\frac{1}{r_{12}}\phi_k^*(\mathbf{r}_2)\phi_l(\mathbf{r}_2). \tag{5.5}$$

In GF2, as illustrated in Fig. 5.2 for a general case, the calculation of the second-order self-energy according to Eq. 5.4 is done in the imaginary time domain while the Dyson equation from Fig. 5.2 is much easier to solve in the frequency domain.

In our previous implementation, a typical molecular all electron GF2 calculation that involves both core and virtual orbitals may require many thousands of Matsubara frequencies N_ω making the total amount of storage necessary equal to $\mathcal{O}(N_\omega n^2)$ double precision numbers, where n is the number of orbitals. The imaginary time Green's function is represented by $\mathcal{O}(N_\tau n^2)$ double precision numbers, where N_τ is the number of points of the imaginary time grid. Building the self-energy according to Eq. 5.4 scales as $\mathcal{O}(N_\tau n^5)$, and despite that the self-energy calculation at any given imaginary time point is independent and can be made parallel, a large prefactor N_τ is slowing down calculations significantly even when using a power-law grid.

Since employing the orthogonal polynomial transform restricts the imaginary time grid even for the most difficult cases to fewer than 400 points, we implemented it as part of our algorithm. Here, we give a complete step-by-step modified algorithm description.

1. Start with a Hartree–Fock (HF) reference solution (although starting from a DFT reference is equally possible and advantageous for cases that are difficult

to converge using HF) and build the initial Matsubara Green's function in the non-orthogonal AO basis according to:

$$\mathbf{G}_0(i\omega_n) = \left[(\mu + i\omega_n)\mathbf{S} - \mathbf{F}\right]^{-1}, \tag{5.6}$$

where $\mathbf{S}$ is the overlap matrix, $\mathbf{F}$ is the Fock matrix and μ is the chemical potential.

2. Perform discrete Fourier transform of $\mathbf{G}_0(i\omega_n)$ to its imaginary time counterpart $\mathbf{G}_0(i\tau)$. Alternatively, at this point, it is possible to avoid discrete Fourier transform if one starts directly from the imaginary time HF (DFT) Green's function constructed from HF (DFT) orbital energies ϵ

$$\mathbf{G}_0(i\tau_n) = \theta(i\tau_n)\left(n(\mathbf{E}) - 1\right)e^{-i\tau_n\mathbf{E}} + \theta(-i\tau_n)n(\mathbf{E})e^{-i\tau_n\mathbf{E}}, \tag{5.7}$$

where $\theta(x)$ is the Heaviside step function, $\mathbf{E} = \epsilon - \mu$ and $n(\mathbf{E}) = \left[e^{\beta\mathbf{E}} + \mathbb{1}\right]^{-1}$ is the Fermi distribution. Since the Green's function from Eq. 5.7 is constructed using MO orbital energies, it should be transformed to the AO basis before proceeding to the next step.

3. Calculate the self-energy on the imaginary time grid according to Eq. 5.4. It is at this point where we first take advantage of the Legendre polynomial representation of self-energy, since the Legendre representation allows us to use small imaginary time grids with only a fraction of points of the grid we used in our original implementation [37].

4. Obtain the Legendre expansion coefficients by performing an integration of the self-energy $\mathbf{\Sigma}(i\tau)$ according to Eq. 5.2. Since different imaginary time points are computed in parallel, it is advantageous if for every imaginary time point $i\tau$ we first calculate the self-energy $\mathbf{\Sigma}(i\tau)$ and then immediately use it to calculate its

contribution to $\mathbf{\Sigma}^l$. This allows us to avoid storing full $\mathbf{\Sigma}(i\tau)$.

5. Build the imaginary frequency self-energy $\mathbf{\Sigma}(i\omega)$ by performing a transform of Legendre coefficients according to Eq. 5.3.

6. Solve the Dyson equation to obtain an updated Green's function.

7. Find the chemical potential μ to ensure that a proper number of electrons is present in the system.

8. Calculate the density matrix and use it to update Fock matrix.

9. Go to point 6 and iterate until the density matrix and chemical potential μ converge.

10. Calculate the one-body energy as

$$E_{1\mathrm{b}} = \frac{1}{2}\mathrm{Tr}\left[\left(\mathbf{h} + \mathbf{F}\right)\mathbf{P}\right], \tag{5.8}$$

where $\mathbf{h}$ is the core-Hamiltonian matrix, $\mathbf{P} = -2\mathbf{G}(i\tau = \beta)$ is the correlated density matrix and the Fock matrix $\mathbf{F}$ is evaluated using this correlated density matrix.

The two-body energy can be evaluated using

$$E_{2\mathrm{b}} = \frac{2}{\beta}\sum_{n=0}^{N_\omega}\mathrm{Tr}[\mathbf{G}(i\omega_n)\mathbf{\Sigma}(i\omega_n)], \tag{5.9}$$

for details see Ref. [50].

11. Transform $\mathbf{G}(i\omega)$ to $\mathbf{G}(i\tau)$ and go to step 3 and iterate until the total energy converges.

5.4 Results and discussion

In this section, we provide results of atomic and molecular calculations with the above introduced GF2 algorithm. To assess the accuracy and efficiency of the algorithm described above, we performed several benchmark calculations with large basis sets using diffuse orbitals. These basis sets usually require the most extensive imaginary time grid and are necessary to reach quantitative accuracy and converge with basis set size.

Additionally, we also tested our algorithm on a few systems with transition metal atoms with ecp-sdd-DZ [51–54] basis set containing pseudopotentials for inner shell electrons. We investigated systems with pseudopotentials since these are frequently used in solid state calculations and it is our interest to assess how compact the grids can become for such systems.

Our investigations can be divided into two groups evoking our original questions about **(i)** the size of the grid necessary to calculate the Legendre coefficients accurately and **(ii)** the compactness of the Legendre expansion.

5.4.1 Convergence of the electronic energy with respect to the grid size

We calculated the electronic correlation energy according to Eq. 5.9 for the grids defined in Section 5.2.5 and compared it to the energy obtained using our previous GF2 implementation with sufficiently large imaginary time grids. Our previous implementation required at least an order of magnitude larger grids than the current one using the Legendre expansion.

In Fig. 5.5, we plot the error in electronic correlation energy obtained by using different number of imaginary time points that are used to produce Legendre expansion of self-energy consisting of 200 expansion coefficients. Let us first note that using 200

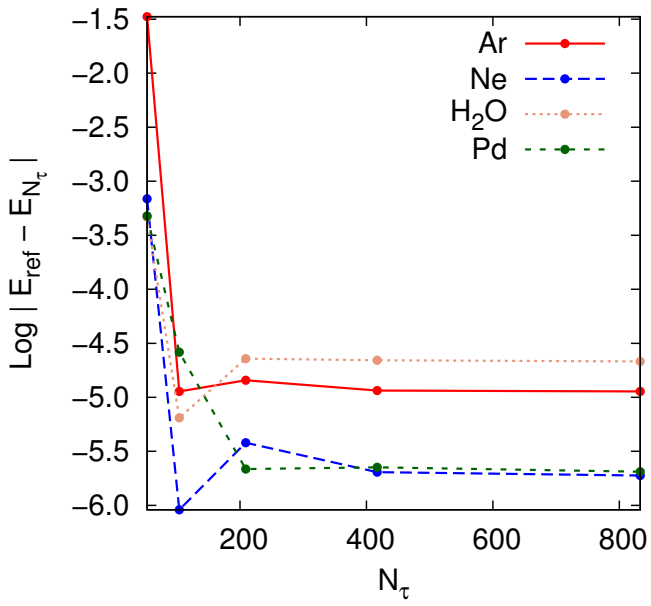

Figure 5.5: Convergence of the electron correlation energy as the function of number of imaginary time points used to obtain the Legendre expansion of the self-energy for several atoms and molecules.

Legendre coefficients results on average in 20 or less μE_h error in the correlation energy.

If we set the value of correlation energy using 200 Legendre polynomials as a reference then it is evident from Fig. 5.5 that with only 104 imaginary time grid points an acceptable accuracy (less than 50 μE_h from the exact answer) can be achieved. This is already far below the commonly accepted chemical accuracy of ≈ 1 kcal·mol^{-1}. Using fewer than 100 grid points is not advisable since for 53 points for every examined case the correlation energy was about 0.5 mE_h away from the reference correlation energy that is unacceptable in almost any quantum chemical calculation. For imaginary time grids with 209 and more points the accuracy reaches a plateau since for 200 Legendre coefficients a grid of 209 time points is sufficient to produce these coefficients with accuracy reaching numerical precision. If we desired to reach better accuracy than μE_h level, then a larger number of the Legendre expansion coefficients and time points should be employed in our calculation.

5.4.2 Compactness of the Legendre expansion

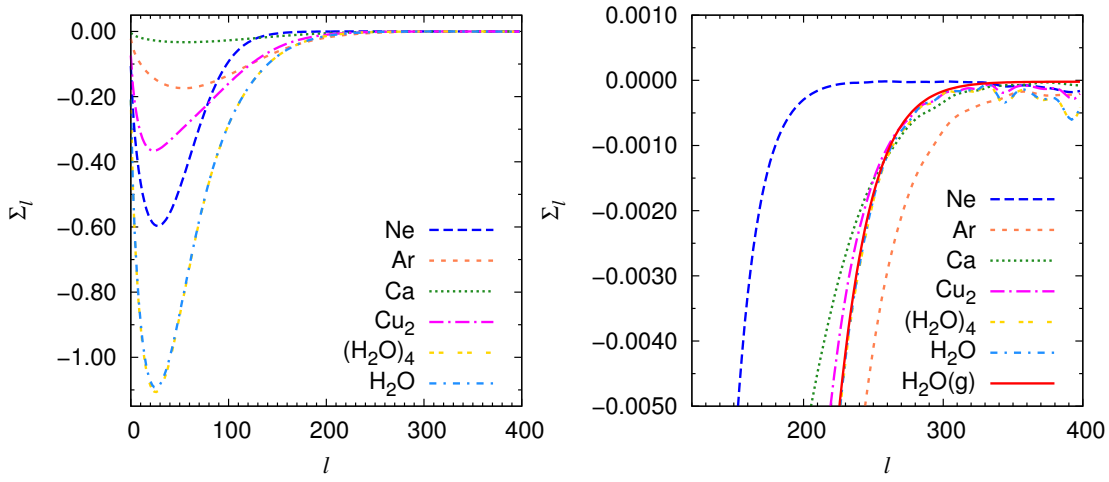

Figure 5.6: Even coefficients of Legendre expansion of self-energy calculated using imaginary time grid consisting of 417 points for atoms and molecules. Right panel shows zoomed in region where $\mathbf{\Sigma}^l \approx 0$ where Gibbs oscillations start to develop.

Next, we will study how the accuracy of our calculations depends on the number of terms in the Legendre expansion of the self-energy. We fix the size of imaginary time grid to 417 points because, as it is seen from Fig. 5.5, this number of grid points is sufficient to produce at least 200 accurate Legendre coefficients in the expansion of the self-energy.

First, we will look at values of expansion coefficients Σ^l_{00} determined by integrating the self-energy according to Eq. 5.2. In Fig. 5.6 we plotted the even Legendre coefficients for a few atoms and molecules. Odd coefficients show very similar behavior in almost all cases. As seen from the left panel of Fig. 5.6, Legendre coefficients decay monotonically, converging to zero with a decay rate that is system-specific. For all cases studied in this work, we observe a fast decay of Legendre expansion coefficients used to represent the imaginary time self-energy. Thus, the Legendre polynomials form a compact representation not only for the Hubbard model [33] but also for atoms and molecules. Since realistic molecular systems have diffuse orbitals and span a large

energy spectrum an increase in the number of expansion terms in comparison to the Hubbard model is to be expected.

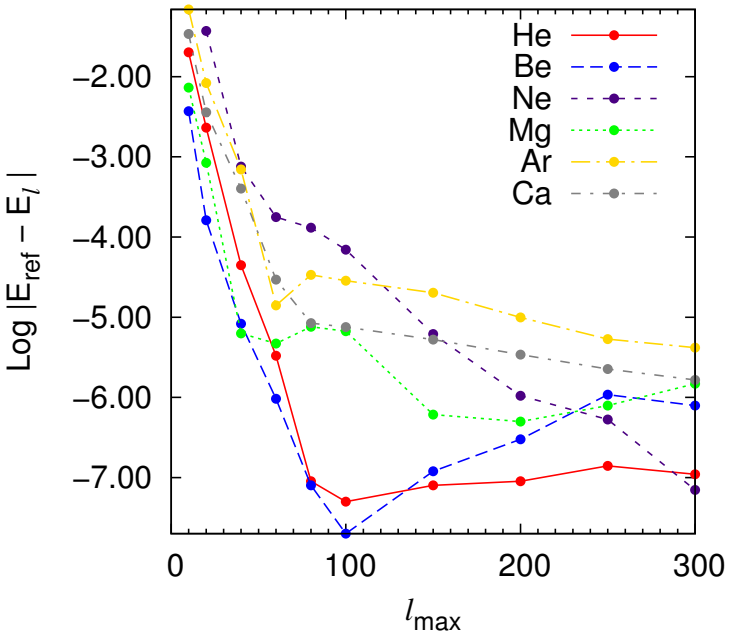

Figure 5.7: Difference between the standard GF2 correlation energy and correlation energy obtained by using Legendre expansion of the self-energy for several closed-shell atoms with aug-cc-pVDZ basis set (cc-pVDZ basis set was used for Ca).

The right panel of Fig. 5.6 shows a zoom in for the region where the expansion coefficients are close to zero. A closer look at the values of Σ_{00}^{l} reveals a numerical noise. This noise is known as Gibbs oscillations [55] and arises when too few imaginary time grid points are used to evaluate higher order Legendre coefficients.

To confirm that Gibbs oscillations are arising from the insufficient number of imaginary time points necessary to resolve high order Legendre coefficients, we evaluated Legendre expansion using 6657 imaginary time points. These coefficients in Fig. 5.6 for H_2O molecule (red line) show no numerical noise when compared to coefficients (light blue line) evaluated using 417 points.

In order to prevent numerical noise buildup affecting very high orders of the Legendre expansion, one should truncate the expansion once oscillations are detected.

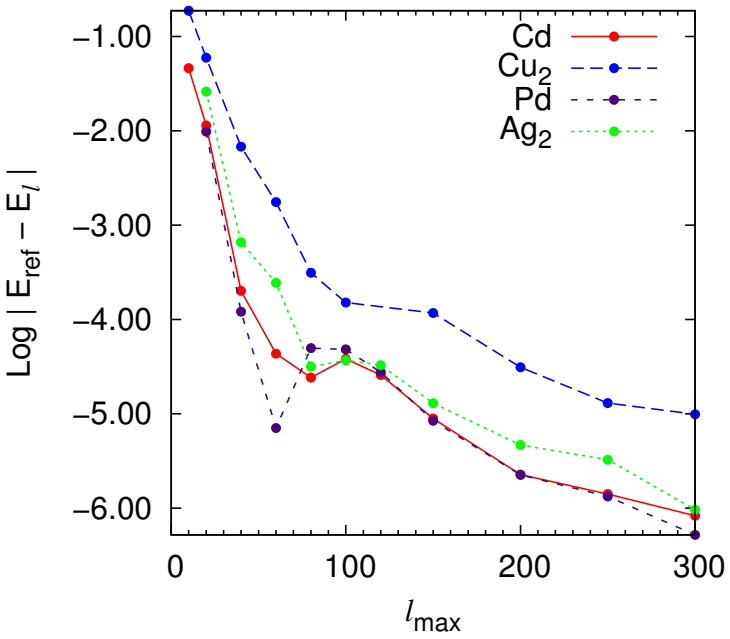

Figure 5.8: Difference between the standard GF2 correlation energy and correlation energy obtained by using Legendre expansion of the self-energy for several transition metal atoms and diatomic clusters with ecp-sdd-DZ basis set.

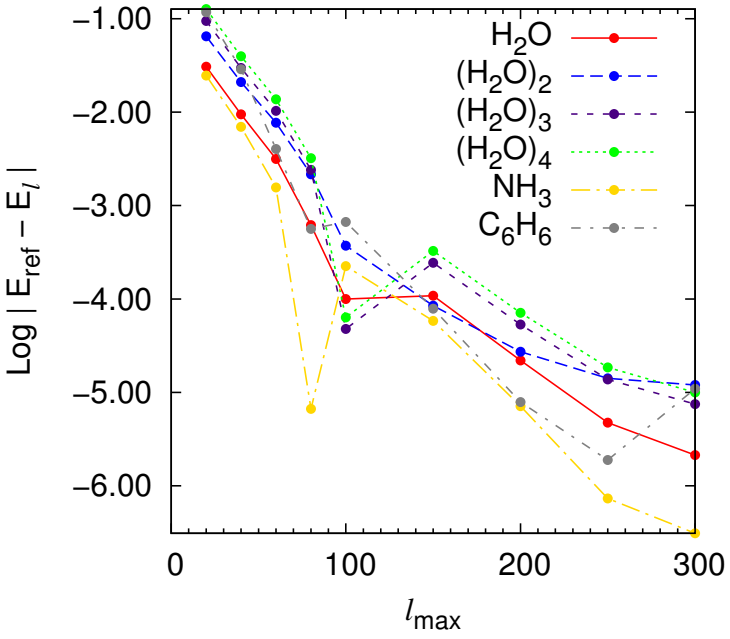

Figure 5.9: Difference between the standard GF2 correlation energy and correlation energy obtained by using Legendre expansion of the self-energy for several small molecules with TZ(Dunning) basis set.

Table 5.1: Error in μE_h of the correlation energy for different number of Legendre expansion coefficients for several atoms and molecules[a].

Atom or molecule	Basis set	Size of Legendre basis		
		l=200	l=100	l=40
He	aug-cc-pVDZ	0	0	−44
Be	aug-cc-pVDZ	0	0	−8
Ne	aug-cc-pVDZ	−1	−70	−177
Mg	aug-cc-pVDZ	1	−7	−6
Ar	aug-cc-pVDZ	−10	−29	697
Ca	cc-pVDZ [56]	−3	−9	401
H_2O[b]	TZ(Dunning) [57]	−22	−100	9478
$(H_2O)_2$[b]	TZ(Dunning)	−27	372	21049
$(H_2O)_3$[b]	TZ(Dunning)	−53	48	29737
$(H_2O)_4$[b]	TZ(Dunning)	−71	63	39669
HCN	TZ(Dunning)	−8	−346	11658
CO_2	TZ(Dunning)	−37	−12	25042
BH_3	DZ(Dunning) [58]	0	78	−2451
CH_4	TZ(Dunning)	−1	−108	4814
C_2H_4	TZ(Dunning)	−3	−218	9591
C_2H_2	TZ(Dunning)	8	−208	9559
MgO	aug-cc-pVDZ	1	19	−168
MgH_2	aug-cc-pVDZ	−1	−16	−40
BN	TZ(Dunning)	−7	−262	9433
NaOH	aug-cc-pVDZ	1	51	−155
LiH	aug-cc-pVDZ	−1	−1	−16
AlH	aug-cc-pVDZ	−1	−19	−39
NaH	aug-cc-pVDZ	0	−11	−35
H_2O_2	TZ(Dunning)	−30	258	20592
H_2CO	TZ(Dunning)	−24	−164	14592
NH_3	TZ(Dunning)	−7	−225	6954
C_6H_6	TZ(Dunning)	−8	−668	28779
Cd	ecp-sdd-DZ	−2	−38	201
Cu_2[c]	ecp-sdd-DZ	−31	−151	6794
Pd	ecp-sdd-DZ	−2	−48	121
Ag_2[d]	ecp-sdd-DZ	−5	−37	659

[a] Experimental geometries were taken from NIST Computational Chemistry Comparison and Benchmark Database [59].
[b] Geometry was taken from Ref. [60].
[c] d(Cu-Cu)=3.63 a.u.
[d] d(Ag-Ag)=5.46 a.u.

Another method is to damp Gibbs oscillations by introducing an integral kernel function [55]. This option has been previously explored in the context of the Hubbard model [41]. The particular choice of integral kernel function depends on several factors and is not convenient, especially if a black-box method is desired.

Motivated by our aspiration to make the user impact minimal, we took the first route and studied how the truncation of the Legendre expansion of the self-energy influences the accuracy of the method. Truncation criteria can be easily implemented and do not require any special care from the user and hence can be introduced as a part of any black-box computational package.

We performed calculations for our test set containing atoms and simple molecules truncating the Legendre series after various number of terms $\Sigma_{ij}^{l} = 0$ for $l > l_{\max}$. Results for a few atoms and molecules are shown in Figs. 5.7−5.9. More results can be found in Tab. 5.1 for $l = 40$, 100, and 200 Legendre polynomials. Our calculations show that only a couple hundred of Legendre expansion coefficients are necessary to yield very accurate results. All these results were calculated using 417 imaginary time points. In all cases very fast convergence was achieved and less then 100 Legendre polynomials were needed to converge correlation energy to 1 $m\mathrm{E}_h$. We observe that for all atoms considered here the correlation energy continues to converge to the reference one and about 200 Legendre polynomials are needed to recover it up to the $\mu\mathrm{E}_h$. Similar observations can be made for calculations involving pseudopotentials and thus our method can be reliably applied to calculations of complex systems containing both transition metals and light atoms. A somewhat slower convergence was observed in the

case of molecular calculations. In this case more than 200 but less than 300 Legendre polynomials were necessary to get within a few μE_h from the reference correlation energy.

In some cases the correlation energy obtained with a larger number of Legendre polynomials happens to be further from the reference correlation energy than the correlation energy obtained with fewer Legendre polynomials. This behavior was observed for Pd atom, when the number of Legendre polynomials changed from 60 to 80, for NH_3 molecule when number of Legendre polynomials changed from 80 to 100, and for $(H_2O)_3$ and $(H_2O)_4$ molecules when number of Legendre polynomials increased from 100 to 150. When very few Legendre coefficients (below 100) are used the convergence of the correlation energy is not monotonic and the correlation energy can show large oscillations and be below or above the reference energy. Once a sufficient number of Legendre polynomials (usually 200−300) is employed the correlation energy reaches a plateau smoothly. We observe that for all examples studied 300 Legendre polynomials were sufficient to reach overall convergence to within 10 μE_h. Small fluctuations in the correlation energy observed in atomic calculations shown in Fig. 5.7 happen only below 1 μE_h and are purely a numerical artifact since the convergence criterion in our GF2 calculations was 1 μE_h.

5.5 Summary and Conclusions

The frequency—time duality is present in many temperature-dependent methods and $\mathbf{G}(i\tau)$ or $\mathbf{\Sigma}(i\tau)$ can be transformed to $\mathbf{G}(i\omega)$ or $\mathbf{\Sigma}(i\omega)$ depending if handling the time or frequency object is more computationally advantageous. Both the frequency and time Green's functions have to be represented on a numerical grid, and thus a small number of grid points is crucial for achieving computational efficiency.

While the construction of imaginary time grids is a well-studied problem and ap-

pears in Laplace-transformed Møller–Plesset (LT-MP2) perturbation theory, such grids are appropriate for the zero-temperature Green's function and cannot be employed to study the temperature-dependent Green's function.

In this Chapter, we have presented a method that makes the transform between imaginary time and imaginary frequency temperature-dependent Green's functions converge much faster with respect to the number of necessary imaginary time points than the traditional uniform and power-law grid. To achieve this goal we have used a combination of a very sparse power-law grid together with an explicit transform based on a Legendre expansion of the self-energy. We have shown that to converge the Legendre coefficients necessary to perform the explicit transform we need an order of magnitude fewer imaginary time points than when doing the numerical Fourier transform.

Moreover, we have also shown that even for realistic systems in basis sets with a significant energy spread only a few hundred (200−300) Legendre coefficients are necessary to reach the accuracy of $\mu \mathrm{E}_h$ when compared with the fully converged result. Overall the orthogonal polynomial representation of the self-energy offers a fast, accurate, and less storage demanding solution for practical realistic calculations.

We have also applied such a representation of the self-energy to the GF2 method resulting in very accurate energies for atoms and molecules while using only a limited number of imaginary time grid points and only couple hundred (200−300) of Legendre expansion coefficients.

While at present no large scale realistic calculations are performed including temperature coming from the electronic effects, due to the increasing interest in new materials, we believe that such calculations will become important in the near future, and thus identifying and overcoming major bottlenecks connected to the efficient representation of the Green's function and self-energy in the imaginary time domain is an important step in this new direction.

Bibliography

[1] A. D. Becke, "A multicenter numerical integration scheme for polyatomic molecules", *J. Chem. Phys.* **88**, 2547 (1988).

[2] C. W. Murray, N. C. Handy, and G. J. Laming, "Quadrature schemes for integrals of density functional theory", *Mol. Phys.* **78**, 997 (1993).

[3] P. M. Gill, B. G. Johnson, and J. A. Pople, "A standard grid for density functional calculations", *Chem. Phys. Lett.* **209**, 506 (1993).

[4] M. E. Mura and P. J. Knowles, "Improved radial grids for quadrature in molecular density-functional calculations", *J. Chem. Phys.* **104**, 9848 (1996).

[5] P. M. W. Gill and S.-H. Chien, "Radial quadrature for multiexponential integrands", *J. Comput. Chem.* **24**, 732 (2003).

[6] J. Almlof, "Elimination of energy denominators in møller-plesset perturbation theory by a Laplace transform approach", *Chem. Phys. Lett.* **181**, 319 (1991).

[7] M. Häser and J. Almlof, "Laplace transform techniques in Møller–Plesset perturbation theory", *J. Chem. Phys.* **96**, 489 (1992).

[8] A. F. Izmaylov and G. E. Scuseria, "Resolution of the identity atomic orbital Laplace transformed second order Moller-Plesset theory for nonconducting periodic systems", *Phys. Chem. Chem. Phys.* **10**, 3421 (2008).

[9] B. Doser, D. S. Lambrecht, and C. Ochsenfeld, "Tighter multipole-based integral estimates and parallel implementation of linear-scaling AO-MP2 theory", *Phys. Chem. Chem. Phys.* **10**, 3335 (2008).

[10] D. Kats, D. Usvyat, and M. Schutz, "On the use of the Laplace transform in local correlation methods", *Phys. Chem. Chem. Phys.* **10**, 3430 (2008).

[11] P. Y. Ayala and G. E. Scuseria, "Linear scaling second-order Moller-Plesset theory in the atomic orbital basis for large molecular systems", *J. Chem. Phys.* **110**, 3660 (1999).

[12] M. Kaltak, J. Klimeš, and G. Kresse, "Low scaling algorithms for the random phase approximation: Imaginary time and Laplace transformations", *J. Chem. Theory Comput.* **10**, 2498 (2014).

[13] M. Bugeanu, R. Di Remigio, K. Mozgawa, S. S. Reine, H. Harbrecht, and L. Frediani, "Wavelet formulation of the polarizable continuum model. II. Use of piecewise bilinear boundary elements", *Phys. Chem. Chem. Phys.* **17**, 31566 (2015).

[14] S. Nagy and J. Pipek, "An economic prediction of the finer resolution level wavelet coefficients in electronic structure calculations", *Phys. Chem. Chem. Phys.* **17**, 31558 (2015).

[15] M. Zuzovski, A. Boag, and A. Natan, "An auxilliary grid method for the calculation of electrostatic terms in density functional theory on a real-space grid", *Phys. Chem. Chem. Phys.* **17**, 31550 (2015).

[16] N. Scott Bobbitt, G. Schofield, C. Lena, and J. R. Chelikowsky, "High order forces and nonlocal operators in a Kohn-Sham Hamiltonian", *Phys. Chem. Chem. Phys.* **17**, 31542 (2015).

[17] H.-J. Flad, G. Harutyunyan, and B.-W. Schulze, "Singular analysis and coupled cluster theory", *Phys. Chem. Chem. Phys.* **17**, 31530 (2015).

[18] D. Chakraborty, S. Kar, and P. K. Chattaraj, "Orbital free DFT versus single density equation: a perspective through quantum domain behavior of a classically chaotic system", *Phys. Chem. Chem. Phys.* **17**, 31516 (2015).

[19] A. Natan, "Fock-exchange for periodic structures in the real-space formalism and the KLI approximation", *Phys. Chem. Chem. Phys.* **17**, 31510 (2015).

[20] V. Khoromskaia and B. N. Khoromskij, "Tensor numerical methods in quantum chemistry: from Hartree-Fock to excitation energies", *Phys. Chem. Chem. Phys.* **17**, 31491 (2015).

[21] E. A. Toivanen, S. A. Losilla, and D. Sundholm, "The grid-based fast multipole method - a massively parallel numerical scheme for calculating two-electron interaction energies", *Phys. Chem. Chem. Phys.* **17**, 31480 (2015).

[22] T. L. Beck, "A real-space stochastic density matrix approach for density functional electronic structure", *Phys. Chem. Chem. Phys.* **17**, 31472 (2015).

[23] L. A. Espinosa Leal, A. Karpenko, M. A. Caro, and O. Lopez-Acevedo, "Optimizing a parametrized Thomas-Fermi-Dirac-Weizsacker density functional for atoms", *Phys. Chem. Chem. Phys.* **17**, 31463 (2015).

[24] S. Mohr, L. E. Ratcliff, L. Genovese, D. Caliste, P. Boulanger, S. Goedecker, and T. Deutsch, "Accurate and efficient linear scaling DFT calculations with universal applicability", *Phys. Chem. Chem. Phys.* **17**, 31360 (2015).

[25] J. S. Kottmann, S. Hofener, and F. A. Bischoff, "Numerically accurate linear response-properties in the configuration-interaction singles (CIS) approximation", *Phys. Chem. Chem. Phys.* **17**, 31453 (2015).

[26] E. Tsuchida, Y.-K. Choe, and T. Ohkubo, "An adaptive finite-element method for large-scale ab initio molecular dynamics simulations", *Phys. Chem. Chem. Phys.* **17**, 31444 (2015).

[27] J. Kim, K. Hong, S. Choi, S.-Y. Hwang, and W. Youn Kim, "Configuration interaction singles based on the real-space numerical grid method: Kohn-Sham versus Hartree-Fock orbitals", *Phys. Chem. Chem. Phys.* **17**, 31434 (2015).

[28] A. Nakata, D. R. Bowler, and T. Miyazaki, "Optimized multi-site local orbitals in the large-scale DFT program CONQUEST", *Phys. Chem. Chem. Phys.* **17**, 31427 (2015).

[29] D. Baye and J. Dohet-Eraly, "Confined helium on Lagrange meshes", *Phys. Chem. Chem. Phys.* **17**, 31417 (2015).

[30] X. Andrade, D. Strubbe, U. De Giovannini, A. H. Larsen, M. J. T. Oliveira, J. Alberdi-Rodriguez, A. Varas, I. Theophilou, N. Helbig, M. J. Verstraete, L. Stella, F. Nogueira, A. Aspuru-Guzik, A. Castro, M. A. L. Marques, and A. Rubio, "Real-space grids and the Octopus code as tools for the development of new simulation approaches for electronic systems", *Phys. Chem. Chem. Phys.* **17**, 31371 (2015).

[31] T. Yanai, G. I. Fann, G. Beylkin, and R. J. Harrison, "Multiresolution quantum chemistry in multiwavelet bases: excited states from time-dependent Hartree-Fock and density functional theory via linear response", *Phys. Chem. Chem. Phys.* **17**, 31405 (2015).

[32] W. Hu, L. Lin, and C. Yang, "Edge reconstruction in armchair phosphorene nanoribbons revealed by discontinuous Galerkin density functional theory", *Phys. Chem. Chem. Phys.* **17**, 31397 (2015).

[33] L. Boehnke, H. Hafermann, M. Ferrero, F. Lechermann, and O. Parcollet, "Orthogonal polynomial representation of imaginary-time Green's functions", *Phys. Rev. B* **84**, 075145 (2011).

[34] H. N. Rojas, R. W. Godby, and R. J. Needs, "Space-time method for *Ab Initio* calculations of self-energies and dielectric response functions of solids", *Phys. Rev. Lett.* **74**, 1827 (1995).

[35] D. Foerster, P. Koval, and D. Sánchez-Portal, "An O(N3) implementation of hedin's GW approximation for molecules", *J. Chem. Phys.* **135**, 074105 (2011).

[36] E. Gull, A. J. Millis, A. I. Lichtenstein, A. N. Rubtsov, M. Troyer, and P. Werner, "Continuous-time Monte Carlo methods for quantum impurity models", *Rev. Mod. Phys.* **83**, 349 (2011).

[37] J. J. Phillips and D. Zgid, "Communication: The description of strong correlation within self-consistent Green's function second-order perturbation theory", *J. Chem. Phys.* **140**, 241101 (2014).

[38] A. A. Kananenka, E. Gull, and D. Zgid, "Systematically improvable multiscale solver for correlated electron systems", *Phys. Rev. B* **91**, 121111 (2015).

[39] J. J. Phillips, A. A. Kananenka, and D. Zgid, "Fractional charge and spin errors in self-consistent Green's function theory", *J. Chem. Phys.* **142**, 194108 (2015).

[40] M. Abramowitz and I. A. Stegun (Editors), *Handbook of Mathematical Functions with Formulas, Graphs, and Mathematical Tables*, Vol. 55, U.S. National Bureau of Standards: Washington, DC, USA, 10th ed. (1972).

[41] H. Li and D. Liang, "Kernel polynomial representation of imaginary-time Green's functions", *arXiv:1205.2791* (2012).

[42] P. Werner, A. Comanac, L. de' Medici, M. Troyer, and A. J. Millis, "Continuous-time solver for quantum impurity models", *Phys. Rev. Lett.* **97**, 076405 (2006).

[43] P. Werner and A. J. Millis, "Hybridization expansion impurity solver: General formulation and application to Kondo lattice and two-orbital models", *Phys. Rev. B* **74**, 155107 (2006).

[44] L.-F. Arsenault, A. Lopez-Bezanilla, O. A. von Lilienfeld, and A. J. Millis, "Machine learning for many-body physics: The case of the Anderson impurity model", *Phys. Rev. B* **90**, 155136 (2014).

[45] W. Quan-Sheng, W. Yi-Lin, F. Zhong, and D. Xi, "Acceleration of the stochastic analytic continuation method via an orthogonal polynomial representation of the spectral function", *Chin. Phys. Lett.* **30**, 090201 (2013).

[46] W. Ku and A. G. Eguiluz, "Band-gap problem in semiconductors revisited: Effects of core states and many-body self-consistency", *Phys. Rev. Lett.* **89**, 126401 (2002).

[47] D. E. Woon and T. H. Dunning, "Gaussian basis sets for use in correlated molecular calculations. IV. Calculation of static electrical response properties", *J. Chem. Phys.* **100**, 2975 (1994).

[48] T. H. Dunning, "Gaussian basis sets for use in correlated molecular calculations. I. The atoms boron through neon and hydrogen", *J. Chem. Phys.* **90**, 1007 (1989).

[49] D. E. Woon and T. H. Dunning, "Gaussian basis sets for use in correlated molecular calculations. III. The atoms aluminum through argon", *J. Chem. Phys.* **98**, 1358 (1993).

[50] A. L. Fetter and J. D. Walecka, *Quantum Theory of Many-Particle Systems*, Dover Publications Inc.: Mineola, NY, USA (2003).

[51] M. Dolg, U. Wedig, H. Stoll, and H. Preuss, "Energy-adjusted ab initio pseudopotentials for the first row transition elements", *J. Chem. Phys.* **86**, 866 (1987).

[52] H. Stoll, P. Fuentealba, M. Dolg, J. Flad, L. v. Szentpály, and H. Preuss, "Cu and Ag as one-valence-electron atoms: Pseudopotential results for Cu_2, Ag_2, CuH, AgH, and the corresponding cations", *J. Chem. Phys.* **79**, 5532 (1983).

[53] D. Feller, "The role of databases in support of computational chemistry calculations", *J. Comput. Chem.* **17**, 1571 (1996).

[54] K. L. Schuchardt, B. T. Didier, T. Elsethagen, L. Sun, V. Gurumoorthi, J. Chase, J. Li, and T. L. Windus, "Basis set exchange: a community database for computational sciences", *J. Chem. Inf. Model.* **47**, 1045 (2007).

[55] A. Weiße, G. Wellein, A. Alvermann, and H. Fehske, "The kernel polynomial method", *Rev. Mod. Phys.* **78**, 275 (2006).

[56] J. Koput and K. A. Peterson, "Ab initio potential energy surface and vibrational-rotational energy levels of X2σ^+ CaOH", *J. Phys. Chem. A* **106**, 9595 (2002).

[57] T. H. Dunning, "Gaussian basis functions for use in molecular calculations. III. Contraction of (10s6p) atomic basis sets for the first-row atoms", *J. Chem. Phys.* **55**, 716 (1971).

[58] T. H. Dunning, "Gaussian basis functions for use in molecular calculations. I. Contraction of (9s5p) atomic basis sets for the firstrow atoms", *J. Chem. Phys.* **53**, 2823 (1970).

[59] R. D. Johnson, "NIST Computational Chemistry Comparison and Benchmark Database", Standard Reference Database Number 101 Release 16a.

[60] D. J. Wales and M. P. Hodges, "Global minima of water clusters $(H_2O)_n$, n$\leq$21, described by an empirical potential", *Chem. Phys. Lett.* **286**, 65 (1998).

Chapter 6

Efficient temperature-dependent Green's function methods for realistic systems: using cubic spline interpolation to approximate Matsubara Green's functions

A. A. Kananenka, A. R. Welden, T. N. Lan, E. Gull and D. Zgid

Journal of Chemical Theory and Computation, **12 (5)** 2250–2259 (2016)

6.1 Introduction

Finite-temperature Green's function calculations have a long history in condensed matter physics [1–4]. Most commonly the finite-temperature formalism is employed to study low-energy effective models, such as the Hubbard [5] model, either by numerical or analytical means [6–10]. Much less is known about employing finite-temperature Green's functions for realistic systems while maintaining "chemical accuracy" of 1 kcal·mol^{-1}. In quantum chemistry, or in any realistic calculations beyond model systems, the eigenvalue spread of realistic Hamiltonians is very broad; thus, the finite-temperature Green's function formalism, when applied to realistic problems, has to describe energy levels far outside the window described by model Hamiltonians. This makes the realistic calculations much more challenging than the model ones. In prac-

tical calculations, temperature-dependent Green's functions are expressed as functions of imaginary time or imaginary frequency (Matsubara Green's function) that are mutually connected by a Fourier transform. Both imaginary time and Matsubara Green's functions are discretized on imaginary time and imaginary frequency grid, yielding $G(1:N,1:N,1:N_\tau)$ and $G(1:N,1:N,1:N_\omega)$ matrices, where N, N_τ, and N_ω are the number of orbitals, imaginary time, and imaginary frequency grid points, respectively. The size of these grids depends on the energy spread of a system and the temperature-dependent grid spacing. Since realistic Hamiltonians have a wide spread of orbital energies, both grids need to contain hundreds of thousands of grid points to reach high numerical accuracy at low temperatures that result in small grid spacing. Even though in a parallel calculation each grid point can be processed independently, computation requirements are still very high and both the time and memory necessary to handle Green's function operations grow steeply. Thus, for accurate and affordable realistic calculations, it is highly desirable to find compact representations of both imaginary time and Matsubara Green's functions.

Recently, Boehnke *et al.* [11] employed orthogonal polynomial representation of Green's functions to compactly express Hubbard Green's functions. Using this approach for realistic systems, we have shown that very accurate results can be obtained exploiting only a fraction of the original imaginary time grid points necessary to illustrate the energy spread of the realistic Hamiltonian [12]. In practical calculations, since many Green's functions manipulations are easier in frequency space it is important to have a compact representation of the Matsubara Green's function. In this Chapter, we focus on finding a representation that will result in using compact Matsubara frequency grids for realistic problems.

The regular imaginary frequency Matsubara grid is equidistant and the grid spacing is directly related to the physical temperature. Let us note, however, that while the grid spacing for low frequencies is essential to illustrate the physical temperature, for

larger frequencies the Green's function is a slowly and smoothly changing function of frequency. Consequently, it should be possible to keep the original spacing for few frequency points near zero and have a prescription to systematically evaluate more points for higher frequencies with larger than the near-zero spacing without any loss of accuracy.

Since the Matsubara Green's function or self-energy is smoothly and slowly changing between grid points, numerical interpolation is especially suitable to accurately describe it. Linear interpolation is the simplest choice but it lacks smoothness. While a polynomial of higher degree may be used to interpolate and ensures smoothness, this type of interpolation may result in large Runge oscillations between the data points. Consequently, we decided to employ spline interpolation using cubic polynomials over a polynomial interpolation since it will result in a procedure with much smaller interpolation errors, greater stability and low computational cost.

In chemical physics, cubic spline interpolation has been applied as a basis to solve a complex differential and integral Schrödinger [13–15], Dirac [16], and Sham–Schlüter Equations [17], Thomas–Fermi model [18], in calculations of vibrational and rotational spectra [19] and many other cases [20–32]. Since the derivatives of third and higher order polynomials are discontinuous, cubic spline interpolation is limited to applications that are not sensitive to the smoothness of derivatives higher than second order. Applications of cubic spline interpolation algorithm in Green's function theory are known in the context of dynamical mean-field theory (DMFT) [8, 33, 34].

Finally, cubic spline interpolation algorithm is popular because it is very easy to implement and use. Several libraries provide built-in functions for cubic spline interpolation. For example, FORTRAN provides both procedural and object-oriented interfaces for the FITPACK library [35].

This Chapter is organized as follows. In Section 6.2, we shortly review the background necessary to understand finite-temperature Green's functions and our motiva-

tion behind applying them to realistic calculations. Additionally, we focus on illustrating the difficulties of extending the Green's function approach to large basis sets used in chemistry. In Section 6.3, we describe the spline interpolation procedure that we use for realistic systems and its implementation in the second-order Green's function theory. We list and discuss the numerical results of our algorithm as applied to realistic atomic and molecular calculations in Section 6.4. Finally, we present conclusions in Section 6.5.

6.2 Theory

In this section, we briefly review some aspects of fermionic Green's function theory relevant to this work. For a more detailed introduction to Green's function theory readers are suggested to consult textbooks on the subject, see e. g. Refs. [1, 4, 36].

First, let us note that Green's functions can be expressed in the real or imaginary frequency domain. In general a real time or real frequency one-body Green's function is a function used to describe spectral properties such as ionization potentials, electron affinities, or the single-particle spectral function. Methods such as the random phase approximation (RPA) and GW usually express the Green's function using real frequencies to obtain spectra at zero temperature [37, 38]. The real frequency zero-temperature Green's function is a rational function in the complex plane. Its low energy behavior can often be approximated by a series of relatively few appropriately chosen exponentially decaying terms [37]. However, the rational structure implies the existence of poles, for which iterative algorithms (such as the DMFT or the self-energy embedding theory (SEET) [39, 40]) require pole shifting algorithms [41–43]. Iterating zero-temperature Green's functions in this way has proven to be difficult, and we therefore employ the finite-temperature formulation in which these problems are absent.

The imaginary frequency Matsubara Green's function $\mathbf{G}(i\omega_n)$ is used to describe

single-particle properties of a statistical ensemble where many excited states (besides the ground state) are potentially accessible at a given finite temperature. While not commonly employed in molecular quantum chemistry calculations, such Green's functions are desirable for materials science calculations where a small electronic band gap allows multiple electronic states to be populated even at low temperatures. The Matsubara Green's function is expressed on the imaginary grid $i\omega_n = (2n+1)\pi/\beta$ [44], where $n = 0, 1, 2, ...$, $\beta = 1/(k_{\mathrm{B}}T)$ is the inverse temperature, and k_{B} is the Boltzmann constant. Note that the $2\frac{\pi}{\beta}$ spacing of the grid is set by the physical temperature T. Using such a grid, the Matsubara Green's function is then defined as

$$\mathbf{G}(i\omega_n) = \left[(i\omega_n + \mu)\mathbf{S} - \mathbf{F} - \mathbf{\Sigma}(i\omega_n)\right]^{-1}, \tag{6.1}$$

where $\mathbf{S}$ and $\mathbf{F}$ are the overlap and Fock matrices correspondingly, and μ is the chemical potential chosen such that a proper number of electrons is present in the system. The self-energy $\mathbf{\Sigma}(i\omega_n)$ is a correction to the noninteracting Green's function $\mathbf{G}_0(i\omega_n) = [(i\omega_n + \mu)\mathbf{S} - \mathbf{F}]^{-1}$ describing static and dynamical many-body correlation effects at the single-particle level.

Both real and imaginary parts of the Green's function on a Matsubara grid are smooth and converge to zero in the limit of large frequencies. In this high-frequency limit, $i\omega_n \to \infty$, the Matsubara Green's function can be expressed as a series

$$\mathbf{G}(i\omega_n) = \frac{\mathbf{G}_1}{i\omega_n} + \frac{\mathbf{G}_2}{(i\omega_n)^2} + \frac{\mathbf{G}_3}{(i\omega_n)^3} + \mathcal{O}\left(\frac{1}{(i\omega_n)^4}\right), \tag{6.2}$$

with the expansion coefficients given by

$$[G_k]_{ij} = (-1)^{(k-1)}\langle\Psi|\{\left[\hat{H}, \hat{c}_i\right]_k, \hat{c}_j^\dagger\}|\Psi\rangle, \tag{6.3}$$

where $|\Psi\rangle$ is the Heisenberg ground state of the system, $\hat{H}$ is the full many-body

Hamiltonian of the system

$$\hat{H} = \sum_{ij}^{N} h_{ij} \hat{c}_i^\dagger \hat{c}_j + \frac{1}{2} \sum_{ijkl}^{N} v_{ijkl} \hat{c}_i^\dagger \hat{c}_k^\dagger \hat{c}_l \hat{c}_j, \tag{6.4}$$

where $\hat{c}_i$ ($\hat{c}_i^\dagger$) is the electron annihilation (creation) operator from orbital i, h_{ij} is the one-body part of the Hamiltonian

$$h_{ij} = \int d\mathbf{r}_1 \phi_i^*(\mathbf{r}_1) \left(-\frac{1}{2} \nabla_{\mathbf{r}_1}^2 - \sum_A \frac{Z_A}{|\mathbf{r}_1 - \mathbf{R}_A|} \right) \phi_j(\mathbf{r}_1), \tag{6.5}$$

and v_{ijkl} are two-electron integrals defined as

$$v_{ijkl} = \int \int d\mathbf{r}_1 d\mathbf{r}_2 \phi_i^*(\mathbf{r}_1) \phi_j(\mathbf{r}_1) \frac{1}{r_{12}} \phi_k^*(\mathbf{r}_2) \phi_l(\mathbf{r}_2). \tag{6.6}$$

It was shown in Ref. [45] that the coefficients of high-frequency expansion in a non-orthogonal orbital basis for Hamiltonians with full Coulomb interactions are given by

$$\mathbf{G}_1 = \mathbf{S}^{-1}, \tag{6.7}$$

$$\mathbf{G}_2 = \mathbf{S}^{-1} \left(\mathbf{F} - \mu \mathbf{S} \right) \mathbf{S}^{-1}. \tag{6.8}$$

In a typical calculation, see Fig. 6.1, the self-energy $\mathbf{\Sigma}$ is evaluated either on the Matsubara frequency or imaginary time grid by a variety of solvers ranging from quantum Monte Carlo methods [7, 46–48] to perturbative [49–54] and configuration interaction type of methods [55, 56]. In the next step, a Green's function is calculated by means of the Dyson equation

$$\mathbf{G}(i\omega_n)^{-1} = \mathbf{G}_0(i\omega_n)^{-1} - \mathbf{\Sigma}(i\omega_n). \tag{6.9}$$

Using the correlated Green's function and self-energy, one evaluates quantities of

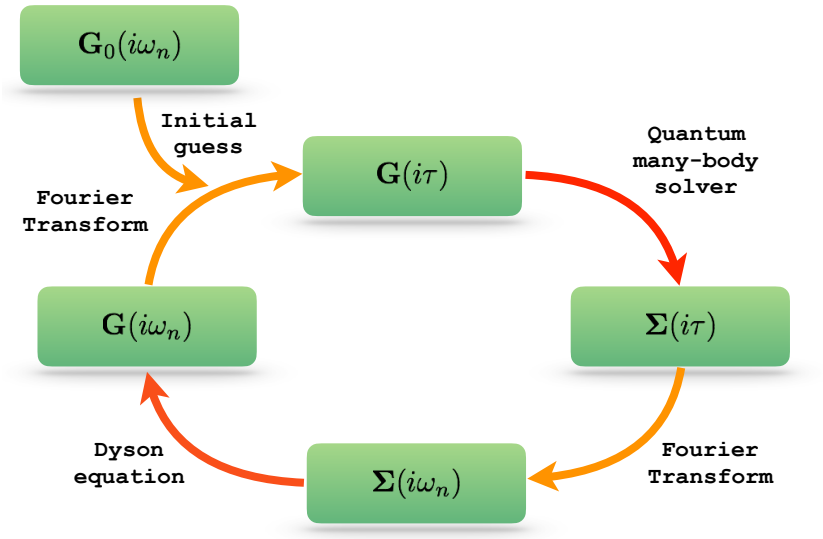

Figure 6.1: A typical self-consistent Green's function calculation consists of the following steps. Generating an initial guess is followed by the Fourier transform from the Matsubara domain to the imaginary time domain. Then a quantum many-body problem is solved using a many-body solver. This step is usually done in the imaginary time domain. The inverse Fourier transform back to the Matsubara domain and solution of the Dyson equation conclude the iteration and the next iteration starts with updated Green's function. The most computationally expensive steps are the solution of quantum many-body problem and the solution of the Dyson equation.

interest such as the one-particle density matrix

$$\mathbf{P} = \frac{2}{\beta} \sum_{n}^{N_\omega} e^{i\omega_n 0^+} \mathbf{G}(i\omega_n), \tag{6.10}$$

and using it the correlated one-body energy

$$E_{1\mathrm{b}} = \frac{1}{2} \mathrm{Tr} \left[(\mathbf{h} + \mathbf{F}) \, \mathbf{P} \right], \tag{6.11}$$

where $\mathbf{h}$ is the one-body part of the Hamiltonian.

Different prescriptions can be used to compute the two-body correlation energy $E_{2\mathrm{b}}$. The Galitskii–Migdal formula [57] is used to evaluate the internal energy

$$E_{2\mathrm{b}}^{\mathrm{GM}} = \frac{2}{\beta} \sum_{n}^{N_\omega} \mathrm{Tr} \left[\mathbf{G}(i\omega_n) \mathbf{\Sigma}(i\omega_n) \right], \tag{6.12}$$

where N_ω is the total number of imaginary frequencies. Similarly, the Luttinger–Ward [58] functional Φ consisting of irreducible energy diagrams of the self-energy can be used to calculate the grand-canonical potential

$$\Omega[\mathbf{G}] = \mathrm{Tr} \left[\ln \left(\mathbf{\Sigma} - \mathbf{G}_0^{-1} \right) + \mathbf{\Sigma G} \right] - \Phi[\mathbf{G}], \tag{6.13}$$

which at low temperatures reduces to $\Omega = E - \mu N_{\mathrm{el}}$, where $E = E_{1\mathrm{b}} + E_{2\mathrm{b}}$ is the internal energy and N_{el} is the total number of electrons in the system. For higher temperatures, $\Omega = E - TS - \mu N_{\mathrm{el}}$ can be used to find the free energy and thermodynamic properties of the system under study. For self-consistent calculations at low temperature the stationary value of Ω corresponds to the energy obtained from Galitskii–Migdal formula up to a shift of μN_{el}.

In practical calculations, a finite number of imaginary frequencies N_ω is used to span the Matsubara Green's function. Insufficient size of the Matsubara frequency

grid leads to errors in the one- and two-body energy as well as the one-particle density matrix.

A practical way to decide how many frequencies have to be used to represent the Matsubara Green's function before applying the high-frequency expansion can be based on measuring the distance between the inverse of the overlap matrix $\mathbf{S}^{-1}$ and the numerically evaluated coefficient of high-frequency expansion of Green's function $\mathbf{G}_1 = \mathbf{G}(i\omega_n) \cdot i\omega_n$. In the limit of infinite number of Matsubara frequencies $\mathbf{D}_{\mathbf{G}_1} = \lim_{N_\omega \to \infty} (\mathbf{G}(i\omega_n) \cdot i\omega_n - \mathbf{S}^{-1}) \to \mathbb{0}$. A finite number of Matsubara frequencies always results in an error. To illustrate the magnitude of this error, we plot in the left panel of Fig. 6.2 the Frobenius norm $||\mathbf{D}_{\mathbf{G}_1}||_{\mathrm{F}} \equiv \sqrt{\sum_i^m \sum_j^n |(D_{G_1})_{ij}|^2}$ of $\mathbf{D}_{\mathbf{G}_1}$ as a function of the number of Matsubara frequencies N_ω for seven realistic atomic and molecular systems. After an initial plateau, where no improvement is seen, the Frobenius norm starts to decay linearly in the logarithmic plot. Consequently, to reduce the error in the Frobenius norm by an order of magnitude, an order of magnitude more Matsubara frequencies is necessary. The right panel of Fig. 6.2 shows the convergence of $||\mathbf{D}_{\mathbf{G}_1}||_{\mathrm{F}}$ as a function of a basis set for the Kr atom. Generally, employing larger basis sets or adding diffuse functions requires an increase of the number of Matsubara frequencies. This is due to the fact that the spread of Hamiltonian eigenvalues increases as larger basis sets are used. Thus, the fastest decay of $||\mathbf{D}_{\mathbf{G}_1}||_{\mathrm{F}}$ is observed in cc-pVDZ [59] basis with 27 basis function and the slowest in the aug-cc-pVQZ [59] with 97 functions. Note that even when a basis with a pseudopotential that has only basis functions describing the valence orbitals is employed, to be in the linear regime requires more than 10,000 frequencies.

During a calculation, the Matsubara Green's function may need to be stored in memory. Storing a single Green's function requires $\mathcal{O}(N_\omega N^2)$ complex double precision numbers, where N is the number of orbitals in a basis set. Thus, for the large orbital bases and large number of frequencies necessary to reach quantum chemical

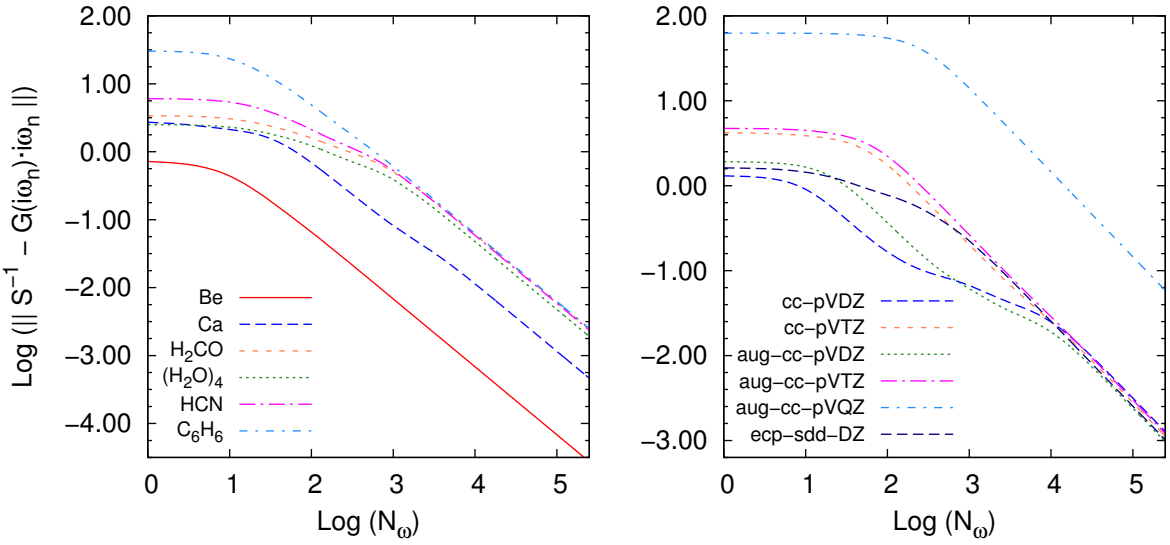

Figure 6.2: Left panel: The convergence of $||\mathbf{D}_{\mathbf{G}_1}||_{\mathrm{F}}$ for the Hartree–Fock Green's function as a function of the number of Matsubara frequencies. We used aug-cc-pVDZ basis set for Be, cc-pVDZ [60] basis set for Ca and TZ(Dunning) [61] basis set for molecules. Right panel: The effect of the basis set on the convergence of $||\mathbf{D}_{\mathbf{G}_1}||_{\mathrm{F}}$ for the Kr atom, β=100 [1/a.u.]. Log denotes the base 10 logarithm.

quantitative accuracy, the required memory becomes a significant bottleneck. Even if the memory bottleneck is avoided and the Green's function is evaluated one the fly, when necessary, the computational complexity of all operations involving the Green's functions grows rapidly with the number of Matsubara frequencies. Examples of such operations include solving the Dyson equation 8.15, which requires $\mathcal{O}(N_\omega N^3)$ evaluations. Even if all these operations can be made parallel over the frequency index, having to take into account this large number of Matsubara frequencies can significantly slow down a computation.

To see why the frequency grid requirements are so demanding when chemical accuracy is desired, it is instructive to look at Matsubara Green's functions evaluated in large basis sets. In the left panel of Fig. 6.3, we plotted several of the largest elements of the imaginary part of the Matsubara Green's function for the H_2CO molecule calculated using the second-order Green's function theory (GF2) [51, 52, 62] with TZ(Dunning)

basis set. In the right panel of Fig. 6.3, we plotted several largest matrix elements of the real part of the Matsubara Green's function for the H_2CO molecule. First, let us note that different elements of $[G(i\omega_n)]_{ij}$ decay differently. Secondly, as expected, the

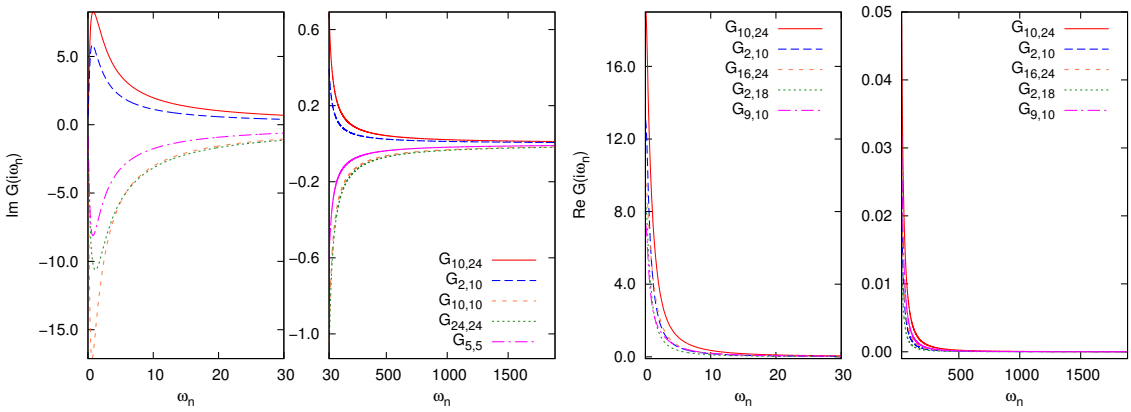

Figure 6.3: The five largest elements of Im$\mathbf{G}(i\omega_n)$ (left two plots) and the five largest matrix elements of Re$\mathbf{G}(i\omega_n)$ (right two plots) for H_2CO molecule calculated with the second-order Green's function perturbation theory GF2 with TZ(Dunning) basis set and β=100 [1/a.u.]. Note that the frequency axis of the Im$\mathbf{G}(i\omega_n)$ and Re$\mathbf{G}(i\omega_n)$ is discontinuous to show that the most rapid change of the Green's function happens in the low-frequency range while for the remaining frequencies the Green's function converges slowly to the high-frequency limit.

most rapid change in both real and imaginary parts of the Green's function occurs in the low-frequency range. Lastly, the slow convergence of the Green's function to its high-frequency limit is responsible for the large Matsubara grid when low temperatures are used. Similar observations can be made about the convergence of sums involving Matsubara frequencies [63, 64].

Motivated by these observations, in the next section we will compute the Matsubara Green's function for only a few low-frequency points to preserve the temperature dependence and have various interpolation techniques to approximate values of the Green's function for higher frequencies.

6.2.1 Spline interpolation

We adopted the commonly used cubic spline interpolation technique and modified it appropriately for the efficient use in Green's function calculations. For the description of a standard cubic spline interpolation, readers are referred to textbooks on numerical methods, e.g. Refs. [65, 66].

We consider a subset of Matsubara frequencies $\mathcal{S} = \{i\omega_n | n \in [0, N_\omega]\}$ chosen from original equidistant Matsubara grid and Green's function $G_{ij}(i\omega_n)$ evaluated on this subset. We focus on a particular frequency interval $[\omega_l, \omega_{l+1}], \omega_l, \omega_{l+1} \in \mathcal{S}$. We define a local polynomial between interval endpoints as a modified Legendre interpolation formula

$$\tilde{G}(i\omega_n) = aG(i\omega_l) + bG(i\omega_{l+1}) + cG''(i\omega_l) + dG''(i\omega_{l+1}), \tag{6.14}$$

where $n \in [l, l+1]$, $G''(i\omega_l)$ is the second derivative of Green's function at the point $i\omega_l$, and a, b, c, d are interpolation coefficients determined as

$$a = \frac{i\omega_{l+1} - i\omega_n}{i\omega_{l+1} - i\omega_l}, \tag{6.15}$$

$$b = \frac{i\omega_n - i\omega_l}{i\omega_{l+1} - i\omega_l}, \tag{6.16}$$

$$c = \frac{1}{6}\left(a^3 - a\right)\left(i\omega_{l+1} - i\omega_l\right)^2, \tag{6.17}$$

$$d = \frac{1}{6}\left(b^3 - b\right)\left(i\omega_{l+1} - i\omega_l\right)^2. \tag{6.18}$$

Polynomials $\tilde{G}(i\omega_n)$ from all intervals $[i\omega_l, i\omega_m] \subset [i\pi/\beta, i\omega_{N_\omega}]$ can be combined and used as an approximation to the Green's function $G(i\omega_n)$. Equation 6.14 generates continuous second derivatives both within the interval and at its boundaries, thus making a smooth transition between intervals, but approximating the third derivatives by a constant. Note, that a simple linear interpolation is not a good choice here

because the second derivative is undefined at the boundaries of the intervals and is zero inside. A construction of a local polynomial (Eq. 6.14) requires the knowledge of second derivatives for every given point $i\omega_l$. Analytical second derivatives are not available for a correlated Matsubara Green's function and numerical derivatives must be used. The second derivatives can be approximated, for example, using central difference formula

$$G''(i\omega_l) = \frac{G(i\omega_l + \zeta) - 2G(i\omega_l) - G(i\omega_l - \zeta)}{2\zeta}, \tag{6.19}$$

where ζ is a small increment. An application of the central difference formula for every interval results in the following $M-2$ equations for second derivatives

$$\begin{aligned} &\frac{i\omega_l - i\omega_{l-1}}{6} G''_{l-1} + \frac{i\omega_{l+1} - i\omega_{l-1}}{3} G''_l + \frac{i\omega_{l+1} - i\omega_l}{6} G''_{l+1} = \\ =&\frac{G''(i\omega_{l+1}) - G''(i\omega_l)}{i\omega_{l+1} - i\omega_l} - \frac{G''(i\omega_l) - G''(i\omega_{l-1})}{i\omega_l - i\omega_{l-1}}. \end{aligned} \tag{6.20}$$

Since there are only $M-2$ equations for M unknowns to find a unique solution two more equations have to be provided. In this work we chose to simply set second derivatives at global boundaries to zero $G''(i\omega_{n=0}) = 0$ and $G''(i\omega_{n=N_\omega}) = 0$. In the numerical analysis literature, it is known as a natural spline [65]. Now, the resulting M equations can be written as a matrix equation and finding second derivatives amounts to solving a system of linear equations. Since the coefficient matrix is tridiagonal there is a unique solution that can be obtained in $\mathcal{O}(M)$ operations using a sparse linear solver.

Once the second derivatives are known and coefficients $a, \ldots, d$ are calculated, the Green's function can be reconstructed using Eq. 6.14 at any requested frequency point. Our algorithm consists of the following basic steps:

1. We begin by choosing a small number of grid points explicitly and forming a small preliminary grid that usually does not exceed a few hundred points. Most of these points are located near zero frequency and preserve the natural Matsubara spacing to encode information about the inverse temperature β. It is not particularly important how the points are chosen further away from zero frequency because later, iteratively, more points are added when necessary. However, to keep the number of operations small it is recommended to take advantage of the shape of Green's function and create a denser grid in the low-frequency region and a sparser grid everywhere else.

2. At these preliminary grid points we evaluate the Green's function $G(i\omega)$.

3. For every pair of labels ij of the Green's function $[G(i\omega)]$, we solve a system of Eqs. 6.20 for second derivatives in every interval between adjacent grid points and use it to infer the magnitude of change of the Green's function.

4. Since we use cubic polynomials the forth derivative $|G^{IV}|$ must vanish. We calculate and compare the absolute value of $|G^{IV}|$ to the predetermined desired threshold value δ. If $|G^{IV}| < \delta$ then the Green's function does not change on the $[i\omega_l, i\omega_{l+1}]$ interval appreciably and no more frequency points should be added, otherwise a midpoint $i\omega_{(2l+1)/2}$ is inserted.

5. We evaluate and store the Green's function at the midpoint frequency $G(i\omega_{(2l+1)/2})$.

6. We repeat step 3 until $|G^{IV}|$ indicate that the Green's function does not change anymore on every interval for all the ij labels.

Depending on the value of δ a different number of imaginary frequency points are selected and hence the accuracy of the spline can be systematically improved by decreasing δ.

Since the Matsubara Green's function is a complex quantity the cubic spline interpolation algorithm can be applied to either real or imaginary part of it. The real part of the Green's function contributes to the density matrix and the one-body energy. The imaginary part of the Green's function influences the two-body energy. We observed that an insufficient grid causes the largest error in the density matrix and consequently the one-body energy. For this reason, we decided to apply the cubic spline interpolation algorithm to the real part of Green's function to minimize δ and we use the resulting grid to evaluate both the real and imaginary part of the Green's function.

6.3 Computational details

The algorithm for creating a Green's function spline introduced above is suitable for calculating Green's functions or self-energies in a systematic manner and improving its accuracy as a function of the spline accuracy δ and the grid size. In this Chapter, we tested this algorithm on a series of Green's functions coming from GF2 calculations. GF2 is a perturbative many-body Green's function method that has many attractive properties. It is as accurate as Møller–Plesset perturbation theory (MP2) [67] for weakly correlated systems but, unlike many methods suitable for weakly correlated systems such as MP2 or CCSD [68], it is reasonably well behaved for strongly correlated systems [52]. GF2 has both small fractional charge and fractional spin errors [69], affordable computational scaling $\mathcal{O}(N_\tau N^5)$ and can be carried out self-consistently, making it reference independent. The self-consistency guarantees that the Luttinger–Ward functional constructed from the converged GF2 Green's function and GF2 self-energy and the total energy is stationary with respect to the Green's function. Therefore, at convergence different ways of calculating correlation energy agree within numerical precision. This is a significant advantage because it means that one is free to choose the simplest way of evaluating the correlation energy e. g. using Galitskii–Migdal formula

rather than Luttinger–Ward functional.

In GF2, the imaginary time self-energy $\mathbf{\Sigma}(i\tau)$ is calculated using an imaginary time Green's function $\mathbf{G}(i\tau)$ according to

$$\Sigma_{ij}(i\tau) = -\sum_{klmnpq} G_{kl}(i\tau) G_{mn}(i\tau) G_{pq}(-i\tau) v_{ikmq} \left(2v_{ljpn} - v_{pjln}\right), \tag{6.21}$$

GF2 calculations proceed as shown in Fig. 6.1 and operate in both imaginary time and Matsubara domains. This choice simplifies the numerical evaluation of the self-energy and the solution of the Dyson equation, for details see Refs. [1, 3]. A broad variety of complex numerical algorithms and procedures, involved in the GF2 calculation, require handling Matsubara grids such as the calculation of the Matsubara Green's functions, fast Fourier transform from the Matsubara frequencies to imaginary time and back, solution of the Dyson equation and the evaluation of sums over Matsubara frequencies in the Galitskii–Migdal energy calculation. This makes GF2 an ideal candidate for testing our algorithm. The details of the GF2 algorithm can be found in Ref. [52]. To accelerate calculations of the imaginary time self-energy a Legendre polynomial basis was used as described in Ref. [12].

The reference data involving full frequency grid was obtained by performing self-consistent GF2 calculations for several atoms and simple molecules with Matsubara frequency grids large enough to achieve convergence in total energy to 10 $\mu\mathrm{E}_h$ and in the total number of electrons to 10^{-5}. From the converged GF2 Green's functions and self-energies we calculated the reference one-body density matrix using Eq. 6.10, the total number of electrons, the one-body energy using Eq. 6.11, and the Galitskii–Migdal and Luttinger–Ward energies using Eqs. 6.12 and 6.13 respectively.

6.4 Results and discussion

In this section, we benchmark realistic atomic and molecular GF2 calculations using the cubic spline interpolation algorithm described above. Our test set is comprised of 3 closed-shell atoms: Be, Mg, Ar; 21 closed-shell molecules: H_2O, $(H_2O)_2$, $(H_2O)_3$, $(H_2O)_4$, HCN, CH_4, C_2H_4, CO, CO_2, H_2CO, NH_3, BN, H_2O_2, C_6H_6, LiH, NaH, MgH_2, AlH, NaOH, MgO, NaF; and 4 transition metal atoms and diatomic clusters: Cd, Pd, Cu_2, Ag_2. The aug-cc-pVDZ [70–72] basis set was used for atoms, the TZ(Dunning) basis set was used for molecules except for LiH, NaH, MgH_2, AlH, NaOH, MgO and NaF where the aug-cc-pVDZ basis set was used. For transition-metal containing compounds, a basis set with pseudopotentials ecp-sdd-DZ [73–76] was employed. We studied systems with pseudopotentials because they are frequently used in solid-state calculations thus giving us an insight into behavior of the realistic Green's function in such systems. Moreover, without using pseudoptentials the grid requirements for such electron rich systems are enormous.

All systems studied in this work have a small dependence on temperature due to a large HOMO-LUMO gap and thus variations of inverse temperature β do not change results qualitatively. Lowering the temperature (increasing β) corresponds to decreasing the Matsubara spacing, so that correspondingly more frequencies are required to reach the same accuracy for frequency sums and energies. Consequently, to challenge our algorithm we have chosen a relatively large value of inverse temperature $\beta = 100$ [1/a.u.].

To test the accuracy of our algorithm, we applied it to converged GF2 Green's functions using several values of the threshold $\delta = 10^{-n}, n \in \{2, 3, 4, 5, 6\}$. For every value of the threshold, we used the cubic spline interpolation algorithm to obtain a new small grid — a set of not necessarily equidistant imaginary frequency points satisfying conditions discussed in the previous section. A spline evaluated using such a small

grid was used to calculate the one-body density matrix (Eq. 6.10), total number of electrons, one-body energy (Eq. 6.11), and Galitskii–Migdal (Eq. 6.12) and Luttinger–Ward (Eq. 6.13) energies.

First, we consider the size of new smaller grids used to create a spline and their dependence on the value of the threshold δ. The interpolation algorithm applied to a smooth function such as Matsubara Green's function produces sets of points with increasing cardinality as the value of threshold decreases. This guarantees a monotonic convergence to the original grid (usually containing thousands of points) in the limit of $\delta \to 0$, thus making our algorithm controlled and systematically convergent when applied to Green's functions.

The numerical manifestation of the statement above is shown in Tab. 6.1, where we summarized results for several atoms and molecules with different basis sets. Before a Green's function calculation is started the number of points in the full Matsubara grid has to be predetermined. This number can be determined by converging the HF energy to a predetermined accuracy by using the HF Green's function. The convergence in total HF energy to 10 $\mu\mathrm{E}_h$ was used to obtain the maximum number of the grid points listed in the VIII column of Tab. 6.1. Alternatively, one can define an accuracy threshold $\epsilon = \max|A_{ij}|$, where $\mathbf{A} = \mathbf{G}_1^n - \mathbf{G}_1^a$, is the maximum matrix element of a difference between the numerical $\mathbf{G}_1^n = \mathbf{G}(i\omega_n) \cdot i\omega_n$ and the analytical $\mathbf{G}_1^a = \mathbf{S}^{-1}$ high-frequency coefficient and determine how many points are necessary to converge the calculation to match a certain ϵ.

It is clear from Tab. 6.1 that for most systems to recover either the highly accurate HF energy or $\mathbf{G}_1$ to at least $\epsilon = 0.1$ accuracy frequently more than 10,000 Matsubara frequencies are required. Additionally, we observe that for most systems, besides few atomic examples, the size of the grid requiring an ϵ between $0.1 - 0.01$ is enough to converge the HF energy to a high accuracy. Thus, while we can predetermine how large the grid should be, such size of the grids cannot be easily explicitly tractable since for

Table 6.1: The number of grid points as a function of the threshold δ used in our cubic spline interpolation algorithm for several atoms and molecules[a] as compared to the number of points in the input Matsubara grid listed in column VIII. Columns IX−X show the number of points in the Matsubara grid required to recover the $\mathbf{G}_1$ coefficient of the high-frequency expansion of Green's function to $\epsilon = 0.1$ and $\epsilon = 0.01$ accuracy threshold.

Atom or	Basis	δ					N_ω	ϵ	
molecule	set	10^{-2}	10^{-3}	10^{-4}	10^{-5}	10^{-6}	used	10^{-1}	10^{-2}
Be	aug-cc-pVDZ	169	229	337	501	943	$3{\cdot}10^4$	$6.7{\cdot}10^2$	$6.8{\cdot}10^3$
Mg	aug-cc-pVDZ	157	216	328	512	1027	$2{\cdot}10^4$	$7.7{\cdot}10^3$	$7.8{\cdot}10^4$
NaH	aug-cc-pVDZ	217	343	546	1046	2098	$2{\cdot}10^4$	$9.1{\cdot}10^3$	$9.1{\cdot}10^4$
Ar	aug-cc-pVDZ	573	682	841	1231	1811	$2{\cdot}10^5$	$1.9{\cdot}10^4$	$1.9{\cdot}10^5$
NaF	aug-cc-pVDZ	262	417	755	1502	3087	$2{\cdot}10^4$	$2.7{\cdot}10^4$	$2.7{\cdot}10^5$
C_2H_4	TZ(Dunning)	241	384	761	1931	4078	$2{\cdot}10^4$	$3.1{\cdot}10^4$	$3.1{\cdot}10^5$
Cd	ecp-sdd-DZ	255	380	598	1478	3196	$5{\cdot}10^4$	$3.1{\cdot}10^4$	$3.1{\cdot}10^5$
MgH_2	aug-cc-pVDZ	298	469	875	1693	3752	$3{\cdot}10^4$	$3.2{\cdot}10^4$	$3.2{\cdot}10^5$
Ag_2[b]	ecp-sdd-DZ	294	421	657	1927	4064	$7{\cdot}10^4$	$3.4{\cdot}10^4$	$3.4{\cdot}10^5$
NH_3	TZ(Dunning)	211	344	734	1612	3478	$2{\cdot}10^4$	$4.6{\cdot}10^4$	$4.6{\cdot}10^5$
HCN	TZ(Dunning)	264	411	834	1941	3864	$2{\cdot}10^4$	$4.7{\cdot}10^4$	$4.7{\cdot}10^5$
$(H_2O)_2$[c]	TZ(Dunning)	326	496	885	2117	4463	$8{\cdot}10^4$	$6.1{\cdot}10^4$	$6.1{\cdot}10^5$
$(H_2O)_3$[c]	TZ(Dunning)	252	419	894	2335	5074	$4{\cdot}10^4$	$6.1{\cdot}10^4$	$6.1{\cdot}10^5$
H_2CO	TZ(Dunning)	230	373	770	1971	4078	$3{\cdot}10^4$	$6.1{\cdot}10^4$	$6.1{\cdot}10^5$
C_6H_6	TZ(Dunning)	322	497	918	1330	2581	$2{\cdot}10^4$	$9.0{\cdot}10^4$	$9.0{\cdot}10^5$

[a] Experimental geometries were taken from NIST Computational Chemistry Comparison and Benchmark Database [77].
[b] d(Ag−Ag)=5.46 a.u.
[c] Geometry was taken from Ref. [78].

small molecules such as those shown in the Tab. 6.1, if larger basis set are employed, the grid can approach a size of 100,000 or more Matsubara frequencies. This is a numerical explanation why finite-temperature Green's function calculations for realistic systems have not yet become routine. In this light, our cubic spline interpolation approximation is an important step towards reliable finite-temperature Green's function calculations. As Tab. 6.1 shows, when using the spline interpolation procedure, the reduction in the size of imaginary frequency grids is approximately two orders of magnitude if $\delta = 10^{-4}$ is used and by about one order for lower values of δ. For the most demanding system studied in this work, we only require fewer than 3,000 frequency points to produce a new Green's function using spline which is guaranteed to be in a very good agreement with the reference one since the threshold value is very small $\delta = 10^{-6}$. Overall, when $\delta = 10^{-4}$ is used, the number of frequency points necessary to create a spline grid is around 5% of the original Matsubara grid size which is a remarkable reduction.

To put our efforts in reduction of the Matsubara frequency grid to several thousands points in perspective, it is worth mentioning that grids containing the same order of magnitude of points are used in quantum chemistry, e.g. in the evaluation of the contribution of the exchange-correlation potential in DFT and other numerical algorithms [79–83].

Next, in Fig. 6.4, we examine the convergence of all quantities considered such as the one-particle density matrix, one-body energy, etc. as a function of threshold δ. To illustrate the trend, we selected a few systems from the test set.

In the first panel of Fig. 6.4, we plotted the logarithm of the error in the one-particle density matrix defined as $\Delta P = \sum_{ij} \left[\mathbf{P} - \mathbf{P}^{\text{ref}}\right]_{ij}$ as the function of the threshold δ. For all systems studied in this work, we observed almost perfect linear convergence. Thus, an order of magnitude improvement in the accuracy of the one-particle density matrix can be achieved by decreasing the threshold by a factor of ten. For small systems such as atoms, the value of threshold roughly corresponds to the accuracy of the one-particle

density matrix. For bigger systems using the smallest threshold yields inaccurate one-body density matrices. Thus at least $\delta = 10^{-3}$ should be used if quantities that rely on an accurate determination of a one-particle density matrix are of interest.

The one-body energy is calculated using the one-body density matrix. Consequently, we note based on the upper center panel of Fig. 6.4, that the rate of convergence of the one-body energy is that of the one-particle density matrix. The overall accuracy of the one-body energy is worse than that of the one-particle density matrix but insignificantly. Nonetheless for all systems considered here the convergence of about 10 μE_h is achieved for $\delta = 10^{-6}$.

The total number of electrons is another quantity calculated from the one-particle density matrix. The δ-dependence of the total number of electrons is shown in the upper right panel of Fig. 6.4. Overall convergence of the total number of electrons is fast and the accuracy is generally better than one of the one-particle density matrix. For the majority of systems considered in this work, it is enough to set $\delta = 10^{-4}$ to recover the total number of electrons to 10^{-5} accuracy.

The convergence of the Galitskii–Migdal two-body energy is shown in the bottom left panel of Fig. 6.4. We observe that the Galitskii–Migdal energy is converging the most rapidly and for all the systems studied $\delta = 10^{-3}$ is enough to achieve a $\mu\mathrm{E}_h$ accuracy. Thus, the cubic spline interpolation algorithm is an extremely efficient way to calculate the two-body energy and to replace a simple sum over Matsubara frequencies which is known to be numerically challenging. Small fluctuations in the Galitskii–Migdal energy observed for $\delta = 10^{-5}$ and $\delta = 10^{-6}$ are purely numerical artifacts and only happen after a very good convergence to 0.1 μE_h is achieved.

Next, we examine the convergence of the Luttinger–Ward (E^{LW}) energy shown in the bottom center panel of Fig. 6.4. The Luttinger–Ward energy converges at a slower rate than Galitskii–Migdal energy but still an acceptable accuracy of 10 $\mu\mathrm{E}_h$ can be achieved with $\delta = 10^{-5}$ or $\delta = 10^{-6}$ threshold depending on the system under

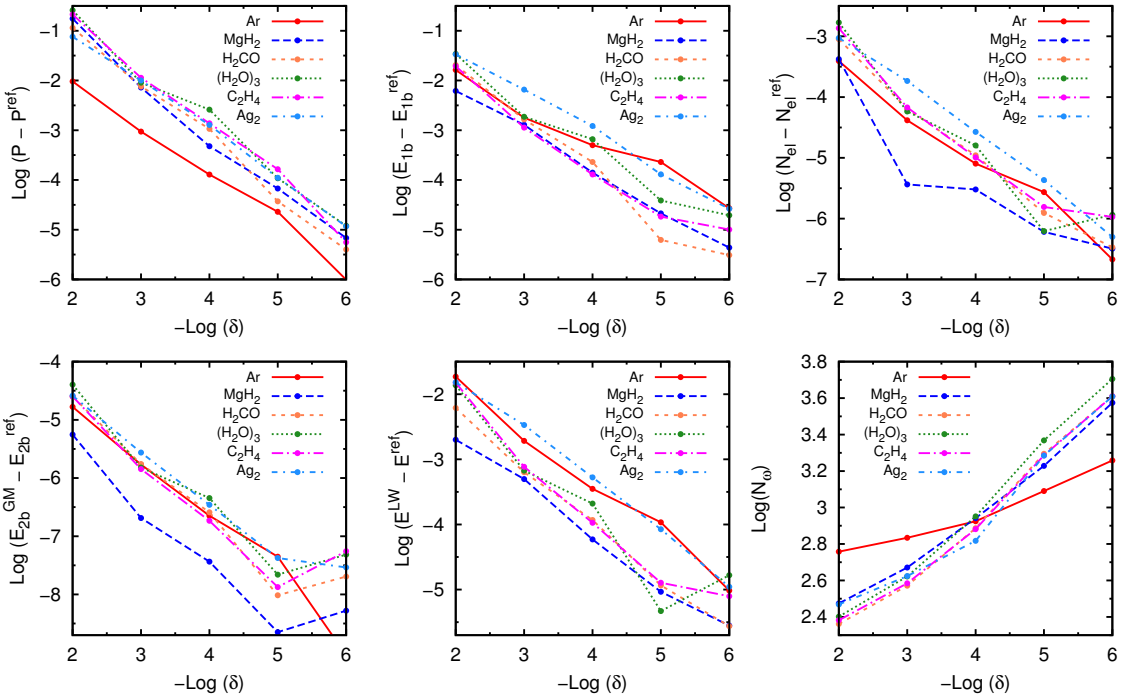

Figure 6.4: Errors in the density matrix $\mathrm{Log}(\sum_{ij}\left[\mathbf{P}-\mathbf{P}^{\mathrm{ref}}\right]_{ij})$, one-body energy $\mathrm{Log}(E_{1\mathrm{b}}-E_{1\mathrm{b}}^{\mathrm{ref}})$, total number of electrons $\mathrm{Log}(N_{\mathrm{el}}-N_{\mathrm{el}}^{\mathrm{ref}})$, two-body Galitskii–Migdal energy $\mathrm{Log}(E_{2\mathrm{b}}^{GM}-E_{2\mathrm{b}}^{\mathrm{ref}})$ and Luttinger–Ward energy $\mathrm{Log}(E^{LW}-E^{\mathrm{ref}})$ as a function of the threshold $\mathrm{Log}(\delta)$ for selected atoms and molecules with different basis sets. Last panel shows the dependence of the grid size $\mathrm{Log}(N_\omega)$ on the threshold $\mathrm{Log}(\delta)$. Log denotes the base 10 logarithm.

consideration. The oscillations in the Luttinger–Ward energy, which are numerical artifacts, may also happen but only after initial convergence to less than 10 μE_h is achieved.

Finally, last panel of Fig. 6.4 shows the sizes of imaginary frequency grids that correspond to particular value of the threshold δ. As expected, simpler atomic systems even with basis sets containing polarization functions generally do not require large grids and changing the threshold δ does not result in a significant change of the size of the imaginary frequency grid, indicating that a convergence is achieved with relatively low value of δ. For bigger systems with lower spatial symmetry, the convergence of the grid size is slower and larger values of the threshold δ may be necessary.

As the results above indicate, decreasing the threshold δ indeed results in generating more extensive grids with the increase of $1.5-2.0$ for every order of magnitude decrease of δ (see Tab. 6.1). This has an important consequence for the computational complexity of realistic calculations. In order to achieve an order of magnitude improvement in convergence of the Green's function using standard equidistant Matsubara frequency grid the next successive grid must be at least an order of magnitude larger than previous one (Fig. 6.2). It follows from Fig. 6.4 that if a cubic spline interpolation algorithm is used, an order of magnitude improvement in the calculated quantity can be achieved if the value of threshold δ is changed by a factor of ten which results in changing the number of frequencies necessary only by a factor of $1.5-2$. This means that upon going to bigger systems one should not expect the spline grid to grow as fast as the standard Matsubara frequency grid.

Finally, since basis set significantly affects the grid requirements, in Fig. 6.5, we plot the results for all the 28 systems considered here according to the basis set. We plot 1/Log(error) versus $-\text{Log}(\delta)$ using bars since we attempt to show errors which differ by orders of magnitude on one plot. These plots should be read as follows. Each bar represents the mean average error in the calculated quantity and longer bars

correspond to larger errors.

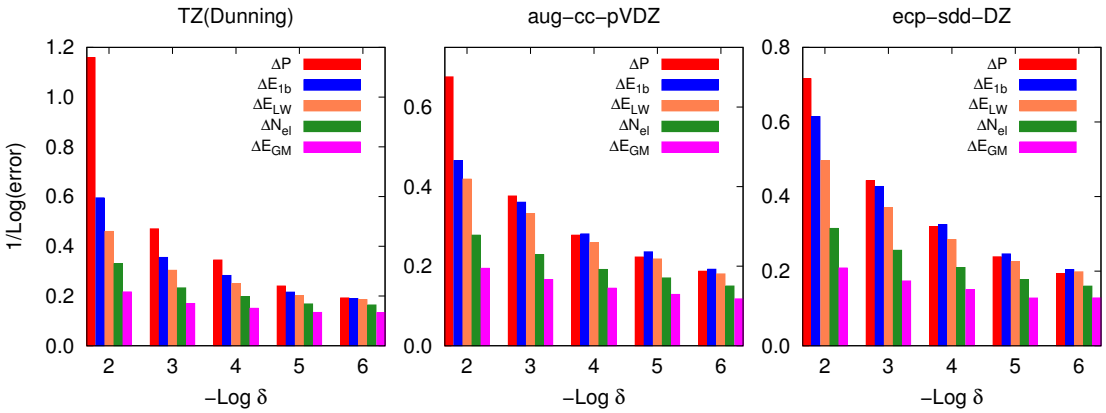

Figure 6.5: The mean average errors in one-body density matrix ΔP, total number of electrons ΔN_{el}, one-body energy ΔE_{1b}, two-body energy $\Delta E_{\mathrm{2b}}^{GM}$ calculated using Galitskii–Migdal formula and Luttinger–Ward energy ΔE^{LW} as a function of the threshold δ for various basis sets. This composite plot summarizes errors for all the 28 systems considered in this work. Log denotes the base 10 logarithm.

Fig. 6.5 shows the errors in one-particle density matrix, total number of electrons as well as one- and two-body energies for three different basis sets employed in our calculations: TZ(Dunning), aug-cc-pVDZ and ecp-sdd-DZ. As seen from Fig. 6.5, changing threshold from loose (10^{-2}) to tight (10^{-6}) leads to monotonic improvement in the accuracy for all the quantities considered. For all the basis sets employed, the biggest error is in the one-particle density matrix and consequently the one-body energy. Smaller errors are observed in the Luttinger–Ward energy and the total number of electrons. The error in the two-body energy using the Galitskii–Migdal formula is the smallest and it is almost grid size independent. Thus, one can expect that only a small number of grid points can be used to construct a spline that is used to evaluate a product of two frequency dependent quantities (like two-body energy from Eq. 6.12), while a larger grid is required when the quantity calculated is directly dependent on the accuracy of the one-body Green's function (like the one-body density matrix which is related to the Green's function by a Fourier transform). By comparing the magnitude of all

errors, we conclude that they are the largest for the TZ(Dunning) basis set. This is not surprising since we used TZ(Dunning) basis set for bigger molecules as opposed to aug-cc-pVDZ basis set used for atoms and smaller molecules. This trend is in agreement with regular Matsubara frequency grid requirements shown in Tab. 6.1.

6.5 Conclusions

If equidistant numerical grids are used, finite-temperature Green's function calculations of molecular systems or solids in large basis sets seem hardly possible due to highly inefficient grid spacing. However, since the Matsubara Green's function is a smoothly and slowly varying function of frequency even a simple cubic spline interpolation algorithm can help reduce the number of grid points at which the Green's function is evaluated explicitly, thereby making realistic calculations tractable. We carefully investigated this idea on a series of atomic and molecular calculations with realistic Hamiltonians. We demonstrated that only around 5% of the original equidistant Matsubara frequency grid was necessary to obtain very accurate results for the density matrix or total energy.

Our interpolation algorithm introduces a single threshold parameter—the magnitude of the fourth derivative, that systematically controls the spline accuracy. To keep the value of this threshold constant and below a user desired level, our algorithm detects the regions where the Matsubara Green's function changes rapidly and ensures that more grid points are used in these regions while fewer points are necessary in the regions with a slowly changing Green's function.

We established that irrespective of the basis set or the actual system under study, the magnitude of the spline fourth derivative is directly proportional to the accuracy of the results. Thus, in a black-box manner, by changing the value of this parameter we can achieve a desirable high accuracy while maintaining a low computational cost.

One of the most important features of our algorithm shown here is that the growth of the spline grid necessary to evaluate the one-body density matrix or energies to a desired accuracy is much slower than that of standard equidistant Matsubara frequency grid. While the Matsubara frequency grid grows by an order to magnitude to get an order of magnitude improvement in the accuracy, the spline grid only grows by a factor or $1.5-2$. Consequently, to achieve a very high $\mu\mathrm{E}_h$ convergence of energy with respect to the grid size, the number of points at which the Green's function is evaluated explicitly is within only couples of thousands while a traditional Matsubara frequency grid requires hundreds of thousands of explicit evaluations.

This study, when combined with our recently proposed algorithm for efficient reduction of the size of the imaginary time grid in Ref. [12], is a step towards reliable and computationally affordable Green's function calculations in quantum chemistry and materials science.

Bibliography

[1] A. L. Fetter and J. D. Walecka, *Quantum Theory of Many-Particle Systems*, Dover Publications: Mineola, NY, USA (2003).

[2] A. A. Abrikosov, L. P. Gorkov, and I. E. Dzyaloshinski, *Methods of Quantum Field Theory in Statistical Physics*, Dover Publications: NY, USA (1963).

[3] R. D. Mattuck, *A guide to Feynman Diagrams in the Many-Body Problem*, Dover Publications: NY, USA (1992).

[4] G. Stefanucci and R. van Leeuwen, *Nonequilibrium Many-Body Theory of Quantum Systems: A Modern Introduction*, Cambridge University Press: Cambridge, UK (2013).

[5] J. Hubbard, "Electron correlations in narrow energy bands", *Proc. R. Soc. London A.* **276**, 238 (1963).

[6] M. Imada, A. Fujimori, and Y. Tokura, "Metal-insulator transitions", *Rev. Mod. Phys.* **70**, 1039 (1998).

[7] E. Gull, A. J. Millis, A. I. Lichtenstein, A. N. Rubtsov, M. Troyer, and P. Werner, "Continuous-time Monte Carlo methods for quantum impurity models", *Rev. Mod. Phys.* **83**, 349 (2011).

[8] A. Georges, G. Kotliar, W. Krauth, and M. J. Rozenberg, "Dynamical mean-field theory of strongly correlated fermion systems and the limit of infinite dimensions", *Rev. Mod. Phys.* **68**, 13 (1996).

[9] G. Kotliar, S. Y. Savrasov, K. Haule, V. S. Oudovenko, O. Parcollet, and C. A. Marianetti, "Electronic structure calculations with dynamical mean-field theory", *Rev. Mod. Phys.* **78**, 865 (2006).

[10] D. J. Scalapino, "A common thread: The pairing interaction for unconventional superconductors", *Rev. Mod. Phys.* **84**, 1383 (2012).

[11] L. Boehnke, H. Hafermann, M. Ferrero, F. Lechermann, and O. Parcollet, "Orthogonal polynomial representation of imaginary-time Green's functions", *Phys. Rev. B* **84**, 075145 (2011).

[12] A. A. Kananenka, J. J. Phillips, and D. Zgid, "Efficient temperature-dependent Green's functions methods for realistic systems: Compact grids for orthogonal polynomial transforms", *J. Chem. Theory Comput.* **12**, 564 (2016).

[13] B. W. Shore, "Solving the radial Schrödinger equation by using cubic-spline basis functions", *J. Chem. Phys.* **58**, 3855 (1973).

[14] B. W. Shore, "Use of the Rayleigh-Ritz-Galerkin method with cubic splines for constructing single-particle bound-state radial wavefunctions: The hydrogen atom and its spectrum", *J. Phys. B: Atomic and Molecular Physics* **6**, 1923 (1973).

[15] D. O. Odero, J. L. Peacher, and D. H. Madison, "Numerical solutions of quantum mechanical problems using the basis-spline collocation method", *Int. J. Mod. Phys. C* **12**, 1093 (2001).

[16] W. R. Johnson, S. A. Blundell, and J. Sapirstein, "Finite basis sets for the Dirac equation constructed from B splines", *Phys. Rev. A* **37**, 307 (1988).

[17] M. Hellgren and U. von Barth, "Correlation potential in density functional theory at the GWA level: Spherical atoms", *Phys. Rev. B* **76**, 075107 (2007).

[18] S. Raynor, "Cubic spline method for solving second-order differential equations theory and application to the Thomas-Fermi model for ions", *Chem. Phys.* **66**, 409 (1982).

[19] P. Cremaschi, "The use of cubic splines in vibration-rotation problems of diatomic molecules", *Mol. Phys.* **41**, 759 (1980).

[20] A. J. Williamson, R. Q. Hood, and J. C. Grossman, "Linear-scaling quantum Monte Carlo calculations", *Phys. Rev. Lett.* **87**, 246406 (2001).

[21] T. Gilbert and P. Bertoncini, "The spline representation", *Chem. Phys. Lett.* **29**, 569 (1974).

[22] M. Brosolo and P. Decleva, "Variational approach to continuum orbitals in a spline basis: An application to H_2^+ photoionization", *Chem. Phys.* **159**, 185 (1992).

[23] J. Jiang and J. S. Hutchinson, "Quantum-mechanical isomerization of a rotationally and vibrationally excited triatomic model molecule", *J. Chem. Phys.* **95**, 4044 (1991).

[24] B. W. Shore, "On the threshold behaviour of bound-bound and bound-free photoabsorption for the screened Coulomb potentials", *J. Phys. B: Atomic and Molecular Physics* **8**, 2023 (1975).

[25] J. L. Gázquez and H. J. Silverstone, "Piecewise polynomial electronic wavefunctions", *J. Chem. Phys.* **67**, 1887 (1977).

[26] D. P. Carroll, H. J. Silverstone, and R. M. Metzger, "Piecewise polynomial configuration interaction natural orbital study of $1s^2$ helium", *J. Chem. Phys.* **71**, 4142 (1979).

[27] J. S. Hutchinson, "Quantum dynamics of vibrational overtone induced photodissociation of a model polyatomic", *J. Chem. Phys.* **85**, 7087 (1986).

[28] J. Jiang and J. S. Hutchinson, "A time-dependent wave packet analysis of the dynamics of transition state spectroscopy in one dimension", *J. Chem. Phys.* **87**, 6973 (1987).

[29] P. Decleva, A. Lisini, and M. Venuti, "Accurate CI expansion in a spline basis of the helium ground-state wave function", *Int. J. Quantum Chem.* **56**, 27 (1995).

[30] H. Bachau, E. Cormier, P. Decleva, J. E. Hansen, and F. Martín, "Applications of B-splines in atomic and molecular physics", *Rep. Prog. Phys.* **64**, 1815 (2001).

[31] P. W. Thulstrup, "Smooth interpolation, Fourier transformation, and two-center overlap integrals for numerical atomic orbitals", *Int. J. Quantum Chem.* **9**, 789 (1975).

[32] J. H. D'Arcy, S. J. Kolmann, and M. J. T. Jordan, ""plug-and-play" potentials: Investigating quantum effects in $(H_2)_2$-Li^+-benzene", *J. Chem. Phys.* **143**, 074311 (2015).

[33] N. Blümer, "Mott-hubbard metal-insulator transition and optical conductivity in high dimensions", Ph.D. thesis, Universität Augsburg, **2003**.

[34] T. Maier, M. Jarrell, T. Pruschke, and M. H. Hettler, "Quantum cluster theories", *Rev. Mod. Phys.* **77**, 1027 (2005).

[35] P. Dierckx, *Curve and Surface Fitting with Splines*, Monographs on numerical analysis, Oxford University Press: Oxford, UK (1995).

[36] A. R. Jishi, *Feynman Diagram Techniques in Condensed Matter Physics*, Cambridge University Press: Cambridge, UK (2014).

[37] M. Kaltak, J. Klimeš, and G. Kresse, "Low scaling algorithms for the random phase approximation: Imaginary time and Laplace transformations", *J. Chem. Theory Comput.* **10**, 2498 (2014).

[38] M. Govoni and G. Galli, "Large scale GW calculations", *J. Chem. Theory Comput.* **11**, 2680 (2015).

[39] A. A. Kananenka, E. Gull, and D. Zgid, "Systematically improvable multiscale solver for correlated electron systems", *Phys. Rev. B* **91**, 121111 (2015).

[40] T. N. Lan, A. A. Kananenka, and D. Zgid, "Communication: Towards ab initio self-energy embedding theory in quantum chemistry", *J. Chem. Phys.* **143**, 241102 (2015).

[41] Y. Lu, M. Höppner, O. Gunnarsson, and M. W. Haverkort, "Efficient real-frequency solver for dynamical mean-field theory", *Phys. Rev. B* **90**, 085102 (2014).

[42] D. Van Neck, K. Peirs, and M. Waroquier, "Self-consistent solution of Dyson's equation up to second order for atomic systems", *J. Chem. Phys.* **115**, 15 (2001).

[43] K. Peirs, D. Van Neck, and M. Waroquier, "Self-consistent solution of Dyson's equation up to second order for open-shell atomic systems", *J. Chem. Phys.* **117**, 4095 (2002).

[44] T. Matsubara, "A new approach to quantum-statistical mechanics", *Prog. Theor. Phys.* **14**, 351 (1955).

[45] A. A. Rusakov, J. J. Phillips, and D. Zgid, "Local Hamiltonians for quantitative Green's function embedding methods", *J. Chem. Phys.* **141**, 194105 (2014).

[46] A. N. Rubtsov, V. V. Savkin, and A. I. Lichtenstein, "Continuous-time quantum Monte Carlo method for fermions", *Phys. Rev. B* **72**, 035122 (2005).

[47] P. Werner, A. Comanac, L. de' Medici, M. Troyer, and A. J. Millis, "Continuous-time solver for quantum impurity models", *Phys. Rev. Lett.* **97**, 076405 (2006).

[48] P. Werner and A. J. Millis, "Hybridization expansion impurity solver: General formulation and application to Kondo lattice and two-orbital models", *Phys. Rev. B* **74**, 155107 (2006).

[49] A. Georges and G. Kotliar, "Hubbard model in infinite dimensions", *Phys. Rev. B* **45**, 6479 (1992).

[50] H. Kajueter and G. Kotliar, "New iterative perturbation scheme for lattice models with arbitrary filling", *Phys. Rev. Lett.* **77**, 131 (1996).

[51] N. E. Dahlen and R. van Leeuwen, "Self-consistent solution of the Dyson equation for atoms and molecules within a conserving approximation", *J. Chem. Phys.* **122**, 164102 (2005).

[52] J. J. Phillips and D. Zgid, "Communication: The description of strong correlation within self-consistent Green's function second-order perturbation theory", *J. Chem. Phys.* **140**, 241101 (2014).

[53] L. Hedin, "New method for calculating the one-particle Green's function with application to the electron-gas problem", *Phys. Rev.* **139**, A796 (1965).

[54] F. Aryasetiawan and O. Gunnarsson, "The GW method", *Rep. Prog. Phys.* **61**, 237 (1998).

[55] D. Zgid, E. Gull, and G. K.-L. Chan, "Truncated configuration interaction expansions as solvers for correlated quantum impurity models and dynamical mean-field theory", *Phys. Rev. B* **86**, 165128 (2012).

[56] M. Caffarel and W. Krauth, "Exact diagonalization approach to correlated fermions in infinite dimensions: Mott transition and superconductivity", *Phys. Rev. Lett.* **72**, 1545 (1994).

[57] V. M. Galitskii and A. B. Migdal, "Application of quantum field theory methods to the many body problem", *J. Exptl. Theoret. Phys.* **34**, 139 (1958).

[58] J. M. Luttinger and J. C. Ward, "Ground-state energy of a many-fermion system. II", *Phys. Rev.* **118**, 1417 (1960).

[59] A. K. Wilson, D. E. Woon, K. A. Peterson, and T. H. Dunning, "Gaussian basis sets for use in correlated molecular calculations. IX. The atoms gallium through krypton", *J. Chem. Phys.* **110**, 7667 (1999).

[60] J. Koput and K. A. Peterson, "Ab initio potential energy surface and vibrational-rotational energy levels of X2σ^+ CaOH", *J. Phys. Chem. A* **106**, 9595 (2002).

[61] T. H. Dunning, "Gaussian basis functions for use in molecular calculations. III. Contraction of (10s6p) atomic basis sets for the first-row atoms", *J. Chem. Phys.* **55**, 716 (1971).

[62] L. J. Holleboom and J. G. Snijders, "A comparison between the Møller-Plesset and Green's function perturbative approaches to the calculation of the correlation energy in the many-electron problem", *J.Chem. Phys.* **93**, 5826 (1990).

[63] A. Nieto, "Evaluating sums over the Matsubara frequencies", *Comp. Phys. Comm.* **92**, 54 (1995).

[64] E. Oliver, "On the evaluation of Matsubara sums", *Math. Comput.* **79**, 1709 (2010).

[65] W. H. Press, S. A. Teukolsky, W. T. Vetterling, and B. P. Flannery, *Numerical Recipes in C. The Art of Scientific Computing*, Cambridge University Press: Cambridge, UK (1992).

[66] B. Bradie, *A Friendly Introduction to Numerical Analysis*, Pearson Education, Inc.: Upper Saddle River, NJ, USA (2006).

[67] C. Møller and M. S. Plesset, "Note on an approximation treatment for many-electron systems", *Phys. Rev.* **46**, 618 (1934).

[68] J. Čížek, "On the use of the cluster expansion and the technique of diagrams in calculations of correlation effects in atoms and molecules", *Adv. Chem. Phys.* pp. 35–89 (2007).

[69] J. J. Phillips, A. A. Kananenka, and D. Zgid, "Fractional charge and spin errors in self-consistent Green's function theory", *J. Chem. Phys.* **142**, 194108 (2015).

[70] D. E. Woon and T. H. Dunning, "Gaussian basis sets for use in correlated molecular calculations. IV. Calculation of static electrical response properties", *J. Chem. Phys.* **100**, 2975 (1994).

[71] T. H. Dunning, "Gaussian basis sets for use in correlated molecular calculations. I. The atoms boron through neon and hydrogen", *J. Chem. Phys.* **90**, 1007 (1989).

[72] D. E. Woon and T. H. Dunning, "Gaussian basis sets for use in correlated molecular calculations. III. The atoms aluminum through argon", *J. Chem. Phys.* **98**, 1358 (1993).

[73] M. Dolg, U. Wedig, H. Stoll, and H. Preuss, "Energy-adjusted ab initio pseudopotentials for the first row transition elements", *J. Chem. Phys.* **86**, 866 (1987).

[74] H. Stoll, P. Fuentealba, M. Dolg, J. Flad, L. v. Szentpály, and H. Preuss, "Cu and Ag as one-valence-electron atoms: Pseudopotential results for Cu_2, Ag_2, CuH, AgH, and the corresponding cations", *J. Chem. Phys.* **79**, 5532 (1983).

[75] D. Feller, "The role of databases in support of computational chemistry calculations", *J. Comput. Chem.* **17**, 1571 (1996).

[76] K. L. Schuchardt, B. T. Didier, T. Elsethagen, L. Sun, V. Gurumoorthi, J. Chase, J. Li, and T. L. Windus, "Basis set exchange: a community database for computational sciences", *J. Chem. Inf. Model.* **47**, 1045 (2007).

[77] R. D. Johnson, "NIST Computational Chemistry Comparison and Benchmark Database", Standard Reference Database Number 101 Release 16a.

[78] D. J. Wales and M. P. Hodges, "Global minima of water clusters $(H_2O)_n$, n$\leq$21, described by an empirical potential", *Chem. Phys. Lett.* **286**, 65 (1998).

[79] A. D. Becke, "A multicenter numerical integration scheme for polyatomic molecules", *J. Chem. Phys.* **88**, 2547 (1988).

[80] C. W. Murray, N. C. Handy, and G. J. Laming, "Quadrature schemes for integrals of density functional theory", *Mol. Phys.* **78**, 997 (1993).

[81] P. M. Gill, B. G. Johnson, and J. A. Pople, "A standard grid for density functional calculations", *Chem. Phys. Lett.* **209**, 506 (1993).

[82] M. E. Mura and P. J. Knowles, "Improved radial grids for quadrature in molecular density-functional calculations", *J. Chem. Phys.* **104**, 9848 (1996).

[83] P. M. W. Gill and S.-H. Chien, "Radial quadrature for multiexponential integrands", *J. Comput. Chem.* **24**, 732 (2003).

Chapter 7

Rigorous *ab initio* quantum embedding for quantum chemistry using Green's function theory: screened interaction, non-local self-energy relaxation, orbital basis, and chemical accuracy

T. N. Lan, A. A. Kananenka and D. Zgid,

Journal of Chemical Theory and Computation, **12 (10)** 4856–4870 (2016)

7.1 Introduction

In molecular systems the interplay between the localized (strongly correlated) and delocalized (weakly correlated) electrons is the chief reason causing a difficulty in describing these systems since a robust quantum chemistry method has to be able to treat both types of electrons simultaneously with a comparable effectiveness and yield molecular energies reaching chemical accuracy. Similar challenges are faced by condensed matter methods where both itinerant and localized electrons present in a solid have to be accounted for by a computational method that yields thermodynamic quantities and spectra.

In quantum chemistry, complete active space second-order perturbation the-

ory (CASPT2) [1, 2], n-electron valence state second-order perturbation theory (NEVPT2) [3, 4], multi-reference coupled cluster (MRCC) [5–10], multi-reference configuration interaction (MRCI) [11], and multi-configurational density functional theory (MC-DFT) [12–16] belong to a class of methods capable of addressing the problem of strongly correlated electrons in the presence of weakly correlated ones. These are primarily wavefunction methods that are at least in principle systematically improvable and aim to produce very accurate energies for the ground state and couple of low-lying excited states.

In the condensed matter community, when solids are described by a realistic Hamiltonian, dynamical mean-field theory (DMFT) [17–19] on top of GW [20] method (GW+DMFT) [21, 22] formulated in a many-body Green's function language is the primary tool to describe the intricate nature of realistic systems and give information about the spectral function and thermodynamic properties.

A natural direction is to find a common ground between approaches present in different communities and create a method that could yield not only thermodynamic quantities and spectra but also a satisfactory chemical accuracy while using the Green's function language. We have developed the self-energy embedding theory (SEET) [23, 24] where the self-energy describing a couple of strongly correlated orbitals is embedded into the self-energy coming from the weakly correlated orbitals present in the physical problem. Consequently, SEET is a hybrid approach where we use two Green's function methods, a weakly correlated and strongly correlated ones. In SEET, the second-order Green's function (GF2) [25–30] method is used as a weakly correlated approach presenting a useful compromise between the computational cost and accuracy. We have demonstrated that GF2 can describe moderately correlated systems well [25], can be successfully used to find strongly correlated orbitals, and can deliver information about periodic systems [31] and their thermodynamic properties [32]. The accurate correlated method that is used to describe a chosen set of strongly correlated orbitals

is in our case a quantum impurity solver based on configuration interaction (CI) with various levels of wavefunction truncation [33, 34].

We have applied SEET to the 2D Hubbard model [23] and small molecular problems [24] obtaining in both cases excellent results when compared against other established methods. For the 2D Hubbard model at half- and away from half-filling, SEET self-energies matched very well the self-energies obtained from the continuous-time auxiliary field quantum Monte Carlo (CT-QMC) [35, 36] calculations at all interaction strengths analyzed. In Ref. [24] using molecular examples, we have demonstrated that SEET, which is a perturb and diagonalize scheme, can reach a level of accuracy that is comparable to other quantum chemistry methods such as NEVPT2 and CASPT2. Moreover, we have shown that SEET can be potentially be extended to periodic systems since in contrast to NEVPT2/CASPT2 it does not require preparing one-, two-, three- or four-body reduced density matrices and only one-body Green's function and self-energy are sufficient to perform all calculations. Additionally, SEET in the CI-in-GF2 variant does not suffer from the intruder state problem resulting in denominator divergences present in CASPT2.

In this Chapter, we are further examining all the aspects of SEET and we are focusing on describing all the requirements that have to be fulfilled to make SEET systematically improvable and applicable to a wide variety of systems. We base our discussion on the molecular systems where the near exact (or very accurate) solutions at zero temperature are known from a variety of methods such as density matrix renormalization group (DMRG) [37–43] or NEVPT2/CASPT2. These simple benchmark systems allow us to establish the best way of treating molecular systems using Green's function methods.

This Chapter is organized in the following way. In Section 7.2.1, we present a theoretical motivation behind SEET. In Section 7.2.2, we describe the GF2 theory that allows us to produce the self-energy for weakly correlated orbitals. Subsequently,

in Section 7.2.3, we proceed to explaining how SEET is related to DMFT-type approaches that use on-site effective interactions. SEET can be executed using various strongly correlated orbital selection schemes either based on energy or spatial criteria as discussed in Section 7.2.4. To ensure that a very high accuracy and a systematic improvability is maintained during SEET calculations, it is essential to use Green's function quantum impurity solvers that can describe full realistic Hamiltonian for the impurity orbitals. We discuss possible implications of this fact in Section 7.2.5. Finally, we present numerical results in Section 7.3 and conclude this Chapter in Section 7.4.

7.2 Theoretical description

7.2.1 Self-energy embedding theory (SEET)

Let us assume that we would like to calculate properties of a realistic system described by a Hamiltonian

$$H = \sum_{ij} t_{ij} a_i^\dagger a_j + \frac{1}{2} \sum_{ijkl} v_{ijkl} a_i^\dagger a_k^\dagger a_j a_l, \tag{7.1}$$

where t_{ij} and v_{ijkl} are the one- and two-body integrals in an orbital basis that can be either orthogonal or non-orthogonal. Many realistic systems are correlated enough that low-level many-body methods cannot describe them with a sufficient accuracy. While high-level many-body methods can deliver accurate answers, for many interesting systems the total number of orbitals N may be too large to compute the whole problem using a high-level method. However, for most realistic cases only few orbitals contribute significantly to the physics or chemistry of the total problem. Consequently, these physically or chemically important orbitals, which we will call active or strongly correlated orbitals, can be described by a high-level method, while all the other inactive or weakly correlated orbitals can be described by a lower level method.

The separation of the orbital space into active and inactive or strongly and weakly correlated orbitals implies in the Green's function language that we will express the self-energy of the strongly correlated orbitals u and v as

$$[\mathbf{\Sigma}]_{uv} = [\mathbf{\Sigma}_{non-local}]_{uv} + [\mathbf{\Sigma}_{local}]_{uv}, \tag{7.2}$$

where we assume that the self-energy contains both the frequency dependent and independent parts $\mathbf{\Sigma} = \mathbf{\Sigma}_{\infty} + \mathbf{\Sigma}(i\omega)$. A given self-energy matrix element $[\mathbf{\Sigma}]_{uv}$ is composed out of the local self-energy coming from the active orbitals themselves and a non-local self-energy contribution coming from environment or inactive orbitals that influence the self-energy of the active orbitals. This self-energy separation itself is formally exact, however, various approximation can be used to describe the different self-energy contributions, namely

$$[\mathbf{\Sigma}]_{uv} = [\mathbf{\Sigma}^{low-level}_{non-local}]_{uv} + [\mathbf{\Sigma}^{high-level}_{local}]_{uv}. \tag{7.3}$$

Here, a low-level (eg. perturbative) method is used to evaluate the non-local contribution to the self-energy, while a high-level, accurate method is employed to evaluate the local self-energy contribution for the strongly correlated orbitals. Note that the separation of the self-energy presented in Eq. 7.3 is characteristic for embedding methods and thus is general without necessarily specifying how the low- and high-level self-energies are evaluated in practice. Here, few major routes exist **(i)** either by a variational minimization of the free energy functional (that depends on the self-energy and Green's function), **(ii)** by an explicit construction of the diagrammatic series necessary to represent different parts of the self-energy, **(iii)** or by a perturbative construction that allows for updating the hybridization between the embedded system and the environment. Clearly while a multitude of approximations are possible, the choice of a particular route should depend on the physics of the system under study.

In our two previous papers [23, 24] and in this Chapter, we use the third option and construct an impurity model for the strongly correlated orbitals that then has its self-energy evaluated in DMFT-type iterations; however, we would like to stress that the self-energy partitioning is general and our choice of evaluating the two parts of self-energy is one of many possible choices. The separation of the self-energy contributions allows us to evaluate the non-local part of the self-energy at a perturbative, inexpensive level, while the local, strongly correlated part is expressed as an impurity problem and is evaluated with more accurate method.

Consequently, one of the most important questions is how to choose orbitals that are strongly correlated and ought to be treated by a higher level method. To make such a choice based on the physics and not only on our intuition, we first perform a low-level perturbative calculation and analyze occupations, energy, or spatial domains of the orbitals involved. The details of such a procedure will be discussed in Section 7.2.4.

For now, let us assume that using one of the possible criteria (orbital occupations, energies, or spatial domains), we have chosen the active (strongly correlated) orbitals that we denote $u, v, t, w, ...$, while μ, λ are the inactive (weakly correlated) orbitals, and b stands for a bath orbital index. We define the active space Green's function as

$$\mathbf{G}_{act}(i\omega) = \left[i\omega\mathbf{1} - \mathbf{f}^{nodc}_{act} - \mathbf{\Delta}(i\omega) - \mathbf{\Sigma}_{act}(i\omega)\right]^{-1}, \tag{7.4}$$

where subscript *act* stands for the active space. A molecular Fock matrix without double counting is denoted as $\mathbf{f}^{nodc}$. The double counting between the mean-field and high-level treatments in the active space is removed since the mean-field Coulomb interaction in the active space is exactly subtracted. Explicitly, the above operation is given by

$$f^{nodc}_{uv} = h_{uv} + \sum_{\mu\lambda} P_{\mu\lambda}\left(v_{uv\mu\lambda} - \frac{1}{2}v_{u\lambda\mu v}\right) - \sum_{tw} P_{tw}\left(v_{uvtw} - \frac{1}{2}v_{tvuw}\right), \tag{7.5}$$

where $\mathbf{P}$ is the one-body density matrix obtained from a perturbative method. Note that the chemical potential has been included in the one-body electron integral matrix, $\mathbf{h}$, for convenience.

SEET is general and multiple perturbative methods such as GF2, GW, or FLEX [44, 45], etc. can be used to describe the inactive orbitals and deliver initial density and Fock matrices describing all the orbitals. We have chosen to use GF2 since it contains an exchange diagram that is important for reaching the chemical accuracy in molecular systems. The details of the GF2 procedure will be listed in Section 7.2.2. In GF2, the one-body density matrix $\mathbf{P}$ is obtained using Eq. 7.22.

The hybridization $\mathbf{\Delta}(i\omega)$ from Eq. 7.4 describes the coupling of the active orbitals to the remaining weakly correlated ones. While at later iterations the active space Green's function and self-energy are evaluated by a more accurate many-body methods, in the first iteration of SEET, to initialize these matrices, we express them as sub-matrices of the GF2 Green's function and self-energy in the subset of active orbitals,

$$\mathbf{G}_{act}(i\omega) = [\mathbf{G}^{GF2}(i\omega)]_{act} \tag{7.6}$$

$$\mathbf{\Sigma}_{act}(i\omega) = [\mathbf{\Sigma}^{GF2}(i\omega)]_{act} \ . \tag{7.7}$$

The initial hybridization is then computed by substituting $\mathbf{G}_{act}(i\omega)$ and $\mathbf{\Sigma}_{act}(i\omega)$ into Eq. 7.4.

The infinite, continuum bath that describes the hybridization can be approximated by a finite, discrete one. A finite number of bath orbital energies ϵ_b and the impurity-bath couplings V_{ub} are then fitted to recover the hybridization $\mathbf{\Delta}(i\omega)$,

$$[\mathbf{\Delta}(i\omega)]_{uv} \approx [\mathbf{\Delta}^{fit}(i\omega)]_{uv} = \sum_{b}^{N} \frac{V_{ub}^{*} V_{vb}}{i\omega - \epsilon_b} \tag{7.8}$$

in order to produce the impurity Hamiltonian in a finite basis. Note that the indices $b = 1, \ldots, N_b$ are running over bath sites while the u, v indices are used to number the

impurity orbitals. In general, the bath orbital energies ϵ_b and the impurity-bath couplings V_{ub} are always chosen such that the overall fitting error, $[\mathbf{\Delta}(i\omega)]_{uv} - [\mathbf{\Delta}^{fit}(i\omega)]_{uv}$, is minimized. Helpful details of the bath fitting procedure are discussed in the condensed matter literature [46].

To compute the active space Green's function from Eq. 7.4 using quantum impurity solvers that need an explicit Hamiltonian formulation, one needs to formulate the Anderson impurity Hamiltonian as follows [47]

$$H_{act+bath} = H_{act} + H_{coupling} + H_{bath}, \tag{7.9}$$

where H_{act} is the full active space Hamiltonian

$$H_{act} = \sum_{uv} f_{uv}^{nodc} a_u^\dagger a_v + \frac{1}{2} \sum_{uvtw} v_{uvtw} a_u^\dagger a_t^\dagger a_v a_w, \tag{7.10}$$

where H_{bath} describes the non-interacting bath, and $H_{coupling}$ stands for the coupling between the active space and non-interacting bath,

$$H_{bath} = \sum_{b} \epsilon_b a_b^\dagger a_b, \tag{7.11}$$

$$H_{coupling} = \sum_{ub} V_{ub} \left(a_u^\dagger a_b + a_b^\dagger a_u \right). \tag{7.12}$$

Multiple numerical methods have been developed to solve the impurity Hamiltonian from Eq. 7.9. Quantum chemistry approaches that use an explicit Hamiltonian formulation and properly capture strong correlations in the active space can be extended to become Green's function impurity solvers. A discussion concerning the exact diagonalization (ED) or full configuration interaction (FCI) solvers and a later class of solvers based on a truncated configuration interaction (CI) or restricted active space configuration interaction (RASCI) approaches can be found in Refs. [33, 34, 46, 48–50]. We employ a RASCI solver in SEET if the total number of orbitals (impurity

+ bath) in the impurity Hamiltonian exceeds 16 orbitals and is intractable with FCI. This quantum chemistry RASCI solver that works with Hamiltonians containing general two-body interactions is important since it allows us to achieve chemical accuracy in molecular *ab initio* SEET.

As an alternative to the CI solvers, the continuous-time quantum Monte Carlo (CT-QMC) methods, which introduce an explicit temperature-dependence and treat infinite number of bath orbitals can also be used with SEET. In Section 7.2.5, we will discuss in more details how realistic interactions impact the impurity problem and solvers.

After obtaining the active space Green's function using the impurity Hamiltonian from Eq. 7.9, the active space self-energy is evaluated using the Dyson equation. Combining the non-local self-energy obtained from a perturbative method (e.g. GF2, see Eq. 7.18) and the active space self-energy obtained from a high level many-body method, we construct the molecular self-energy for strongly correlated orbitals as

$$[\mathbf{\Sigma}_{mol}(i\omega)]_{uv} = [\mathbf{\Sigma}^{GF2}_{non-local}(i\omega)]_{uv} + [\mathbf{\Sigma}^{high-level}_{local}(i\omega)]_{uv}, \tag{7.13}$$

where the non-local part of the self-energy coming from a perturbative method does not contain any double counting of diagrams, for details see Section 7.2.2.

The inactive orbitals are described using only the self-energy obtained from a perturbative method and consequently

$$[\mathbf{\Sigma}_{mol}(i\omega)]_{\mu\lambda} = [\mathbf{\Sigma}^{GF2}(i\omega)]_{\mu\lambda}. \tag{7.14}$$

In SEET, the impurity Hamiltonian is solved using bare interactions since the frequency dependent field coming from all the other orbitals is described by $\mathbf{\Sigma}^{GF2}_{non-local}(i\omega)$. However, to connect to the condensed matter and materials science community that uses screened interactions in the impurity Hamiltonian, we present a discussion of how these interactions can be evaluated in SEET in Section 7.2.3.

The new molecular Green's function, which contains the GF2 self-energy coming from all the inactive, weakly correlated orbitals as well as the strongly correlated self-energy from the active space orbitals, is reconstructed as

$$\mathbf{G}_{mol}(i\omega) = \left[i\omega\mathbf{1} - \mathbf{f}^{modc} - \mathbf{\Sigma}_{mol}(i\omega)\right]^{-1}. \tag{7.15}$$

This $\mathbf{G}_{mol}(i\omega)$ is an $N \times N \times w_{max}$ matrix and has elements for all the orbitals present in the molecular problem $N = N_{inactive} + N_{active}$.

The hybridization $\mathbf{\Delta}(i\omega)$ present in Eq. 7.4 is then updated using the new Green's function and self-energy, and subsequent iterations are performed until convergence is achieved.

In SEET, the self-consistency procedure is made out of two loops. The inner loop has DMFT-like iterations and in this loop the matrices such as $\mathbf{G}_{mol}$, $\mathbf{\Sigma}_{mol}(i\omega)$, and $\mathbf{\Delta}(i\omega)$ are determined self-consistently. At the convergence of the DMFT-like loop, the quantities of interest, such as the density matrix, molecular energy, and density of states, can be evaluated using the converged Green's function and self-energy.

In the outer loop of SEET, we use the converged Green's function that contains the self-energy obtained using an accurate many-body method and we pass it back to the perturbative method as a zeroth-order Green's function. Note that in the case of GF2 only a single iteration is performed in the SEET outer loop. (Otherwise, due to the self-consistent nature of GF2, the converged GF2 Green's function will be the same as the one obtained previously.)

An overall scheme of SEET self-consistency is summarized as follows.

1. Generate Hartree–Fock (HF) or density functional theory (DFT) Green's function as an initial guess.

2. Perform a self-consistent GF2 calculation for the whole molecule, see Ref. [25] for details of the GF2 iterative loop.

3. Evaluate the one-body density matrix $\mathbf{P}$ using Eq. 7.22 and construct a desired orbital basis such as natural orbitals, localized orbitals, or orthogonal atomic orbitals.

4. Transform all quantities from the atomic orbital (AO) basis to the new desired orbital basis.

5. Construct the impurity Hamiltonian in which two-electron term is either a subset of bare Coulomb or screened interactions in the active space.

6. Perform DMFT-like loop:

   (a) Use an impurity solver (RASCI/FCI or CT-HYB) to obtain the active space Green's function $\mathbf{G}_{act}(i\omega)$ and extract the active space self-energy $\mathbf{\Sigma}_{act}(i\omega)$. At the first iteration the hybridization $\mathbf{\Delta}(i\omega)$ is initialized using GF2 quantities.

   (b) Set up the molecular self-energy according to Eqs. 7.13−7.14 if a non-local self-energy is used or Eq. 7.19 if screened interactions are used.

   (c) Reconstruct the molecular Green's function via the Dyson equation and adjust the chemical potential to obtain a correct electron number for the whole molecule.

   (d) Update the hybridization $\mathbf{\Delta}(i\omega)$ using the new molecular Green's function and self-energy.

   (e) Go back to step 6(a) and iterate until convergence is reached.

7. Pass the converged molecular Green's function to a GF2 calculation and perform only a single GF2 iteration.

8. Go back to step 3 and iterate until outer loop convergence is reached.

Steps 7 and 8 are optional. In the past, we have investigated a single-shot scheme of DMFT-like iterations on top of GF2 without any further self-consistent iterations (steps 7 and 8). In practical calculations, we found that when the embedding was done in the energy domain then performing single-shot calculations was almost always sufficient. The outer loop was necessary to relax the non-local self-energy when the embedding construction was executed using spatial fragments.

7.2.2 GF2 non-local self-energy

In the first step of SEET, a low-level Green's function method is used to obtain a non-local self-energy. In our work, we employ the *ab initio* self-consistent GF2 method using either HF or DFT Green's function as an initial guess. The GF2 self-energy in the imaginary time domain reads

$$\left[\Sigma^{GF2}_{mol}(\tau)\right]_{ij} = -\sum_{klmnpq} \left[G^{GF2}_{mol}(\tau)\right]_{kl} \left[G^{GF2}_{mol}(\tau)\right]_{mn} \left[G^{GF2}_{mol}(-\tau)\right]_{pq} v_{ikmq} \left(2v_{ljpn} - v_{pjln}\right), \tag{7.16}$$

where $\mathbf{G}^{GF2}_{mol}(\tau)$ is the imaginary time GF2 Green's function and

$$v_{ijkl} = \int d\mathbf{r}_1 d\mathbf{r}_2 \phi^*_i(\mathbf{r}_1)\phi_j(\mathbf{r}_1) v(\mathbf{r}_1 - \mathbf{r}_2)\phi^*_k(\mathbf{r}_2)\phi_l(\mathbf{r}_2) \tag{7.17}$$

are two-electron integrals in the AO basis. The resulting $\mathbf{\Sigma}^{GF2}_{mol}(\tau)$ matrix is then transformed to the imaginary frequency domain $\mathbf{\Sigma}^{GF2}_{mol}(i\omega)$ using either a traditional Fourier transform (FT) or a Fourier transform in the basis of orthogonal polynomials [51]. The non-local part of the GF2 self-energy without the double counting is directly defined as a difference between the GF2 self-energy obtained from Eq. 7.16 while summing over all the molecular orbitals and that obtained by summing only over the local (active)

part

$$\mathbf{\Sigma}^{GF2}_{non-local}(i\omega) = \mathbf{\Sigma}^{GF2}_{mol}(i\omega) - \mathbf{\Sigma}^{GF2}_{act}(i\omega), \tag{7.18}$$

where $\mathbf{\Sigma}^{GF2}_{act}(i\omega)$ is evaluated using local interactions within the active space. The inclusion of this non-local self-energy into the DMFT-like iterations of SEET eliminates the need for screened, effective interactions in the active space since the non-local self-energy term accounts for all the non-local interactions between the active and remaining orbitals. We will elaborate on this point in Section 7.2.3.

Recently, a comprehensive comparison between approximate diagrammatic schemes including second-order perturbation theory ($\Sigma^{(2)}$), GW, FLEX, and $T-$matrix approximation (TMA) [52] was performed for the 2D Hubbard model [53] where formally exact results are known for multiple regimes. This study showed that the GW, FLEX, and TMA methods consisting of partial summations of bubble and/or ladder diagrams can yield worse results than the second-order perturbation theory. More importantly, when combined with DMFT, $\Sigma^{(2)}$ non-local self-energy is more reliable than that from other methods including partial diagrammatic summations [53]. We have chosen GF2 as the low-level perturbative method since we expect that similar conclusions will hold for realistic systems, particularly for molecular systems, where it is widely acknowledged that an exchange diagram is important if chemical accuracy is required.

The main bottleneck of GF2 is the evaluation of the second-order self-energy from Eq. 7.16. However, a highly parallel scheme consisting of factorizations and multiplications can easily make the GF2 calculation possible for a couple of hundred orbitals.

The other bottleneck in the GF2 calculation is the size of the imaginary frequency and time grids necessary to express the self-energy and Matsubara Green's function. To reach chemical accuracy for realistic systems, these grids can have up to ten or even hundred thousand of points, leading to computations that are both processor

and memory demanding. Recently, we have optimized these numerical grids. First, a Fourier transform in the basis of orthogonal polynomials [51] was used to transform the second-order self-energy from the imaginary time to the Matsubara frequency domain instead of a conventional Fourier transformation. The imaginary time grid can be therefore reduced to a couple of hundred points, while preserving a micro-Hartree accuracy in the energy evaluation. Later, the cubic spline interpolation was implemented to approximate the equidistant Matsubara frequency grid [54]. We showed that the chemical accuracy can be maintained with a very sparse subset of imaginary frequency points (only a few percent of the full imaginary frequency grid). These new grids significantly lower the required computation time and memory storage for the the self-energy and Matsubara Green's function.

7.2.3 Screened interactions in SEET

In a molecular system, the active space self-energy obtained from an impurity described by the bare interactions v_{bare} combined with the the self-energy $[\mathbf{\Sigma}^{GF2}_{non-local}(\tau, v_{bare})]_{uv}$ evaluated by summing over all weakly correlated (inactive) orbitals is equivalent to the self-energy evaluated for an impurity problem described by screened interactions $U(\tau)$. Numerically, this amounts to requiring that the impurity self-energy evaluated using imaginary time dependent screened interactions recovers the full second-order self-energy at every τ point

$$[\mathbf{\Sigma}_{mol}(\tau)]_{uv} = [\mathbf{\Sigma}^{GF2}_{non-local}(\tau, v_{bare})]_{uv} + [\mathbf{\Sigma}_{act}(\tau, v_{bare})]_{uv} = [\mathbf{\Sigma}_{act}(\tau, U(\tau))]_{uv}. \quad (7.19)$$

Consequently, in multiple theories present in condensed matter and materials science the non-local field coming from all the other electrons is described by $U(\tau)$, while in SEET this non-local field is described by $[\mathbf{\Sigma}^{GF2}_{non-local}(\tau, v_{bare})]_{uv}$. Typically, screened interactions are obtained by a *downfolding procedure* of the full realistic band structure

or infinite lattice Hamiltonian to an effective impurity model with only few correlated orbitals [55–58]. In SEET, we avoid the explicit downfolding procedure by including the $\mathbf{\Sigma}^{GF2}_{non-local}(\tau, v_{bare})$ matrix in the DMFT-like self-consistency.

However, in order to connect to the many-body condensed matter and materials science community, we demonstrate how to evaluate on-site screened interactions in molecular problems and by numerical examples (Section 7.3.1) show that both the procedures, SEET and DMFT with screened interactions, give similar numerical answers.

In our previous work, we proposed a procedure for finding screened interactions that reached satisfactory chemical accuracy for molecular systems [59]. In this work, we capitalize on the previous procedure, and we require that for a single strongly correlated orbital we fulfill the following relationship

$$[\Sigma^{GF2}_{mol}(\tau)]_{ii} = [\Sigma^{GF2}_{act}(\tau, U(\tau))]_{ii} = -\left[G^{GF2}_{mol}(\tau)\right]^2_{ii}\left[G^{GF2}_{mol}(-\tau)\right]_{ii}[U(\tau)]^2, \tag{7.20}$$

for the on-site GF2 imaginary time self-energy (Eq. 7.16). The on-site screened interaction $U(\tau)$ is then obtained as follows

$$U(\tau) = -\sqrt{\frac{[\Sigma^{GF2}_{mol}(\tau)]_{ii}}{[G^{GF2}_{mol}(\tau)]^2_{ii}[G^{GF2}_{mol}(-\tau)]_{ii}}}. \tag{7.21}$$

It is worth mentioning that while the non-local self-energy in Eq. 7.18 for multiple-orbital active spaces can be straightforwardly evaluated, the generalization of the on-site screened interaction to treat multiple orbitals, unfortunately, is non-trivial. This is due to the multiple choices of screened interactions $U_{ijkl}(\tau)$ and the parametrization not always being unique [59]. Additional advantages of using the non-local self-energy as compared to using the screened interaction in SEET will be numerically demonstrated in Section 7.3.1.

Now, let us shortly discuss the main distinction between SEET using the GF2 non-

local self-energy and GW+DMFT. First, in GW+DMFT, the GW non-local self-energy is given by a product of Green's functions and the dynamically screened interaction W. Thus, in GW+DMFT, when the realistic band structure or infinite lattice Hamiltonian is mapped onto an effective low energy model, it is mandatory to reconstruct the local components of both G and screened interaction W [21]. This leads to "the *double* embedding in both Green's function G and dynamically screened interaction W" [58]. In SEET, the GF2 non-local self-energy is computed using bare Coulomb interactions (Eq. 7.16), it is therefore unnecessary to reconstruct the local component for the interaction in the active space, which can be directly taken from the bare interaction matrix. Second, because of the dynamical nature of local screened interactions, the rigorous solution of the impurity problem without neglecting the τ-dependence of the interactions in GW+DMFT can be only obtained by a CT-QMC solver. In SEET, any existing quantum impurity solver can be used to tackle the impurity problem. GW+DMFT is known to yield good results for realistic materials such as NiO, it remains to be established if SEET can yield accurate results for these systems. However, for molecular systems, SEET with the GF2 non-local self-energy is a fully *ab initio*, systematically improvable, and self-consistent procedure able to give results with chemical accuracy.

7.2.4 Orbital basis

After a self-consistent GF2 calculation is performed, the next step in the SEET procedure is to construct an orbital basis in which active orbitals are chosen. Here, as we have mentioned earlier, two general schemes are possible: either to perform the selection based on the orbital energies or spatial domains criteria, depending on system studied. As an example, in Fig. 7.1, we present the selection of impurities using the aforementioned criteria for the H_8 chain.

To construct the orbital basis in the energy domain, the one-body density matrix

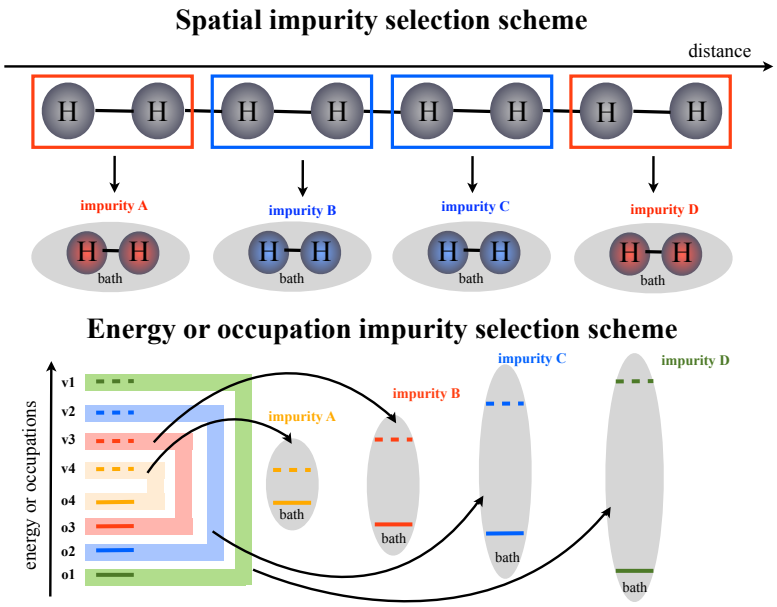

Figure 7.1: Two schemes for selecting orbitals used to construct impurities for the H_8 chain. Note that in the spatial selection scheme there are two pairs of degenerate impurities (A, D) and (B, C). In the energy or occupation scheme, there is no such degeneracy and impurities are built using bonding and corresponding antibonding orbitals.

$\mathbf{P}$ is first evaluated using the converged GF2 Green's function,

$$\mathbf{P} = -2\mathbf{G}^{GF2}_{mol}(\tau = \beta). \tag{7.22}$$

Here, $\tau = \beta$ means that the value of τ is taken at the last grid point equal to β, where $\beta = 1/(k_B T)$ is the inverse temperature.

Then, this molecular one-body density matrix is diagonalized to obtain natural orbitals (NOs) and occupation numbers. The active orbitals are then chosen from this set of NOs based on their occupations, as it is done in traditional CAS type methods. The strongly correlated orbitals have occupations significantly different from 0 or 2, while the weakly correlated orbitals are mostly empty or doubly occupied. In SEET performed in the NO basis, if the number of active orbitals is too large to be included in a single impurity, the orbitals can be easily split into different groups (impurities) belonging to different fragments or different symmetries without any further

implementation as shown in Fig. 7.1, for numerical examples see Tab. 7.4.

In the spatial domain, the localized orbitals can be formally obtained by localizing NOs using the well-known Pipek–Mezey [60] and Boys [61] localization schemes. Note that Boys orbitals are a molecular analogue of Wannier orbitals [62]. In this work, we use the Löwdin orthogonalized AO (SAO) basis when dealing with a minimal basis set, while the so-called regional natural orbital (RNO) basis [63, 64] is employed for larger basis sets than the minimal one. The construction of RNO basis for SEET can be briefly described as follows. Starting from AO density matrix $\mathbf{P}^{\mathrm{AO}}$, the density matrix in SAO basis $\mathbf{P}^{\mathrm{SAO}}$ can be obtained by the Löwdin orthogonalization,

$$\mathbf{P}^{\mathrm{SAO}} = \mathbf{S}^{1/2}\mathbf{P}^{\mathrm{AO}}\mathbf{S}^{1/2}, \tag{7.23}$$

where $\mathbf{S}$ is an AO overlap matrix. In the next step of RNO basis construction, we separately diagonalize a block density matrix of predefined fragments i

$$\mathbf{P}_i^{\mathrm{RNO}} = \mathbf{U}_i^{\dagger}\mathbf{P}_i^{\mathrm{SAO}}\mathbf{U}_i. \tag{7.24}$$

The transformation matrix from SAO to RNO basis for a molecule consisting of n molecular fragments is a direct summation of all block eigenvectors $\mathbf{U}_i$

$$\mathbf{U} = \mathbf{U}_1 \oplus \mathbf{U}_2 \oplus ... \oplus \mathbf{U}_n. \tag{7.25}$$

The density matrix in RNO basis can be obtained as follows

$$\mathbf{P}^{\mathrm{RNO}} = \mathbf{U}^{\dagger}\mathbf{P}^{\mathrm{SAO}}\mathbf{U}. \tag{7.26}$$

Finally, the RNO coefficients present in the non-orthogonal AO basis are obtained by

a back transformation

$$\mathbf{C}^{\mathrm{RNO}} = \mathbf{S}^{-1/2}\mathbf{U}. \tag{7.27}$$

The active orbitals are then chosen from RNOs belonging to particular molecular fragments.

It is worth mentioning that in the original description of the RNO construction [63, 64], the RNO density matrix (Eq. 7.26) is further diagonalized using the Jacobi rotation to obtain the bonding between fragments. However, since our purpose is to approximately disentangle the bonding between fragments, we will not proceed according to the original description.

Generally, depending on a system under study, we can use either NO or SAO/RNO bases. If the entanglement between molecular fragments is large, the NO basis should be used to correctly describe the bonding between fragments. On the other hand, if molecular fragments are only weakly coupled, we approximately can separate them and employ SAO/RNO bases. The advantages and disadvantages of each orbital basis will be carefully demonstrated using numerical results in Section 7.3.3.

7.2.5 Implications for impurity solvers to reach chemical accuracy

For the SEET procedure to be computationally well behaved and accurate one has to fulfill multiple requirements: **(i)** orthogonality of the orbital basis to properly carry out the embedding procedure when an explicit bath representation for a CI solver is necessary, **(ii)** including a realistic Hamiltonian in the impurity problem, **(iii)** hybridizations that simplify the bath fitting procedure, **(iv)** locality to make the self-energy decay fast with respect to the distance, and **(v)** a possibility of treating many strongly correlated orbitals by an impurity solver. All of these requirements have implications for the

possible quantum impurity solvers that can be used in SEET or DMFT procedures.

For molecules, if chemical accuracy is desired, any modification of the realistic Hamiltonian containing full one- and two-body interactions to a simplified Hamiltonian including only a subset of all interactions may have a detrimental effect [65]. Many of the off-diagonal elements of the realistic Hamiltonian can have a similar magnitude to the diagonal elements, thus presenting no justification for neglecting them and keeping only the diagonal elements. Moreover, solutions obtained by such modifications usually cannot be improved in a systematic manner. Consequently, for molecular calculations the safest option for preserving chemical accuracy is to use a class of quantum impurity solvers that employ a full realistic Hamiltonian for the impurity orbitals. This requirement allows us to use two classes of solvers: either based on CI expansions or continuous-time hybridization expansion quantum Monte Carlo (CT-HYB QMC [66–69]).

Solvers based on CI expansions such as restricted active space CI (RASCI) allow us to comfortably include around 8 orbitals in the impurity and around $16-24$ bath orbitals. They usually work in the zero (or low) temperature formulation and require a bath discretization that can be a potential source of errors. The hybridization expansion solvers can handle an infinite bath but face difficulties with Monte Carlo sign problem that gets especially pronounced for non-diagonal hybridizations and low temperatures. Consequently, for both classes of solvers non-diagonal hybridizations lead to problems.

For CI solvers non-diagonal hybridizations lead to a large number of bath orbitals necessary to fit the discrete bath accurately since a given number of bath orbitals has to not only minimize the error for the diagonal $[\mathbf{\Delta}(i\omega)]_{ii} - [\mathbf{\Delta}^{fit}(i\omega)]_{ii}$ but also for the off-diagonal $[\mathbf{\Delta}(i\omega)]_{ij} - [\mathbf{\Delta}^{fit}(i\omega)]_{ij}$ hybridization elements.

For hybridization expansion solvers, non-diagonal hybridizations lead to long computation times due to sign problem. Thus, a crucial challenge is to define a set of

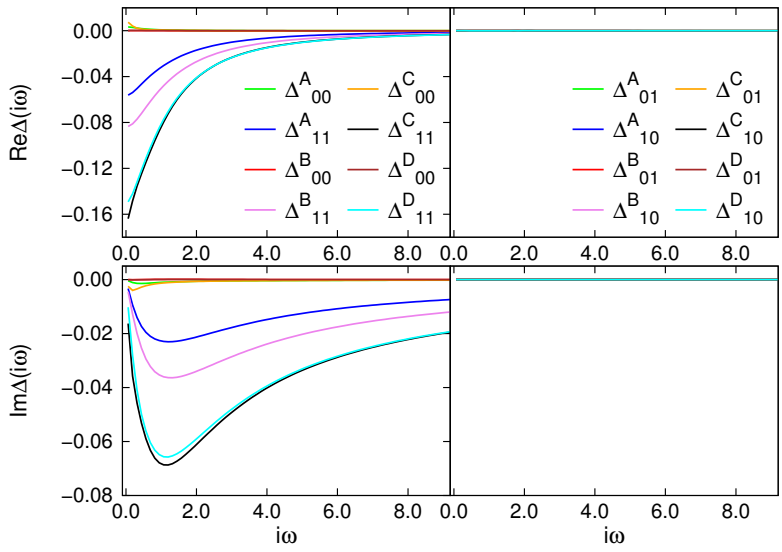

Figure 7.2: Real and imaginary parts of diagonal (left) and off-diagonal (right) hybridization matrix elements $[\mathbf{\Delta}(i\omega)]_{ij}$ in the NO basis for all the impurities present in the H_8 chain in the 6-31G basis set at $\beta = 50$ a.u. Note that the off-diagonal hybridization elements are zero.

orbitals that either diagonalizes hybridization or minimizes its off-diagonal elements for a range of frequencies.

To gain insight into the possibility of making the hybridization as diagonal as possible, we plot in Figs. 7.2 and 7.3 hybridizations for different impurities in the H_8 chain in the 6-31G basis [70] using different selection schemes presented in Fig. 7.1. Spatially localized orbitals are obtained using the Boys localization method implemented in GAUSSIAN 09 [71]. It is evident that NOs yield a diagonal hybridization while Boys orbitals yield hybridization containing off-diagonal elements of large magnitudes. This insight explains some of our observations that NOs are quite advantageous for SEET calculations since the bath fitting procedure can be done using relatively few bath sites.

We also consider how different orbital basis, by influencing hybridization behavior, can change the performance of CT-HYB QMC, in Tabs. 7.1 and 7.2. Let us note in passing that for a minimal basis (STO-3G [70]), SAOs are very similar to Boys orbitals and the off-diagonal elements of hybridization are significant for SAOs. It is evident

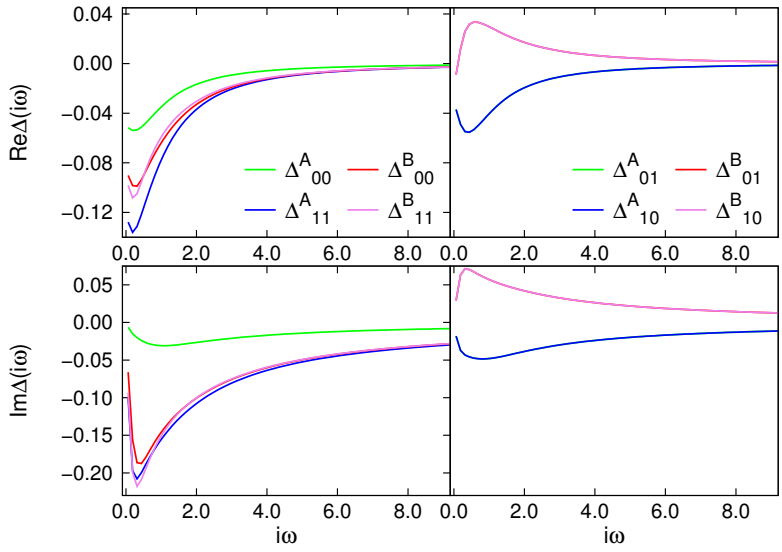

Figure 7.3: Real and imaginary parts of diagonal (left) and off-diagonal (right) hybridization matrix elements $[\mathbf{\Delta}(i\omega)]_{ij}$ in Boys orbitals for the impurities A and B present in the H_8 chain in the 6-31G basis set at $\beta = 50$ a.u. Note that the off-diagonal hybridization elements are of a similar magnitude as the diagonal elements.

that CT-HYB QMC has a much worse average sign and larger perturbation order in orbital bases that yield non-diagonal hybridizations, thus making such calculations particularly challenging especially at low temperatures since the average perturbation order in CT-HYB QMC calculations grows when temperature decreases. We observe that even for high temperatures the difference in CT-HYB QMC performance is present and the NO basis is still favored. Moreover, this difference in performance is independent of the number of orbitals present in a given basis and the trend is maintained when a larger orbital basis such as 6-31G is employed. Our observations indicate that for molecular examples NOs are advantageous when used with the CT-HYB QMC solver since due to the minimization of the sign problem they lead to a significant computational speed up. A similar conclusion was reached in a CT-HYB QMC study of the Hubbard model [72] where the Monte Carlo sign error was minimized by a canonical transformation that brought the hybridization matrix to a diagonal form.

In CI calculations, NOs lead to fewer bath orbitals—also resulting in an increased

Table 7.1: Different values of the average sign and perturbation order (PO) for four possible impurities present in SAO and NO bases for the H_8 molecule in the STO-3G basis set. Fig. 7.1 illustrates our impurity selection scheme using SAOs or Boys orbitals (spatial selection) and NOs (occupation selection). TRIQS [73] program was used to perform CT-HYB calculations.

β	Basis	Impurity A		Impurity B		Impurity C		Impurity D	
		$\langle$sign$\rangle$	$\langle$PO$\rangle$	$\langle$sign$\rangle$	$\langle$PO$\rangle$	$\langle$sign$\rangle$	$\langle$PO$\rangle$	$\langle$sign$\rangle$	$\langle$PO$\rangle$
10	SAO	0.688	4	0.653	6	0.653	6	0.688	4
10	NO	0.845	0	0.705	1	0.478	3	0.500	2
50	SAO	0.232	16	0.262	28	0.262	28	0.232	16
50	NO	0.977	2	0.982	3	0.971	4	0.980	4
100	SAO	0.050	32	0.065	55	0.065	55	0.055	32
100	NO	0.914	4	0.946	6	0.970	8	0.978	9

computational efficiency; however, here the savings are not so dramatic since including additional bath orbitals in truncated CI schemes does not result in a significant cost increase.

It is important to showcase one more aspect necessary for a high accuracy quantum impurity solver for realistic problems. A quantum impurity solver capable of treating multiple regimes from weakly to strongly correlated ones, should be able to treat multiple partially occupied orbitals present in the impurity+bath system. To illustrate this statement, in Tab. 7.3, we list impurity+bath occupations (8 impurity and 8 bath orbitals) for the H_{10} chain in the cc-pVDZ basis (with a total of 50 orbitals). It is evident that for short interatomic distances this impurity+bath system has very few partial occupations, however for the stretched geometries, the number of partially occupied orbitals is significant. Consequently, if quantum chemistry methods are used as solvers for the impurity problems, they should be capable of treating many partially occupied orbitals - prompting us to conclude that single reference methods will generally not be capable of treating these impurity problems successfully.

Table 7.2: Different values of the average sign and perturbation order (PO) for four possible impurities present in Boys and NO bases for the H_8 molecule in 6-31G basis set. Fig. 7.1 illustrates our impurity selection scheme using SAOs or Boys orbitals (spatial selection) and NOs (occupation selection). TRIQS [73] program was used to perform CT-HYB calculations.

β	Basis	Impurity A		Impurity B		Impurity C		Impurity D	
		$\langle$sign$\rangle$	$\langle$PO$\rangle$	$\langle$sign$\rangle$	$\langle$PO$\rangle$	$\langle$sign$\rangle$	$\langle$PO$\rangle$	$\langle$sign$\rangle$	$\langle$PO$\rangle$
10	Boys	0.652	3	0.730	5	0.730	5	0.652	3
10	NO	0.633	1	0.468	3	0.377	3	0.370	4
50	Boys	0.009	21	0.072	28	0.072	28	0.009	21
50	NO	0.919	2	0.922	3	0.931	5	0.964	8
100	Boys	0.000	42	0.004	56	0.004	56	0.000	42
100	NO	0.722	5	0.741	7	0.823	10	0.907	16

Table 7.3: Orbital occupations from RASCI calculations for an impurity+bath problem consisting of 8 active (impurity) and 8 bath orbitals at $R = 1.8$ and 3.6 a.u for the H_{10} chain in the cc-pVDZ basis. The total number of electrons in the impurity+bath problems at $R = 1.8$ and 3.6 a.u. are 8 and 16, respectively. The SEET calculation was performed in the NO basis.

Orbitals	R(H-H) = 1.8 a.u.	R(H-H) = 3.6.a.u
1	1.9827	2.0000
2	1.9693	2.0000
3	1.9412	2.0000
4	1.8699	2.0000
5	0.1377	1.8220
6	0.0577	1.7618
7	0.0275	1.6206
8	0.0139	1.3374
9	0.0001	0.6679
10	0.0000	0.3804
11	0.0000	0.2375
12	0.0000	0.1723
13	0.0000	0.0000
14	0.0000	0.0000
15	0.0000	0.0000
16	0.0000	0.0000

7.3 Numerical illustrations

Unless otherwise noted, the ORCA program [74] was used for all calculations using standard methods, e.g. FCI, complete active space self-consistent field (CASSCF) [75–77], and NEVPT2. The local modified version of the DALTON code [78] was employed to generate an RHF input necessary for GF2 and to evaluate (full) CI active space Green's functions [34]. Throughout this article, to compute potential energy curves accurately and to converge the electronic energy to 5×10^{-4} a.u. with respect to the inverse temperature β and the number of frequencies w_{max}, we employ different values of β and w_{max} along a single potential energy curve that yield a converged energy for different geometry points. We denote our method as SEET(CI/GF2)[$m \times n$o], where m and n are number of active spaces (impurity+bath problems) and number of orbitals in active spaces (number of impurity orbitals), respectively. The RASCI solver will be used when the impurity+bath problem is intractable with the FCI solver. Note that all the chains studied in this Chapter are non-periodic linear configurations with open boundary conditions.

7.3.1 Non-local self-energy and screened interactions

First, let us show that SEET, where the non-local GF2 self-energy is included in the DMFT-like iterations, yields numerically very similar results to a DMFT procedure with screened interactions. As an example, we consider the H_6 chain in the STO-6G basis [79]. All SEET calculations were performed in the SAO basis. In this work, we employ a statically screened impurity model, in which the screened interaction was obtained using GF2 and is defined via Eq. 7.21 at several chosen τ points. The effective impurity model present during the DMFT self-consistency is then solved using the FCI impurity solver.

The left panel of Fig. 7.4 shows the on-site bare Coulomb interaction and screened

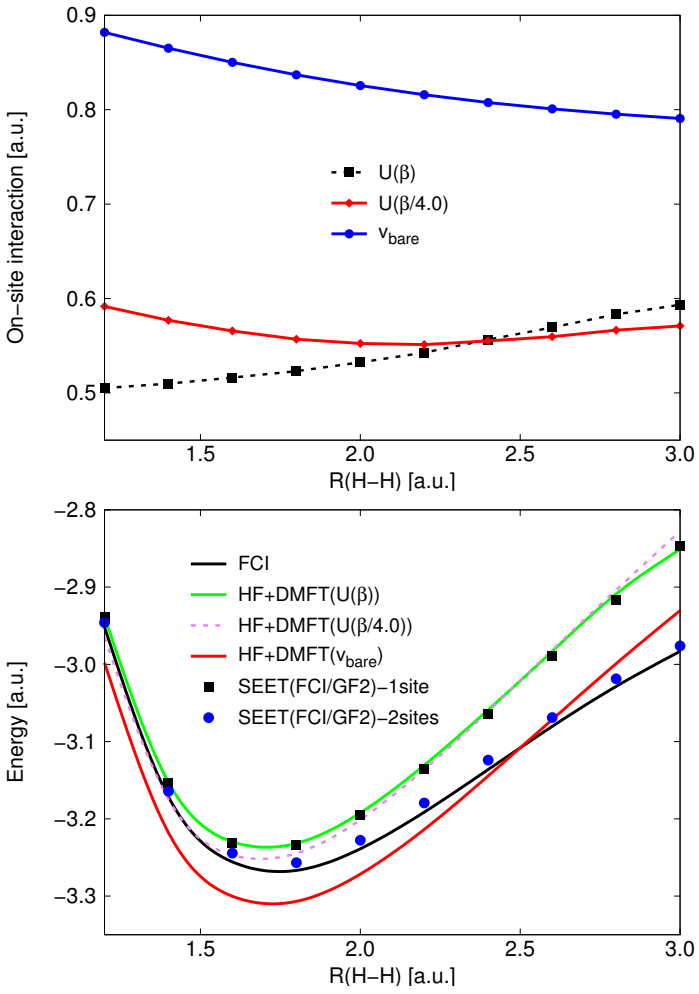

Figure 7.4: Upper panel: The on-site screened interaction $U(\tau)$, with $\tau = \beta$ and $\beta/4.0$, and bare Coulomb interaction as functions of the interatomic distance for the H_6 chain in the STO-6G basis. Lower panel: Potential energy curves of the H_6 chain in the STO-6G basis calculated using on-site bare and screened interactions. Results from FCI, SEET(FCI/GF2) with a single-site and two sites impurities are also provided for comparison.

interaction $U(\tau)$ at $\tau = \beta$ and $\beta/4.0$ as a function of the interatomic distance R. Note that the on-site bare Coulomb interaction in the SAO basis is not constant and changes with the distance. The on-site screened interaction should be equal to the bare interaction at large distances when the non-local interactions between atoms vanish. For short interatomic distances, due to the presence of large non-local interactions, the screened interaction is about twice smaller than the bare interaction.

The potential energy curves calculated with the on-site bare interaction, screened interactions, and SEET(FCI/GF2) are shown in the right panel of Fig. 7.4. The curves from FCI and SEET(FCI/GF2) with one site and two sites impurities are also plotted for comparison. It is well-known that the HF+DMFT curve with an on-site bare interaction falls bellow the FCI result around the equilibrium geometry [65]. When the on-site screened interactions $U(\beta)$ or $U(\beta/4.0)$ are used, the curves move up closer to the FCI result around the equilibrium.

Interestingly, SEET(FCI/GF2)-1site gives a very similar curve to that of HF+DMFT with $U(\beta)$, indicating the equivalence between using the non-local self-energy and screened interactions. To get more accurate results, a larger number of sites than a single site treated by accurate many-body solvers are required. While, as mentioned previously, the extension of the on-site screened interaction to multiple-orbital spaces may not be straightforward, SEET(FCI/GF2) with larger number of impurity orbitals, for example two sites, can be performed trivially and, as indicated by our results, it significantly improves upon the results of SEET with a single site.

Since the difference between $U(\beta)$ and $U(\beta/4.0)$ curves is relatively small but not negligible, using statically screened interactions may not be very robust if chemical accuracy is desired. To fully reach chemical accuracy, a more complicated procedure needs to be carried out to evaluate the dynamically screened interaction $U(\tau)$ for all τ points, as is done in condensed matter physics [58]. However, this procedure leads to a computational bottleneck for realistic molecules where the active space is usually large,

thus a significant memory would be necessary to store the $U_{ijkl}(\tau)$ matrix for larger orbital spaces. In contrast, realistic molecular SEET with the non-local self-energy instead of screened interactions requires storing only $[\mathbf{\Sigma}^{GF2}(\tau)]_{ij}$ matrix thus making it less memory demanding.

7.3.2 SEET outer loop: non-local self-energy relaxation

As we have mentioned in the SEET self-consistency description, SEET can be done as a *one-shot* procedure where $\mathbf{\Sigma}^{GF2}_{non-local}(i\omega)$ coming from the initial self-consistent GF2 is not updated, or can be performed fully self-consistently where the non-local GF2 self-energy is updated during subsequent outer iterations involving GF2. Here, we would like to compare the one-shot and self-consistent procedures.

In systems where the entanglement between atoms is equivalent (for instance, in a hydrogen ring), separating the whole system into spatial fragments in the stretched regime will give rise to an incompatibility between the local self-energy from a high level theory and the non-local self-energy from a low level theory. Moreover, GF2 is not providing the self-energy that is accurate enough since the correlations are strong in the stretched regime. Consequently, in this regime, it is essential to carry out the outer iterations and update $\mathbf{\Sigma}^{GF2}_{non-local}(\tau)$ while starting from the zeroth order Green's function that contains the strong correlation effects included due to the DMFT-like inner SEET iterations.

To reveal the importance of the non-local self-energy relaxation, especially, for the spatial fragment based embedding scheme, we plot the potential curves from SEET(FCI/GF2)[3×2o]/SAO calculations for the H_6 ring and the H_6 chain in the STO-6G basis set. These results are summarized in Fig. 7.5.

Around the equilibrium, for both the H_6 ring and H_6 chain, one-shot and self-consistent GF2-DMFT schemes give almost identical results since the effect of non-local self-energy relaxation is negligible in the weakly correlated regime. When the inter-

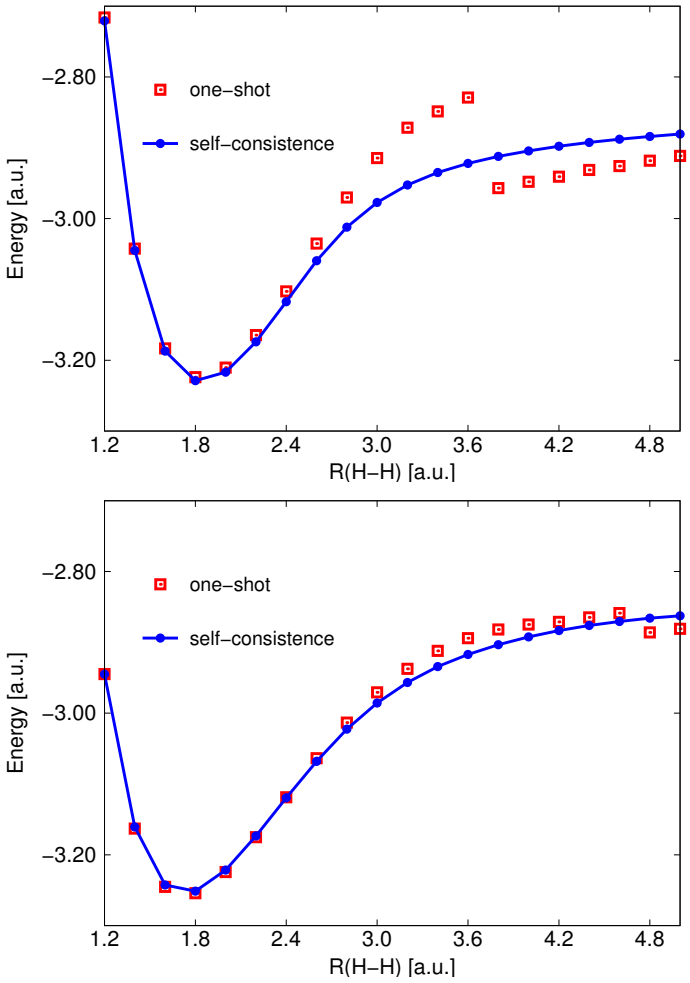

Figure 7.5: Potential energy curves for the H_6 ring (upper panel) and H_6 chain (lower panel) from the one-shot and self-consistent SEET(FCI/GF2)[3×2o]/SAO calculations. The STO-6G basis set was used.

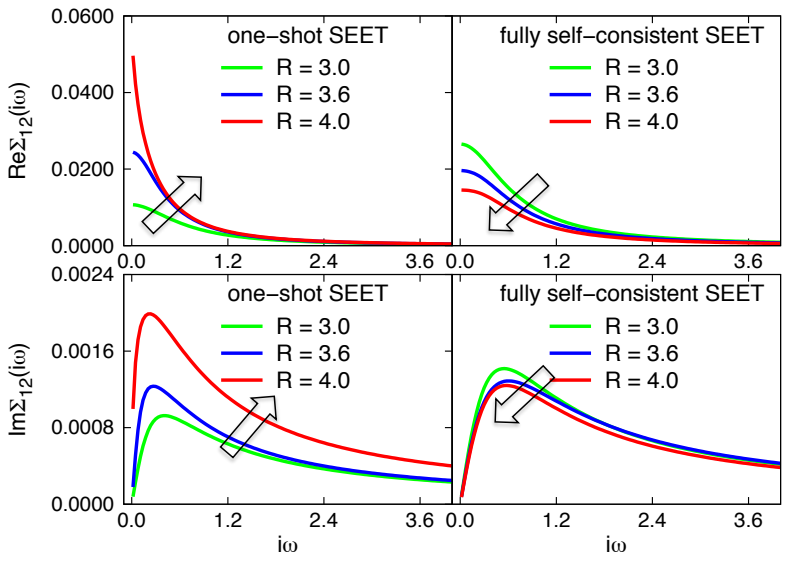

Figure 7.6: Real (upper panel) and imaginary (lower panel) parts of the non-local self-energy $\Sigma_{12}(i\omega)$ after the one shot (left) and fully self-consistent (right) SEET(FCI/GF2)[3×2o]/SAO calculation for the H_6 ring in the STO-6G basis. Arrows indicate the overall trend of the non-local self-energy with the increasing H-H bond length.

atomic distance is large, the one-shot and self-consistent curves significantly differ from each other and the former breaks down at the dissociation limit. A smooth dissociation curve is achieved when the GF2 non-local self-energy is relaxed in the presence of the FCI local self-energy. Obviously, the effect of the non-local self-energy relaxation is more pronounced for the H_6 ring than for the H_6 chain since the entanglement between unit cells in the former is much stronger than that in the latter.

The relaxation of the non-local self-energy is further explored in Fig. 7.6, where we examine the case of H_6 ring. In principle, the non-local self-energy should decrease with the increasing inter-fragment distance since the non-local two-electron integrals v_{ijkl} where i, j, k, l belong to different fragments/orbitals should be vanishing. In practice, however, the non-local integrals do not decay fast enough giving rise to a quantitatively inaccurate GF2 self-energy in the stretched atoms regime. Consequently, the non-local GF2 self-energy erroneously increases as a function of bond distance instead of decreasing, see Fig. 7.6. The gradual decrease can only be observed after employing a

fully self-consistent SEET when the non-local GF2 self-energy is relaxed in the presence of the FCI self-energy accounting correctly for the strong correlations present at large bond distances. The fully self-consistent SEET yields a smooth transition from the weakly to strongly correlated regime as shown in Fig. 7.5.

7.3.3 Energy and spatial domain based embedding

The embedding procedure can be performed either in the energy or spatial domain. In the former the active orbitals are chosen as the most important NOs, whereas in the latter the whole system is split into different spatial fragments (SAOs/RNOs) that are physically/chemically meaningful.

At first, we consider the H_6 chain in the TZ basis set [80] as shown in the left panel of Fig. 7.7. An excellent agreement between SEET in NO basis and FCI curve can be observed when a full active space composed of six orbitals, SEET(FCI/GF2)[6o]/NO, is used. Now, let us consider how splitting the full active space into different groups of NOs and RNOs (3×2o means three groups of two orbitals) is influencing the results. At short distances, both SEET(FCI/GF2)[3×2o] in NO and RNO bases give very similar results. However, in the stretched regime, energies from the calculation in the RNO basis are much closer to the FCI curve than these from the calculation in the NO basis.

To gain an insight into the behavior of different orbital bases at dissociation, in the right panel of Fig. 7.7, we plot the occupations of six valence orbitals for the H_6 chain in the TZ basis. We compare the orbital occupations from SEET(FCI/GF2)[3×2o] in both RNO and NO bases to the exact ones calculated using FCI.

Note that there is a degeneracy of two pairs of active orbitals in the RNO basis corresponding to the two ends of the chain. FCI yields occupation numbers that smoothly transit from the weakly to strongly correlated regime as the bond length increases. At short distances, i.e. $R \leq 2.0$ a.u., NO occupancies are quite close to the FCI ones, while those in the RNO basis have slightly overestimated partial occupations.

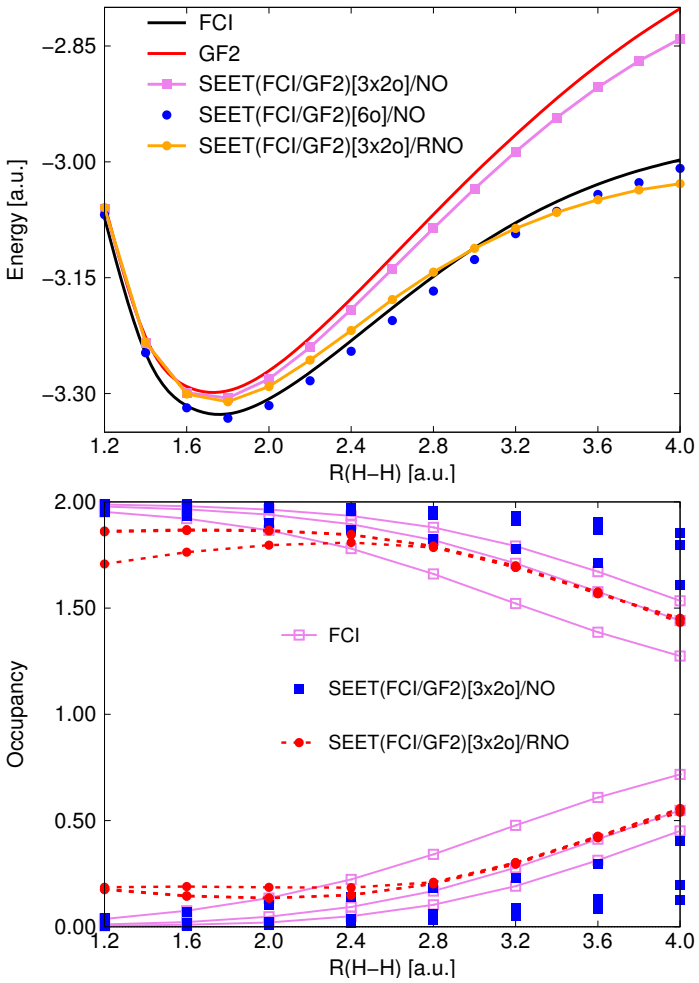

Figure 7.7: Upper panel: potential energy curve for the H_6 chain in the TZ basis. Lower panel: Orbital occupations as a function of bond length.

This difference can be understood in the following way. Since the correlation in the short bond regime is weak and the orbitals are mostly unoccupied or doubly occupied, SEET in the NO basis with the active space that is split into several groups is able to capture all the correlation effects well. In fact, even GF2 alone is good enough to describe correlation effects in this regime. However, since in the short bond regime in the RNO basis the coupling between fragments is non-negligible, splitting the molecule into several fragments leads to missing the inter-fragment bonding, thus leading to less accurate results.

Upon bond stretching, fragments become nearly isolated and this is reflected by the degeneracy of all pairs of active orbitals in the RNO basis. Evidently, in the RNO basis the occupation numbers in the strongly correlated regime are almost parallel to the FCI ones. Thus, SEET in the RNO basis can yield a dissociation curve closely following the FCI one at long distances where the correlations are strong. In the NO basis, splitting the full active space into orbital groups is not sufficient to correctly describe the physics at the dissociation limit. In this case, only the highest occupied molecular orbital (HOMO) and the lowest unoccupied molecular orbital (LUMO) have reasonable occupations, while all the other orbitals have significantly different occupations from the FCI ones.

We now investigate a 2×4 hydrogen lattice, which is a more complicated example than the H_6 chain. The minimal STO-6G basis was used, so that dividing the whole system into spatial fragments can be done in the SAO basis. Fig. 7.8 shows the potential energy curves of 2×4 hydrogen lattice from SEET(FCI/GF2)[2×4o] in NO and SAO bases along with GF2 and FCI dissociation curves. For comparison, we also plot the curve from SEET(FCI/HF)[2×4o] in the SAO basis, i.e. non-local self-energy $\mathbf{\Sigma}^{GF2}_{non-local}(i\omega)$ is not taken into account for this case. As mentioned previously, due to the lack of self-energy terms describing non-local correlations, around equilibrium the energy from SEET(FCI/HF) with bare interactions is lower than FCI one, while

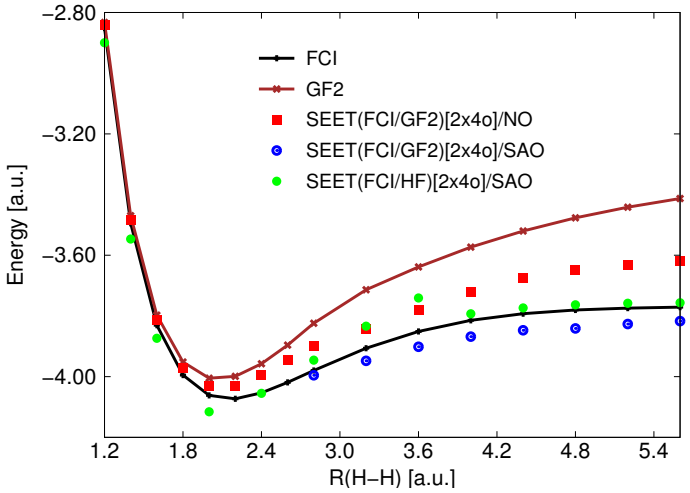

Figure 7.8: Potential energy curves for the 2×4 hydrogen lattice in the STO-6G basis.

in the intermediate regime the SEET(FCI/HF) energy is above the FCI one. Beyond the dissociation limit, the lattice is separated into isolated atoms, thus the electron interaction in such a system is actually just the on-site bare interaction. Therefore, in the dissociation limit, SEET(FCI/HF) gives energies in a good agreement with FCI results, however, the SEET(FCI/HF) curve is not smooth and has a discontinuity when a transition to the stretched regime happens. In the short bond region, energies from SEET(FCI/GF2)[2×4o] in the NO basis are better than GF2 energies and quite close to FCI ones, whereas SEET(FCI/GF2)[2×4o] in the SAO basis has difficulty converging because of the large entanglement between fragments. In contrast, far away from the equilibrium, SEET(FCI/GF2) energies in the SAO basis are much closer to the exact ones than SEET(FCI/GF2) energies in the NO basis. However, since GF2 overestimates the non-local self-energy between unit cells at long distances, the SAO curve is below FCI.

7.3.4 Comparison with ground state wave-function methods

After discussing technical aspects of SEET, now we turn to showcase quantitative accuracy of SEET as compared to standard quantum chemistry ground state wave-function

methods. As mentioned previously, SEET(FCI/GF2) when a full active space is used can be directly compared to methods such as CASPT2 or NEVPT2 since in both of these methods, in an analogous manner to SEET, the strongly correlated (or active) orbitals are described by a higher level method than the weakly correlated (inactive) orbitals. In cases of CASPT2, NEVPT2, and SEET(FCI/GF2) the perturbative description involves a low level perturbative expansion. Therefore, it is necessary and interesting to make a numerical comparison between SEET(FCI/GF2) and CASPT2 or NEVPT2. We have done such comparison in our earlier work [24] but only for SEET in the NO basis.

7.3.5 $(LiH)_2$ and $(LiH)_4$ chains in TZ basis

Here, we further analyze SEET results in the RNO basis. In Fig. 7.9, we present potential energy curves of $(LiH)_2$ and $(LiH)_4$ chains in the TZ basis. For the RNO basis, $(LiH)_n$ chain (with $n = 2, 4$) is divided into n LiH fragments and the active orbitals that are used to construct the Anderson impurity models are constructed from two valence orbitals of each fragment. Both CASSCF and NEVPT2 correctly describe the dissociation. While GF2 yields accurate energies around the equilibrium, its curve is not parallel to the FCI one at long distances. However, when static correlation is properly treated using SEET(FCI/GF2), in both bases NO and RNO, the dissociation regime is described correctly. In particular for $(LiH)_2$, as seen in the left panel of Fig. 7.10, although the SEET(FCI/GF2)[4o] in the NO basis yields a curve below the exact one, errors are of the same order as those of NEVPT2(4e,4o). SEET(FCI/GF2)[2×2o] in the RNO basis closely follows the NEVPT2 curve for all the distances considered here, thus having an error essentially equivalent to NEVPT2.

For $(LiH)_4$, we cannot evaluate FCI, thus we compare our results against NEVPT2. In the right panel of Fig. 7.10, we plot the error in the energy per fragment for $(LiH)_2$ and $(LiH)_4$ molecules when compared to NEVPT2 energies per fragment. Interestingly,

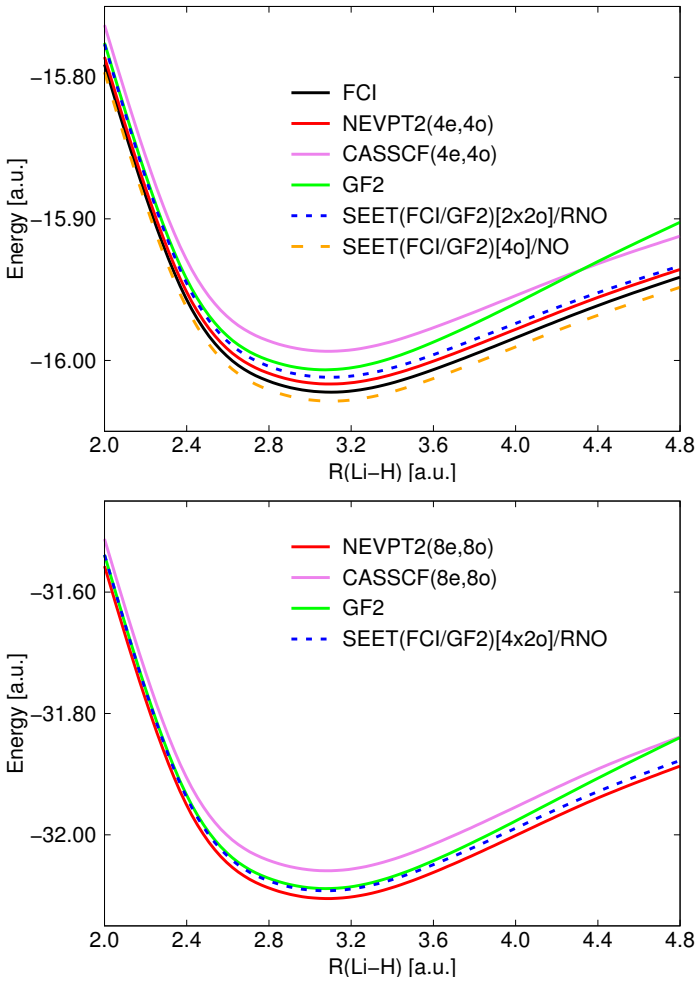

Figure 7.9: Potential energy curves evaluated using different methods for $(LiH)_2$ (upper panel) and $(LiH)_4$ (lower panel) chains in the TZ basis.

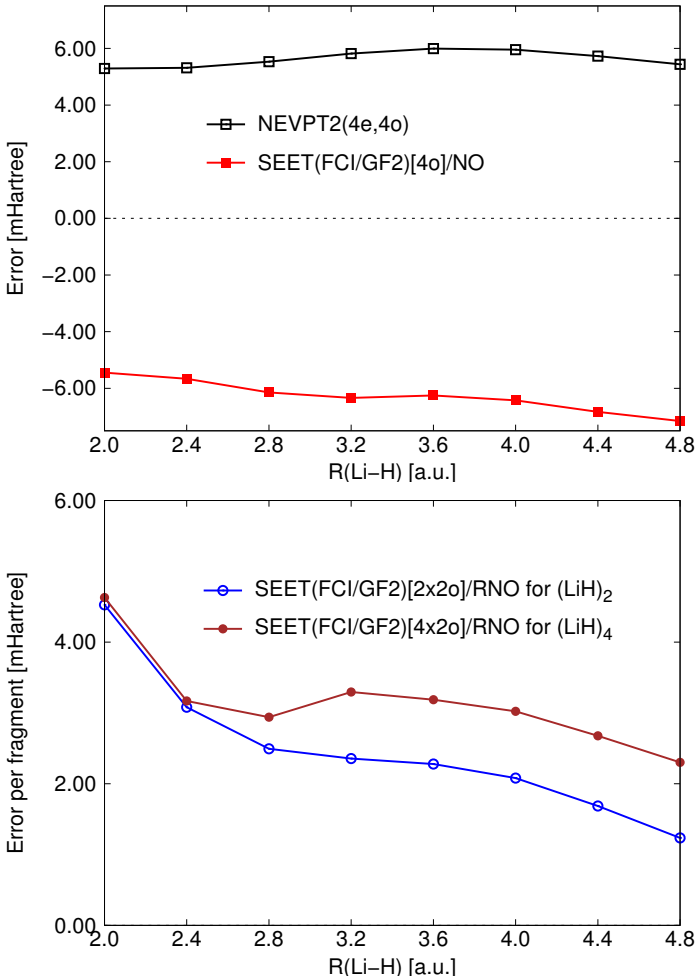

Figure 7.10: Upper panel: $(\mathrm{LiH})_2$ chain in the TZ basis. Energy errors (in mHartree) $E_{\mathrm{FCI}} - E_{\mathrm{X}}$ for X = NEVPT2(4e,4o) and SEET(FCI/GF2)[4o]/NO as a function of bond distances. Lower panel: Energy errors per fragment (in mHartree) $(E_{\mathrm{NEVPT2}} - E_X)/N$ for SEET in the RNO basis for $N = 2, 4$ for both $(\mathrm{LiH})_2$ and $(\mathrm{LiH})_4$ in the TZ basis.

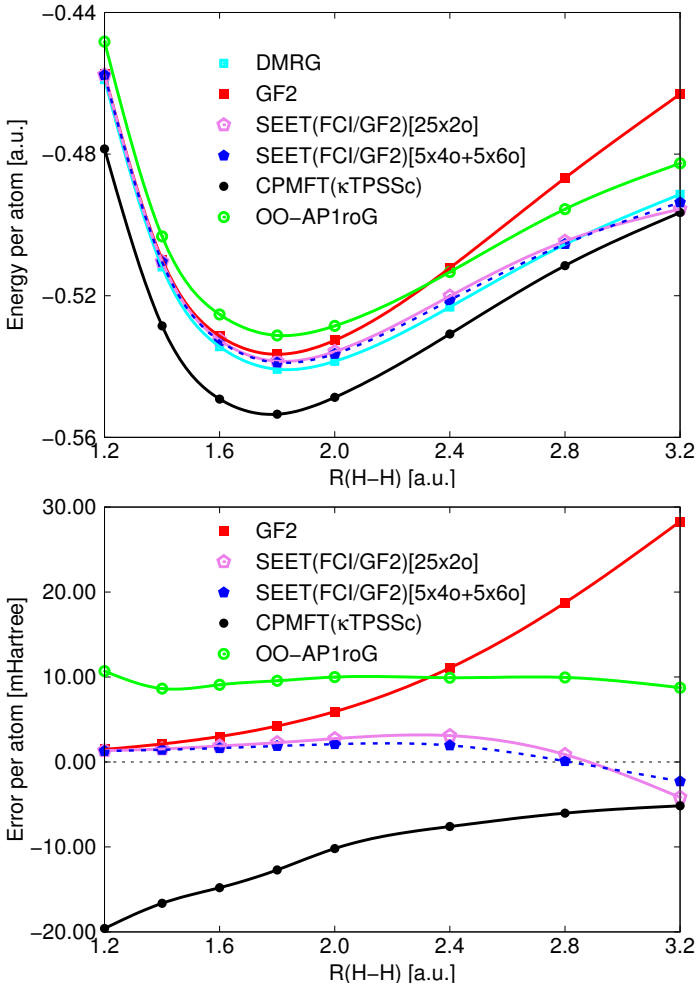

Figure 7.11: Upper panel: potential energy curves for the H_{50} chain in the STO-6G basis. DMRG, CPMFT(κTPSSc), and OO-AP1roG data are taken from Refs. [81–83]. Lower panel: energy error per atom (in mHartree) with respect to the DMRG data.

the difference between errors per fragment of $(LiH)_2$ and $(LiH)_4$ cases are very small ($\leq$ 1.0 mHartree), indicating that the correct description of SEET(FCI/GF2) using LiH fragment as a repeating unit holds true regardless of the length of the system.

7.3.6 H_{50} chain in STO-6G basis

Now we test SEET(FCI/GF2) in the SAO basis on a well-known, non-trivial benchmark system, H_{50} chain in the STO-6G basis. The exact solution is available from DMRG calculations [81]. For a full comparison, we also present results from estab-

lished theories capable of targeting strongly correlated molecules such as the orbital-optimized antisymmetric product of 1-reference-orbital geminals (OO-AP1roG) [83] and the constrained-pairing mean-field theory combined with κTPSSc functional [CPMFT(κTPSSc)] [82]. Potential energy curves and errors relative to DMRG energies are displayed in the left and right panels of Fig. 7.11.

OO-AP1roG and CPMFT(κTPSSc) curves are far above and far below the DMRG reference, respectively. While the CPMFT(κTPSSc) curve displays huge non-parallelity errors near the equilibrium geometry, the OO-AP1roG curve remains nicely parallel to the DMRG curve. GF2 gives very good energies for short distances; however, it largely deviates from DMRG at long distances. SEET(FCI/GF2)[25×2o], where 25 Anderson impurities containing two impurity orbitals are embedded in the GF2 self-energy, yields a significantly improved energies at long distances when compared to GF2 alone. These errors can be further minimized when a SEET(FCI/GF2)[5×4o+5×6o] calculation is carried out.

7.3.7 H_{10} chain in cc-pVDZ basis

Here, we explore the concept of active space splitting where the full number of active orbitals is divided into several groups of orbitals used to build Anderson impurity models. To demonstrate that SEET is systematically improvable, when the number of orbitals used to build the impurities is increased, we performed calculations with different number of orbitals in the impurities for H_{10} chain in the cc-pVDZ basis [84]. The total number of orbitals in this basis set is 50 while the size of full active space is 10 orbitals. SEET results are summarized in Tab. 7.4 along with GF2, NEVPT2(10e,10o) and DMRG [85] energies for comparison. The DMRG data were computed using the BLOCK program [86, 87]. The errors relative to DMRG are shown in Fig. 7.12 as a function of bond length. At short distances ($R < 2.0$ a.u.), GF2 energies are comparable to those from the NEVPT2(10e,10o) calculation. Upon bond stretching,

Table 7.4: Potential energies (in a.u.) as a function of bond distance (in a.u.) for the H_{10} chain in the cc-pVDZ basis. Energies from GF2 and SEET with different number of impurity orbitals building the active space are compared to NEVPT2(10e,10o) and DMRG energies [85]. FCI solver is used to treat [2o+2×4o] and [4o+6o] impurities, while RASCI solver is used for the [2o+8o] impurity. The non-parallelity error [NPE] (a.u.) which is the difference between the largest and smallest errors with respect to DMRG references are also provided.

R(H-H)	GF2	SEET(CI/GF2)			NEVPT2(10e,10o)	DMRG
		[2o+2×4o]	[4o+6o]	[2o+8o]		
1.4	–5.367 9	–5.380 6	–5.385 6	–5.388 5	–5.358 9	–5.408 7
1.6	–5.525 5	–5.540 0	–5.547 7	–5.552 9	–5.520 6	–5.570 2
1.8	–5.564 6	–5.582 1	–5.593 6	–5.598 8	–5.570 3	–5.614 1
2.0	–5.539 5	–5.559 3	–5.569 7	–5.583 2	–5.551 8	–5.594 9
2.4	–5.403 9	–5.431 7	–5.445 4	–5.463 2	–5.442 9	–5.476 1
2.8	–5.235 2	–5.271 4	–5.292 1	–5.320 4	–5.305 7	–5.334 4
3.2	–5.074 1	–5.119 3	–5.148 7	–5.192 9	–5.185 3	–5.212 5
3.6	–4.935 3	–4.995 0	–5.032 8	–5.082 2	–5.095 4	–5.123 8
NPE	0.147 7	0.100 8	0.068 6	0.028 8	0.021 5	

when compared to DMRG, the GF2 error strongly increases, while NEVPT2(10e,10o) one slowly decreases. We can see that the errors of GF2 are significantly reduced when a SEET(FCI/GF2)[2o+2×4o] calculation is carried out. For stretched distances, a systematic reduction of errors can be observed when the number of impurity orbitals is systematically enlarged starting from (2o+2×4o), (4o+6o), to (2o+8o). Interestingly, this error reduction with an increasing number of impurity orbitals is very systematic and is independent of the distances on the potential energy curve.

Consequently, one can expect that in cases where the number of active space orbitals is too large to be treated within one impurity, it is possible to split the active space orbitals among several impurities and systematically improve the answer. We would like to stress that this systematic improvement will become crucial for systems where the exact answer is unknown, thus the only way of assessing if the level of accuracy given by SEET is sufficient will be coming from internal SEET criteria and checking if

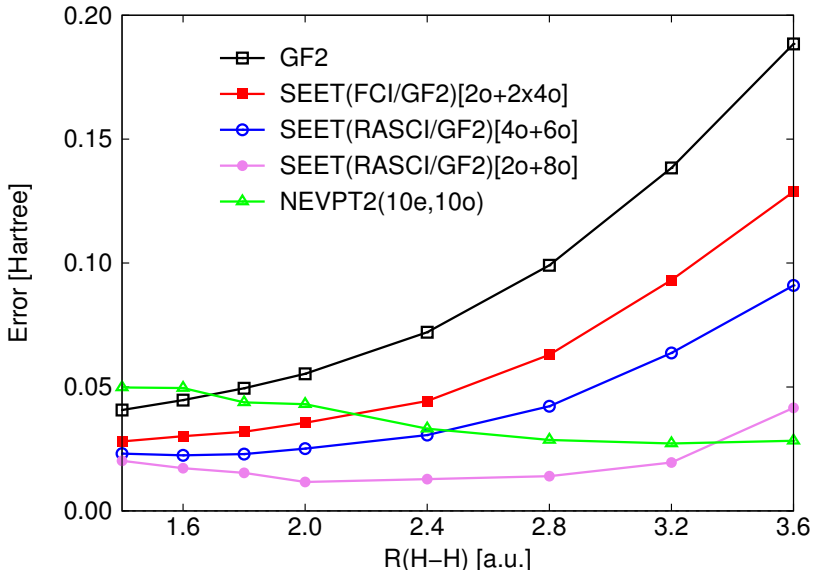

Figure 7.12: Errors in energy (in a.u.) with respect to DMRG reference as a function of R(H-H) for GF2, SEET with different active spaces in the NO basis, and NEVPT2(10e,10o). All energies (in a.u.) are presented in Tab. 7.4.

the answer obtained does not change drastically upon enlarging the number of impurity orbitals.

7.4 Conclusions

In this Chapter, we have presented a detailed discussion of the molecular Green's function quantum embedding scheme called SEET. The self-energy separation characteristic for SEET onto strongly correlated/active/subsystem and weakly correlated/inactive/environment parts is completely general and does not specify how the self-energies for these fragments will be evaluated in practice. While many schemes are possible, in this Chapter we used a scheme where first the whole molecule is treated by the perturbative self-consistent GF2 approach and then selected strongly correlated orbitals are used to build impurity+bath models that are solved in a DMFT-like procedure in the presence of the self-energy coming from weakly correlated/inactive/environment orbitals.

We aim for SEET to be systematically improvable, without empirical parameters, and reaching chemical accuracy. Consequently, we discussed many aspects of SEET that were developed by us to fulfill these strict demands. SEET is a Green's function method capable not only of delivering ground state energies but also many more physically relevant quantities such as free energies, ionization potentials (IP) and electron affinities (EA), or temperature-dependent magnetic susceptibility; however, here we focused on analyzing SEET results for small molecular examples where multiple ground state methods are known to give excellent results and ground state energies can be easily used to asses the SEET performance.

We started our considerations by explaining the double self-consistency loop present in SEET, where in the inner DMFT-like loop, the active space/impurity self-energy is updated using an accurate many-body solver. The outer loop requires an update of the self-energy for inactive orbitals performed here at the GF2 level; however other inexpensive *ab initio* methods could also be used for the calculation of the inactive orbitals self-energy. We observed, when analyzing numerical results, that this outer loop's self-energy update is crucial for classes of systems where the initial perturbative description was not quantitative.

Next, we have analyzed different schemes for selecting the strongly correlated/active/subsystem orbitals either based on the energy (occupations) or spatial criteria. We stress that in the energy (or occupation) scheme the strongly correlated orbital selection is done mainly based on the occupations of a correlated one-body density matrix, thus not only relying on any intuitive means. Moreover, in the results section for the H_{10} chain, we have demonstrated that the results of such a selection scheme can be systematically improved. We have also analyzed how different orbital bases, SAO, RNO, and NO influence SEET results. As expected, we found that the NO basis, which allows us easily to describe a large inter-orbital entanglement, yields very good results for equilibrium geometries; however, in the limit of separated fragments

bases that localize orbitals, such as SAOs/RNOs, yield better energies.

We discussed optimal impurity solvers that can be used with SEET, stressing that a full realistic Hamiltonian should be employed for strongly correlated orbitals if one desires systematically improvable and accurate results. Moreover, we have observed that suitable solvers (to be applicable in multiple regimes from weakly to strongly correlated) must be able to deal with near degeneracy and have to be able to treat multiple strongly correlated impurity orbitals. Finally, we highlighted the influence of the orbital basis onto the performance of impurity solvers by noticing that for molecular examples the NO basis seems to be particularly advantageous for the CT-HYB and RASCI solvers.

In SEET, the influence of the non-local interactions on the strongly correlated/active/embedded system is contained in the non-local self-energy evaluated at the perturbative level. We have compared SEET results with DMFT results where the non-local interactions are accounted for by employing the effective on-site interactions $U(\tau)$ present in the impurity model. We found that for molecular examples both methods give almost identical results, thus showing that SEET with bare Coulomb interactions present in the impurity model solved in the presence of self-energy coming from the inactive orbitals allows us to avoid the downfolding procedure and constructing an effective Hamiltonian for the impurity model.

Finally, we have performed multiple total energy comparisons against established quantum chemistry methods such as NEVPT2 and DMRG. For calculations in the NO basis and when a full active space is used, SEET can be considered as a Green's function analog of a CASPT2 or NEVPT2 procedure. We have demonstrated that when employing a full set of active space orbitals, SEET(CI/GF2) yields energies that are very close to NEVPT2. However, unlike CASPT2 or NEVPT2, SEET(CI/GF2) is a perturb and diagonalize scheme that does not require storing or evaluating of two-, three-, or four-body reduced density matrices and avoids the intruder state problem

present in CASPT2. Here, we focused on analyzing how the splitting of the full set of active orbitals into several impurities can be done in a systematic manner leading to an improvable and controlled procedure. We have shown that both in the spatial and energy domains, SEET results can be systematically improved by using multi-site impurities. We analyzed the spatial domain using the example of the H_{50} chain in STO-6G basis, while the energy domain was examined on the example of the H_{10} chain in the cc-pVDZ basis. Moreover, we have shown that SEET results in a small non-parallelity error when compared against DMRG and other established multi-reference methods. These results that indicate systematic trends provide us with a number of important self-contained assessment tools that in the future can be used to help us rigorously analyze the accuracy of SEET in the absence of known results.

We believe that the considerations and results presented here are further establishing SEET as a quantum embedding Green's function method that is controlled, systematically improvable, and not only able to reach accuracy comparable to the currently established active space quantum chemistry methods but also is flexible enough to yield spectral and thermodynamic quantities rather than just the ground state energies.

Bibliography

[1] G. Ghigo, B. O. Roos, and P. Å. Malmqvist, "A modified definition of the zeroth-order Hamiltonian in multiconfigurational perturbation theory (CASPT2)", *Chem. Phys. Lett.* **396**, 142 (2004).

[2] K. Andersson, P. Å. Malmqvist, B. O. Roos, A. J. Sadlej, and K. Wolinski, "Second-order perturbation theory with a CASSCF reference function", *J. Phys. Chem.* **94**, 5483 (1990).

[3] C. Angeli, R. Cimiraglia, S. Evangelisti, T. Leininger, and J.-P. Malrieu, "Introduction of n-electron valence states for multireference perturbation theory", *J. Chem. Phys.* **114**, 10252 (2001).

[4] C. Angeli, R. Cimiraglia, and J.-P. Malrieu, "n-electron valence state perturbation theory: A spinless formulation and an efficient implementation of the strongly contracted and of the partially contracted variants", *J. Chem. Phys.* **117**, 9138 (2002).

[5] R. J. Bartlett and M. Musiał, "Coupled-cluster theory in quantum chemistry", *Rev. Mod. Phys.* **79**, 291 (2007).

[6] B. Jeziorski and H. J. Monkhorst, "Coupled-cluster method for multideterminantal reference states", *Phys. Rev. A* **24**, 1668 (1981).

[7] B. Jeziorski and J. Paldus, "Spin-adapted multireference coupled-cluster approach: Linear approximation for two closed-shell-type reference configurations", *J. Chem. Phys.* **88**, 5673 (1988).

[8] M. Musiał, A. Perera, and R. J. Bartlett, "Multireference coupled-cluster theory: The easy way", *J. Chem. Phys.* **134**, 114108 (2011).

[9] I. Lindgren, "A coupled-cluster approach to the many-body perturbation theory for open-shell systems", *Int. J. Quant. Chem.* **14**, 33 (1978).

[10] D. Mukherjee, R. K. Moitra, and A. Mukhopadhyay, "Correlation problem in open-shell atoms and molecules", *Mol. Phys.* **30**, 1861 (1975).

[11] P. G. Szalay, T. Müller, G. Gidofalvi, H. Lischka, and R. Shepard, "Multiconfiguration self-consistent field and multireference configuration interaction methods and applications", *Chem. Rev.* **112**, 108 (2012).

[12] J. Gräfenstein and D. Cremer, "The combination of density functional theory with multi-configuration methods–CAS-DFT", *Chem. Phys. Lett.* **316**, 569 (2000).

[13] J. Gräfenstein and D. Cremer, "Development of a CAS-DFT method covering non-dynamical and dynamical electron correlation in a balanced way", *Mol. Phys.* **103**, 279 (2005).

[14] R. Pollet, A. Savin, T. Leininger, and H. Stoll, "Combining multideterminantal wave functions with density functionals to handle near-degeneracy in atoms and molecules", *J. Chem. Phys.* **116**, 1250 (2002).

[15] G. Li Manni, R. K. Carlson, S. Luo, D. Ma, J. Olsen, D. G. Truhlar, and L. Gagliardi, "Multiconfiguration pair-density functional theory", *J. Chem. Theory Comput.* **10**, 3669 (2014).

[16] R. K. Carlson, D. G. Truhlar, and L. Gagliardi, "Multiconfiguration pair-density functional theory: A fully translated gradient approximation and its performance for transition metal dimers and the spectroscopy of $Re_2Cl_8^{2-}$", *J. Chem. Theory Comput.* **11**, 4077 (2015).

[17] A. Georges, G. Kotliar, W. Krauth, and M. J. Rozenberg, "Dynamical mean-field theory of strongly correlated fermion systems and the limit of infinite dimensions", *Rev. Mod. Phys.* **68**, 13 (1996).

[18] G. Kotliar, S. Y. Savrasov, K. Haule, V. S. Oudovenko, O. Parcollet, and C. A. Marianetti, "Electronic structure calculations with dynamical mean-field theory", *Rev. Mod. Phys.* **78**, 865 (2006).

[19] T. Maier, M. Jarrell, T. Pruschke, and M. H. Hettler, "Quantum cluster theories", *Rev. Mod. Phys.* **77**, 1027 (2005).

[20] L. Hedin, "New method for calculating the one-particle Green's function with application to the electron-gas problem", *Phys. Rev.* **139**, A796 (1965).

[21] S. Biermann, F. Aryasetiawan, and A. Georges, "First-principles approach to the electronic structure of strongly correlated systems: Combining the GW approximation and dynamical mean-field theory", *Phys. Rev. Lett.* **90**, 086402 (2003).

[22] J. M. Tomczak, M. Casula, T. Miyake, F. Aryasetiawan, and S. Biermann, "Combined GW and dynamical mean-field theory: Dynamical screening effects in transition metal oxides", *EPL (Europhys. Lett.)* **100**, 67001 (2012).

[23] A. A. Kananenka, E. Gull, and D. Zgid, "Systematically improvable multiscale solver for correlated electron systems", *Phys. Rev. B* **91**, 121111 (2015).

[24] T. N. Lan, A. A. Kananenka, and D. Zgid, "Communication: Towards ab initio self-energy embedding theory in quantum chemistry", *J. Chem. Phys.* **143**, 241102 (2015).

[25] J. J. Phillips and D. Zgid, "Communication: The description of strong correlation within self-consistent Green's function second-order perturbation theory", *J. Chem. Phys.* **140**, 241101 (2014).

[26] N. E. Dahlen and R. van Leeuwen, "Self-consistent solution of the Dyson equation for atoms and molecules within a conserving approximation", *J. Chem. Phys.* **122**, 164102 (2005).

[27] L. J. Holleboom and J. G. Snijders, "A comparison between the Møller-Plesset and Green's function perturbative approaches to the calculation of the correlation energy in the many-electron problem", *J.Chem. Phys.* **93**, 5826 (1990).

[28] N. E. Dahlen, R. van Leeuwen, and U. von Barth, "Variational energy functionals of the Green function and of the density tested on molecules", *Phys. Rev. A* **73**, 012511 (2006).

[29] D. Van Neck, K. Peirs, and M. Waroquier, "Self-consistent solution of Dyson's equation up to second order for atomic systems", *J. Chem. Phys.* **115**, 15 (2001).

[30] K. Peirs, D. Van Neck, and M. Waroquier, "Self-consistent solution of Dyson's equation up to second order for open-shell atomic systems", *J. Chem. Phys.* **117**, 4095 (2002).

[31] A. A. Rusakov and D. Zgid, "Self-consistent second-order Green's function perturbation theory for periodic systems", *J. Chem. Phys.* **144**, 054106 (2016).

[32] A. R. Welden, A. A. Rusakov, and D. Zgid, "Exploring connections between statistical mechanics and Green's functions for realistic systems: Temperature dependent electronic entropy and internal energy from a self-consistent second-order Green's function", *J. Chem. Phys.* **145**, 204106 (2016).

[33] D. Zgid and G. K.-L. Chan, "Dynamical mean-field theory from a quantum chemical perspective", *J. Chem. Phys.* **134**, 094115 (2011).

[34] D. Zgid, E. Gull, and G. K.-L. Chan, "Truncated configuration interaction expansions as solvers for correlated quantum impurity models and dynamical mean-field theory", *Phys. Rev. B* **86**, 165128 (2012).

[35] E. Gull, P. Werner, O. Parcollet, and M. Troyer, "Continuous-time auxiliary-field Monte Carlo for quantum impurity models", *EPL (Europhys. Lett.)* **82**, 57003 (2008).

[36] E. Gull, P. Staar, S. Fuchs, P. Nukala, M. S. Summers, T. Pruschke, T. C. Schulthess, and T. Maier, "Submatrix updates for the continuous-time auxiliary-field algorithm", *Phys. Rev. B* **83**, 075122 (2011).

[37] S. R. White, "Density matrix formulation for quantum renormalization groups", *Phys. Rev. Lett.* **69**, 2863 (1992).

[38] S. R. White and R. L. Martin, "Ab initio quantum chemistry using the density matrix renormalization group", *J. Chem. Phys.* **110**, 4127 (1999).

[39] G. K.-L. Chan and M. Head-Gordon, "Exact solution (within a triple-zeta, double polarization basis set) of the electronic Schrödinger equation for water", *J. Chem. Phys.* **118**, 8551 (2003).

[40] G. K.-L. Chan, "An algorithm for large scale density matrix renormalization group calculations", *J. Chem. Phys.* **120**, 3172 (2004).

[41] D. Zgid and M. Nooijen, "The density matrix renormalization group self-consistent field method: Orbital optimization with the density matrix renormalization group method in the active space", *J. Chem. Phys.* **128**, 144116 (2008).

[42] Y. Kurashige and T. Yanai, "High-performance ab initio density matrix renormalization group method: Applicability to large-scale multireference problems for metal compounds", *J. Chem. Phys.* **130**, 234114 (2009).

[43] K. H. Marti and M. Reiher, "New electron correlation theories for transition metal chemistry", *Phys. Chem. Chem. Phys.* **13**, 6750 (2011).

[44] N. Bickers and D. Scalapino, "Conserving approximations for strongly fluctuating electron systems. I. Formalism and calculational approach", *Ann. Phys.* **193**, 206 (1989).

[45] N. E. Bickers, D. J. Scalapino, and S. R. White, "Conserving approximations for strongly correlated electron systems: Bethe-Salpeter equation and dynamics for the two-dimensional Hubbard model", *Phys. Rev. Lett.* **62**, 961 (1989).

[46] A. Liebsch and H. Ishida, "Temperature and bath size in exact diagonalization dynamical mean field theory", *J. Phys.: Condensed Matter* **24**, 053201 (2012).

[47] P. W. Anderson, "Localized magnetic states in metals", *Phys. Rev.* **124**, 41 (1961).

[48] E. R. Davidson, "The iterative calculation of a few of the lowest eigenvalues and corresponding eigenvectors of large real-symmetric matrices", *J. Comput. Phys.* **17**, 87 (1975).

[49] M. Capone, L. de' Medici, and A. Georges, "Solving the dynamical mean-field theory at very low temperatures using the Lanczos exact diagonalization", *Phys. Rev. B* **76**, 245116 (2007).

[50] H. Lin, J. Gubernatis, H. Gould, and J. Tobochnik, "Exact diagonalization methods for quantum systems", *Comput. Phys.* **7**, 400 (1993).

[51] A. A. Kananenka, J. J. Phillips, and D. Zgid, "Efficient temperature-dependent Green's functions methods for realistic systems: Compact grids for orthogonal polynomial transforms", *J. Chem. Theory Comput.* **12**, 564 (2016).

[52] V. M. Galitskii, "The energy spectrum of a non-ideal Fermi gas", *Zh. Eksp. Teor. Fiz.* **34**, 151 (1958).

[53] J. Gukelberger, L. Huang, and P. Werner, "On the dangers of partial diagrammatic summations: Benchmarks for the two-dimensional Hubbard model in the weak-coupling regime", *Phys. Rev. B* **91**, 235114 (2015).

[54] A. A. Kananenka, A. R. Welden, T. N. Lan, E. Gull, and D. Zgid, "Efficient temperature-dependent Green's function methods for realistic systems: Using cubic spline interpolation to approximate Matsubara Green's functions", *J. Chem. Theory Comput.* **12**, 2250 (2016).

[55] M. Cococcioni and S. de Gironcoli, "Linear response approach to the calculation of the effective interaction parameters in the LDA + U method", *Phys. Rev. B* **71**, 035105 (2005).

[56] F. Aryasetiawan, M. Imada, A. Georges, G. Kotliar, S. Biermann, and A. I. Lichtenstein, "Frequency-dependent local interactions and low-energy effective models from electronic structure calculations", *Phys. Rev. B* **70**, 195104 (2004).

[57] P. Werner and A. J. Millis, "Dynamical screening in correlated electron materials", *Phys. Rev. Lett.* **104**, 146401 (2010).

[58] P. Werner and M. Casula, "Dynamical screening in correlated electron systems-from lattice models to realistic materials", *J. Phys.: Condensed Matter* **28**, 383001 (2016).

[59] A. A. Rusakov, J. J. Phillips, and D. Zgid, "Local Hamiltonians for quantitative Green's function embedding methods", *J. Chem. Phys.* **141**, 194105 (2014).

[60] J. Pipek and P. G. Mezey, "A fast intrinsic localization procedure applicable for abinitio and semiempirical linear combination of atomic orbital wave functions", *J. Chem. Phys.* **90**, 4916 (1989).

[61] S. F. Boys, "Construction of some molecular orbitals to be approximately invariant for changes from one molecule to another", *Rev. Mod. Phys.* **32**, 296 (1960).

[62] N. Marzari and D. Vanderbilt, "Maximally localized generalized wannier functions for composite energy bands", *Phys. Rev. B* **56**, 12847 (1997).

[63] P. de Silva, M. Giebultowski, and J. Korchowiec, "Fast orbital localization scheme in molecular fragments resolution", *Phys. Chem. Chem. Phys.* **14**, 546 (2012).

[64] F. L. Gu, Y. Aoki, J. Korchowiec, A. Imamura, and B. Kirtman, "A new localization scheme for the elongation method", *J. Chem. Phys.* **121**, 10385 (2004).

[65] N. Lin, C. A. Marianetti, A. J. Millis, and D. R. Reichman, "Dynamical mean-field theory for quantum chemistry", *Phys. Rev. Lett.* **106**, 096402 (2011).

[66] P. Werner, A. Comanac, L. de' Medici, M. Troyer, and A. J. Millis, "Continuous-time solver for quantum impurity models", *Phys. Rev. Lett.* **97**, 076405 (2006).

[67] P. Werner and A. J. Millis, "Hybridization expansion impurity solver: General formulation and application to Kondo lattice and two-orbital models", *Phys. Rev. B* **74**, 155107 (2006).

[68] E. Gull, "Continuous-time quantum monte carlo algorithms for fermions", Ph.D. thesis, ETH Zürich, **2008**.

[69] E. Gull, A. J. Millis, A. I. Lichtenstein, A. N. Rubtsov, M. Troyer, and P. Werner, "Continuous-time Monte Carlo methods for quantum impurity models", *Rev. Mod. Phys.* **83**, 349 (2011).

[70] W. J. Hehre, R. F. Stewart, and J. A. Pople, "Self-consistent molecular-orbital methods. I. Use of Gaussian expansions of Slater-type atomic orbitals", *J. Chem. Phys.* **51**, 2657 (1969).

[71] M. J. Frisch, G. W. Trucks, H. B. Schlegel, G. E. Scuseria, M. A. Robb, J. R. Cheeseman, G. Scalmani, V. Barone, B. Mennucci, G. A. Petersson, H. Nakatsuji, M. Caricato, X. Li, H. P. Hratchian, A. F. Izmaylov, J. Bloino, G. Zheng, J. L. Sonnenberg, M. Hada, M. Ehara, K. Toyota, R. Fukuda, J. Hasegawa, M. Ishida, T. Nakajima, Y. Honda, O. Kitao, H. Nakai, T. Vreven, J. A. Montgomery, Jr., J. E. Peralta, F. Ogliaro, M. Bearpark, J. J. Heyd, E. Brothers, K. N. Kudin, V. N. Staroverov, R. Kobayashi, J. Normand, K. Raghavachari, A. Rendell, J. C. Burant, S. S. Iyengar, J. Tomasi, M. Cossi, N. Rega, J. M. Millam, M. Klene, J. E. Knox, J. B. Cross, V. Bakken, C. Adamo, J. Jaramillo, R. Gomperts, R. E. Stratmann, O. Yazyev, A. J. Austin, R. Cammi, C. Pomelli, J. W. Ochterski, R. L. Martin, K. Morokuma, V. G. Zakrzewski, G. A. Voth, P. Salvador, J. J. Dannenberg, S. Dapprich, A. D. Daniels, Ö. Farkas, J. B. Foresman, J. V. Ortiz, J. Cioslowski, and D. J. Fox, "Gaussian 09 Revision A.01", Gaussian, Inc., Wallingford, CT, 2009.

[72] P. Sémon and A.-M. S. Tremblay, "Importance of subleading corrections for the mott critical point", *Phys. Rev. B* **85**, 201101 (2012).

[73] P. Seth, I. Krivenko, M. Ferrero, and O. Parcollet, "TRIQS/CTHYB: A continuous-time quantum Monte Carlo hybridisation expansion solver for quantum impurity problems", *Comp. Phys. Comm.* **200**, 274 (2016).

[74] F. Neese, "The ORCA program system", *Wiley Interdiscip. Rev. Comput. Mol. Sci.* **2**, 73 (2012).

[75] B. O. Roos, P. R. Taylor, and P. E. Siegbahn, "A complete active space SCF method (CASSCF) using a density matrix formulated super-CI approach", *Chem. Phys.* **48**, 157 (1980).

[76] B. O. Roos, "The complete active space SCF method in a fock-matrix-based super-CI formulation", *Int. J. Quantum Chem.* **18**, 175 (1980).

[77] P. E. M. Siegbahn, J. Almlf, A. Heiberg, and B. O. Roos, "The complete active space SCF (CASSCF) method in a Newton-Raphson formulation with application to the HNO molecule", *J. Chem. Phys.* **74**, 2384 (1981).

[78] K. Aidas, C. Angeli, K. L. Bak, V. Bakken, R. Bast, L. Boman, O. Christiansen, R. Cimiraglia, S. Coriani, P. Dahle, E. K. Dalskov, U. Ekström, T. Enevoldsen, J. J. Eriksen, P. Ettenhuber, B. Fernández, L. Ferrighi, H. Fliegl, L. Frediani, K. Hald, A. Halkier, C. Hättig, H. Heiberg, T. Helgaker, A. C. Hennum, H. Hettema, E. Hjertenæs, S. Høst, I.-M. Høyvik, M. F. Iozzi, B. Jansík, H. J. Aa. Jensen, D. Jonsson, P. Jørgensen, J. Kauczor, S. Kirpekar, T. Kjærgaard, W. Klopper, S. Knecht, R. Kobayashi, H. Koch, J. Kongsted, A. Krapp, K. Kristensen, A. Ligabue, O. B. Lutnæs, J. I. Melo, K. V. Mikkelsen, R. H. Myhre, C. Neiss, C. B. Nielsen, P. Norman, J. Olsen, J. M. H. Olsen, A. Osted, M. J. Packer, F. Pawlowski, T. B. Pedersen, P. F. Provasi, S. Reine, Z. Rinkevicius, T. A. Ruden, K. Ruud, V. V. Rybkin, P. Sałek, C. C. M. Samson, A. S. de Merás, T. Saue, S. P. A. Sauer, B. Schimmelpfennig, K. Sneskov, A. H. Steindal, K. O. Sylvester-Hvid, P. R. Taylor, A. M. Teale, E. I. Tellgren, D. P. Tew, A. J. Thorvaldsen, L. Thøgersen, O. Vahtras, M. A. Watson, D. J. D. Wilson, M. Ziolkowski, and H. Ågren, "The Dalton quantum chemistry program system", *Wiley Interdiscip. Rev. Comput. Mol. Sci.* **4**, 269 (2014).

[79] W. J. Hehre, R. Ditchfield, and J. A. Pople, "Self-consistent molecular orbital methods. XII. Further extensions of gaussian-type basis sets for use in molecular orbital studies of organic molecules", *J. Chem. Phys.* **56**, 2257 (1972).

[80] T. H. Dunning, "Gaussian basis functions for use in molecular calculations. III. Contraction of (10s6p) atomic basis sets for the first-row atoms", *J. Chem. Phys.* **55**, 716 (1971).

[81] J. Hachmann, W. Cardoen, and G. K.-L. Chan, "Multireference correlation in long molecules with the quadratic scaling density matrix renormalization group", *J. Chem. Phys.* **125**, 144101 (2006).

[82] T. Tsuchimochi and G. E. Scuseria, "Strong correlations via constrained-pairing mean-field theory", *J. Chem. Phys.* **131**, 121102 (2009).

[83] K. Boguslawski, P. Tecmer, P. W. Ayers, P. Bultinck, S. De Baerdemacker, and D. Van Neck, "Efficient description of strongly correlated electrons with mean-field cost", *Phys. Rev. B* **89**, 201106 (2014).

[84] T. H. Dunning, "Gaussian basis sets for use in correlated molecular calculations. I. The atoms boron through neon and hydrogen", *J. Chem. Phys.* **90**, 1007 (1989).

[85] U. Ray and G. K.-L. Chan, "DMRG data for H_{10} chain in cc-pVDZ basis set", (2016), private communication.

[86] S. Sharma and G. K.-L. Chan, "Spin-adapted density matrix renormalization group algorithms for quantum chemistry", *J. Chem. Phys.* **136**, 124121 (2012).

[87] R. Olivares-Amaya, W. Hu, N. Nakatani, S. Sharma, J. Yang, and G. K.-L. Chan, "The ab-initio density matrix renormalization group in practice", *J. Chem. Phys.* **142**, 034102 (2015).

Chapter 8

Combining density functional theory and Green's function theory: range-separated, non-local, dynamic, and orbital-dependent hybrid functional

A. A. Kananenka and D. Zgid,

Journal of Chemical Theory and Computation (submitted)

8.1 Introduction

Kohn–Sham density functional theory (DFT) [1–3] has become a method of choice for unraveling the ground state properties of mostly single reference molecular and condensed matter systems. Its popularity is due to an attractive compromise between the accuracy and computational cost, provided by numerous approximations to the exchange-correlation functional. The best approximate functionals offer a decent description of the short-range dynamical correlation which justifies their use for near-equilibrium geometries. Another attractive feature of density functionals is their weak dependence on the one-electron basis set. Despite their large success, however, local and semilocal density functionals fail to describe a number of important properties, for example, charge transfer excitations [4], dynamical long-range correlations important

in weak van der Waals complexes bound by London dispersion forces [5], and Rydberg excitation energies [6]. The reason for this failure is well understood and is rooting in a wrong asymptotic behavior of the exchange-correlation potential which in turn is a consequence of a self-interaction error [7].

Many-body wave-function methods such as the Møller–Plesset perturbation theory (MP2) [8], coupled cluster (CC) [9] or multiconfigurational self-consistent field (MCSCF) [10] approaches are capable of providing a correct description when density functionals fail. However, for these *ab initio* methods, in addition to a steep computational cost and long configuration expansion of the wave function also large basis sets are required to describe the dynamical correlation accurately and reach an agreement with experiments. These features make the application of *ab initio* methods to very large systems quite challenging and much larger system sizes can be reached when density functional approximations are used.

In recent years, there has been a substantial progress in the development of density functionals that mix both the standard local or semilocal density functional approximation with the wave-function theory. The mixing is done rigorously by separating the two-electron interaction operator into short-range and long-range components [11–13] resulting in so-called range-separated hybrid functionals [14]. They are meant to combine the best features of the respective approaches. The least computationally expensive range-separated hybrid functional is obtained when a non-local Hartree–Fock-type exchange is introduced to replace the long-range exchange density functional [15–19]. Such functionals were proved successful in a partial correction of the long-range behavior of the exchange-correlation potential [17, 20]. However, they are also known to perform worse than standard density functionals in some cases [15, 21].

The combination of explicit many-body wave-function methods with the density-functional theory by means of range separation has been previously quite extensively explored. Long-range MP2 [22–25], second-order n-electron valence state perturbation

theory (NEVPT2) [26], coupled cluster (CCSD(T)) [27], random-phase approximation (RPA) [28–30], configuration interaction (CI) [12, 31], MCSCF [32, 33], and the density-matrix-functional theory [34, 35] have been combined with short-range local and semilocal density functionals [13, 16, 27, 36, 37]. These range-separated functionals were successfully applied to weakly interacting molecular systems [22, 27, 29, 30, 38–41]. In comparison to corresponding standard many-body wave-function approaches, the range-separated functionals have additional advantages such as a rapid convergence with respect to the basis set size [22, 24, 27–30, 42–46] and smaller basis-set superposition errors. In these approaches, the long-range correlation energy is usually added as a post-SCF correction to the total energy from a range-separated calculation without the long-range correlation functional. Therefore, they do not yield the exact energy even with the exact short-range exchange-correlation functional, for example see ref 30.

Since the new functional introduced in this work combines both the density functional theory and the Green's function theory, we aim to provide a self-contained and detailed description that can be useful to both these communities. Therefore, to bring the readers to a common ground, we found it helpful to list some key theory concepts from both communities.

Finite-temperature single-particle Green's function methods have been long known in the context of condensed matter physics [47–49] and now are making inroads into quantum chemistry [50–54]. These methods are rigorous and offer several advantages. The single-particle Green's function formalism is based entirely on one-electron operators avoiding the necessity of dealing with wave functions. A single-particle Green's function determines the expectation value of single-particle operators, the two-electron correlation energy, and provides access to the spectral density, ionization potentials and electron affinities.

In this work, we present a rigorous self-consistent framework combining a short-range density functional approximation with a long-range single-particle Green's func-

tion method. As a specific example, we implemented and benchmarked the short-range local density approximation (LDA) [55, 56] with the second-order Green's function theory (GF2) [50, 57, 58]. To further motivate this work, it is worth to briefly list differences between the method presented here and the already existing plethora of range-separated hybrid functionals. Most methods that have been previously applied to the long-range interactions were not self-consistent. In contrast to non-self-consistent methods, which are starting point dependent, the approach presented here, irrespective of the initial guess, recovers the exact total electronic energy provided that both the exact short-range exchange-correlation functional and the exact long-range Green's function method are used. An iterative nature of GF2 results in multiple implications. The overall accuracy of GF2 for weakly correlated systems is close to that of MP2 or CCSD, however, unlike these two approaches, GF2 does not display divergences for strongly correlated systems [50]. GF2 is a one-electron self-interaction free method, while methods such as RPA contain a significant one-electron self-interaction error [59]. Furthermore, a Matsubara axis GF2 formalism is explicitly temperature-dependent.

The range-separated hybrid functional presented here also shares some commonalities with other combinations of DFT with Green's function methods. For example, the LDA+DMFT [60] method that combines LDA with the dynamical mean-field theory (DMFT) [61] is often used in solid state calculations of strongly correlated systems. However, LDA+DMFT is known to suffer from a so-called double counting problem [60, 62], where some electronic correlations are accounted for by both LDA and DMFT. In the LDA+DMFT method, these two sources of electronic correlations cannot be rigorously separated [60, 63, 64]. We would like to stress that the double counting problem does not appear in the framework presented here since the exact separation of the electron-electron interaction into long- and short-range components is used.

Range-separated hybrid functionals employ a single range separation parameter

controlling the spatial extent of the short-range contribution. The optimal value of this system-dependent parameter [65–67] can be determined either by empirical fitting against available experimental data [15, 18, 68, 69] or in an *ab initio* fashion in a self-consistent procedure [14, 68]. In our current work, we have adopted the latter view and applied the optimal tuning strategy based on calculations of ionization potentials to find optimal values of the range separation parameter for several atoms and molecules. Additionally, we have also investigated the two-electron self-interaction error, basis set dependence, dynamical correlation as well as the implications of the hybrid functional presented here for the Green's function based embedding methods and periodic calculations.

8.2 Theory

The exact electronic ground state energy of a system of N interacting electrons in the presence of external potential $v(\mathbf{r})$ (e.g., the potential of the nuclei) can be obtained by a two-step minimization of the following functional [70]

$$E_{\text{tot}}[\rho] = \min_{\rho \to N} \Big\{ F[\rho] + \int d\mathbf{r} v(\mathbf{r}) \rho(\mathbf{r}) \Big\}, \tag{8.1}$$

where $\rho(\mathbf{r})$ is an electron density and $F[\rho]$ is the universal functional of the electron density defined as

$$F[\rho] = \min_{\Psi \to \rho} \langle \Psi | \hat{T} + \hat{V}_{ee} | \Psi \rangle, \tag{8.2}$$

where $\hat{T} = -\frac{1}{2} \sum_i^N \nabla_i^2$ is the kinetic energy operator, $\hat{V}_{ee} = \frac{1}{2} \sum_{i \neq j}^N \hat{v}_{ee}(r_{ij})$ is the electron-electron interaction operator, $r_{ij} = |\mathbf{r}_i - \mathbf{r}_j|$ and $\mathbf{r}_i$ is the coordinate vector of electron i. The minimization is first carried out over all normalized antisymmetric wave functions Ψ that produce a given density $\rho(\mathbf{r})$, and then over all densities yielding N electrons. The existence and uniqueness of the universal functional $F[\rho]$ is guaranteed

by the Hohenberg–Kohn theorem [1]. Regrettably, an explicit variation of Eq. 8.1 has not become practical since no exact form of the universal functional is available and due to its absence all practical applications are based on the Kohn–Sham scheme [2]. This procedure uses an approximation to the exchange-correlation part of the universal functional. One of the most successful approaches taken along this way is the combination of two (or more) density functional approximations into one so-called hybrid exchange-correlation functional using the adiabatic connection theorem [71–74].

Range-separated density functional approximations belong to a particular class of hybrid functionals [14]. The essence of range-separated hybrid functionals lies in the decomposition of the Coulomb electron-electron interaction operator into a sum of short-range and long-range counterparts [11, 12, 75],

$$\frac{1}{r_{ij}} = \hat{v}_{ee}^{sr,\lambda}(r_{ij}) + \hat{v}_{ee}^{lr,\lambda}(r_{ij}) = \underbrace{\frac{1 - f\left(\lambda r_{ij}\right)}{r_{ij}}}_{\text{short-range}} + \underbrace{\frac{f\left(\lambda r_{ij}\right)}{r_{ij}}}_{\text{long-range}}, \tag{8.3}$$

with the parameter λ controlling the range separation. The function $f(\lambda r)$ satisfies the following properties $f(\lambda r \rightarrow \infty) = 1$ and $f(\lambda r \rightarrow 0) = 0$. From a physical and computational standpoint the standard error function $f(\lambda r) = \mathrm{erf}(\lambda r)$ is one of the most convenient choices. The decomposition in Eq. 8.3 is exact and presents a convenient starting point for developing range-separated hybrid functionals by mixing a short-range density functional approximation with a long-range method. The universal functional from Eq. 8.2 is partitioned accordingly [13]

$$F[\rho] = \min_{\Psi \rightarrow \rho} \langle \Psi^{\lambda} | \hat{T} + \hat{V}_{ee}^{lr,\lambda} | \Psi^{\lambda} \rangle + E_{\mathrm{H}}^{sr,\lambda}[\rho] + E_{\mathrm{xc}}^{sr,\lambda}[\rho], \tag{8.4}$$

where the first term defines the long-range universal functional $F^{lr,\lambda}[\rho]$, the second term $E_{\mathrm{H}}^{sr,\lambda}[\rho]$ is the short-range Hartree functional, and the third term $E_{\mathrm{xc}}^{sr,\lambda}[\rho]$ is the short-range exchange-correlation functional. The total energy from Eq. 8.1, therefore,

can be rewritten as

$$E_{\rm tot}[\rho] = \min_{\rho\to N}\Big\{F^{lr,\lambda}[\rho] + E_{\rm H}^{sr,\lambda}[\rho] + E_{\rm xc}^{sr,\lambda}[\rho] + \int d\mathbf{r} v(\mathbf{r})\rho(\mathbf{r})\Big\}. \tag{8.5}$$

To formulate a self-consistent theory including long-range exchange and correlation energies coming from a Green's function method, we redefine the long-range functional $F^{lr,\lambda}[\rho]$ as the following functional of a single-particle Green's function G

$$F^{lr,\lambda}[\rho] = \min_{G\to\rho}\{T[G] + E_{ee}^{lr,\lambda}[G]\}. \tag{8.6}$$

Here, $T[G]$ is the kinetic energy functional and $E_{ee}^{lr,\lambda}[G]$ is the long-range interaction functional of a single-particle Green's function. The search is performed over all single-particle Green's functions yielding a given density $\rho(\mathbf{r})$. Consequently, we can write the ground state electronic energy as a functional of a single-particle Green's function

$$\begin{aligned} E_{\rm tot}[\rho] &= \min_{\rho\to N}\Big\{\min_{G\to\rho}\{T[G] + E_{ee}^{lr,\lambda}[G]\} + E_{\rm H}^{sr,\lambda}[\rho] + E_{\rm xc}^{sr,\lambda}[\rho] + \int d\mathbf{r} v(\mathbf{r})\rho(\mathbf{r})\Big\} \qquad (8.7)\\ &= \min_{G\to N}\Big\{T[G] + E_{ee}^{lr,\lambda}[G] + E_{\rm H}^{sr,\lambda}[\rho] + E_{\rm xc}^{sr,\lambda}[\rho] + \int d\mathbf{r} v(\mathbf{r})\rho(\mathbf{r})\Big\}, \end{aligned}$$

where the electron density $\rho(\mathbf{r})$ is calculated from the Green's function $G \to \rho$. Note that the single-particle Green's function minimizing Eq. 8.8 yields both the exact electron density ρ and proper total number of electrons N. Therefore, we can define the total energy functional as

$$E_{\rm tot}[G] = T[G] + E_{ee}^{lr,\lambda}[G] + E_{\rm H}^{sr,\lambda}[G] + E_{\rm xc}^{sr,\lambda}[\rho] + \int d\mathbf{r} v(\mathbf{r})\rho(\mathbf{r}). \tag{8.8}$$

The long-range electron-electron interaction energy can be decomposed into the Hartree

long-range energy and the long-range exchange-correlation energy

$$E_{ee}^{lr,\lambda}[G] = E_{\mathrm{H}}^{lr,\lambda}[G] + E_{\mathrm{xc}}^{lr,\lambda}[G]. \tag{8.9}$$

The short-range and long-range Hartree energies can be folded into one term describing the all-range Hartree energy $E_{\mathrm{H}}[\rho]$. This leads to the following expression for the energy functional defined in Eq. 8.8

$$E_{\mathrm{tot}}[G] = T[G] + E_{\mathrm{H}}[\rho] + E_{\mathrm{xc}}^{sr,\lambda}[G] + E_{xc}^{lr,\lambda}[G] + \int d\mathbf{r} v(\mathbf{r})\rho(\mathbf{r}). \tag{8.10}$$

This energy functional (that depends on a Green's function) provides an exact decomposition of the total energy into short-range and long-range components. In particular, there is no double counting of correlation effects. The minimization of this functional with respect to a single-particle Green's function yields the ground state energy. It should be noted that with the exact long-range Green's function method and exact short-range density functional the minimization of Eq. 8.10 will produce the exact ground state electronic energy for all possible range separation parameters λ.

In practical calculations of realistic systems, both short-range and long-range methods must be approximated. When employed in a range-separated framework, the standard density functional approximations are modified to describe short-range interactions. The short-range exchange-correlation energy is calculated as

$$E_{\mathrm{xc}}^{sr,\lambda} = \int d\mathbf{r}\rho(\mathbf{r})\epsilon_{\mathrm{xc}}^{sr,\lambda}(\rho), \tag{8.11}$$

where $\epsilon_{\mathrm{xc}}^{sr,\lambda}(\rho)$ is the short-range exchange-correlation energy density. The short-range LDA exchange energy density $\epsilon_{\mathrm{x},\sigma}^{sr,\lambda}(\rho)$ can be derived from the exchange hole of the homogeneous electron gas interacting with a short-range electron-electron interaction potential [36]. Its functional form depends on the choice of the function $f(\lambda r)$ [13] and

for the error function the short-range exchange energy density $\epsilon_{\mathrm{x},\sigma}^{sr,\lambda}(\rho)$ is given by [17]

$$\begin{aligned}\epsilon_{\mathrm{x},\sigma}^{sr,\lambda}(\rho) = & - \frac{1}{2}\left(\frac{3}{4\pi}\right)^{1/3}\rho_\sigma^{1/3}(\mathbf{r})\left(1-\frac{8}{3}a_\sigma\left[\sqrt{\pi}\mathrm{erf}\left(\frac{1}{2a_\sigma}\right)\right.\right. \\ & + \left.\left.\left(2a_\sigma - 4a_\sigma^3\right)\exp\left(-\frac{1}{4a_\sigma^2}\right) - 3a_\sigma + 4a_\sigma^3\right]\right), \end{aligned} \tag{8.12}$$

where $a_\sigma = \lambda/(2k_{F,\sigma})$, k_σ is the Fermi momentum given by $k_{F,\sigma} = (6\pi^2\rho_\sigma)^{1/3}$ and $\sigma = \alpha, \beta$ is the spin index. This approximation reduces to the standard LDA exchange energy density at $\lambda = 0$ and has a correct asymptotic expansion for $\lambda \to \infty$ [13]. Thus, it provides an interpolation between LDA and the correct limit as $\lambda \to \infty$. LDA was shown to be exact at the short-range [76] and, when combined with the many-body perturbation theory, such a hybrid method is expected to give an improved description of the dynamical correlation both in comparison to LDA and the perturbation theory. Consequently, in this case LDA is used to recover a fraction of the dynamical correlation that is missing in the finite order of perturbation theory. In Section 8.4.2, we provide numerical results supporting this discussion by investigating dynamical correlation in diatomic molecules.

In order to calculate the short-range correlation energy density $\epsilon_c^{sr,\lambda}(\rho)$, we adopted a scheme based on the following rational approximant [36, 37]

$$\epsilon_c^{sr,\lambda}(r_s) = \frac{\epsilon_c(r_s)}{1 + c_1(r_s)\lambda + c_2(r_s)\lambda^2}, \tag{8.13}$$

where $\epsilon_c(r_s)$ is the correlation energy density for the standard Coulomb interactions ($\lambda = 0$) evaluated for the Wigner–Seitz radius $r_s(\rho) = (3/(4\pi\rho))^{1/3}$ with $\rho(\mathbf{r}) = \rho_\alpha(\mathbf{r}) + \rho_\beta(\mathbf{r})$. Equation 8.13 provides a way to interpolate between $\lambda = 0$ and $\lambda \to \infty$ limits and is applicable not only for the interpolation of the correlation energy density, but can also be used for the exchange energy density [13]. Particular forms of $c_1(r_s)$ and $c_2(r_s)$ depend on the quantity interpolated. In this work, we used $c_1(r_s)$ and $c_2(r_s)$ determined

by Toulouse *et al.* by analytical parameterization of the long-range correlation energy density from CCD and Fermi-hypernetted-chain calculations of the uniform electron gas [36]. The short-range correlation energy density was then calculated as a difference between all-range and long-range correlation energy densities. In this work, we have investigated two local density approximations for the correlation energy: Vosko–Wilk–Nusair (VWN5) functional ("form V" parametrization in ref 56) as well as the Perdew and Wang (PW92) functional [77]. PW92 uses the same spin-interpolation formula as the VWN functional but employs different expressions for the paramagnetic correlation energy density and the ferromagnetic correction to it. After performing several test calculations, we noticed that total energies from the short-range VWN5 functional were within 1 kcal·mol^{-1} of those of the short-range PW92 functional. Consequently, we proceeded by using short-range VWN5 functional and all results reported in this work were obtained with it.

Having discussed theoretical background behind short-range density functionals and our specific choices, we now turn to the discussion of the long-range electron-electron interaction energy. The long-range exchange energy is defined exactly in terms of the Fock exchange integral as

$$E_{\mathrm{x}}^{lr,\lambda} = -\frac{1}{2}\sum_{\sigma}\int d\mathbf{r}\int d\mathbf{r}'\frac{|\gamma_{\sigma}(\mathbf{r},\mathbf{r}')|^2\mathrm{erf}(\lambda|\mathbf{r}-\mathbf{r}'|)}{|\mathbf{r}-\mathbf{r}'|}, \tag{8.14}$$

where $\gamma_{\sigma}(\mathbf{r},\mathbf{r}')$ is the one-electron reduced density matrix. Note that the incorporation of the screening provided by the error function leads to a faster decaying long-range exchange contribution and, especially for metallic systems, can result in reducing the computational cost.

In this work, we propose to calculate the long-range correlation energy using single-particle Green's function methods. In a Green's function formalism, it is possible to correct a zeroth order Green's function $\mathcal{G}(\omega)$ (which in certain cases can be a non-

interacting Green's function) using the Dyson equation [47]

$$\mathbf{G}_\sigma(\omega) = \left[\mathcal{G}_\sigma(\omega)^{-1} - \mathbf{\Sigma}_\sigma(\omega)\right]^{-1}, \tag{8.15}$$

where $\mathbf{\Sigma}_\sigma(\omega)$ is the self-energy of the system. The self-energy is an effective single-particle potential that incorporates all many-body effects present in the system. At this point, a connection to the density functional theory can be made. The frequency-dependent self-energy $\mathbf{\Sigma}(\omega)$ shares some similarities with the exchange-correlation potential of DFT $v_{\mathrm{xc}}(\rho)$ since $v_{\mathrm{xc}}(\rho)$ also connects interacting and non-interacting systems. We stress, however, that unlike $v_{\mathrm{xc}}(\rho)$ in Kohn–Sham DFT, the self-energy is a dynamic, nonlocal and orbital-dependent quantity. This implies that a treatment of such potentials is beyond the Kohn–Sham scheme and it requires the so-called generalized Kohn–Sham framework (GKS) [78].

Calculating either the exact exchange-correlation potential or the exact self-energy is an inconceivably complicated task. Fortunately, a hierarchy of systematically improvable approximations to the self-energy is provided by the many-body perturbation theory [48, 79]. Examples of such approaches include GF2, GW [80, 81], and FLEX [82, 83] approximations.

Since both the long-range exchange and the long-range correlation energy should be calculated self-consistently with their short-range counterparts, it is important that such a self-consistent evaluation can be carried out easily. Moreover, for Green's function methods, only fully iterative schemes respect the conservation laws and ensure that quantities obtained by a thermodynamic or coupling constant integration from non-interacting limits are consistent [84, 85]

This is why in our work, we did not employ any real axis single-particle Green's functions $\mathbf{G}(\omega)$ that are rational functions in the complex plane. The rational structure of $\mathbf{G}(\omega)$ implies the existence of poles, for which iterative algorithms require pole

shifting techniques [86–88]. Consequently, the real axis Green's functions methods are known to present problems during self-consistent schemes.

We employ an imaginary axis, single-particle Green's function $\mathbf{G}(i\omega_n)$ that is a smooth function of the imaginary argument $i\omega_n$ and is used to describe single-particle properties of a statistical ensemble. Due to the smooth structure, $\mathbf{G}(i\omega_n)$ is a convenient quantity for self-consistent calculations. The imaginary frequency (Matsubara) Green's function $\mathbf{G}(i\omega_n)$ is expressed on a discrete grid of imaginary frequencies located at $i\omega_n = i(2n+1)\pi/\beta$ [89], where $n = 0, 1, 2, \ldots$, $\beta = 1/(k_{\mathrm{B}}T)$ is the inverse temperature, k_{B} is the Boltzmann constant and T is the physical temperature. Providing that the imaginary frequency self-energy and Green's function were self-consistently determined [48], the long-range correlation energy can be calculated using the Galitskii–Migdal formula [90]

$$E_{\mathrm{c}}^{lr,\lambda} = k_B T \sum_n \mathrm{Re}\left[\mathrm{Tr}\left[\mathbf{G}_\alpha^\lambda(i\omega_n)\mathbf{\Sigma}_\alpha^{lr,\lambda}(i\omega_n) + \mathbf{G}_\beta^\lambda(i\omega_n)\mathbf{\Sigma}_\beta^{lr,\lambda}(i\omega_n)\right]\right]. \tag{8.16}$$

We have presented equations for calculating long-range exchange (Eq. 8.14) and long-range correlation energies (Eq. 8.16), however, as we mentioned before, is important that they are calculated self-consistently with their short-range counterparts.

Here, we outline an algorithm that allows us to perform such a self-consistent evaluation. It should be noted that the formalism presented in this work is general and not limited to a specific choice of the Green's function method and the density functional approximation.

1. The calculation begins with an initial guess for the density matrix $\mathbf{P}$. For all calculations presented in this work, the Hartree–Fock density matrix was used for this purpose. The method is, however, reference-independent, and different choices of the initial density matrix are possible and the same converged solution should be reached irrespective of the starting point.

2. The electron density is calculated using a finite set of L basis functions $\{\phi_i(\mathbf{r})\}$

$$\rho_\sigma(\mathbf{r}) = \sum_{ij}^{L} P_{ij}^{\sigma} \phi_i(\mathbf{r}) \phi_j(\mathbf{r}). \tag{8.17}$$

3. The density matrix is used to calculate the all-range Hartree contribution to the Fock matrix according to

$$J_{ij} = \sum_{kl} \left(P_{kl}^{\alpha} + P_{kl}^{\beta} \right) v_{ijkl}, \tag{8.18}$$

where v_{ijkl} are unscreened two-electron integrals

$$v_{ijkl} = \int d\mathbf{r} \int d\mathbf{r}' \frac{\phi_i^*(\mathbf{r}) \phi_j(\mathbf{r}) \phi_k^*(\mathbf{r}') \phi_l(\mathbf{r}')}{|\mathbf{r} - \mathbf{r}'|}. \tag{8.19}$$

4. The short-range exchange-correlation energy is calculated using Eqs. 8.11, 8.12, 8.13 and the corresponding contributions to the Fock matrix are given by

$$\begin{aligned} \left[V_{\mathrm{x},\sigma}^{sr,\lambda} \right]_{ij} &= \int d\mathbf{r} v_{\mathrm{x},\sigma}^{sr,\lambda}(\rho) \phi_i(\mathbf{r}) \phi_j(\mathbf{r}), \\ \left[V_{\mathrm{c},\sigma}^{sr,\lambda} \right]_{ij} &= \int d\mathbf{r} v_{\mathrm{c},\sigma}^{sr,\lambda}(\rho) \phi_i(\mathbf{r}) \phi_j(\mathbf{r}), \end{aligned} \tag{8.20}$$

where the short-range exchange $v_{\mathrm{x},\sigma}^{sr,\lambda}(\rho)$ and short-range correlation $v_{\mathrm{c}}^{sr,\lambda}(\rho)$ potentials are functional derivatives of short-range exchange and short-range correlation functionals with respect to the electron density: $v_{\mathrm{x},\sigma}^{sr,\lambda}(\rho) = \delta E_{\mathrm{x}}^{sr,\lambda}[\rho]/\delta\rho_\sigma(\mathbf{r})$ and $v_{\mathrm{c},\sigma}^{sr,\lambda}(\rho) = \delta E_{\mathrm{c}}^{sr,\lambda}[\rho]/\delta\rho_\sigma(\mathbf{r})$, respectively.

5. Each of the spin components of the non-interacting Matsubara Green's function is then built according to

$$\mathcal{G}_\sigma(i\omega_n) = \left[(i\omega_n + \mu_\sigma)\mathbf{S} - \mathbf{F}_\sigma \right]^{-1}, \tag{8.21}$$

where μ_σ is the chemical potential, $\mathbf{S}$ is the overlap matrix and $\mathbf{F}_\sigma$ is the Fock matrix containing all-range Hartree and short-range exchange-correlation parts

$$\mathbf{F}_\sigma = \mathbf{H}^{\text{core}} + \mathbf{J} + \mathbf{V}_{\text{x},\sigma}^{sr,\lambda} + \mathbf{V}_{\text{c},\sigma}^{sr,\lambda}, \tag{8.22}$$

where $\mathbf{H}^{\text{core}}$ is the core Hamiltonian matrix

$$H_{ij}^{\text{core}} = \int d\mathbf{r}\phi_i^*(\mathbf{r}) \left(-\frac{1}{2}\nabla_{\mathbf{r}}^2 + v(\mathbf{r}) \right) \phi_j(\mathbf{r}), \tag{8.23}$$

and $v(\mathbf{r})$ is the external potential.

6. The Green's function from step 5 is then used to generate either the long-range self-energy $\mathcal{G}(i\omega_n) \rightarrow \mathbf{\Sigma}^{lr,\lambda}(i\omega_n)$ or directly the correlated Green's function depending on a particular Green's function method used. Both quantities are needed later and the Dyson Eq. 8.15 is used to obtain one from the other.

7. The long-range exchange contribution to the Fock matrix is calculated according to

$$K_{ij,\sigma}^{lr,\lambda} = -\sum_{kl} P_{kl}^{\sigma} v_{ilkj}^{lr,\lambda}. \tag{8.24}$$

The interacting Green's function at this point reads

$$\mathbf{G}_\sigma^\lambda(i\omega_n) = \left[(i\omega_n + \mu_\sigma)\mathbf{S} - \mathbf{F}_\sigma - \mathbf{\Sigma}_\sigma^{lr,\lambda}(i\omega_n) \right]^{-1}, \tag{8.25}$$

where the Fock matrix has now both terms coming from the density functional and the Green's function method

$$\mathbf{F}_\sigma = \mathbf{H}^{\text{core}} + \mathbf{J} + \mathbf{V}_{\text{x},\sigma}^{sr,\lambda} + \mathbf{V}_{\text{c},\sigma}^{sr,\lambda} + \mathbf{K}_\sigma^{lr,\lambda}. \tag{8.26}$$

The long-range self-energy $\mathbf{\Sigma}_\sigma^{lr,\lambda}(i\omega_n)$ describes the dynamical (frequency-

dependent) long-range correlation.

8. The long-range correlation energy is calculated using the correlated Green's function $\mathbf{G}^{\lambda}_{\sigma}(i\omega_n)$ and the long-range self-energy $\mathbf{\Sigma}^{lr,\lambda}_{\sigma}(i\omega_n)$ according to Eq. 8.16.

9. The total electronic energy is calculated according to

$$E_{\mathrm{tot}} = \frac{1}{2}\mathrm{Tr}\left[(\mathbf{H}^{\mathrm{core}} + \mathbf{f}_{\alpha})\mathbf{P}_{\alpha} + (\mathbf{H}^{\mathrm{core}} + \mathbf{f}_{\beta})\mathbf{P}_{\beta}\right] + E^{sr,\lambda}_{\mathrm{xc}} + E^{lr,\lambda}_{\mathrm{x}} + E^{lr,\lambda}_{\mathrm{c}}, \quad (8.27)$$

where

$$\mathbf{f}_{\sigma} = \mathbf{H}^{\mathrm{core}} + \mathbf{J} + \mathbf{K}^{lr,\lambda}_{\sigma}. \quad (8.28)$$

10. The interacting Green's function is then used to update the density matrix

$$\mathbf{P}_{\sigma} = \frac{1}{\beta}\sum_{n} e^{i\omega_n 0^+}\mathbf{G}^{\lambda}_{\sigma}(i\omega_n). \quad (8.29)$$

11. The total electronic energy, density matrix, and Green's function are checked for convergence and, if necessary, a new iteration is started by sending updated density matrix to step 2.

The above algorithm is in principle general and can be used in finite-temperature calculations to evaluate the grand potential as

$$\Omega = \Phi - \mathrm{Tr}(\log \mathbf{G}^{-1}) - \mathrm{Tr}(\mathbf{\Sigma}\mathbf{G}), \quad (8.30)$$

where Φ is the Luttinger–Ward (LW) [91] functional that is a scalar functional of a renormalized Green's function and is defined as the sum of all closed, connected and fully dressed skeleton diagrams. The general $\Phi[\mathbf{G}]$ functional has the following form

$$\Phi[\mathbf{G}] = E_{\mathrm{H}}[\mathbf{G}] + E_{\mathrm{x}}[\mathbf{G}] + E[\mathbf{G}] \quad (8.31)$$

where $E[\mathbf{G}]$ is the correlation energy coming from frequency dependent $\mathbf{\Sigma}(i\omega_n)$ and $\mathbf{G}(i\omega_n)$. Since $\delta\Phi/\delta G_{ij}(i\omega_n) = \Sigma_{ij}(i\omega_n)$, we obtain the following expression for the self-energy

$$\mathbf{\Sigma}_\sigma = \mathbf{J} + \mathbf{K}_\sigma + \mathbf{\Sigma}_\sigma(i\omega_n). \tag{8.32}$$

Application of the decomposition from Eq. 8.3 can be understood as a splitting of interaction lines for every diagram leading to the following expression for the self-energy

$$\mathbf{\Sigma}_\sigma = \mathbf{J} + \mathbf{K}_\sigma^{sr,\lambda} + \mathbf{K}_\sigma^{lr,\lambda} + \mathbf{\Sigma}_\sigma^{sr,\lambda}(i\omega_n) + \mathbf{\Sigma}_\sigma^{lr,\lambda}(i\omega_n). \tag{8.33}$$

Finally, when a hybrid functional with DFT is considered, short-range exchange and short-range correlation self-energies are approximated by static (frequency-independent) corresponding potentials from the density functional approximation: $\mathbf{K}_\sigma^{sr,\lambda} \rightarrow \mathbf{V}_{\mathrm{x},\sigma}^{sr,\lambda}$ and $\mathbf{\Sigma}_\sigma^{sr,\lambda}(i\omega_n) \rightarrow \mathbf{V}_{\mathrm{c},\sigma}^{sr,\lambda}$ resulting in the following expression for the self-energy

$$\mathbf{\Sigma}_\sigma = \mathbf{J} + \mathbf{V}_{\mathrm{x},\sigma}^{sr,\lambda} + \mathbf{V}_{\mathrm{c},\sigma}^{sr,\lambda} + \mathbf{K}_\sigma^{lr,\lambda} + \mathbf{\Sigma}_\sigma^{lr,\lambda}(i\omega_n), \tag{8.34}$$

which enters the expression for the correlated Green's function shown earlier in Eqs. 8.25 and 8.26. While in principle the presented formalism that merges DFT with Green's function theory is temperature dependent and completely general, in our work, we use two simplifications. First, all practical calculations are currently limited to the $T = 0$ case due to lack of reliable explicit finite-temperature density functional approximations. Second, in our work, for simplicity, we employ the finite-temperature self-consistent second-order Green's function theory (GF2) for evaluating $\mathbf{\Sigma}_\sigma^{lr,\lambda}(i\omega_n)$. Consequently, in Eqs. 8.32 to 8.34, we use $\mathbf{\Sigma}_\sigma(i\omega_n) = \mathbf{\Sigma}_{2,\sigma}(i\omega_n)$, $\mathbf{\Sigma}_\sigma^{sr,\lambda}(i\omega_n) = \mathbf{\Sigma}_{2,\sigma}^{sr,\lambda}(i\omega_n)$, and $\mathbf{\Sigma}_\sigma^{lr,\lambda}(i\omega_n) = \mathbf{\Sigma}_{2,\sigma}^{lr,\lambda}(i\omega_n)$. The corresponding second-order Feynman diagrams for Φ are shown in Fig. 8.1. Since for the reasons discussed above, the DFT part of calculations is carried out at $T = 0$, we evaluate the GF2 self-energy and Green's function for large β, corresponding to $T \rightarrow 0$. For gapped systems, these

Figure 8.1: A formal definition of the Luttinger–Ward functional as a skeleton diagrammatic expansion, shown here for the second-order theory. Black solid lines represent Green's functions and red wavy lines denote electron-electron interactions (two-electron integrals).

calculations are equivalent to the $T = 0$ regime.

One of the key advantages of range-separated hybrid functionals stems from the partitioning in Eq. 8.3, which is chosen such that a singularity is only present in the short-range operator at electron-electron coalescence, while the long-range contribution is smooth. The absence of the singularity in the long-range part has significant consequences. Most importantly, a correlated method applied to the long-range electron-electron interactions will not need to represent a cusp using a finite set of one-electron basis functions, thus avoiding basis sets containing functions with very high angular momentum. In contrast to most electron correlation methods, density functionals are weakly basis-set dependent. Therefore, range-separated hybrid functionals usually exhibit faster convergence of the correlation and total energies with the size of the basis set. In Section 8.4.1, we illustrate that this indeed the case for the functional presented in this work.

In practical applications, a value of the range separation parameter λ has to be specified before a calculation is carried out. It is important that this value is chosen such that the respective approximations are evaluated within a regime that is optimal for their performance [14]. The simplest estimate of an optimal value of λ is based on a local approximation [31] $\lambda(\rho) = r_s(\rho)^{-1}$. The physical motivation behind this value is related to the fact that an electron on average occupies the sphere with boundaries defined by the Wigner–Seitz radius (also known as a characteristic length of the exchange). Therefore, electrons begin to enter an occupation sphere of the other electrons when $\lambda(\rho) \geq r_s(\rho)^{-1}$.

More sophisticated ways to find an optimal value of λ are based on the first-principles approaches and amount to finding λ satisfying some relationships that an exact theory should obey. For instance, a vertical ionization potential (IP) of a molecule containing N electrons is defined as

$$\mathrm{IP}_{E(N)}^{E(N-1)} = E_{\mathrm{tot}}(N-1) - E_{\mathrm{tot}}(N), \tag{8.35}$$

where $E_{\mathrm{tot}}(N)$ is the total ground state energy of a cation and $E_{\mathrm{tot}}(N)$ is the total ground state energy of a neutral molecule. In exact theory, $\mathrm{IP}_{E(N)}^{E(N-1)}$ should exactly agree with the IP calculated from the real frequency Green's function of an N-electron (neutral) system $\mathbf{G}_N(\omega)$. The general idea of the IP tuning approach is therefore to require that the IP from $\mathbf{G}_N(\omega)$ is as close as possible to the IP calculated from total energies of $N-1$ and N electron systems. Therefore, an optimal value of λ can be found by a minimization of the following bijective function

$$\mathcal{T}_N(\lambda) = \left| \mathrm{IP}\left[\mathbf{G}_N^{\lambda}(\omega)\right] - \mathrm{IP}_{E(N)}^{E(N-1)} \right|, \tag{8.36}$$

where $\mathrm{IP}\left[\mathbf{G}_N^{\lambda}(\omega)\right]$ is the IP calculated from the real frequency Green's function for a given value of λ. The minimum of $\mathcal{T}_N(\lambda)$ defines an optimal λ for which the ionization potential from a Green's function calculated for N-electron system is the closest to the ionization potential calculated from total energies of $N-1$ and N electron systems. It is important to emphasize that such tuning procedure does not require any empirical input.

Several methods of calculating IP from a single-particle Matsubara Green's function of an N-electron system including the extended Koopmans theorem (EKT) [92–95] have been proposed. In this work, we adopted the following approach. First, the converged Fock matrix $\mathbf{F}$ coming from the imaginary axis GF2 calculation is transformed to the canonical representation $\mathcal{E}$. Then the real frequency Green's function is constructed

according to

$$\mathbf{G}(\omega) = [\omega + \mu - \mathcal{E}]^{-1}, \tag{8.37}$$

where ω is the real frequency grid point. Then the second-order self-energy on the real frequency axis is calculated as follows [96]

$$\Sigma_{ij}(\omega) = \frac{1}{2}\sum_{ars}\frac{\langle rs||ia\rangle\langle ja||rs\rangle}{\omega + \mathcal{E}_a - \mathcal{E}_r - \mathcal{E}_s} + \frac{1}{2}\sum_{abr}\frac{\langle ab||ir\rangle\langle jr||ab\rangle}{\omega + \mathcal{E}_r - \mathcal{E}_a - \mathcal{E}_b}, \tag{8.38}$$

where i, j denote both occupied and virtual spin orbitals, a, b denote the occupied spin orbitals only, and r, s label virtual spin orbitals, $\langle rs||ia\rangle$ are the antisymmetrized two-electron integrals. Occupied and virtual orbitals are defined with respect to the Hartree–Fock determinant. The self-energy is then used to construct an updated real frequency Green's function according to

$$\mathbf{G}(\omega) = [\omega + \mu - \mathcal{E} - \mathbf{\Sigma}(\omega)]^{-1}. \tag{8.39}$$

The spectral function $\mathbf{A}(\omega)$ is then evaluated as

$$\mathbf{A}(\omega) = -\frac{1}{\pi}\mathrm{Im}\mathbf{G}(\omega). \tag{8.40}$$

All peaks of $\mathbf{A}(\omega)$ were shifted by the chemical potential μ and IP was set to the closest to $\omega = 0$ peak $\tilde{\omega}$ from ω^- side

$$\mathrm{IP}\left[\mathbf{G}_N^{\lambda}(\omega)\right] = -(\tilde{\omega} + \mu). \tag{8.41}$$

Results of the IP-tuning approach described above are illustrated in Section 8.4.3.

Another constraint that an exact electronic structure theory should comply with is based on the energy of fractional electron systems. It is well-known that the total electronic energy should vary linearly in the fractional electron occupancy between integer

electron numbers [97–99]. Inexact methods satisfy this condition only approximately. To the extent that a method deviates from this condition such a method possesses the many-electron self-interaction error. We have investigated this condition on the example of a two-electron system. Results are presented and discussed in Section 8.4.4.

8.3 Computational details

In this work, we present the range-separated hybrid functional srSVWN5—lrGF2 that combines the SVWN5 density functional with the self-consistent second-order perturbative many-body Green's function method (GF2). In GF2, the long-range second-order self-energy is calculated in the imaginary time domain according to [54]

$$\begin{aligned}
\left[\Sigma_{\alpha}^{lr,\lambda}(\tau)\right]_{ij} &= -\sum_{klmnpq}\left[G_{\alpha}^{\lambda}(\tau)\right]_{kl}\left[G_{\alpha}^{\lambda}(\tau)\right]_{mn}\left[G_{\alpha}^{\lambda}(-\tau)\right]_{pq} v_{ikmq}^{lr,\lambda}\left(v_{ljpn}^{lr,\lambda}-v_{pjln}^{lr,\lambda}\right) \\
&\quad -\left[G_{\alpha}^{\lambda}(\tau)\right]_{mn}\left[G_{\beta}^{\lambda}(\tau)\right]_{kl}\left[G_{\beta}^{\lambda}(-\tau)\right]_{pq} v_{ikmq}^{lr,\lambda} v_{ljpn}^{lr,\lambda}, \\
\left[\Sigma_{\beta}^{lr,\lambda}(\tau)\right]_{ij} &= -\sum_{klmnpq}\left[G_{\beta}^{\lambda}(\tau)\right]_{kl}\left[G_{\beta}^{\lambda}(\tau)\right]_{mn}\left[G_{\beta}^{\lambda}(-\tau)\right]_{pq} v_{ikmq}^{lr,\lambda}\left(v_{ljpn}^{lr,\lambda}-v_{pjln}^{lr,\lambda}\right) \\
&\quad -\left[G_{\beta}^{\lambda}(\tau)\right]_{mn}\left[G_{\alpha}^{\lambda}(\tau)\right]_{kl}\left[G_{\alpha}^{\lambda}(-\tau)\right]_{pq} v_{ikmq}^{lr,\lambda} v_{ljpn}^{lr,\lambda},
\end{aligned} \tag{8.42}$$

where $G_{kl}^{\lambda}(\tau)$ is the imaginary time Green's function. The algorithm outlined above has been implemented using a locally modified version of the DALTON [100] program for the calculation of long-range two-electron integrals and the short-range SVWN5 exchange-correlation energy and exchange-correlation potential. An in-house GF2 code [50] was used to perform the self-consistent procedure and to calculate the long-range second-order self-energy. The imaginary time Green's function and self-energy that were optimized for realistic systems were evaluated using the Legendre representation [101] and a cubic spline interpolation algorithm [102] was employed to optimize imaginary frequency quantities. The convergence of the total energy with respect to the size of the Legendre expansion, imaginary time and imaginary frequency grids was verified.

Total electronic energies were converged to $5{\cdot}10^{-6}$ a.u. The inverse temperature was set to $\beta = 100$ a.u., corresponding to a physical temperature below the excitation energy necessary to occupy the lowest unoccupied level of all systems considered in this work. Results of standard methods: SVWN5, CCSD(T) and FCI, reported in this work, were obtained with GAUSSIAN 09 [103] program.

8.4 Results and discussion

In this section, we present and analyze numerical results of the application of the srSVWN5—lrGF2 functional to concepts discussed above.

8.4.1 Basis set convergence

In this section, for a series of aug-cc-pVXZ augmented correlation-consistent polarization Dunning basis sets [104–106], we investigated the convergence of the srSVWN5—lrGF2 total energy as a function of the range separation parameter λ for three systems: He and Mg atoms as well as H_2 molecule at the equilibrium distance R(H−H) = 1.4 a.u. We studied the convergence of the total energy with respect to the cardinal number X, corresponding to the highest angular momentum in a given basis set $\mathcal{L}$ (note that for He $X = \mathcal{L} - 1$). The following values of X were used: $X \in \{D, T, Q, 5\}$ for He and $X \in \{D, T, Q\}$ for H_2 and Mg. Relative to the total energy, obtained for a basis set with X=5 for He and X=4 for H_2 and Mg, the total electronic energies of the srSVWN5—lrGF2 functional are plotted in Fig. 8.2.

In Fig. 8.2, SVWN5 energies corresponding to the orange lines with triangles confirm that density functional approximations converge very rapidly with respect to the basis set size. GF2 energies, illustrated by gray lines with diamonds, result in the slowest convergence for every system studied in this work. Any mixture of SVWN5 and GF2 leads to an improved convergence when compared to GF2. For $\lambda < 1$, srSVWN5—

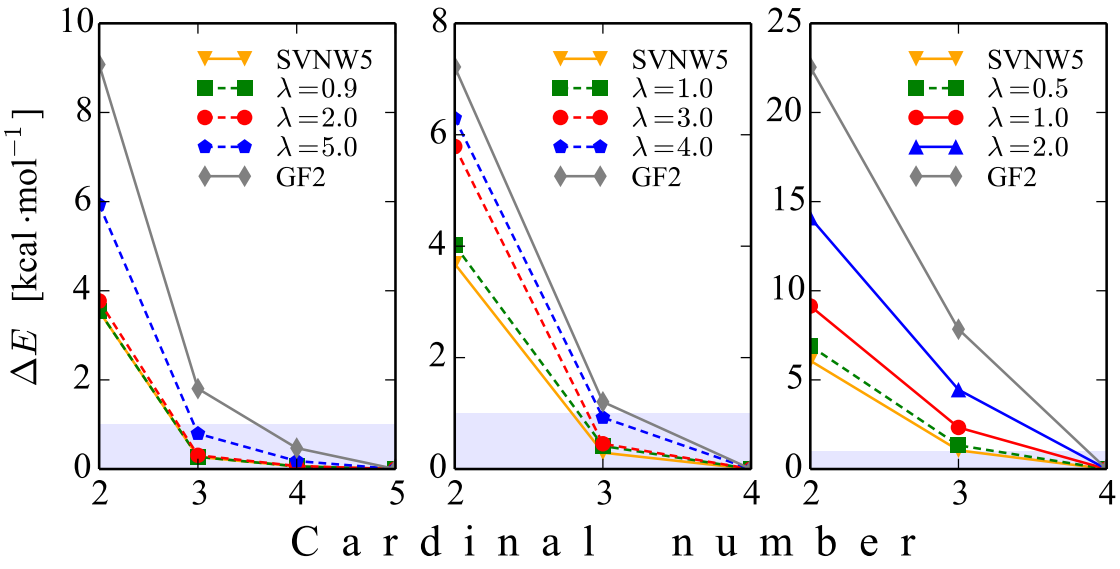

Figure 8.2: Basis set convergence as a function of the range separation parameter λ. $\Delta E = |E_{\text{aug-cc-pVYZ}} - E_{\text{aug-cc-pVXZ}}|$ is plotted on the y-axis, while the cardinal number X is plotted on the x-axis. ΔE is given in kcal·mol^{-1}. The shaded area shown in every plot corresponds to 1 kcal·mol^{-1}. Left panel: Results for the He atom with $X \in \{D, T, Q, 5\}$, $Y = 5$. Middle panel: Results for the H_2 molecule at the equilibrium bond length R(H−H)=1.4 a.u., with $X \in \{D, T, Q\}$, $Y = 4$. Right panel: Results for the Mg atom with $X \in \{D, T, Q\}$, $Y = 4$.

lrGF2 converges as fast as SVWN5 for all the systems considered here. For values of $\lambda > 1$, for both H_2 molecule and Mg atom, the convergence of the srSVWN5—lrGF2 functional is much slower than that one of the parent SVWN5 functional. Filled area shown in every plot corresponds to a difference of 1 kcal·mol^{-1} from the largest basis set used for the system. For all three systems, SVWN5 calculations converged within 1 kcal·mol^{-1} away from the largest basis set for cc-pVTZ (X=3) basis set. For the same basis set, the GF2 energy became almost converged only for H_2 molecule. In Fig. 8.2, for each of the cases analyzed, we also show the largest λ for which the total energy for the cc-pVTZ basis set is 1 kcal·mol^{-1} away from the energy in the largest basis set used in that system. It corresponds to $\lambda = 5$, $\lambda = 4$ and $\lambda = 0.5$ for He, H_2 and Mg respectively.

Similarly to wave-function methods, pure Green's function methods converge fairly slowly with respect to the basis set size. By using the density functional method to describe short-range interactions a faster converge with respect to the basis set size is achieved.

8.4.2 Potential energy curves of diatomic molecules

The accuracy of popular density functionals around equilibrium geometries stems from a satisfactory description of the short-range dynamical correlation. In this section, we illustrate the dynamical correlation in the srSVWN5—lrGF2 functional by analyzing energy of diatomic molecules as a function of internuclear separation.

First, for the H_2 molecule, we looked at the absolute values of the total electronic energy near the equilibrium geometry. We performed spin-restricted total energy calculations using the srSVWN5—lrGF2 functional for different values of the range separation parameter λ scanning over values of interatomic distances around the equilibrium geometry using the cc-pVQZ [104] basis set. The results are illustrated in Fig. 8.3. Full configuration interaction (FCI) energies are shown for comparison. It is clear that GF2

energies are much closer to FCI than SVWN5 ones. This suggests that GF2 recovers the dynamical correlation better than SVWN5. However, obviously due to a finite order truncation, GF2 does not recover all of the dynamical correlation. GF2, SVWN5, and srSVWN5—lrGF2 tend to be inaccurate far away from equilibrium. This is not surprising since all these methods are not well-suited for systems with a significant strong correlation. As the contribution from GF2 increases (orange line $\rightarrow$ green line $\rightarrow$ cyan line, etc), the total energy gradually approaches the FCI energy and when $\lambda \in [0.7, 0.8]$ the total energy becomes almost stationary with respect to changes in λ. For example, E(λ=0.8) $-$ E(λ=0.7) = 0.1 kcal$\cdot$mol^{-1}. In particular, $\lambda = 0.7$ corresponds to the best match of the dynamical correlation coming from two respective approaches and produces an equilibrium distance energy which is only 1.7 kcal$\cdot$mol^{-1} away from FCI. For the same internuclear distance, SVWN5 and GF2 errors are 23.1 kcal$\cdot$mol^{-1} and 4.5 kcal$\cdot$mol^{-1}, respectively. Overall we conclude that the short-range SVWN5 functional is efficient in adding the missing dynamical correlation to GF2.

The second case we considered was the energy of the HF molecule as a function of internuclear separation. Rather than looking at the absolute values of the electronic energy, here we focus on the electronic energies relative to the minimum of the curve. These energies are responsible for the shape of the dissociation curve. The reference energies are provided by CCSD(T) [9, 107] method. The cc-pVQZ basis set was used in all calculations. The results are illustrated in Fig. 8.4. It should be noted that the shape of the GF2 curve is in a very good agreement with that of CCSD(T), while the SVWN5 energy grows too slow with the increasing internuclear separation beyond the equilibrium distance. Mixing GF2 and SVWN5 for small λ up to $\lambda = 0.3 - 0.4$ fixes this behavior and produces the shape approaching the CCSD(T) quality. As λ increases past $\lambda = 0.4$, the energy as a function of the internuclear separation starts to grow too fast. Mixing in a larger fraction of GF2 turns this behavior around and for $\lambda > 1$, srSVWN5—lrGF2 energies start to slowly approach GF2 energies. For in-

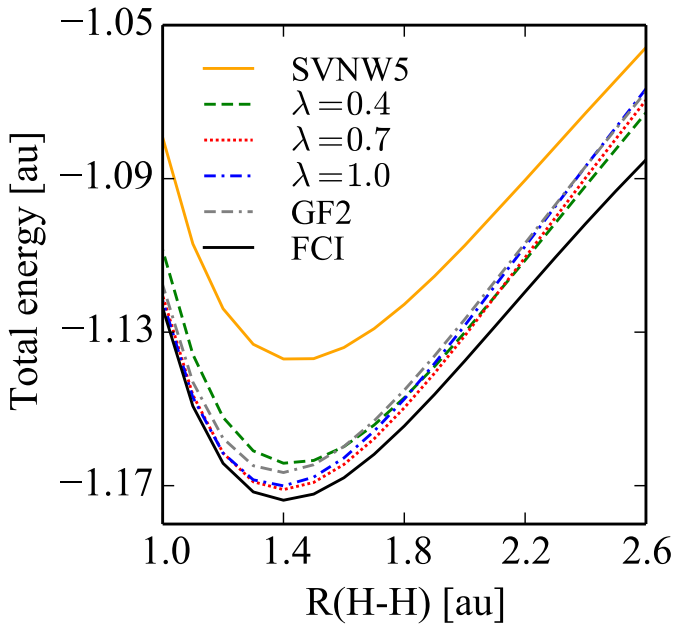

Figure 8.3: The energy of the H_2 molecule as a function of internuclear separation calculated using the srSVWN5—lrGF2 functional for different values of λ. The SVWN5, GF2, and FCI results are shown for comparison. All calculations employed the cc-pVQZ basis set.

ternuclear distances up to R(H−F)=2.3 a.u., $\lambda = 0.5$ produces relative energies closely matching those of GF2 and CCSD(T) methods. We conclude that the srSVWN5—lrGF2 functional is able to reproduce correctly the shape of the dissociation curve near the equilibrium geometry. The srSVWN5—lrGF2 functional does not improve upon GF2, since GF2 being an *ab initio*, perturbative method already correctly describes the dynamical correlations in the HF molecule. Nonetheless, an apparent improvement comes from the fact that with the srSVWN5—lrGF2 functional these energies can be reached using basis sets with a lower angular momentum when compared to standard GF2, as illustrated in the previous Section 8.4.1.

8.4.3 IP tuning of range-separation parameter λ

Following the prescription given in Section 8.2, we have employed an IP-based tuning approach to find optimal values of the range separation parameter λ for seven closed-

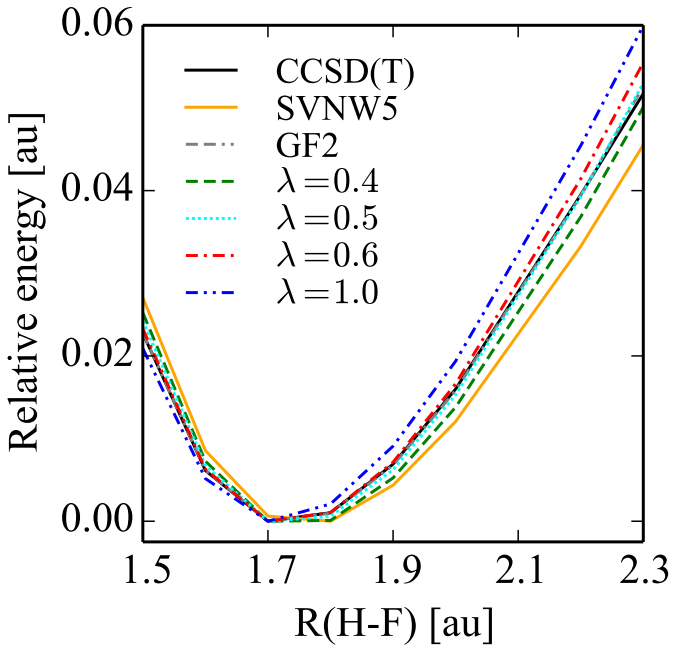

Figure 8.4: The energy of the HF molecule as a function of internuclear separation calculated using the srSVWN5—lrGF2 functional for different values of λ. The SVWN5, GF2 and CCSD(T) results are shown for comparison. All calculations employed the cc-pVQZ basis set.

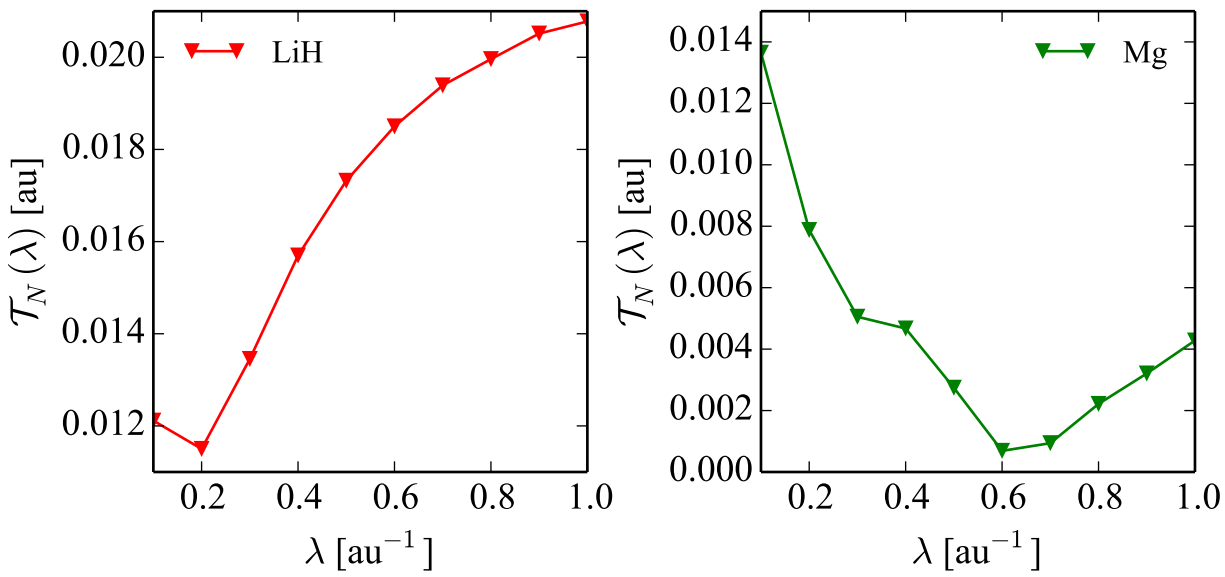

Figure 8.5: The absolute difference, as a function of the range separation parameter λ, between IPs calculated from the Green's function $\mathbf{G}_N^{\lambda}(\omega)$ and $\mathrm{IP}_{E(N)}^{E(N-1)}$ (from Eq. 8.35) using the srSVWN5—lrGF2 functional for LiH molecule (left panel) and Mg atom (right panel). All calculations were performed in the cc-pVTZ basis set.

shell atoms: He, Be, Ne, Mg, Ca, Ar, and Kr, as well as fifteen closed-shell molecules: H_2CO, CH_4, NH_3, N_2, Li_2, CO_2, CO, LiH, CH_3OH, H_2O_2, N_2H_4, H_2S, PH_3, Na_2, and HCN. Experimental geometries were taken from Ref. 108. The cc-pVTZ [104, 106, 109–111] basis set was used for calculations of both atoms and molecules present in this test set. For the cc-pVTZ and larger basis sets, the value of λ remained constant indicating that it is converged with respect to the basis set size.

To find an optimal value of the range separation parameter for each system in the test set, a series of calculations were performed for $\lambda \in [0.1, 1.5]$ with the step-size set to $\Delta\lambda = 0.1$. In most cases, the $\mathcal{T}_N$ norm as a function of λ was found to have one pronounced minimum that was taken as an optimal λ. For illustration purposes, we show $\mathcal{T}_N(\lambda)$ norm for LiH molecule and Mg atom in Fig. 8.5. In the case of Mg atom, a very small discrepancy between the two ways of calculating IP was found for $\lambda = 0.6$ with the error $\mathcal{T}_N \approx 7 \cdot 10^{-4}$ while for LiH molecule the smallest difference between IP $\left[\mathbf{G}_N^{\lambda}(\omega)\right]$ and $\mathrm{IP}_{E(N)}^{E(N-1)}$ turned out to be larger and equal to $\mathcal{T}_N \approx 0.011$

corresponding to the optimal value of $\lambda = 0.2$.

Note that if smaller differences are desired, a further fine-tuning of λ can be performed by using a root-finding algorithm such as bisection [112]. In this work, we adopted a commonly used approach and narrowed the optimal value of λ down to only one decimal point. In a similar way, optimal values of the range separation parameter λ were obtained for all systems in this test set.

To examine how accurately IPs can be calculated based on such an IP-tuning approach, we used the optimally tuned srSVWN5—lrGF2 functional to calculate IPs and compared them with IPs calculated using standard SVWN5 and GF2 methods, as well as experiment. The experimental vertical IPs were taken from Ref. 108. For consistency IPs for GF2, srSVWN5—lrGF2 with the optimal λ, and SVWN5 were calculated according to Eq. 8.35 and listed in Tab. 8.1. It is worth noting that noble gases starting from Ne atom require the same value of $\lambda = 0.5$ and, in general, moving down the periodic table leads to larger optimal values of λ. The mean absolute errors of the srSVWN5—lrGF2 functional, the standard SVWN5 functional, and GF2 are 0.24 eV, 0.26 eV and 0.23 eV, respectively. For the srSVWN5—lrGF2 functional, evaluating the IP either from a Green's function (Eq. 8.41) or from the difference between energies of N and $N-1$ electron systems (Eq. 8.35) leads to the same results and these results are converged with respect to the basis set size. In contrast, for GF2, evaluating the IP from Eq. 8.41 or Eq. 8.35 leads to significantly different results. The GF2 IPs calculated from Eq. 8.41 have large errors since the cc-pVTZ basis set is not large enough. The IPs calculated from Eq. 8.35 benefit from the cancellation of the basis set error. Consequently, the GF2 magnitude of the error that is presented in Tab. 8.1 benefits from fortuitous cancellations of errors. The benefit of using the range separated functional is in the agreement of IP when using both definitions and in avoiding the need of large basis sets. As we observe from Tab. 8.1, GF2 tends to predict better IPs for atoms while the srSVNW5—lrGF2 functional is more accurate for molecules.

Table 8.1: Ionization potentials (IP) calculated as IP = $E_{\text{tot}}(N-1) - E_{\text{tot}}(N)$ using SVWN5, GF2, and srSVWN5—lrGF2 methods. The cc-pVTZ basis set was employed in all calculations. For srSVWN5—lrGF2 calculations, the optimal value of λ is listed in the second column[a].

	Opt.	srSVWN5—lrGF2		GF2		SVWN5		Expt.
	λ	IP	Error	IP	Error	IP	Error	
				Atoms				
He	0.9	24.59	0.00	24.36	0.23	24.30	0.29	24.59
Be	0.1	9.17	0.15	8.83	0.49	9.02	0.30	9.32
Ne	0.5	22.16	0.60	21.50	0.06	22.09	0.53	21.56
Mg	0.6	7.52	0.13	7.31	0.34	7.72	0.07	7.65
Ar	0.5	15.97	0.21	15.66	0.10	16.08	0.32	15.76
Ca	0.7	5.98	0.13	5.93	0.18	6.21	0.10	6.11
Kr	0.5	14.33	0.33	14.03	0.03	14.44	0.44	14.00
				Molecules				
H_2CO	0.1	10.98	0.09	10.86	0.03	10.88	0.01	10.89
CH_4	0.1	14.29	0.06	14.32	0.03	14.02	0.33	14.35
NH_3	0.8	10.72	0.10	10.70	0.12	11.01	0.19	10.82
N_2	0.1	15.66	0.08	15.15	0.43	15.58	0.00	15.58
Li_2	0.3	5.34	0.61	4.94	0.21	5.31	0.58	4.73
CO_2	0.1	14.32	0.55	13.88	0.11	13.99	0.22	13.77
CO	0.1	14.14	0.13	13.72	0.29	14.07	0.06	14.01
CH_3OH	0.1	10.89	0.07	10.96	0.00	10.76	0.20	10.96
LiH	0.2	8.30	0.40	7.75	0.15	8.21	0.31	7.90
H_2O_2	0.1	11.46	0.24	11.19	0.51	11.40	0.30	11.70
N_2H_4	0.1	9.53	0.55	9.56	0.58	9.41	0.43	8.98
H_2S	0.5	10.54	0.04	10.33	0.17	10.63	0.13	10.50
PH_3	0.6	10.57	0.02	10.47	0.12	10.65	0.06	10.59
HCN	1.2	12.09	0.70	12.90	0.70	14.04	0.44	13.60
Na_2	0.6	4.94	0.05	4.68	0.21	5.25	0.36	4.89
m.a.v.			0.24		0.23		0.26	

a Experimental geometries and vertical IPs were taken from NIST Database [108].

8.4.4 Many-electron self-interaction error

The one- and many-electron self-interaction error in approximate density functionals originates from an incomplete cancellation of the spurious electrons self-repulsion by the exchange energy. GF2 includes all the proper exchange and Hartree self-energy diagrams up to the second order and is, therefore, one-electron self-interaction free. We have previously illustrated that GF2 also has a very small two-electron self-interaction error [54]. On the other hand, LDA, is known to have pronounced one- and many-electron self-interaction errors due to a wrong asymptotic decay of the exchange-correlation potential [113]. It seems very likely that an application of GF2 to long-range interactions while keeping LDA within the short range would provide an improvement over LDA by itself. In this section, we analyze in detail the self-interaction error of the srSVWN5—lrGF2 functional. As we mentioned earlier, the fractional charge error is directly related to the self-interaction error. To observe it, we calculated the total electronic energy of He atom as a function of the fractional electron number: $N = 1 + \delta$ for $\delta \in [0, 1]$. In Fig. 8.6, we plot the deviation from the linearity: $\Delta E = E^{\mathcal{M}}(N) - E^{\mathcal{M}}_{\text{lin}}$, where $E^{\mathcal{M}}(N)$ is the energy from method $\mathcal{M}$ calculated for a system with N electrons and $E^{\mathcal{M}}_{\text{lin}}$ is the linear interpolation between integer electron points for the same method $\mathcal{M}$. The IP-tuned optimal value of $\lambda = 0.9$ was used in srSVWN5—lrGF2 calculations. The aug-cc-pVTZ [105] basis set was employed in all calculations. It is clear from Fig. 8.6 that GF2 has a very small fractional charge error showing a small concave behavior, therefore indicating a small localization error. SVWN5 exhibits a massive fractional charge error and pronounced convex character. This opposite behavior of SVWN5 indicates a delocalization error common for local, semilocal, and hybrid density functionals [114]. On the other hand, srSVWN5—lrGF2 calculations for the IP-tuned range separation parameter λ display only a slightly convex behavior and errors that are very similar to GF2, thus greatly improving over SVWN5. We conclude

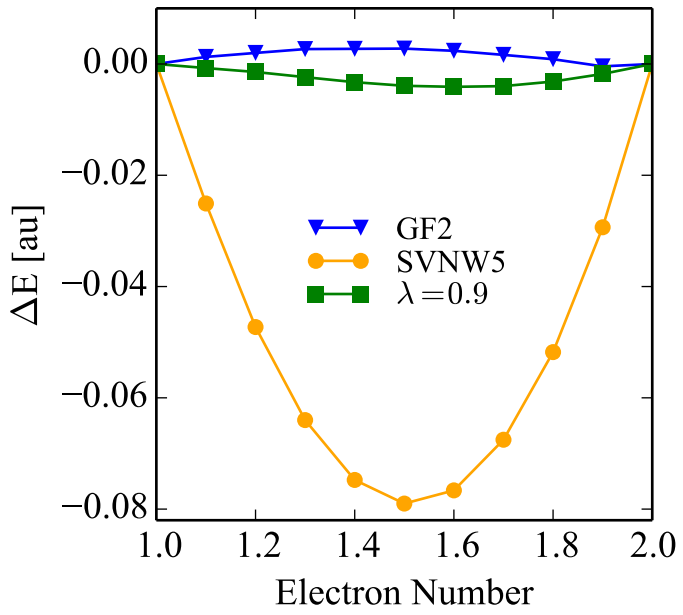

Figure 8.6: The energy difference $\Delta E = E^{\mathcal{M}} - E^{\mathcal{M}}_{\text{lin}}$ for He atom, calculated using the srSVWN5—lrGF2 functional with the IP-tuned optimal value of $\lambda = 0.9$ in comparison to that of SVWN5 and GF2 with the aug-cc-pVTZ basis set. $E^{\mathcal{M}}$ is the energy evaluated with a fractional electron number, and $E^{\mathcal{M}}_{\text{lin}}$ is the linear interpolation between integer electron points for method $\mathcal{M}$.

that adding a fraction of the many-body Green's function method can significantly mitigate the self-interaction error present in the standard density functionals. In this regard, the srSVWN5—lrGF2 functional is similar to popular range-separated hybrid functionals employing the exact exchange for long-range interactions.

8.4.5 Locality of self-energy

In this section, we discuss implications of using range separated hybrid functionals for the self-energy. It is expected that by varying λ the magnitude of self-energy can be gradually changed. To illustrate this, srSVWN5—lrGF2 calculations were performed for three ethylene molecules, each at the experimental geometry [108], placed 2.5 Å apart from each other (see the top panel of Fig. 8.7). A matrix element of the imaginary frequency self-energy between $2p$ orbitals of the two most distant carbon atoms, denoted by red stars on the top panel of Fig. 8.7, is calculated as a function of λ using the DZP [115] basis set. Real and imaginary parts of self-energy for different λ values are shown in the bottom panel of Fig. 8.7 using solid and dashed lines, respectively. Colors from the lightest to the darkest correspond to an increasing fraction of GF2. The self-energy increases most rapidly for small values of λ, up to $\lambda \approx 0.7 - 0.9$, then it begins to slowly converge to the GF2 self-energy. To see it more clearly, in the top panel of Fig. 8.7, we plotted the real part of self-energy for the $n = 0$ Matsubara frequency. It grows most rapidly for the small fractions of GF2. Overall this behavior resembles the error function which is used to scale the two-electron integrals to obtain the long-range terms. The possibility to arbitrarily scale the self-energy in the range separated approach has important consequences. For example, the srSVWN5—lrGF2 calculation is less computationally demanding comparing to the standard GF2 calculation since the evaluation of the self-energy according to Eq. 8.42 can be carried over a truncated set of orbitals due to the faster decay of its matrix elements. Additionally, using a range-separated Green's function functional as a low-level method e.g. in

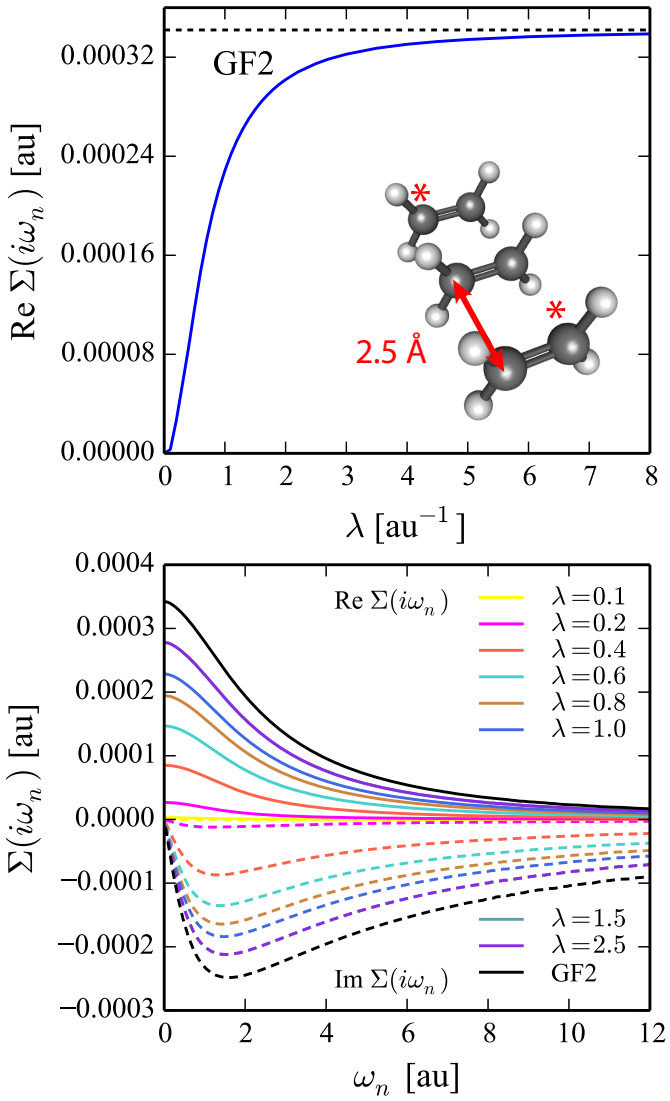

Figure 8.7: Top panel: The real part of the srSVWN5—lrGF2 self-energy matrix element between two carbon atoms denoted by red stars for the $n = 0$ imaginary frequency as a function of the range separation parameter λ for three ethylene molecules arranged as shown in the inset. Bottom panel: Both real (solid lines) and imaginary (dashed lines) parts of the self-energy as a function of the imaginary frequency calculated for different values of λ. All calculations are with DZP basis set.

self-energy embedding theory [51–53, 116] calculations of periodic systems can be beneficial since, as we demonstrated before, such hybrids require smaller basis sets than the original *ab initio* Green's function methods. Consequently, they possibly eliminate many problems such as linear dependencies that happen when large, diffuse basis sets are used in calculations of periodic systems. Moreover, using these hybrid approaches, the number of unit cells required to evaluate the self-energy matrix is lowered due to a faster decay of its intercell matrix elements.

8.5 Conclusions and Outlook

In this paper, we have discussed the theoretical framework for building a range-separated hybrid functional combining both DFT and Green's function methods. In principle, this framework is general and can be used to combine various DFT functionals and Green's function methods. In particular, to maintain the generality of our discussion, we have focused on describing the relationship of this range-separated functional to the Luttinger-Ward functional which is temperature dependent. Since at present, only the zero temperature DFT functionals are well established, we executed all the practical applications of the short-range DFT – long-range Green's function functional using the zero temperature SVWN5 functional in the short range and the temperature dependent GF2 method setting $T \to 0$ in the long range.

We believe that the presented range-separated hybrid functional called srSVWN5—lrGF2 is interesting for two communities. In condensed matter, among the LDA+DMFT practitioners, there has been a long-standing problem of removing the double counting of electron correlation present when LDA is combined with the DMFT treatment employing the Green's function methods. We believe that our presentation of the short-range DFT – long-range Green's function functional is directly relevant to this community and gives a rigorous prescription how to avoid the double counting

problem by employing the range separation of Coulomb integrals. Provided that the range separation parameter λ can be optimized based on one of the exact properties of either the DFT or the Green's function methods, such a range-separated hybrid provides an *ab initio* treatment of realistic systems.

On the other hand, the short-range DFT – long-range Green's function hybrid functional is obviously relevant to the DFT community since it can be viewed as a higher rung of the "Jacob's ladder" of functionals. Similarly to other high rungs, srSVWN5—lrGF2 employs unoccupied orbitals, is non-local, and has an explicit frequency dependence. Provided that explicitly temperature dependent short-range DFT functionals become established enough, the presented functional can also be made temperature dependent in a straightforward manner.

We have demonstrated that our functional offers several attractive advantages compared to the methods used in its construction. Similarly to range-separated hybrid functionals with other many-body methods such as CI, MP2, CASCF, NEVPT2, CCSD, and RPA, srSVWN5—lrGF2 exhibits a rapid convergence with respect to the one-electron basis set. This fast convergence with respect to the basis set size, for the Green's function methods provides an additional advantage, since smaller basis sets require fewer imaginary time and imaginary frequency grid points, resulting in reduced computational cost. Additionally, we have illustrated that the srSVWN5—lrGF2 functional has a smaller self-interaction error in comparison with the standard SVNW5 functional. This is beneficial in calculations involving molecular thermochemistry, reaction barriers, binding energy in charge transfer complexes, polarizabilities, and molecular conductance. Even though the standard density functionals provide an accurate description of the short-range dynamical correlation, we have shown on the example of the HF and H_2 molecules that the srSVWN5—lrGF2 functional can describe the dynamical correlation even more accurately.

Moreover, we presented a first principles approach to finding an optimal value of the

range separation parameter based on the calculation of ionization potentials of atoms and molecules. While the overall accuracy of the IPs evaluated using srSVWN5—lrGF2 is similar to that of GF2 evaluated as the difference between total electronic energies of N and $N-1$ electron systems, srSVWN5—lrGF2 results are converged with respect to the basis set size and do not rely on any fortuitous cancellation of errors. Moreover, for srSVWN5—lrGF2 evaluating the IP directly from the Green's function poles or using the energy difference between N and $N-1$ electron systems results in the same answer. This is not the case for GF2 when the calculations are carried out in a basis set that is not large enough.

We have demonstrated that using the range-separated Coulomb integrals the magnitude of the self-energy in the Green's function method can be modified as a function of the range separation parameter λ. These results demonstrate that srSVWN5—lrGF2 functional can be useful for self-energy embedding calculations as well as for Green's function-based calculations of extended systems since for certain values of the parameter λ the decay of self-energy elements is fast and can contribute to an additional sparsity of the problem. Consequently, a fewer number of self-energy elements need to be evaluated resulting in an overall reduction of the computational cost.

Finally, we believe that there are several directions to further develop short-range DFT with long-range Green's functions hybrid functionals. In its current implementation the local density functional describes not only the short-range interactions but also the coupling region between short-range and long-range correlations [36]. It has been shown [44] that when the coupling region is treated by many-body methods instead of density functionals, such a calculation results in a further improvement of the functional properties. Therefore, the development of such range-separated double-hybrid functionals [117] based on long-range Green's function methods may be worth pursuing.

Another interesting direction for the functional proposed in this work is the study

of metallic systems or systems with small band gaps. Green's function expansions that do not include the infinite sum of bubble diagrams such as a Møller–Plesset Green's function diverge for metallic systems. Such divergences can be efficiently eliminated by screening the electron-electron interactions provided by e. g. the error function. Therefore, functionals employing a range separation similar to the one presented here, may also be applied to periodic calculations of metallic systems in order to avoid a divergent behavior. Furthermore, several choices other than GF2 such as GW or FLEX are possible as long-range Green's function methods. On the density functional side, it is worth investigating short-range semilocal density functionals within the range separation framework.

Bibliography

[1] P. Hohenberg and W. Kohn, "Inhomogeneous electron gas", *Phys. Rev.* **136**, B864 (1964).

[2] W. Kohn and L. J. Sham, "Self-consistent equations including exchange and correlation effects", *Phys. Rev.* **140**, A1133 (1965).

[3] E. Engel and R. Dreizler, *Density Functional Theory: An Advanced Course*, Springer: Berlin, Heidelberg, Germany (2011).

[4] A. Dreuw, J. L. Weisman, and M. Head-Gordon, "Long-range charge-transfer excited states in time-dependent density functional theory require non-local exchange", *J. Chem. Phys.* **119**, 2943 (2003).

[5] S. Kristyán and P. Pulay, "Can (semi)local density functional theory account for the London dispersion forces?", *Chem. Phys. Lett.* **229**, 175 (1994).

[6] D. J. Tozer and N. C. Handy, "Improving virtual Kohn-Sham orbitals and eigenvalues: Application to excitation energies and static polarizabilities", *J. Chem. Phys.* **109**, 10180 (1998).

[7] J. P. Perdew and A. Zunger, "Self-interaction correction to density-functional approximations for many-electron systems", *Phys. Rev. B* **23**, 5048 (1981).

[8] C. Møller and M. S. Plesset, "Note on an approximation treatment for many-electron systems", *Phys. Rev.* **46**, 618 (1934).

[9] R. J. Bartlett and M. Musiał, "Coupled-cluster theory in quantum chemistry", *Rev. Mod. Phys.* **79**, 291 (2007).

[10] B. Roos, R. Lindh, P. Malmqvist, V. Veryazov, and P. Widmark, *Multiconfigurational Quantum Chemistry*, Wiley & Sons, Inc.: Hoboken, NJ (2016).

[11] H. Stoll and A. Savin, in *Density functional Methods in Physics*, edited by R. M. Dreizler and J. da Providência, Plenum Press: New York, NY, USA (1985).

[12] T. Leininger, H. Stoll, H.-J. Werner, and A. Savin, "Combining long-range configuration interaction with short-range density functionals", *Chem. Phys. Lett.* **275**, 151 (1997).

[13] J. Toulouse, F. Colonna, and A. Savin, "Long-range-short-range separation of the electron-electron interaction in density-functional theory", *Phys. Rev. A* **70**, 062505 (2004).

[14] R. Baer, E. Livshits, and U. Salzner, "Tuned range-separated hybrids in density functional theory", *Annu. Rev. Phys. Chem.* **61**, 85 (2010).

[15] T. Yanai, D. P. Tew, and N. C. Handy, "A new hybrid exchange-correlation functional using the Coulomb-attenuating method (CAM-B3LYP)", *Chem. Phys. Lett.* **393**, 51 (2004).

[16] J. Heyd, G. E. Scuseria, and M. Ernzerhof, "Hybrid functionals based on a screened Coulomb potential", *J. Chem. Phys.* **118**, 8207 (2003).

[17] H. Iikura, T. Tsuneda, T. Yanai, and K. Hirao, "A long-range correction scheme for generalized-gradient-approximation exchange functionals", *J. Chem. Phys.* **115**, 3540 (2001).

[18] J.-D. Chai and M. Head-Gordon, "Systematic optimization of long-range corrected hybrid density functionals", *J. Chem. Phys.* **128**, 084106 (2008).

[19] O. A. Vydrov and G. E. Scuseria, "Assessment of a long-range corrected hybrid functional", *J. Chem. Phys.* **125**, 234109 (2006).

[20] Y. Tawada, T. Tsuneda, S. Yanagisawa, T. Yanai, and K. Hirao, "A long-range-corrected time-dependent density functional theory", *J. Chem. Phys.* **120**, 8425 (2004).

[21] M. J. G. Peach, T. Helgaker, P. Salek, T. W. Keal, O. B. Lutnaes, D. J. Tozer, and N. C. Handy, "Assessment of a Coulomb-attenuated exchange-correlation energy functional", *Phys. Chem. Chem. Phys.* **8**, 558 (2006).

[22] J. G. Ángyán, I. C. Gerber, A. Savin, and J. Toulouse, "van der Waals forces in density functional theory: Perturbational long-range electron-interaction corrections", *Phys. Rev. A* **72**, 012510 (2005).

[23] E. Fromager and H. J. A. Jensen, "Self-consistent many-body perturbation theory in range-separated density-functional theory: A one-electron reduced-density-matrix-based formulation", *Phys. Rev. A* **78**, 022504 (2008).

[24] O. Kullie and T. Saue, "Range-separated density functional theory: A 4-component relativistic study of the rare gas dimers He_2, Ne_2, Ar_2, Kr_2, Xe_2, Rn_2 and Uuo_2", *Chem. Phys.* **395**, 54 (2012).

[25] J. G. Ángyán, "Rayleigh-Schrödinger many-body perturbation theory for density functionals: A unified treatment of one- and two-electron perturbations", *Phys. Rev. A* **78**, 022510 (2008).

[26] E. Fromager, R. Cimiraglia, and H. J. A. Jensen, "Merging multireference perturbation and density-functional theories by means of range separation: Potential curves for Be_2, Mg_2, and Ca_2", *Phys. Rev. A* **81**, 024502 (2010).

[27] E. Goll, H.-J. Werner, and H. Stoll, "A short-range gradient-corrected density functional in long-range coupled-cluster calculations for rare gas dimers", *Phys. Chem. Chem. Phys.* **7**, 3917 (2005).

[28] B. G. Janesko, T. M. Henderson, and G. E. Scuseria, "Long-range-corrected hybrids including random phase approximation correlation", *J. Chem. Phys.* **130**, 081105 (2009).

[29] J. Toulouse, I. C. Gerber, G. Jansen, A. Savin, and J. G. Ángyán, "Adiabatic-connection fluctuation-dissipation density-functional theory based on range separation", *Phys. Rev. Lett.* **102**, 096404 (2009).

[30] J. Toulouse, W. Zhu, J. G. Ángyán, and A. Savin, "Range-separated density-functional theory with the random-phase approximation: Detailed formalism and illustrative applications", *Phys. Rev. A* **82**, 032502 (2010).

[31] R. Pollet, A. Savin, T. Leininger, and H. Stoll, "Combining multideterminantal wave functions with density functionals to handle near-degeneracy in atoms and molecules", *J. Chem. Phys.* **116**, 1250 (2002).

[32] E. Fromager, F. Réal, P. Wåhlin, U. Wahlgren, and H. J. A. Jensen, "On the universality of the long-short-range separation in multiconfigurational density-functional theory. II. Investigating f0 actinide species", *J. Chem. Phys.* **131**, 054107 (2009).

[33] E. Fromager, J. Toulouse, and H. J. A. Jensen, "On the universality of the long-/short-range separation in multiconfigurational density-functional theory", *J. Chem. Phys.* **126**, 074111 (2007).

[34] K. Pernal, "Long-range density-matrix-functional theory: Application to a modified homogeneous electron gas", *Phys. Rev. A* **81**, 052511 (2010).

[35] D. R. Rohr, J. Toulouse, and K. Pernal, "Combining density-functional theory and density-matrix-functional theory", *Phys. Rev. A* **82**, 052502 (2010).

[36] J. Toulouse, A. Savin, and H.-J. Flad, "Short-range exchange-correlation energy of a uniform electron gas with modified electron-electron interaction", *Int. J. Quantum Chem.* **100**, 1047 (2004).

[37] P. Gori-Giorgi and A. Savin, "Properties of short-range and long-range correlation energy density functionals from electron-electron coalescence", *Phys. Rev. A* **73**, 032506 (2006).

[38] I. C. Gerber and J. G. Ángyán, "Potential curves for alkaline-earth dimers by density functional theory with long-range correlation corrections", *Chem. Phys. Lett.* **416**, 370 (2005).

[39] R.-F. Liu, C. A. Franzese, R. Malek, P. S. Żuchowski, J. G. Ángyán, M. M. Szczęśniak, and G. Chałasiński, "Aurophilic interactions from wave function, symmetry-adapted perturbation theory, and rangehybrid approaches", *J. Chem. Theory Comput.* **7**, 2399 (2011).

[40] W. Zhu, J. Toulouse, A. Savin, and J. G. Ángyán, "Range-separated density-functional theory with random phase approximation applied to noncovalent intermolecular interactions", *J. Chem. Phys.* **132**, 244108 (2010).

[41] J. Paier, B. G. Janesko, T. M. Henderson, G. E. Scuseria, A. Grüneis, and G. Kresse, "Hybrid functionals including random phase approximation correlation and second-order screened exchange", *J. Chem. Phys.* **132**, 094103 (2010).

[42] O. Franck, B. Mussard, E. Luppi, and J. Toulouse, "Basis convergence of range-separated density-functional theory", *J. Chem. Phys.* **142**, 074107 (2015).

[43] B. G. Janesko and G. E. Scuseria, "Coulomb-only second-order perturbation theory in long-range-corrected hybrid density functionals", *Phys. Chem. Chem. Phys.* **11**, 9677 (2009).

[44] Y. Cornaton, A. Stoyanova, H. J. A. Jensen, and E. Fromager, "Alternative separation of exchange and correlation energies in range-separated density-functional perturbation theory", *Phys. Rev. A* **88**, 022516 (2013).

[45] B. G. Janesko, T. M. Henderson, and G. E. Scuseria, "Long-range-corrected hybrid density functionals including random phase approximation correlation: Application to noncovalent interactions", *J. Chem. Phys.* **131**, 034110 (2009).

[46] R. M. Irelan, T. M. Henderson, and G. E. Scuseria, "Long-range-corrected hybrids using a range-separated Perdew-Burke-Ernzerhof functional and random phase approximation correlation", *J. Chem. Phys.* **135**, 094105 (2011).

[47] A. L. Fetter and J. D. Walecka, *Quantum Theory of Many-Particle Systems*, Dover Publications: Mineola, NY, USA (2003).

[48] G. Stefanucci and R. van Leeuwen, *Nonequilibrium Many-Body Theory of Quantum Systems: A Modern Introduction*, Cambridge University Press: Cambridge, UK (2013).

[49] A. Abrikosov, L. Gorkov, and I. E. Dzyaloshinski, *Methods of Quantum Field Theory in Statistical Physics*, Dover Publications, Inc.: New York, USA (1963).

[50] J. J. Phillips and D. Zgid, "Communication: The description of strong correlation within self-consistent Green's function second-order perturbation theory", *J. Chem. Phys.* **140**, 241101 (2014).

[51] A. A. Kananenka, E. Gull, and D. Zgid, "Systematically improvable multiscale solver for correlated electron systems", *Phys. Rev. B* **91**, 121111 (2015).

[52] T. N. Lan, A. A. Kananenka, and D. Zgid, "Communication: Towards ab initio self-energy embedding theory in quantum chemistry", *J. Chem. Phys.* **143**, 241102 (2015).

[53] T. N. Lan and D. Zgid, "Generalized self-energy embedding theory", *J. Phys. Chem. Lett.* **8**, 2200 (2017).

[54] J. J. Phillips, A. A. Kananenka, and D. Zgid, "Fractional charge and spin errors in self-consistent Green's function theory", *J. Chem. Phys.* **142**, 194108 (2015).

[55] P. A. M. Dirac, "Note on exchange phenomena in the Thomas atom", *Math. Proc. Cambridge Philos. Soc.* **26**, 376 (1930).

[56] S. H. Vosko, L. Wilk, and M. Nusair, "Accurate spin-dependent electron liquid correlation energies for local spin density calculations: a critical analysis", *Can. J. Phys.* **58**, 1200 (1980).

[57] L. J. Holleboom and J. G. Snijders, "A comparison between the Møller-Plesset and Green's function perturbative approaches to the calculation of the correlation energy in the many-electron problem", *J.Chem. Phys.* **93**, 5826 (1990).

[58] N. E. Dahlen and R. van Leeuwen, "Self-consistent solution of the Dyson equation for atoms and molecules within a conserving approximation", *J. Chem. Phys.* **122**, 164102 (2005).

[59] P. Mori-Sánchez, A. J. Cohen, and W. Yang, "Failure of the random-phase-approximation correlation energy", *Phys. Rev. A* **85**, 042507 (2012).

[60] G. Kotliar, S. Y. Savrasov, K. Haule, V. S. Oudovenko, O. Parcollet, and C. A. Marianetti, "Electronic structure calculations with dynamical mean-field theory", *Rev. Mod. Phys.* **78**, 865 (2006).

[61] A. Georges and G. Kotliar, "Hubbard model in infinite dimensions", *Phys. Rev. B* **45**, 6479 (1992).

[62] J. Lee and K. Haule, "Dynamical mean field theory for diatomic molecules and the exact double counting", *Phys. Rev. B* **91**, 155144 (2015).

[63] V. I. Anisimov, F. Aryasetiawan, and A. I. Lichtenstein, "First-principles calculations of the electronic structure and spectra of strongly correlated systems: the LDA + U method", *J. Phys. Cond. Mat.* **9**, 767 (1997).

[64] K. Haule, C.-H. Yee, and K. Kim, "Dynamical mean-field theory within the full-potential methods: Electronic structure of $CeIrIn_5$, $CeCoIn_5$, and $CeRhIn_5$", *Phys. Rev. B* **81**, 195107 (2010).

[65] M. A. Rohrdanz and J. M. Herbert, "Simultaneous benchmarking of ground- and excited-state properties with long-range-corrected density functional theory", *J. Chem. Phys.* **129**, 034107 (2008).

[66] T. Stein, H. Eisenberg, L. Kronik, and R. Baer, "Fundamental gaps in finite systems from eigenvalues of a generalized Kohn-Sham method", *Phys. Rev. Lett.* **105**, 266802 (2010).

[67] T. Körzdörfer, J. S. Sears, C. Sutton, and J.-L. Brédas, "Long-range corrected hybrid functionals for π-conjugated systems: Dependence of the range-separation parameter on conjugation length", *J. Chem. Phys.* **135**, 204107 (2011).

[68] E. Livshits and R. Baer, "A well-tempered density functional theory of electrons in molecules", *Phys. Chem. Chem. Phys.* **9**, 2932 (2007).

[69] J.-W. Song, T. Hirosawa, T. Tsuneda, and K. Hirao, "Long-range corrected density functional calculations of chemical reactions: Redetermination of parameter", *J. Chem. Phys.* **126**, 154105 (2007).

[70] M. Levy, "Universal variational functionals of electron densities, first-order density matrices, and natural spin-orbitals and solution of the v-representability problem", *Proc. Natl. Acad. Sci. U.S.A.* **76**, 6062 (1979).

[71] J. Harris and R. O. Jones, "The surface energy of a bounded electron gas", *J. Phys. F: Met. Phys.* **4**, 1170 (1974).

[72] O. Gunnarsson and B. I. Lundqvist, "Exchange and correlation in atoms, molecules, and solids by the spin-density-functional formalism", *Phys. Rev. B* **13**, 4274 (1976).

[73] D. C. Langreth and J. P. Perdew, "Exchange-correlation energy of a metallic surface: Wave-vector analysis", *Phys. Rev. B* **15**, 2884 (1977).

[74] J. Harris, "Adiabatic-connection approach to Kohn-Sham theory", *Phys. Rev. A* **29**, 1648 (1984).

[75] J. P. Dombroski, S. W. Taylor, and P. M. W. Gill, "KWIK: Coulomb energies in O(N) work", *J. Phys. Chem.* **100**, 6272 (1996).

[76] P. M. W. Gill, R. D. Adamson, and J. A. Pople, "Coulomb-attenuated exchange energy density functionals", *Mol. Phys.* **88**, 1005 (1996).

[77] J. P. Perdew and Y. Wang, "Accurate and simple analytic representation of the electron-gas correlation energy", *Phys. Rev. B* **45**, 13244 (1992).

[78] A. Seidl, A. Görling, P. Vogl, J. A. Majewski, and M. Levy, "Generalized Kohn-Sham schemes and the band-gap problem", *Phys. Rev. B* **53**, 3764 (1996).

[79] R. Jishi, *Feynman Diagram Techniques in Condensed Matter Physics*, Cambridge University Press: Cambridge, UK (2014), pp 179-210.

[80] L. Hedin, "New method for calculating the one-particle Green's function with application to the electron-gas problem", *Phys. Rev.* **139**, A796 (1965).

[81] F. Aryasetiawan and O. Gunnarsson, "The GW method", *Rep. Prog. Phys.* **61**, 237 (1998).

[82] N. E. Bickers, D. J. Scalapino, and S. R. White, "Conserving approximations for strongly correlated electron systems: Bethe-Salpeter equation and dynamics for the two-dimensional Hubbard model", *Phys. Rev. Lett.* **62**, 961 (1989).

[83] N. Bickers and D. Scalapino, "Conserving approximations for strongly fluctuating electron systems. I. Formalism and calculational approach", *Ann. Phys.* **193**, 206 (1989).

[84] G. Baym and L. P. Kadanoff, "Conservation laws and correlation functions", *Phys. Rev.* **124**, 287 (1961).

[85] G. Baym, "Self-consistent approximations in many-body systems", *Phys. Rev.* **127**, 1391 (1962).

[86] Y. Lu, M. Höppner, O. Gunnarsson, and M. W. Haverkort, "Efficient real-frequency solver for dynamical mean-field theory", *Phys. Rev. B* **90**, 085102 (2014).

[87] D. Van Neck, K. Peirs, and M. Waroquier, "Self-consistent solution of Dyson's equation up to second order for atomic systems", *J. Chem. Phys.* **115**, 15 (2001).

[88] K. Peirs, D. Van Neck, and M. Waroquier, "Self-consistent solution of Dyson's equation up to second order for open-shell atomic systems", *J. Chem. Phys.* **117**, 4095 (2002).

[89] T. Matsubara, "A new approach to quantum-statistical mechanics", *Prog. Theor. Phys.* **14**, 351 (1955).

[90] V. M. Galitskii and A. B. Migdal, "Application of quantum field theory methods to the many body problem", *J. Exptl. Theoret. Phys.* **34**, 139 (1958).

[91] J. M. Luttinger and J. C. Ward, "Ground-state energy of a many-fermion system. II", *Phys. Rev.* **118**, 1417 (1960).

[92] D. W. Smith and O. W. Day, "Extension of Koopmans' theorem. I. Derivation", *J. Chem. Phys.* **62**, 113 (1975).

[93] O. W. Day, D. W. Smith, and R. C. Morrison, "Extension of Koopmans' theorem. II. Accurate ionization energies from correlated wavefunctions for closed-shell atoms", *J. Chem. Phys.* **62**, 115 (1975).

[94] J. M. O. Matos and O. W. Day, "The extended Koopmans' theorem Fock operator", *Int. J. Quantum Chem.* **31**, 871 (1987).

[95] R. C. Morrison, "The extended Koopmans theorem and its exactness", *J. Chem. Phys.* **96**, 3718 (1992).

[96] A. Szabo and N. Ostlund, *Modern Quantum Chemistry: Introduction to Advanced Electronic Structure Theory*, McGraw-Hill, Inc.: USA (1989).

[97] J. P. Perdew, R. G. Parr, M. Levy, and J. L. Balduz, "Density-functional theory for fractional particle number: Derivative discontinuities of the energy", *Phys. Rev. Lett.* **49**, 1691 (1982).

[98] J. P. Perdew, A. Ruzsinszky, G. I. Csonka, O. A. Vydrov, G. E. Scuseria, V. N. Staroverov, and J. Tao, "Exchange and correlation in open systems of fluctuating electron number", *Phys. Rev. A* **76**, 040501 (2007).

[99] P. Mori-Sánchez, A. J. Cohen, and W. Yang, "Many-electron self-interaction error in approximate density functionals", *J. Chem. Phys.* **125**, 201102 (2006).

[100] K. Aidas, C. Angeli, K. L. Bak, V. Bakken, R. Bast, L. Boman, O. Christiansen, R. Cimiraglia, S. Coriani, P. Dahle, E. K. Dalskov, U. Ekström, T. Enevoldsen, J. J. Eriksen, P. Ettenhuber, B. Fernández, L. Ferrighi, H. Fliegl, L. Frediani, K. Hald, A. Halkier, C. Hättig, H. Heiberg, T. Helgaker, A. C. Hennum, H. Hettema, E. Hjertenæs, S. Høst, I.-M. Høyvik, M. F. Iozzi, B. Jansík, H. J. Aa. Jensen, D. Jonsson, P. Jørgensen, J. Kauczor, S. Kirpekar, T. Kjærgaard, W. Klopper, S. Knecht, R. Kobayashi, H. Koch, J. Kongsted, A. Krapp, K. Kristensen, A. Ligabue, O. B. Lutnæs, J. I. Melo, K. V. Mikkelsen, R. H. Myhre, C. Neiss, C. B. Nielsen, P. Norman, J. Olsen, J. M. H. Olsen, A. Osted, M. J. Packer, F. Pawlowski, T. B. Pedersen, P. F. Provasi, S. Reine, Z. Rinkevicius, T. A. Ruden, K. Ruud, V. V. Rybkin, P. Sałek, C. C. M. Samson, A. S. de Merás, T. Saue, S. P. A. Sauer, B. Schimmelpfennig, K. Sneskov, A. H. Steindal, K. O. Sylvester-Hvid, P. R. Taylor, A. M. Teale, E. I. Tellgren, D. P. Tew, A. J. Thorvaldsen, L. Thøgersen, O. Vahtras, M. A. Watson, D. J. D. Wilson, M. Ziolkowski, and H. Ågren, "The Dalton quantum chemistry program system", *Wiley Interdiscip. Rev. Comput. Mol. Sci.* **4**, 269 (2014).

[101] A. A. Kananenka, J. J. Phillips, and D. Zgid, "Efficient temperature-dependent Green's functions methods for realistic systems: Compact grids for orthogonal polynomial transforms", *J. Chem. Theory Comput.* **12**, 564 (2016).

[102] A. A. Kananenka, A. R. Welden, T. N. Lan, E. Gull, and D. Zgid, "Efficient temperature-dependent Green's function methods for realistic systems: Using cubic spline interpolation to approximate Matsubara Green's functions", *J. Chem. Theory Comput.* **12**, 2250 (2016).

[103] M. J. Frisch, G. W. Trucks, H. B. Schlegel, G. E. Scuseria, M. A. Robb, J. R. Cheeseman, G. Scalmani, V. Barone, B. Mennucci, G. A. Petersson, H. Nakatsuji, M. Caricato, X. Li, H. P. Hratchian, A. F. Izmaylov, J. Bloino, G. Zheng, J. L. Sonnenberg, M. Hada, M. Ehara, K. Toyota, R. Fukuda, J. Hasegawa, M. Ishida,

T. Nakajima, Y. Honda, O. Kitao, H. Nakai, T. Vreven, J. A. Montgomery, Jr., J. E. Peralta, F. Ogliaro, M. Bearpark, J. J. Heyd, E. Brothers, K. N. Kudin, V. N. Staroverov, R. Kobayashi, J. Normand, K. Raghavachari, A. Rendell, J. C. Burant, S. S. Iyengar, J. Tomasi, M. Cossi, N. Rega, J. M. Millam, M. Klene, J. E. Knox, J. B. Cross, V. Bakken, C. Adamo, J. Jaramillo, R. Gomperts, R. E. Stratmann, O. Yazyev, A. J. Austin, R. Cammi, C. Pomelli, J. W. Ochterski, R. L. Martin, K. Morokuma, V. G. Zakrzewski, G. A. Voth, P. Salvador, J. J. Dannenberg, S. Dapprich, A. D. Daniels, Ö. Farkas, J. B. Foresman, J. V. Ortiz, J. Cioslowski, and D. J. Fox, "Gaussian 09 Revision A.01", Gaussian, Inc., Wallingford, CT, 2009.

[104] T. H. Dunning, "Gaussian basis sets for use in correlated molecular calculations. I. The atoms boron through neon and hydrogen", *J. Chem. Phys.* **90**, 1007 (1989).

[105] D. E. Woon and T. H. Dunning, "Gaussian basis sets for use in correlated molecular calculations. IV. Calculation of static electrical response properties", *J. Chem. Phys.* **100**, 2975 (1994).

[106] B. P. Prascher, D. E. Woon, K. A. Peterson, T. H. Dunning, and A. K. Wilson, "Gaussian basis sets for use in correlated molecular calculations. VII. Valence, core-valence, and scalar relativistic basis sets for Li, Be, Na, and Mg", *Theor. Chem. Acc.* **128**, 69 (2011).

[107] K. Raghavachari, G. W. Trucks, J. A. Pople, and M. Head-Gordon, "A fifth-order perturbation comparison of electron correlation theories", *Chem. Phys. Lett.* **157**, 479 (1989).

[108] R. D. Johnson, "NIST Computational Chemistry Comparison and Benchmark Database", Standard Reference Database Number 101 Release 16a.

[109] A. K. Wilson, D. E. Woon, K. A. Peterson, and T. H. Dunning, "Gaussian basis sets for use in correlated molecular calculations. IX. The atoms gallium through krypton", *J. Chem. Phys.* **110**, 7667 (1999).

[110] D. E. Woon and T. H. Dunning, "Gaussian basis sets for use in correlated molecular calculations. III. The atoms aluminum through argon", *J. Chem. Phys.* **98**, 1358 (1993).

[111] J. Koput and K. A. Peterson, "Ab initio potential energy surface and vibrational-rotational energy levels of X2σ^+ CaOH", *J. Phys. Chem. A* **106**, 9595 (2002).

[112] R. Burden and J. Faires, *Numerical analysis*, Brooks/Cole, Cengage Learning: Boston, MA, USA (2010).

[113] R. van Leeuwen and E. J. Baerends, "Exchange-correlation potential with correct asymptotic behavior", *Phys. Rev. A* **49**, 2421 (1994).

[114] A. J. Cohen, P. Mori-Sánchez, and W. Yang, "Challenges for density functional theory", *Chem. Rev.* **112**, 289 (2012).

[115] T. H. Dunning, "Gaussian basis functions for use in molecular calculations. I. Contraction of (9s5p) atomic basis sets for the firstrow atoms", *J. Chem. Phys.* **53**, 2823 (1970).

[116] T. N. Lan, A. A. Kananenka, and D. Zgid, "Rigorous ab initio quantum embedding for quantum chemistry using Greens function theory: Screened interaction, nonlocal self-energy relaxation, orbital basis, and chemical accuracy", *J. Chem. Theory Comput.* **12**, 4856 (2016).

[117] J. Toulouse, P. Gori-Giorgi, and A. Savin, "A short-range correlation energy density functional with multi-determinantal reference", *Theor. Chem. Acc.* **114**, 305 (2005).

Chapter 9

Summary and outlook

This work shows the significant progress achieved in the understanding, development and application of finite-temperature Green's function methods in computational quantum chemistry. New theoretical methods and numerical algorithms presented in this work can be applied to study realistic materials ranging from weakly correlated to strongly correlated in a rigorous and systematically improvable way. The work presented here sucessfully deals with the difficulties arising when established in condensed matter physics finite-temperature Green's function methods are challenged by the *ab initio* Hamiltonians describing real systems. The self-energy embedding theory is ideally suited to study realistic systems with multiple strongly correlated orbitals embedded into many weakly correlated ones. Quantum impurity solvers were applied to the strongly correlated orbitals and two such solvers were explored. SEET with configuration interaction based solver has been shown to produce very accurate results. The finite-temperature effects are only accounted for by the Matsubara grid which is used to represent correlated Green's function. Therefore, the development of explicitly temperature-dependent configuration interaction based solvers is highly desirable and likely to provide even more improvement. Explicitly temperature-dependent continious-time hybridization expansion quantum Monte Carlo solver was also examined in this work. Unfortunately, due to severe sign errors its use is restricted to diagonal hybridizations limiting its applications to model Hamiltonians and weakly

entangled realistic systems.

Several choices of weakly correalted methods are possible too. In this work only second-order Green's function theory has been considered. It is based on truncation of expansion of the correlated Green's function to the second order. Other alternative candidates for a low-level method include methods based on summing specific types of diagrams to infinite order such as GW approximation or FLEX which in addition to GW diagrams also includes ladder diagrams. These methods are frequently considered since they are computationally affordable and can be easily implemented. The work in this direction is currently underway.

Another promising direction that the ideas presented in work can be useful for is the further development of range-separated hybrid functionals. It is known that the second-order Green's function theory applied to metallic systems diverges. However the reverse hybrid combining short-range GF2 and long-range nonperturbative (e.g. density functional theory) method is expected to produce convergent results. This should pave the way to the applications of Green's function methods to realistic metallic systems.

Although several challenges remain, the methodology and algorithms presented in this work certainly advances the field of finite-temperature Green's function methods to the realistic *ab initio* domain.

Appendix

Details of the SEET(ED-in-GF2) scheme

Here we summarize the major algorithmic steps of the SEET(ED-in-GF2) algorithm.

1. We start by converging the iterative DCA procedure using GF2 as a solver for the chosen cluster. Here GF2 can be run either to the first iteration or fully self-consistently and we obtain a correlated Green's function

$$G_{cluster}(i\omega) = \left([G^0_{DCA}(i\omega)^{-1} - \Sigma^{GF2}(i\omega)\right)^{-1}. \tag{9.1}$$

2. Upon DCA convergence, we evaluate the one-body density matrix $\gamma\left[G_{cluster}(i\omega)\right]$ in the cluster and find the natural orbitals. The natural orbitals are the orbitals in which the density matrix diagonal.

3. We choose n strongly correlated orbitals based on the occupations of the density matrix.

4. We construct an impurity model (or several impurity models, see below) using the strongly correlated orbitals.

5. The t operator and the U operator of the strongly correlated orbitals as well as the Green's function are transformed to the basis of natural orbitals. In this basis

the operator U is no longer local

$$[G_{cluster}(i\omega)]_{ij} = \left[i\omega - t - \Sigma^{ED}_{strong}(i\omega) - \Delta(i\omega)^{-1}\right]. \tag{9.2}$$

6. Using $\Delta(i\omega)$ we define the bath orbitals and interactions in the impurity model containing the strongly correlated orbitals.

7. In this impurity model we calculate the self-energy $\Sigma^{ED}_{strong}(i\omega)$ for strongly correlated orbitals using exact diagonalization.

8. We set up the total new self-energy as

$$[\Sigma]_{ij} = \left[\Sigma^{ED}_{strong}\right]_{\mu\nu} + \left[\Sigma^{GF2}\right]_{ij} - \left[\Sigma^{GF2}_{strong}\right]_{ij}. \tag{9.3}$$

   Note that "strong" denotes the correlated subspace formed by $\mu, \nu = 1, \ldots, n$, while "ij" denotes indices of all N orbitals. $\left[\Sigma^{GF2}_{strong}\right]_{\mu\nu}$ is the GF2 self-energy for the strongly correlated orbitals that must be subtracted in order to avoid double counting.

9. We evaluate correlated Green's function using the Dyson equation and pass it to DCA

$$G^{new}_{cluster}(i\omega) = \left([G_{DCA}(i\omega)]^{-1} - \Sigma(i\omega)\right)^{-1}. \tag{9.4}$$

10. DCA performs an iteration to obtain the new Green's function.

11. Using the DCA Green's function go to point 1 upon convergence of total self-energy, exit.

It is possible to construct several impurity models using the correlated orbitals. In this case of four-site cluster we have constructed two impurity models with two impurity orbitals. This implies that cross-correlations between those orbitals will only

be treated on the GF2 level, an approximation that can be validated by choosing different impurities.